

Coriolis effects in bladed discs

Valentina Ruffini

A thesis submitted to Imperial College London for the degree of Doctor of Philosophy and
the Diploma of Imperial College
January 2016

Department of Mechanical Engineering
Imperial College London

Declaration of Originality

I declare that the contents of this thesis are entirely my own work, and that any additional sources of information have been duly cited.

Copyright Declaration

The copyright of this thesis rests with the author and is made available under a Creative Commons Attribution Non-Commercial No Derivatives licence. Researchers are free to copy, distribute or transmit the thesis on the condition that they attribute it, that they do not use it for commercial purposes and that they do not alter, transform or build upon it. For any reuse or redistribution, researchers must make clear to others the licence terms of this work.

Abstract

New aero-engine architectures are currently being developed to satisfy the increasing demand for fuel-efficiency and lower noise, pushing the boundaries of today's design practice. These unproven designs require additional effort to ensure safety to high-cycle fatigue and flutter, widely acknowledged as a main risk for turbomachinery components. This calls for a new focus on phenomena that have been little investigated in the past due to their minor relevance for traditional designs, like the Coriolis effect. The Coriolis effect can cause an increase in the number of resonance frequencies, and generate global travelling-wave modes that can affect performance and flutter stability. Experimentally validated prediction and analysis methods are essential to ensure the accurate evaluation of the impact of the Coriolis effect on future engine designs.

The major finite element (FE) software packages were systematically assessed, and proven to provide reliable simulations of the dynamics of bladed discs when the Coriolis effect is included. Experimental modal tools for the detection and identification of the Coriolis effect are also needed, to provide accurate interpretation of the data for model validation and updating. For this purpose, a dedicated rotating test rig was designed and manufactured. A novel Multiple Input Multiple Output testing framework was developed, based on the use of an array of strain gauges and piezoelectric actuators in combination with a poly-reference identification method, for the extraction of the full set of modal parameters arising in a bladed disc from the Coriolis force.

The new technique allowed the successful recovery of Campbell diagrams, damping and strain mode shapes. Left displacement eigenvectors, which appear in the FRF formulation due to the Coriolis effect, could also be extracted and validated for the first time. An accurate comparison was conducted between the measurement data and the FE results, and confirmed the reliability of the new approach.

Acknowledgements

I am grateful to my supervisor, Dr Christoph Schwingshackl, for giving me the opportunity of pursuing this PhD, and for his advice. I would also like to acknowledge Rolls-Royce plc, which funded this work, and Dr Jeff Green in particular, for providing the big picture.

Many thanks go to Fernando Barbarossa, Dr Mauro Carnevale, Dr Luca di Mare, Luca Pesaresi, Dr Feng Wang, and Fanzhou Zhao of the VUTC, for their technical advice, the tea and sympathy, and for creating an enjoyable work environment.

I wish to thank Mr Leroy Grey, who took care of the installation of the electrical and safety systems for the test rig. He and Mr Vimmendra Patel were always available to provide their expert advice on electrical and electronic components—and to fix the occasional burned micro-resistor.

Mr Peter Higgs, administrator *extraordinaire*, proved himself invaluable, solving any issue thrown his way with efficiency and flair, and often raising the suspicion of his actually possessing the gift of omnipresence.

A big thank-you goes to Giacomo D'Antonio and Alessio Natoli for being the best lab-mates: always ready to lend a hand during the first set-up of the test rig, and for some first-rate banter.

I am deeply indebted to my excellent friends Silvia, Jamian, and Hanla, their infinite reservoirs of kindness and humour, and the calm, dignity and grace with which they weathered my writing-up phase.

I would like to thank all of my family, brother, cousins, uncles, aunts, for nurturing my mad-scientist side. Without my parents, Waila and Mario, their unfailing support and understanding, none of this would have been possible.

Contents

1	Introduction	19
1.1	Overview	19
1.2	Effects of the Coriolis force in rotating bladed discs	20
1.3	Experimental methods for the validation of rotating structures	22
1.3.1	Frequency Response Functions for gyroscopic systems	22
1.3.2	Excitation methods	24
1.3.3	Piezoelectric actuators	25
1.3.4	Measurement systems	26
1.4	Motivation and objectives of the study	28
1.5	Thesis outline	29
2	Modal analysis of rotating bladed discs	31
2.1	Introduction	31
2.2	Dynamic analysis of rotating flexible structures	32
2.2.1	Acceleration of a rotating body	32
2.2.2	Equations of motion of rotating flexible structures	33
2.2.3	Effects of the centrifugal field	36
2.3	Coriolis effects on the modal properties of bladed discs	37
2.3.1	Properties of cyclic-symmetric structures	37
2.3.2	Frequency splits in the gyroscopic eigenproblem	41
2.3.3	Travelling-wave modes	43
2.3.4	Campbell diagram	45
2.3.5	Mistuning	48
2.4	Modal testing of rotating structures	50
2.4.1	Frequency Response Function for rotating systems	50
2.4.2	Strain modal analysis	52
2.4.3	Multiple Input Multiple Output (MIMO) testing	54
2.4.4	pLSCF estimation method	56

2.5	Piezoelectric actuation	59
2.5.1	Piezoelectric materials	59
2.5.2	Dynamics of structures with piezoelectric excitation	61
2.5.3	FRF expression with piezoelectric actuation	62
2.6	Summary and Conclusions	63
3	Coriolis effects in current finite element software	64
3.1	Introduction	64
3.2	Finite element analysis	65
3.3	Test cases	66
3.4	Results	68
3.4.1	Stodola-Green rotor	68
3.4.2	Rotating ring	69
3.4.2.1	Campbell diagrams	69
3.4.2.2	Mode shapes	71
3.4.3	Swept blisk	72
3.4.4	Bladed disc-shaft assembly	74
3.5	Discussion of results	75
3.5.1	Coriolis effects	75
3.5.2	Geometric nonlinearity	77
3.5.3	Left eigenvectors	78
3.5.4	Cyclic symmetry	78
3.6	Conclusions	78
4	Rotating test rig: Design and commissioning	80
4.1	Introduction	80
4.2	Design requirements	80
4.3	Test rig	82
4.3.1	Test chamber and support components	82
4.3.2	Vacuum	83
4.3.3	Drive system	84
4.4	Excitation system	86
4.5	Measurement System	87
4.6	Test piece design	88
4.7	Data acquisition and processing	89
4.7.1	Data acquisition system	89
4.7.2	Synchronisation of the strain gauge data	91
4.7.3	Data processing	92
4.8	Commissioning	93
4.8.1	Test rig and drive system	93
4.8.2	Test piece	96
4.8.3	Characterisation of the piezoelectric actuators	98

4.8.3.1	Excitation configuration	98
4.8.3.2	Linearity	102
4.8.4	Measurement system	102
4.8.4.1	Calibration	102
4.8.4.2	Interaction between strain gauges and MFC actuators	106
4.9	Summary	108
5	Frequency Response Function measurement in rotating bladed discs	109
5.1	Introduction	109
5.2	Piezoelectric excitation for modal analysis in rotating structures	110
5.2.1	Stepped sine excitation	110
5.2.2	Multiple-Input Multiple-Output random excitation	110
5.2.3	Impulse excitation	117
5.2.4	Travelling-wave excitation	121
5.2.5	Comparison of SIMO stepped-sine and MIMO random excitation . . .	122
5.3	FRF behaviour in the rotating blisk	125
5.3.1	Effect of rotation	125
5.3.2	Effect of mistuning	127
5.4	Discussion of results	128
5.5	Summary and Conclusions	132
6	Mode shapes and left eigenvectors: Experiments and validation	134
6.1	Introduction	134
6.2	Experimental mode shapes	135
6.2.1	Complex mode shapes	135
6.2.2	Coriolis effect	141
6.2.3	Effect of mistuning	146
6.2.4	Left eigenvectors	150
6.3	Validation	152
6.3.1	Campbell diagrams	152
6.3.2	Strain mode shapes	154
6.3.3	Left eigenvectors and displacement mode shapes	157
6.4	Discussion of results	161
6.4.1	Mode shapes	161
6.4.2	Mistuning	162
6.4.3	Validation	164
6.4.4	Left eigenvectors	165
6.5	Summary and conclusions	166
7	Conclusions	168
7.1	Main contributions	168
7.1.1	Summary	168
7.1.2	Modal testing and identification methodology for rotating structures .	169

7.1.3	Coriolis effects and mistuning	170
7.1.4	FE modelling of rotating bladed discs	171
7.1.5	Validation of Coriolis effects in bladed discs	172
7.2	Suggestions for future work	173
	References	175
	Appendix A Data for the benchmark test case models	188
	Appendix B Technical drawings	190
	Appendix C Permission to reproduce own publication	199

List of Figures

1.1	Example of Coriolis effect: a Coriolis force is generated by the relative velocity due to vibration of a blade in a rotating bladed-disc shaft assembly. .	21
2.1	Kinematics of a rotating flexible body.	32
2.2	First four ND modes of a 24-sector cyclic-symmetric bladed disc. The colour red corresponds to positive displacement, blue to negative, green to no displacement.	42
2.3	Time response of an eight-sector lumped parameter blisk model, 3ND mode.	45
2.4	Illustrative Campbell diagram for a 12-blade disc.	46
2.5	Campbell diagram of a gyroscopic system in the a) stationary, and b) rotating frame. The first critical speed is circled in red.	48
2.6	Comparison of the dynamic response at the 2ND mode of a 13-sector bladed disc model : ---, tuned case; —, mistuned case.	49
2.7	Multiple Input Multiple Output system.	55
2.8	Crystal structure of a PZT piezoelectric material.	60
2.9	Laminar piezoelectric actuator in d31 operation mode.	61
3.1	Models of the benchmark test cases.	67
3.2	Stodola-Green rotor: Comparison of analytical and FE Campbell diagrams for the 1 st bending mode.	69
3.3	Thin ring: Campbell diagram comparing different FE codes to analytical formula.	70
3.4	2ND mode shape of the thin ring at rest: a) FE model, and b) modal amplitudes of the double mode at 20 equispaced positions along the circumference at rest.	71
3.5	2ND mode shape of the rotating thin ring at 60 rad/s.	72
3.6	Swept blisk: a) Effect of the centrifugal force, and b) Frequency splits.	73
3.7	Bladed disc-shaft assembly: Campbell diagram for pitch angle 90°.	74

3.8	Bladed disc-shaft assembly: Frequency split trends at pitch angles 30°, 45°, and 60° (NX Nastran).	75
3.9	Anomalous behaviour of Code A for 1ND modes in cyclic symmetric structures: Campbell diagram for 1ND first torsion mode of the bladed disc-shaft assembly with pitch angle 60°.	76
4.1	3D CAD drawing of the rig assembly: section view.	82
4.2	First mode of the test rig from FE analysis, at 120 Hz.	83
4.3	Drive system: CAD section view of the bearing housing-shaft assembly	84
4.4	Campbell diagram of the driving shaft and mock test piece.	85
4.5	Multi-function disc: balancing plane, holder for measurement electronics, and shaft-test piece joint.	86
4.6	MFC actuator: global dimensions and reference frame.	87
4.7	FE model of the test piece.	89
4.8	Dynamic FE analysis of the test piece: a) Campbell diagram for the first four ND modes from NX Nastran, and b) 0ND, 2ND, 3ND, and 4ND radial strain mode shapes.	90
4.9	Layout of the data acquisition system.	91
4.10	Synchronisation process.	92
4.11	Front view of the test rig: chamber and support.	94
4.12	Dynamics of the test rig: Accelerance of the shaft from hammer tests by hitting a) on the top right corner of the rig backplate, and b) on the shaft, with and without a representative disc mounted on it	95
4.13	Drive system and signal transmitter.	95
4.14	Strain gauges on the test piece: a) position of the strain gauges on the test piece (the sector SGs are highlighted in blue, while the circumferential SGs are circled in yellow); b) radial strain for the first 3ND mode shape from FE modal analysis.	97
4.15	MFC actuators installed on the rear face of the test piece.	98
4.16	Spectral amplitude of blisk response from MFC actuators: a) single actuator, far from resonance (230 Hz), b) 3EO TW pattern at resonance (260 Hz), and c) 3EO TW pattern off resonance (262 Hz).	101
4.17	Linearity check on the piezoelectric excitation: a) Experimental acceleration data points at different excitation levels, for different bias voltages; b) Dependence of acceleration on excitation amplitude, and best-fit regression line, for 100 V bias.	103
4.18	Calibration of the telemetry modules: a) Preliminary calibration using NI bridge completion system; b) Calibration plot for the telemetry system.	104
4.19	Comparison between the strain spectra in the calibration beam with single-frequency excitation (327 Hz).	105

4.20	Test beam and positions of strain gauges and MFC actuator (dimensions not to scale) for the study of electrical interference in the strain gauges from the piezoelectric actuators.	106
4.21	Investigation of the interaction between piezoelectric patches and strain gauges. FRFs around the resonance frequency for the third bending mode of the test beam: a) shaker excitation; b) MFC actuator, plain twisted wires; c) shielded cable for the MFC patch, shield not grounded; d) shielded cable for the MFC patch, shield grounded.	107
5.1	Characteristics of the response of the blisk in static conditions with sinusoidal single-input piezoelectric excitation: a) amplitude of the velocity and acceleration FRFs, and SFRF; b) phase; c) Nyquist plot of the velocity, and d) of the acceleration FRFs.	111
5.2	Curve-fit results with laser and MIMO random excitation: a) stabilisation diagram; b) magnitude of the velocity FRF in the 160÷320 Hz frequency range at rest; c) phase, and d) Nyquist plot	112
5.3	a) Stabilisation diagram from strain gauge data at rest, and b) representative SFRF and fit.	113
5.4	Multiple coherence at rest: a) laser data, b) SG3 3, and c) zoom on the frequency range around the 3ND split resonance for SG 3.	114
5.5	Curve-fit results from strain gauge data at 300 rpm: a) magnitude of the SFRF in the 250÷270 Hz frequency range, b) phase, and c) Nyquist plot.	116
5.6	Frequency Response Assurance Criterion (FRAC) between the experimental MIMO random SFRFs and the fitted ones at 300 rpm, in the 190÷305 Hz frequency range.	117
5.7	Multiple coherence for strain gauge data at 300 rpm: a) 160÷500 Hz frequency range, and b) zoom on the frequency range around the 3ND split resonance.	118
5.8	Impulse voltage excitation to the MFC actuators. The pulse width is 4 ms.	118
5.9	Time signal of the laser response with impulse excitation (no window applied).	119
5.10	Impulse excitation: a) Amplitude, and b) coherence from seven averages of the SFRF of the blisk.	120
5.11	3EO travelling-wave excitation: Strain amplitude and inter-sector angle for the two opposite excitation directions at 300 rpm. Each line corresponds to a different sector.	122
5.12	Comparison between resonance frequencies extracted from SIMO stepped-sine and MIMO random-excitation tests at various speeds, and best-fit lines of the 3ND mode.	123
5.13	Comparison of damping extracted from SIMO stepped-sine and MIMO random excitation tests against speed.	124
5.14	Evolution of the SFRFs with speed (SG3, input 1, SIMO stepped-sine).	126
5.15	Effect of rotational speed on the phase of the SFRF.	127

5.16 SIMO sine experimental frequency results for 3ND with best-fit lines: a) Campbell diagram, and b) frequency split curve.	127
5.17 MIMO random experimental frequency results for 2ND: a) Campbell diagram, and b) frequency split curve.	128
5.18 Evolution of the phase of the SFRF with rotational speed at the 2ND mode.	129
5.19 Z-mod plot for MIMO random excitation in the 160÷440 Hz frequency range, from strain gauge data.	131
6.1 Modal amplitudes from MIMO random at rest of the a) 3ND1, and b) 3ND2 modes. The modes are normalised so that sector 1 has an amplitude of 1.	135
6.2 Phasor plot of the 3ND mode shape pair at 0 and 390 rpm, from MIMO random. The modes are normalised so that sector 1 has zero phase, and acts as reference.	136
6.3 Comparison of the absolute value of the modal amplitudes normalised to unity, at rest and at 300 rpm.	138
6.4 Time visualisation of the strain travelling wave for the 3ND FW and BW modes at 300 rpm.	139
6.5 Auto-Modal Assurance Criterion (autoMAC) plot of the strain data from a single sector at rest.	140
6.6 AutoMAC plot of the strain data from the eight strain gauges attached to each sector.	141
6.7 AutoMAC plot of the experimental strain data from the reconstructed SG mode (13 SGs).	142
6.8 Linearised Modal Assurance Criterion (LMAC) matrix between 3ND mode pairs at different speeds, MIMO random excitation, circumferential SGs. Two modes are present at each speed side by side, as the 3ND mode is a double mode.	143
6.9 LMAC of the reconstructed strain gauge data (13 SGs), MIMO random, at different speeds, for the 3ND mode pair.	144
6.10 Mode Phase Collinearity (MPC) plot for the 3ND modes at different speeds. a) Comparison between 3ND-1 and 3ND-2 at different speeds. Two modes are present at each speed, as the second and third nodal diameters are double modes. b) MPC for 3ND-1 alone at different speeds (the 3ND-2 mode shows the same behaviour).	145
6.11 Evolution of the spatial DFT components of the 3ND modes with speed.	146
6.12 Evolution of the spatial DFT components of the 2ND modes with speed.	147
6.13 Strain travelling wave for the 2ND-BW mode at different speeds.	148
6.14 Linearised Modal Assurance Criterion (LMAC) matrix between 2ND mode pairs at different speeds, MIMO excitation. Two modes are present at each speed, as the second and third nodal diameters are double modes.	149

6.15 MPC plot for the 2ND modes at different speeds. a) Comparison between 2ND-1 and 2ND-2 at different speeds. Two modes are present at each speed, as the second and third nodal diameters are double modes. b) MPC for 2ND-1 alone at different speeds (the 2ND-2 mode shows the same behaviour).	150
6.16 Modal amplitudes of the left displacement eigenvectors at the eight MFC locations, at rest, normalised to unity.	151
6.17 MAC between left eigenvectors extracted for the first 6 modes, at different speeds, from two different strain gauge configurations: only the eight circumferential SGs, and only the seven sector SGs.	152
6.18 Comparison of the experimental and computed (NX Nastran) Campbell diagrams for the first six modes of the test piece.	153
6.19 Frequency split curves: Comparison between the experimental and NX Nastran data.	153
6.20 Comparison between the experimental and Abaqus reconstructed 3ND mode shapes at 300 rpm.	155
6.21 Comparison between the experimental and Abaqus reconstructed 4ND mode shapes at 300 rpm.	155
6.22 Comparison between the experimental and Abaqus reconstructed 2ND mode shapes at 300 rpm.	156
6.23 MAC between the reconstructed strain mode, MIMO random, and the Abaqus modes.	156
6.24 Left eigenvectors at rest, extracted from the SFRFs at the sector SGs, normalised to unity.	158
6.25 Comparison between the experimental left eigenvectors and Abaqus displacement mode shapes at 300 rpm, for the 2ND mode.	159
6.26 Comparison between the experimental left eigenvectors and Abaqus displacement mode shapes at 300 rpm, for the 3ND mode.	160
6.27 Comparison between the experimental left eigenvectors, and Abaqus displacement mode shapes at 300 rpm, for the 4ND mode.	161
B.1 Vertical back-plate	191
B.2 Base-plate.	192
B.3 Lateral supports.	193
B.4 Cylindrical casing.	194
B.5 Shaft.	195
B.6 Bearing housing.	196
B.7 Multi-function disc: telemetry holder, balancing disc, mounting for test piece.	197
B.8 Test piece.	198

List of Tables

- 3.1 Summary of software capabilities: ✓✓✓, complete feature support; ✓, partial support; ×, non-native/present but problematic; ×××, unsupported. 79

- 4.1 Main dimensions and material characteristics of the test piece. 90
- 4.2 Measurement of the speed difference between motor and shaft due to the belt slip. 96
- 4.3 Natural frequencies and damping of the test piece: Comparison between the results from the FE simulations, and the actual blisk, before and after instrumenting. Mistuning values for the two configuration are also shown. . 99
- 4.4 Natural frequencies of the mounted blisk: frequencies from finite element simulation, experimental frequencies, and their mistuning 100
- 4.5 Calibration parameters for the telemetry modules. 105

- 5.1 Comparison of frequency and damping values from laser and strain gauges data at rest (MIMO). 115
- 5.2 Comparison of frequency and damping values from traditional hammer and piezoelectric impulse testing. 120
- 5.3 Comparison between different excitation methods: MAC and Normalised Modal Difference (NMD) for the reconstructed 3ND mode between SIMO sine and MIMO random excitation. 125

- 6.1 NMD between the reconstructed strain modes, MIMO random, and the Abaqus modes, at rest, and at 300 rpm. 157
- 6.2 Comparison between the experimental and Abaqus displacement mode shapes (left eigenvectors) at rest, and at 300 rpm. 161

Nomenclature

Symbols

D	Dynamic stiffness matrix
G	Coriolis matrix
\mathbf{G}_{ii}	Auto-spectrum of variable i
\mathbf{G}_{ij}	Cross-spectrum of variables i and j
H	Frequency response function matrix
L	Matrix of left eigenvectors of state-space eigenproblem
\mathbf{L}_r	r -th left eigenvector of state-space eigenproblem
\mathbf{M}_b	Generic block-circulant matrix
N	Number of sectors
n	Number of degrees of freedom per sector
N_f	Number of frequency lines
N_i	Number of inputs
N_m	Number of modes
N_o	Number of outputs
N_s	Number of samples
S	Strain vector
T	Stress vector
v	Vector of voltages at input degrees of freedom
V	Matrix of right eigenvectors of state-space eigenproblem
\mathbf{V}_r	r -th right eigenvector of state-space eigenproblem

Greek symbols

ε	Strain
η	Loss factor
θ	Characteristic angle, equal to $\frac{2\pi}{N}$
Λ	Eigenvalue matrix
λ_r	Eigenvalue of mode r
$\mu\varepsilon$	Micro-strain
ξ	Damping ratio
ρ	Material density
φ_k	Inter-Blade Phase Angle corresponding to k ND
$\psi_{L,r}$	r -th left eigenvector of original eigenproblem
$\psi_{R,r}$	r -th right eigenvector of original eigenproblem
Ψ_L	Matrix of left eigenvectors of original eigenproblem
Ψ_R	Matrix of right eigenvectors of original eigenproblem
ω	Frequency, rad/s
Ω	Rotational velocity, rpm or rad/s

Other symbols

boldface	Matrices and vectors
$.^H$	Hermitian transpose
$.^T$	Transpose
$.^*$	Complex-conjugate
\Re	Real part
\Im	Imaginary part
$\tilde{\cdot}$	Reduced matrix from cyclic-symmetry hypothesis
$\ \cdot\ $	Euclidean norm
$[\cdot]$	Floor function

Abbreviations

BW	Backward direction (opposite the direction of rotational speed)
DAQ	Data Acquisition system
DFT	Discrete Fourier Transform

DOF	Degree Of Freedom
EO	Engine Order
EOM	Equation Of Motion
FE	Finite Element
FEA	Finite Element Analysis
FRAC	Frequency Response Assurance Criterion
FRF	Frequency Response Function
FW	Forward direction (same direction of rotational speed)
IBPA	Inter-Blade Phase Angle
IDFT	Inverse Discrete Fourier Transform
LDV	Laser Doppler Vibrometry/Vibrometer
LMAC	Linearised Modal Assurance Criterion
MAC	Modal Assurance Criterion
MFC	Macro-Fiber Composite piezoelectric material
MIMO	Multiple Input Multiple Output
MPC	Mode Phase Collinearity
ND	Nodal Diameter
NMD	Normalised Modal Difference
ODS	Operational Deflection Shape
pLSCF	poly-reference Least Squares Complex Frequency method
PZT	Lead-Zirconate-Titanate piezoelectric material
SFRF	Strain Frequency Response Function
SG	Strain Gauge
SIMO	Single Input Multiple Output
SNR	Signal-to-Noise Ratio
SW	Standing Wave
TW	Travelling Wave

Chapter 1

Introduction

1.1 Overview

Makers of civil aircraft components are facing increasing pressure from both the public and the private sector towards innovation: laws on CO₂ and NO_x emissions and noise are getting stricter, and oil prices can make fuel a high percentage of the operational costs of airline companies. This has spurred a number of initiatives to accelerate the long technology development of the aircraft industry: the Clean Sky consortium, for example, is a partnership between the EU and several private companies with the explicit purpose of providing greener, more efficient aircraft and propulsion systems within a short time span, and similar efforts are being undertaken by NASA in the US.

On the propulsion front, several new architectures have been envisioned as the engine of tomorrow, geared turbofan, lean burn, and open rotors being the the most practicable in the medium term. These novel architectures call into question the established assumptions and design practices established in aero-engine development. The lighter, more flexible structures require additional effort to ensure safety in terms of high-cycle fatigue (HCF) and flutter due to vibrations induced by aerodynamic forces, which have long been acknowledged as the principal risk for turbomachinery components. Very accurate computational methods have been developed to predict the response of the system under the likely working loads and minimise the chance of failure, but the experience matured over the past 50 years in traditional gas turbine engines does not necessarily translate directly to these new designs.

At the moment not all the loads acting on the engine are taken into consideration when conducting dynamic analyses on bladed discs: the Coriolis force is routinely neglected, and the effect of gyroscopic moments coupling the dynamics of bladed discs with that of their supporting shaft are usually treated separately from the detailed design of the blades. The Coriolis force causes splits in the natural frequencies of bladed discs, thus extending the resonance range at which high-amplitude vibration can be expected. It also tends to couple the blades in global synchronised vibration patterns in the form of travelling waves, which

have a significant influence on aeroelastic interaction, and can lead to instability.

Omitting the Coriolis force from design and verification procedures has been acceptable so far, as the effects of this force has been shown to be rather small in current aircraft engines, and this approximation significantly lightens the computational effort. However, experimental results from modern fans, with long blades and strong stagger angles, are already showing dependence on Coriolis effects. This suggests that these simplifications would be even less valid for the next-generation aero-engines, as their distinctive features would lead them to be particularly prone to rotational effects.

This project aims to gain an in-depth understanding of the effects of the Coriolis force on the dynamics of bladed discs through the development of experimentally validated predictive methods. This chapter will review the current knowledge on the Coriolis effects in rotating structures, the state of the art of computational tools, and the past and present experimental efforts undertaken to validate these methods, in order to establish what is available, and what is missing to enable a full integration of the Coriolis effect into the design process of aero-engines.

1.2 Effects of the Coriolis force in rotating bladed discs

The Coriolis force arises in rotating structures, and is proportional to the components of the vibrational velocity perpendicular to the rotational axis. All aero-engine stages experience in-plane vibration during operation, due to the blades, which are mounted on the disc at an angle with the spin axis, or due to small side-ways vibrations of the disc itself (Fig. 1.1). All bladed discs are therefore subject to some level of Coriolis force during operation. Since the most flexible component of a bladed disc are the blades themselves, some studies have focused on the effect of the Coriolis force on the dynamics of the single blade to identify potential issues. It was found that the Coriolis force tends to cause a spread in the spectrum of natural frequencies of a flat blade, causing variations in the value of some resonance frequencies of up to 9% [1]. However, in blades with highly three-dimensional features, adding the Coriolis force to the equations of motion has no effect, if the blade is also thin. On the other hand, thick blades experience both a change in their natural frequencies [2] when the Coriolis effect is included in the modelling, and an influence on their structural stability [3]. In addition, if the blade is inclined with respect to the spin axis, the mode shapes have been demonstrated to exhibit coupled components [4]: while at rest, the displacements are either parallel or perpendicular to the beam faces, but, once the Coriolis force is added [5], the deformation becomes biaxial [6]. In an aero-engine, this could affect the interaction with the incoming flow, and thus efficiency.

This coupling is accompanied by the generation of *complex* mode shapes [7], i.e. of vibration patterns in which all DOFs move at a different phase with respect to each other. This has further consequences when considering the blades not in isolation, but arranged in bladed discs. Bladed discs can be classified as *cyclic symmetric* structures, as they can be divided into N identical sectors that repeat the same pattern in terms of geometry and material for every rotation of the characteristic angle $\varphi = 2\pi/N$. In analogy with

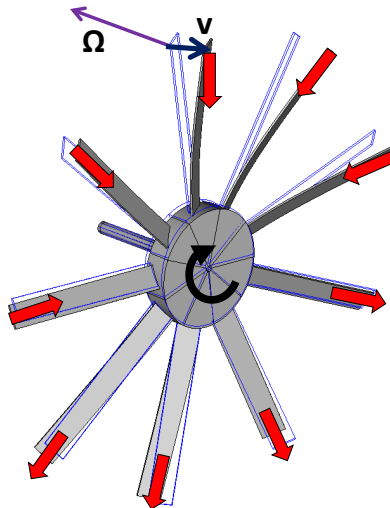


Figure 1.1: Example of Coriolis effect: a Coriolis force is generated by the relative velocity due to vibration of a blade in a rotating bladed-disk shaft assembly.

axisymmetric structures, they possess single and double modes, where double modes are pairs of modes with identical shape at the same frequency, but circumferentially shifted, e.g. orthogonal to each other [8].

The amplitude of the displacements associated to these modes varies sinusoidally along the circumference of the bladed disc. This leads to the appearance of a set of k zero-displacement nodal lines, which are called *nodal diameters* (ND) [9], with $k = 0, \dots, \lfloor N/2 \rfloor$: the corresponding modes are called kND modes. In a cyclic-symmetric structure, any linear combination of the orthogonal mode shapes associated with the same natural frequency is still a mode shape. The double mode shape vectors can be combined to form either a *standing wave*, which means the mode shape is “frozen” in space, or a *travelling wave* (TW), where the point of maximum displacement circulates around the structure. Standing waves correspond to real mode shapes, while TW modes are complex-valued.

With cyclic symmetric structures, the Coriolis effect forces the existence of travelling waves, which can propagate in the same direction of the rotational speed (*forward* (FW) travelling waves), or in the opposite (*backward* (BW) travelling waves). In addition, the two TW modes, despite having the same shape [10], are uniquely associated to different eigenvalues [11]. The Coriolis force thus causes a *split* of the natural frequencies of a structure, and increases the number of potential resonances [12]. Frequency splits have also been observed experimentally in bladed discs characterised by complex, three-dimensional shapes. Splits as high as 2% for all nodal diameters were found in a flat blisk whose blades were bent out of the rotation plane (called *swept blisk*) [13]: if neglected, they would produce a discrepancy between predicted and real resonance frequencies very close to the tolerance commonly accepted in the aero-engine industry for validation data. Experiments were also performed to quantify the effect of the Coriolis force on realistic geometries: in a high-pressure compressor, it was found that the frequency splits, though small in value, still resulted in two noticeable resonance peaks [14].

Each of the peaks is associated to a distinct direction of propagation for the travelling wave vibration patterns. The direction of propagation of the wave is of no consequence in a purely structural analysis, but, when investigating the interaction between fluid and structure, the unsteady aerodynamic excitations acting on the blades are affected by it [15]. This has an impact on their aeroelastic stability, as aerodynamic damping can become negative, i.e. the air-flow can start actively exciting the blades, instead of reducing its vibration through drag, depending on the direction of the travelling wave modes [16].

Mistuning is another physical phenomenon that can cause frequency splits. It originates from the inevitable deviations from the ideal geometries that arise from manufacturing tolerances, wear, etc. Since double modes can only exist in perfectly symmetric structures, mistuning leads to a split of these modes. However, unlike the Coriolis effect, these asymmetries tend to lock the modes in a particular position, and so to force standing-wave modes. Research has thus investigated how the two phenomena, Coriolis effect and mistuning, interact. Huang and Kuang [17] proposed an analytical model of a generic bladed disc with rigid hub subject to both mistuning and the Coriolis force, and found that the latter tends to enhance localisation in the mode shapes. Nikolic [18] used a lumped-parameter model, and through a Montecarlo simulation of various levels of mistuning found that the Coriolis effect can in some cases increase the forced response amplitude of a sector. Xin and Wang [19] modelled a realistic compressor stage in a commercial FE code, and showed that the largest Coriolis-induced frequency splits correspond to the 1ND and 2ND modes, while are negligible for higher nodal diameter families. They also confirmed that, when mistuning is added, the Coriolis force enhances mode localisation. On the experimental side, Almeida et al. [20] observed that, in a mistuned radial impeller, the mode shapes evolve from standing to travelling waves with increasing speed, which was attributed to the Coriolis effect.

The analysis of the literature has highlighted that the effects of the Coriolis force in bladed discs are well understood. However, their modelling relies heavily on simplifying assumptions that allow an analytical or semi-analytical treatment. Very few studies use FE models, which would lead to a more realistic and comprehensive investigation of the phenomenon. In particular, no formal validation has been conducted to assess the actual prediction capabilities of the current computational tools.

1.3 Experimental methods for the validation of rotating structures

1.3.1 Frequency Response Functions for gyroscopic systems

Modal analysis provides a direct link between simulations and experimentation. Its tools can be applied to analytical models and experimental data, and can thus be used to ensure that the models correctly represent the actual structures through validation. The principal means for this is the measurement of a Frequency Response Function (FRF), which correlates excitation and response of the system, and depends on the structural properties

of the system itself. Experimental modal analysis (EMA) allows the recovery of the actual structural parameters of a system, such as the resonance frequencies, damping, and mode shapes, from measured FRFs [21]. All of these data not only provide essential information on the characteristics of the real structure, but also allow to refine models in order to obtain simulations closer to reality (model updating).

In this sense, the possibility to apply EMA to a structure while it is rotating would be very valuable, as it would enable the recovery of the modal parameters in operation. This would in turn allow to control how speed influences the dynamic characteristics. It is known that centrifugal stiffening affects natural frequencies, but can modify damping as well: the contact surfaces between blades and discs, for example, tend to become locked at higher speeds, due to the centrifugal force increasingly pressing them together, thus causing a progressive decrease in damping [22]. Variations in the modal parameters can also signal a change in the structure itself, as, for example, a propagating crack would cause a decrease in the natural frequency of a blade. EMA would then be the necessary foundation for operational condition monitoring [23].

Various studies have therefore proposed experimental methodologies and analytical representations for the FRF of a rotating structure. The main issue is that rotation, through the Coriolis effect, introduces an asymmetry in the dynamics of a spinning system that invalidates the principle of reciprocity. This means that the FRF matrix is no longer symmetric: exciting a structure at point A and measuring the response at point B does *not* yield, in general, the same result as the opposite situation. It also means that the FRF terms do not depend only on the usual modal properties, i.e. mode shapes, damping, and natural frequencies: the *left eigenvectors* of the eigenproblem associated to the equations of motion of the structure are necessary as well to obtain the full response model [24–26]. Since the matrices of left eigenvectors and mode shapes are orthogonal to the matrices of the eigenproblem [24], both sets would need to be recovered to validate a FE model via orthogonality checks [27] between the measured eigenvectors and the system matrices from FE models.

In most non-rotating structures, only a row of the FRF matrix is necessary: this is easily accomplished by applying a known excitation force to a point on the structure, and measure the response at a number of points corresponding to the number of degrees of freedom required. However, in a rotating structure, the existence of left eigenvectors increases the number of unknowns: during experiments, both a column and a row of the FRF matrix \mathbf{H} need to be acquired [28], making it necessary to also vary the point of excitation, while measuring the response at a fixed location. This is a major challenge in the EMA of rotating systems [29], and thus prompted investigations into the possibility of extending the “row method” to gyroscopic systems, but the extreme sensitivity of left eigenvectors to the quality of the measurement data led to mixed results for the suggested approach [30].

1.3.2 Excitation methods

As shown in the previous section, multiple excitation points on the structure are particularly important in the modal analysis of rotating structures with Coriolis effects, as they allow the recovery of left eigenvectors [28], essential for model validation. They are also necessary for forced response studies, where it would be desirable to introduce *engine order* (EO) forcing patterns, which vary around the circumference of a bladed disc due to the presence of cyclic obstructions caused by the presence of other bladed stages upstream (stators and rotors).

Different approaches have been tried, and will be reviewed in this section. Static permanent magnets offer a non-contact, minimally intrusive excitation system, can produce high forcing levels, and arrays of them can be used to simulate EO excitation [31, 32]. However, while the EO can be set arbitrarily by changing the number of magnets [33], the excitation frequency cannot be controlled, as it depends on the rotation speed of the test piece. Even so, it is not possible to selectively excite only one particular frequency, as the passage of the blades in front of the magnet produces an impulse containing several harmonics, potentially lowering the signal to noise ratio [31]. Finally, when used in a vacuum chamber, the eddy currents produced in the test piece, and the consequent heating, can be so strong as to melt the parts of the test piece closer to the magnets [32].

AC magnets mounted on a disc spinning with the test piece are an attractive alternative. The input voltage can be varied to produce the desired amplitudes, frequencies, or excitation types (sinusoidal, random, chirp, etc.) [34]. They can generate forces of 10 N or more [35], but they can be quite bulky, and thus less suitable for using in a rotating application, due to the significant mass loading. With smaller magnets, as the magnetic force is proportional to the inverse of the square of the distance between magnet and specimen, small gaps are required to generate workable forces, thus posing the risk of impact depending on vibration amplitudes in the structure. Finally, as with permanent magnets, the test piece must obviously be made of a magnetic material, which is not always possible, or magnets must be attached to the specimen, which can worsen mistuning, and alter the dynamics of the structure.

Air jets offer another non-contact means of exciting the test structure [36], but they present the same issue as permanent magnets, as they produce an impulse-like excitation, and no control of the forcing frequency is therefore possible. In addition, while they offer the closest approximation to real EO excitation, the use of air is not suitable for vacuum operation. Vacuum is often essential for a test rig, not only to study the structural properties of a system separately from the effects of fluid interaction [22], but also with academic test pieces: the latter are often not necessarily designed to be aerodynamic, and spinning them in air requires both high motor torques, and poses the risk of destroying the blades through flutter [37].

An alternative means of exciting a rotating structure comes from exciting the shaft onto which the test piece is mounted. This method has been applied via shakers connected to a dummy bearing [38, 39], or by magnetic bearings [40–42]. Magnetic bearings, in particular,

present all the advantages of AC magnetic excitation, with none of the drawbacks listed above. The NASA Glenn Research Center Dynamic Spin Rig [40], for example, uses three magnetic bearings to achieve full levitation of the test rotor. The excitation is provided by the bearings themselves, and fiber optical displacement transducers measure the blade vibrations. The fully contact-less excitation, measurement and support system, coupled with the use of a medium-vacuum chamber, allows the accurate study of damping in rotating structures [43]. However, it is not clear from the literature what force levels they can reach, since they excite the test piece only indirectly. Because of this, they would also not qualify as true multiple-input excitation for the blades, as the force is only applied to the shaft.

1.3.3 Piezoelectric actuators

Piezoelectric (PZT) laminar actuators have been steadily gaining popularity over the past twenty years. They consist of flat patches of encapsulated piezoelectric material that can be attached directly to a structure. Their light-weight, good achievable forcing levels, and low cost, allow a distributed configuration of the excitation without significantly altering the dynamics of the underlying structures, making them particularly suited to MIMO applications for modal analysis.

The actuation characteristics come from the coupled electromechanical properties of piezoelectric materials: an applied voltage is able to produce a strain in the material, which can elongate and compress, and transmit a bending moment to the underlying structure through the bond interface [44]. Piezoelectric actuators can thus be incorporated into “smart” structures for active vibration control [45, 46]. However, it was soon recognised that their presence on a structure could be exploited to provide its modal parameters, which could be subsequently used for the control model [47].

The possibility of generating FRFs through piezoelectric actuation has been proven through several studies, initially based on simple cantilever beam models and a single actuator to derive both analytical solutions, and experimental validation data [48, 49]. PZT actuators, however, are particularly well-suited to multiple-input applications [50], due to their small mass, which makes them applicable to lightweight structures [51], and the possibility of being easily attached at several locations on a structure. Multiple piezoelectric actuators have been shown to provide FRFs with better coherence, and, since they can be distributed on the structure to avoid nodal lines, can more easily identify mode pairs with close resonance frequencies [52].

The latter property makes them a very attractive choice in the EMA of cyclic-symmetric systems in particular. Hollkamp and Gordon [53] used eight PZT actuators bonded to each of the blades of their simplified fan model, and used them one at a time to extract mode shape information. Jeffers [54] and Kielb [22] used multiple piezoelectric patches embedded in the blades of a high-pressure turbine using both swept sine and chirp signals. The measured FRFs were then curve-fitted using a single degree-of-freedom model (SDOF) to obtain damping values both in vacuum and operational conditions. The same SDOF ap-

proximation was employed by Kammerer [55] in the analysis of the damping of a centrifugal impeller. FRFs were measured from sinusoidal excitation from PZT patches that were driven by the same voltage signal. While good-quality data could be obtained, the SDOF approximation proved problematic due to the presence of close frequencies from mistuning. Almeida et al. [20] used a single PZT actuator on a similar test piece, and measured Coriolis-induced frequency splits and TW modes by applying a more realistic multi-DOF curve-fitting procedure on the response measured through several strain gauges.

The relevance of TWs to the study of the aeroelastic response of bladed discs has generated interest in the capability of exciting bladed discs directly with a TW forcing pattern. The first rig to exhibit this feature using PZT actuators was presented by Gibert et al. [14]. A high-pressure compressor blisk was equipped with two circumferential rows of PZT patches on the front and rear of the blisk hub. The rows were driven by the same sinusoidal voltage signal, and the generation of a phase difference between them to create a TW relied on their being spatially shifted with respect to each other. An additional constant phase shift was introduced in the control voltage via manual switches on the hub. A pure 4EO TW pattern could be generated. It was also possible to introduce 0EO, 1EO, and 2EO TW patterns, but, because of the spatial distribution of the actuators, and the fixed phase shift allowed by the switches, an additional SW component was inevitable.

An evolution towards the selective excitation of arbitrary EO patterns was presented by Belz et al. [56]. In their test rig, five adjacent blades of an ultra-high-bypass-ratio fan were equipped with Macro Fiber Composite (MFC) piezoelectric actuators. They were all driven by sinusoidal signal at the same frequency, but individually phase-shifted with respect to each other, to reproduce a precise EO excitation.

The review of the literature has highlighted that the modal analysis of a rotating structure requires a MIMO approach, as multiple excitation points are necessary to recover the left eigenvectors of the structure that arise from the action of the Coriolis force, and thus retrieve the full set of modal parameters to be used for validation and model updating purposes. Among the many excitation methods that have been employed in the past, laminar piezoelectric actuators have emerged as an attractive and viable option, especially for bladed discs. Contrary to most other methods, they can be controlled individually, thus decoupling excitation from rotation speed. Being minimally intrusive, they can be distributed across the structure, allowing both a proper MIMO configuration, and arbitrary excitation patterns.

1.3.4 Measurement systems

The acquisition of good-quality data is crucial to obtain FRFs from which to extract reliable modal parameters. This is especially true in rotating structures, where multiple noise sources are present. Research in recent years has particularly focused on non-contact techniques. Being non-intrusive, they allow the recovery of the structural response without adding interference, and, since they do not involve contact with the rotating system, they

do not require slip rings or telemetric devices to transfer the measured signals from the rotor, which could add further uncertainty through noise. In this section, some of the most common measurement techniques will be covered.

Blade Tip Timing (BTT) measures the vibration of the tip of a blade through probes (optical, capacitive, etc.) fixed on the casing of the rotor under test [57]. The probes record the passage of the blade tip, and, by comparing the times of arrival at the probes and the measured deflection to the times expected from the rotor speed, it is possible to reconstruct the vibratory motion. BTT has been successfully used for the measurement of Coriolis-induced TWs in rotating high-pressure compressor blisks at high speeds [58]. However, it cannot be used to measure the response of the full blade, and is thus not suitable for mode shape reconstruction purposes, or for detailed model validation.

Point-tracking Laser Doppler Vibrometry (LDV) [20, 31], on the other hand, can follow the vibration of several single points in succession during rotation, while Continuous Scanning LDV (CSLDV) allows the measurement of the Operational Deflection Shape (ODS) of a whole area, and potentially of a whole blade [59, 60]. In addition, it provides very high-quality signals due to the characteristic high sensitivity of the laser heads. Point-tracking photogrammetry similarly provides full-field measurements, by taking successive photos of the target structure with high-speed cameras, and reconstructing its movement through digital image correlation methods. As the cameras are fixed in space, photogrammetry, contrary to tracking LDV, also measures the rigid body motion due to rotation, which needs to be subtracted during post-processing [61]. The main drawback of both methods is that they are limited by the need for line-of-sight: only the parts of the target that are optically accessible can be measured. This is an issue in bladed discs, as they are usually characterised by a large number of blades and high stagger angles, which means that there is a high degree of overlap between the blades themselves.

Strain gauges, however, would be well-suited to this situation, as they can be attached almost anywhere. Since their response can be directly correlated to stress, they are ubiquitous in turbomachinery monitoring and testing [14, 20, 22, 54, 55, 58, 62–74], even if they need expensive telemetry devices [69, 75] capable of reliably transmitting the low-voltage strain signal from the rotor to the data acquisition system. Since they have to be attached to the blades, they can affect their structural properties, and add mistuning. This effect, however, is limited in low-temperature applications, as they do not need to be encapsulated in protective cement, which is the main source of additional stiffness [76].

The studies listed above mainly use strain gauges for forced response analysis, and not for the sake of modal parameter extraction. However, the theory for strain EMA was established in the late '80s, and it has been successfully applied to extract mode shapes from blisks in rotating conditions [14]. Recently, strain modal analysis has attracted new attention due to the possibility of recovering not only strain, but also displacement mode shapes, from strain FRFs [77–80], but the method has not been extended to rotating structures so far.

1.4 Motivation and objectives of the study

Modern aero-engines have reached a degree of sophistication such that only significant changes could lead to the pronounced improvements required by the present economic and environmental pressures. New architectures like open rotors, or geared fans, constitute a major leap in this direction, both in terms of efficiency and of technological innovation. This calls for a revision of the accepted design practices, and a new focus on phenomena that have been little investigated, either because of their minor effects on current architectures, like the Coriolis effect, or because of the toll it would take on the present computational resources.

The analysis of the available literature has highlighted that including the effects of the Coriolis force into the design process could help push performance boundaries while maintaining high safety standards. Frequency splits, causing the appearance of distinct resonances, have been modelled and experimentally validated. Backward and forward travelling waves generated by the Coriolis effect, which can affect flutter stability, have been observed in real blisks, and their interaction with the standing waves caused by mistuning have also started to be investigated. This underlines how there is a real push towards an ever more comprehensive modellisation of the physical phenomena involved in the operation of an aero-engine.

Two main areas where research needs to be expanded to fulfil the requirements of the next generation of aero-engines have therefore been identified:

- **Modelling of the Coriolis effect:** Many of the studies analysed rely on analytical models based on simplifying assumptions, like rigid hubs. Others depend on *ad hoc* implementations of the finite element method. These approaches are very valuable, especially in an academic context, as they allow fast simulations and a direct understanding of the underlying physics. For an uptake from the turbomachinery industry, and an integration of the Coriolis effect into the standard design and verification process, the use of generalised and automatic methods for arbitrary geometries is needed. In particular, it is not clear what the prediction capabilities of the available commercial FE software packages currently are in terms of rotational effects in bladed discs in general, and the Coriolis effect in particular. A systematic assessment of these capabilities is therefore necessary to prove their accuracy, and highlight potential deficiencies. This assessment must be accompanied by a full independent validation of its results, to provide the industry with confidence in the modelling approach to complex 3D structures like aero-engine stages when Coriolis effects are included.
- **Experimental modal analysis of bladed discs:** Several test rigs and methodologies are present in the literature for the modal identification of bladed discs in rotating conditions. Multiple-input approaches, however, have not yet been taken full advantage of, due to the difficulty of introducing controllable and measurable excitation patterns into a rotating structure. The presence of more than one input increases

the achievable forcing level, and ensures a more uniform distribution of it over the structure, which in turn contributes to higher-quality data. Multiple inputs are also essential for the recovery of left eigenvectors. This particular feature of rotating systems is necessary for a full analysis of their dynamic properties, and its measurement and validation, to the author's knowledge, has never been attempted for a bladed disc. Piezoelectric actuators, in particular, have emerged as viable candidates for this. In addition, the application of strain gauges to modal analysis should be thoroughly assessed and developed, as they are already the sensor of choice in rotating structures. They can also be applied on multiple locations on a structure, allowing the detailed recovery of the vibration pattern. A MIMO testing approach shall therefore be investigated, together with a multi-DOF modal identification method capable of taking advantage of the full data set produced.

1.5 Thesis outline

This project aims to develop a reliable testing methodology for the modal analysis of rotating structures, to be applied to the in-depth understanding of the Coriolis effects on the dynamic response of bladed discs, and to ensure a validation of the existing predictive tools. The thesis is structured as follows:

- Chapter 1 has presented the state-of-the art of research with respect to the investigation of the Coriolis effect in turbomachinery, and the experimental capabilities developed.
- Chapter 2 covers the mathematical framework needed to model the effects of the Coriolis force in bladed discs. The traditional methods of modal analysis are adapted for application to rotating structures. In particular, an explicit definition of strain FRFs for a gyroscopic system is derived for the first time in a MIMO context. Piezoelectric actuators are presented, and the equations of motion of a spinning structure excited by them are reported.
- Chapter 3 presents the assessment of the prediction capabilities of the Coriolis effects in commercial FE software packages. Benchmark test cases were developed, and used to derive the accuracy of the various codes in simulating frequency splits and travelling wave modes.
- Chapter 4 presents the design and commissioning of the rotating test rig developed to provide the experimental validation data.
- Chapter 5 contains an in-depth investigation of the viability of piezoelectric actuators for EMA in rotating conditions. Stepped-sine, MIMO random, TW EO patterns, and impulse excitation are assessed and compared.
- Chapter 6 contains the validation data for the mode shapes and left eigenvectors when the Coriolis effect is present. The experimental strain mode shapes are ex-

tracted using the poly-reference technique adapted in Chapter 2, and compared to the ones obtained from an FE model of the test piece. Very close agreement is observed, proving the reliability of the new testing approach. Discrepancies are noticeable only for modes affected by mistuning. Left eigenvectors are also recovered for the first time: their close agreement with the FE results confirms the soundness of the experimental approach.

- Chapter 7 summarises the main conclusions, and offers suggestions for further research.

Chapter 2

Modal analysis of rotating bladed discs

2.1 Introduction

Rotation adds inertial and elastic effects to the behaviour of flexible structures, due to the interaction between the local deformations of the structure and the global motion of the system. Their effect is well known, but, in the field of turbomachinery, the Coriolis force is rarely included in structural dynamics analyses, and few studies address systematically the issues that can arise from it.

This chapter therefore aims to establish the theoretical foundation for the main targets of this work. The equations of motion for a rotating flexible structure will be presented to highlight the principal dynamic phenomena. The cyclic-symmetry formalism, which can be applied to represent bladed discs, will be described in great detail, as it can be exploited for a quantitative understanding of the effects of the Coriolis force in this type of structures.

Experimental modal analysis offers the tools for the reliable identification of structural parameters like resonance frequencies, damping, and mode shapes, which are essential to verify the behaviour of a system, and ensure the physical structure matches its model, for representative simulations. The other final goal being the development of experimental methods for the investigation of Coriolis effects in bladed discs, the tools of traditional modal analysis will be adapted to rotating structures. In particular, Multiple-Input Multiple-Output (MIMO) testing has been identified as ideal for this purpose, so Frequency Response Functions (FRFs) for MIMO applications will be presented. A FRF expression for use with strain gauges in the presence of the Coriolis effect will be derived, so that modal analysis can be conducted through the most common measurement devices in bladed discs. As piezoelectric actuators were found to be well-suited to a MIMO set-up, their dynamic properties will be explained, and their use for FRF derivation commented on.

2.2 Dynamic analysis of rotating flexible structures

2.2.1 Acceleration of a rotating body

To study the behaviour of a rotating body, it is possible to write the equations of motion (EOMs) in two different, but related, frames of reference: the inertial frame, which is fixed, and is therefore also defined as stationary, and a rotating frame that follows the global spinning motion. The EOMs assume different forms depending on the frame they are expressed in, and the most convenient expression depends on the symmetry characteristics of both the rotating (rotor) and the stationary (stator) parts of the structure.

In the special case of an axisymmetric rotor on symmetric (or *isotropic*) bearings, i.e. bearings with stiffness values identical in all directions, the equations are time-invariant in both frames: for these systems, the EOMs are therefore solved directly in the fixed frame. In the presence of asymmetric (*anisotropic*) bearings, time-varying coefficients appear in the rotating frame. Time-dependent coefficients appear for a non-axisymmetric rotor—e.g. a cyclic symmetric one, such as a bladed disc—with isotropic bearings in the stationary frame, and is therefore solved in the rotating frame. A non-axisymmetric rotor on anisotropic bearings would lead to time-dependent coefficients in both frames [21]. In the rest of this work, only cyclic symmetric structures with isotropic bearings will be considered as they represent bladed discs, and the EOMs will only be derived in the rotating frame.

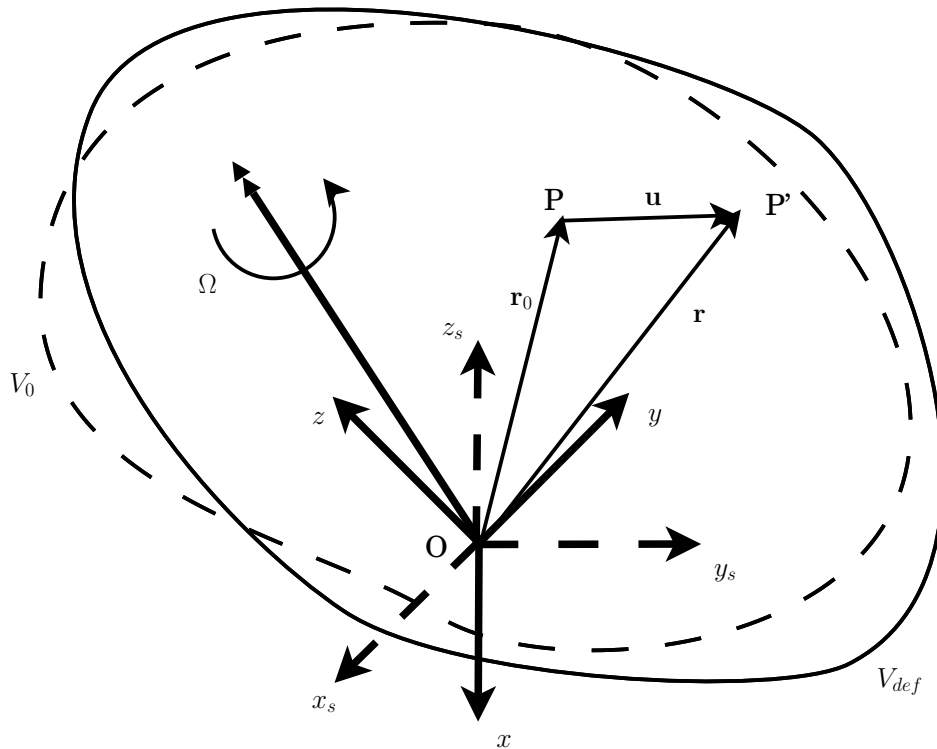


Figure 2.1: Kinematics of a rotating flexible body.

An expression for the acceleration of a flexible body in a reference frame rotating with

velocity Ω is therefore needed to obtain the inertial forces. The rotating frame $Oxyz$ is considered to be attached to the structure, and to share the same origin as the inertial frame $Ox_s y_s z_s$. In these conditions, the position $\mathbf{r} = [x \ y \ z]^T$ of a generic point P belonging to the deformed structure V_{def} (Fig. 2.1) can be expressed as

$$\mathbf{r}(\mathbf{r}_0, t) = \mathbf{r}_0 + \mathbf{u}(\mathbf{r}_0, t), \quad (2.1)$$

where \mathbf{r}_0 is the position of P in the original, undeformed configuration V_0 , and $\mathbf{u}(\mathbf{r}_0, t)$ is the displacement vector of the deformation. Deriving Eq. (2.1) with respect to time, and dropping the dependencies, the velocity can be written as

$$\dot{\mathbf{r}} = \dot{\mathbf{u}} + \boldsymbol{\Omega} \times (\mathbf{r}_0 + \mathbf{u}), \quad (2.2)$$

where $\boldsymbol{\Omega} = [\Omega_x \ \Omega_y \ \Omega_z]^T$.

Assuming constant rotational speed, the acceleration can be written as [6]

$$\ddot{\mathbf{r}} = \ddot{\mathbf{u}} + 2\boldsymbol{\Omega} \times \dot{\mathbf{u}} + \boldsymbol{\Omega} \times \boldsymbol{\Omega} \times \mathbf{r}_0 + \boldsymbol{\Omega} \times \boldsymbol{\Omega} \times \mathbf{u}. \quad (2.3)$$

Three terms are added to the familiar linear acceleration $\ddot{\mathbf{u}}$. The first term, $2\boldsymbol{\Omega} \times \dot{\mathbf{u}}$ is called *Coriolis acceleration*, and is present whenever the vibrational velocity $\dot{\mathbf{u}}$ has components in the rotation plane perpendicular to the axis of rotation. The second term, $\boldsymbol{\Omega} \times \boldsymbol{\Omega} \times \mathbf{r}_0$ is proportional to the the original position vector of point P , \mathbf{r}_0 , and forms the constant part of the *centrifugal acceleration*, while the last term, $\boldsymbol{\Omega} \times \boldsymbol{\Omega} \times \mathbf{u}$ is proportional to the displacement, and causes an inertial force that tends to amplify the displacement itself since it is always acting in the displacement direction: the effect is called *spin softening*, as it makes the rotating structure appear less stiff.

It is well known, however, that the presence of a centrifugal field adds to the apparent structural stiffness [81], and more than compensates for the spin softening effect in most cases, as the centrifugal force behaves as a restoring mechanism tending to realign the deformed structure to its original position. This effect (called *centrifugal* or, more generally, *geometric stiffening*) can only be accounted for by using a nonlinear representation of the deformation [82], and the best way to include it into the equations of motion was the source of some controversy [83–85]. The most general and easily implemented approach uses a nonlinear second order expression for the strain [86], even in presence of small deformations, where the well-known linear strain tensor [87] would otherwise be used.

2.2.2 Equations of motion of rotating flexible structures

The EOMs of rotating flexible structures are seldom derived explicitly in the open literature. Some of the details are therefore presented here to highlight the origin of the main rotational effects, and their consequences on dynamic behaviour. The derivation is based

on the generalised Hamilton principle

$$\int_{t_1}^{t_2} \delta(K - U + W_{nc} + W_{ext})dt = 0, \quad (2.4)$$

where δ is the variational operator [88], K is the kinetic energy of the system, U the internal potential energy, and W_{ext} the work of the external forces, which include non-conservative damping forces. Remembering that the cross product operator $\Omega \times$ can be expressed in matrix form as

$$\mathbf{\Omega} \times = \mathbf{R} = \begin{vmatrix} 0 & -\Omega_z & \Omega_y \\ \Omega_z & 0 & -\Omega_x \\ -\Omega_y & \Omega_x & 0 \end{vmatrix},$$

the kinetic energy can be obtained from Eq. (2.2) as follows:

$$K = \frac{1}{2} \int_V \rho \dot{\mathbf{r}}^T \dot{\mathbf{r}} dV \quad (2.5)$$

where $\rho = \rho(x, y, z)$ is the density of the material. Taking the variation, and noting that $\mathbf{R}^T = -\mathbf{R}$ yields

$$\begin{aligned} \delta K = \frac{1}{2} \int_V \rho (2\delta \dot{\mathbf{u}}^T \dot{\mathbf{u}} + 2\delta \dot{\mathbf{u}}^T \mathbf{R} \mathbf{u} + 2\delta \mathbf{u}^T \mathbf{R}^T \dot{\mathbf{u}} + \\ + \delta \dot{\mathbf{u}}^T \mathbf{R} \mathbf{r}_0 + 2\delta \mathbf{u}^T \mathbf{R}^T \mathbf{R} \mathbf{r}_0 + 2\delta \mathbf{u} \mathbf{R}^T \mathbf{R} \mathbf{u}) dV. \end{aligned} \quad (2.6)$$

The internal potential energy of the system is usually expressed with the volumetric integral $\int_V \sigma \varepsilon dV$ as the work of the internal stresses σ on the strains ε . As anticipated, the linear expression for the strains

$$\varepsilon_{ij} = \frac{1}{2} \left(\frac{\partial u_i}{\partial r_j} + \frac{\partial u_j}{\partial r_i} \right)$$

cannot capture the effect of centrifugal stiffening, and is thus not suitable for modelling rotating structures where this effect is prevalent. The Green strain tensor [89] is used instead, as it contains nonlinear terms due to the representation of finite strain, which is necessary to take centrifugal stiffening into account [90]. The Green vector strain \mathbf{S} can

then be written as [91]

$$\mathbf{S} = \begin{pmatrix} \varepsilon_{xx} \\ \varepsilon_{yy} \\ \varepsilon_{zz} \\ \varepsilon_{xy} \\ \varepsilon_{xz} \\ \varepsilon_{yz} \end{pmatrix} = \begin{pmatrix} \frac{\partial u_1}{\partial x} \\ \frac{\partial u_2}{\partial y} \\ \frac{\partial u_3}{\partial z} \\ \frac{\partial u_1}{\partial y} + \frac{\partial u_2}{\partial x} \\ \frac{\partial u_2}{\partial z} + \frac{\partial u_3}{\partial x} \\ \frac{\partial u_2}{\partial z} + \frac{\partial u_3}{\partial y} \end{pmatrix} + \begin{pmatrix} \frac{1}{2} \left(\left(\frac{\partial u_1}{\partial x} \right)^2 + \left(\frac{\partial u_2}{\partial x} \right)^2 + \left(\frac{\partial u_3}{\partial x} \right)^2 \right) \\ \frac{1}{2} \left(\left(\frac{\partial u_1}{\partial y} \right)^2 + \left(\frac{\partial u_2}{\partial y} \right)^2 + \left(\frac{\partial u_3}{\partial y} \right)^2 \right) \\ \frac{1}{2} \left(\left(\frac{\partial u_1}{\partial z} \right)^2 + \left(\frac{\partial u_2}{\partial z} \right)^2 + \left(\frac{\partial u_3}{\partial z} \right)^2 \right) \\ \left(\frac{\partial u_1}{\partial x} \right) \left(\frac{\partial u_1}{\partial y} \right) + \left(\frac{\partial u_2}{\partial x} \right) \left(\frac{\partial u_2}{\partial y} \right) + \left(\frac{\partial u_3}{\partial x} \right) \left(\frac{\partial u_3}{\partial y} \right) \\ \left(\frac{\partial u_1}{\partial x} \right) \left(\frac{\partial u_1}{\partial z} \right) + \left(\frac{\partial u_2}{\partial x} \right) \left(\frac{\partial u_2}{\partial z} \right) + \left(\frac{\partial u_3}{\partial x} \right) \left(\frac{\partial u_3}{\partial z} \right) \\ \left(\frac{\partial u_1}{\partial y} \right) \left(\frac{\partial u_1}{\partial z} \right) + \left(\frac{\partial u_2}{\partial y} \right) \left(\frac{\partial u_2}{\partial z} \right) + \left(\frac{\partial u_3}{\partial y} \right) \left(\frac{\partial u_3}{\partial z} \right) \end{pmatrix} \quad (2.7)$$

The choice of the Green strain tensor requires the use of the second Piola-Kirchhoff stress tensor, as the two are work-conjugate [91], i.e. they allow an invariant formulation of the internal work [92]. Defining a vector stress \mathbf{T} in a similar way as for the vector strain of Eq. (2.7), the variation δU of the potential energy can be written as

$$\delta U = \frac{1}{2} \int_V \mathbf{T}^T \delta \mathbf{S} dV. \quad (2.8)$$

If the material has linear behaviour, a constitutive relationship between stress and strain of the type $\mathbf{T} = \mathbf{C}_c \delta \mathbf{S}$, where \mathbf{C}_c is the constitutive matrix defining the characteristics of the material, can be assumed. Substituting it into Eq. (2.8), the internal energy can be finally written as

$$\delta U = \frac{1}{2} \int_V \delta \mathbf{S}^T \mathbf{C}_c \delta \mathbf{S} dV. \quad (2.9)$$

At this point, it is useful to introduce some form of discretisation, so that the displacements \mathbf{u} in the continuum can be reduced to a finite number of discrete *degrees of freedom* (DOFs) \mathbf{x} through some *shape function* matrices \mathbf{N}

$$\mathbf{u} = \mathbf{N}_u \mathbf{x}(t) \quad (2.10)$$

$$\mathbf{S} = (\mathbf{N}_{\varepsilon,l} + \mathbf{N}_{\varepsilon,nl}) \mathbf{x}(t). \quad (2.11)$$

The shape functions depend on the type of discretisation method used (e.g. assumed modes, finite elements, etc.). It is sufficient here to note that the displacement shape function \mathbf{N}_u and the strain function $\mathbf{N}_{\varepsilon,l}$ are independent of the displacement, while $\mathbf{N}_{\varepsilon,nl}$ is not, to account for the nonlinear terms of the Green strain formulation [90, 93].

It is possible to substitute Eqs. (2.10) and (2.11) into Eqs. (2.6) and (2.9), respectively, and to further substitute the latter in Eq. (2.4). After further manipulations, which are omitted for brevity as they are beyond the scope of this work (see e.g. [94] for a detailed

derivation), the following discretised system of equations is obtained:

$$\mathbf{M}\ddot{\mathbf{x}}(t) + (\mathbf{G}(\boldsymbol{\Omega}) + \mathbf{C})\dot{\mathbf{x}}(t) + (\mathbf{K} + \mathbf{K}_G(\mathbf{x}(t), \boldsymbol{\Omega}) + \mathbf{K}_S(\boldsymbol{\Omega}))\mathbf{x}(t) = \mathbf{F}_C + \mathbf{F}_{ext}. \quad (2.12)$$

\mathbf{M} , \mathbf{C} , \mathbf{K} are the mass, damping, and stiffness matrices, $\mathbf{F}_{ext}(\boldsymbol{\Omega}, t, \mathbf{x}(t), \dots)$ is the vector of external forces, including the centrifugal force, and $\mathbf{x}(t)$ is the vector of generalised displacements derived from the discretisation process. Vector $\mathbf{F}_C = \mathbf{F}_C(\boldsymbol{\Omega})$ is the steady centrifugal force vector originating from the constant component of the centrifugal acceleration in Eq. (2.3). $\mathbf{F}_{ext} = \mathbf{F}_{ext}(\boldsymbol{\Omega}, t, \mathbf{x}(t), \dots)$, is a generic vector of forces external to the structure, which can include aerodynamic loading, the reactions of the bearings, friction damping, etc., and is time dependent.

These elements are common to the analysis of stationary structures, while the remaining (\mathbf{G} , \mathbf{K}_G , \mathbf{K}_S) are specific to rotating systems, and depend on the rotational speed. The Coriolis matrix

$$\mathbf{G} = 2 \int_V \rho \mathbf{N}_u^T \mathbf{R} \mathbf{N}_u dV$$

depends on the rotational velocity matrix \mathbf{R} , and is therefore skew-symmetric. It is sometimes referred to as a pseudo-damping matrix, as it multiplies the velocity vector like damping matrix \mathbf{C} , but does not introduce any dissipative effects. The geometric stiffness matrix

$$\mathbf{K}_G = \int_V \rho (\mathbf{N}_{\varepsilon,l}^T \mathbf{C}_c \mathbf{N}_{\varepsilon,nl} + \mathbf{N}_{\varepsilon,nl}^T \mathbf{C}_c \mathbf{N}_{\varepsilon,l}) dV$$

introduces the geometric nonlinearity effect, as it originates from the nonlinear definition of the deformation of Eq. (2.7), and comes from the potential energy term in Eq. (2.9). The additional stiffness matrix \mathbf{K}_S

$$\mathbf{K}_S = - \int_V \rho \mathbf{N}_u^T \mathbf{R}^T \mathbf{R} \mathbf{N}_u dV$$

originates from the kinetic energy term in Eq. (2.6), and is related to the spin softening, and is negative-definite: it can thus have a destabilising effect as it tends to reduce the stiffness of the system.

2.2.3 Effects of the centrifugal field

If the displacements in Eq. (2.12) are small, it is possible to eliminate the nonlinearity introduced by the displacement-dependent geometric stiffness matrix \mathbf{K}_G . This geometric nonlinearity can be shown, in rotating structures, to originate from the action of the centrifugal force $\mathbf{F}_C(\boldsymbol{\Omega})$: in blades with stacking lines¹ off the radial direction, the centrifugal force introduces a restoring moment, tending to realign the blade with the radial direction. Due to the increasing flexibility of modern aero-engine blades, the shape of the blade will, in general, change with the rotational speed.

Assuming a periodic forcing, and steady-state analysis, the displacement $\mathbf{x}(t)$ can be

¹The *stacking line* is the line connecting the centres of gravity of the airfoil sections of a blade.

represented by an oscillation $\mathbf{x}_d(t)$ around a static equilibrium position \mathbf{x}_{st}

$$\mathbf{x}(t) = \mathbf{x}_{st} + \mathbf{x}_d(t), \quad (2.13)$$

where the configuration \mathbf{x}_{st} is different from the configuration at rest because of the action of the centrifugal force. By assuming small displacements, the matrix \mathbf{K}_G can be considered constant during a vibration cycle, and therefore it depends only on the static part of the displacement \mathbf{x}_{st} . By substituting Eq. (2.13) into Eq. (2.12), the system can be decoupled into a static (Eq. (2.14)) and a dynamic part (Eq. (2.15))

$$(\mathbf{K} + \mathbf{K}_G(\mathbf{x}_{st}, \Omega) - \mathbf{K}_S(\Omega))\mathbf{x}_{st} = \mathbf{F}_C(\Omega), \quad (2.14)$$

and

$$\mathbf{M}\ddot{\mathbf{x}}_d(t) + (\mathbf{G}(\Omega) + \mathbf{C})\dot{\mathbf{x}}_d(t) + (\mathbf{K} + \mathbf{K}_G(\mathbf{x}_{st}, \Omega) - \mathbf{K}_S(\Omega))\mathbf{x}_d(t) = \mathbf{F}_{ext}. \quad (2.15)$$

Eq. (2.14) reveals the relationship between geometric nonlinearity and centrifugal force in rotating structures. By solving it iteratively, it is possible to find the static configuration \mathbf{x}_{st} and its corresponding matrix $\mathbf{K}_G(\mathbf{x}_{st}, \Omega)$, which can then be used in Eq. (2.15). If the static displacement is small, the solution of Eq. (2.14) is based on linear or linearised stress-strain relationship that lightens the computational load of this preliminary step. In bladed discs, fans in particular, however, the centrifugal force alters the shape of the blades so much that aerodynamic optimisation is performed directly on the *hot shape* of the blades, i.e. the blade configuration as deformed by the centrifugal field (the *cold shape*, i.e. the unloaded shape, is only derived afterwards, for manufacturing purposes). In this case, Eq. (2.14) has to be solved using the actual stress-strain relationship [95], which can be significantly nonlinear.

2.3 Coriolis effects on the modal properties of bladed discs

2.3.1 Properties of cyclic-symmetric structures

The modal analysis of a rotating structure, which allows the recovery of intrinsic dynamic properties like natural frequencies and mode shapes, is based on the solution of the eigenproblem associated to Eq. (2.15). Assuming a solution for $\mathbf{x}_d(t)$ of the type $\Psi e^{\lambda t}$, and neglecting the excitation vector, leads to

$$(\lambda^2 \mathbf{M} + \lambda(\mathbf{C} + \mathbf{G}) + \mathbf{K}_{tot})\Psi = \mathbf{D}(\lambda)\Psi = \mathbf{0}, \quad (2.16)$$

where $\mathbf{K}_{tot} = \mathbf{K} + \mathbf{K}_G - \mathbf{K}_S$, and $\mathbf{D}(\lambda)$ is the *dynamic stiffness* of the system. The solution yields the eigenvalue matrix Λ and the eigenvector matrix Ψ : the eigenvalues give the resonance frequencies of the structure, while the eigenvectors represent its *mode shapes*, i.e. the preferential vibration configurations of the system.

Eq. (2.16) reveals particular algebraic features under the hypothesis of *cyclic-symmetry* in the structure, which can always be made for bladed discs (with one exception, which will

be covered in sect. 2.3.5). This hypothesis allows a more efficient solution of the eigenproblem, and offers further insight into the dynamics of bladed discs. It is also fundamental in order to interpret the effects of the Coriolis force on such structures from a linear-algebra point of view, which is seldom proposed. The application of the cyclic-symmetry hypothesis to Eq. (2.16) and its consequences will therefore be treated in detail in the following.

Cyclic-symmetric structures can be divided into N identical sectors that repeat the same pattern in terms of geometry and material for every rotation of the characteristic angle $\theta = 2\pi/N$. Bladed discs satisfy this hypothesis because of the presence of the blades, which break the axisymmetry of the disc they are mounted on (axisymmetric structures can be considered a particular case of cyclic symmetry). Because of the internal connections between adjacent sectors, the system matrices in Eq. (2.16) are *block-circulant* matrices. Calling \mathbf{M}_b a generic block-circulant matrix, any of the matrices in Eq. (2.16) can be represented as

$$\mathbf{M}_b = \begin{pmatrix} \mathbf{M}_{b1} & \mathbf{M}_{b2} & \mathbf{M}_{b3} & \cdots & \mathbf{M}_{bN-1} & \mathbf{M}_{bN} \\ \mathbf{M}_{bN} & \mathbf{M}_{b1} & \mathbf{M}_{b2} & \cdots & \mathbf{M}_{bN-2} & \mathbf{M}_{bN-1} \\ \mathbf{M}_{bN-1} & \mathbf{M}_{bN} & \mathbf{M}_{b1} & \cdots & \mathbf{M}_{bN-3} & \mathbf{M}_{bN-2} \\ \vdots & \vdots & \vdots & \ddots & \vdots & \vdots \\ \mathbf{M}_{b3} & \mathbf{M}_{b4} & \mathbf{M}_{b5} & \cdots & \mathbf{M}_{b1} & \mathbf{M}_{b2} \\ \mathbf{M}_{b2} & \mathbf{M}_{b3} & \mathbf{M}_{b4} & \cdots & \mathbf{M}_{bN} & \mathbf{M}_{b1} \end{pmatrix}. \quad (2.17)$$

Each \mathbf{M}_{b_i} , $i = 1, \dots, N$ is a sub-matrix of dimensions $n \times n$, where N is the number of sectors, and n the number of DOFs in a single sector. \mathbf{M}_{b1} contains the matrix terms relative to a single sector, and is the same for all because of the cyclic-symmetry hypothesis. The off-diagonal sub-matrices \mathbf{M}_{b_i} , $i \neq 1$ include the coupling terms between different sectors. The system matrices are therefore seldom full for common bladed disc configurations, and usually appear in banded form, as each sector is connected only to the two adjacent ones.

Indicating with \otimes the Kronecker product [96], \mathbf{M}_b can also be expressed as [97]

$$\mathbf{M}_b = \mathbf{Bcirc}[\mathbf{M}_{b1}, \mathbf{M}_{b2}, \dots, \mathbf{M}_{bN}] = \sum_{k=1}^N \mathbf{\Pi}^k \otimes \mathbf{M}_{bk}, \quad (2.18)$$

where

$$\Pi_{ij}^k = \delta_{i(j-k+1)} + \delta_{i(n+i-k+1)}, \quad \mathbf{\Pi}^k \in \mathbb{R}^{n \times n}, \quad i, j = 1, \dots, n$$

is the permutation matrix, and δ is the Kronecker delta. For example, Π^2 is

$$\mathbf{\Pi}^2 = \begin{pmatrix} 0 & 1 & 0 & \cdots & 0 & 0 \\ 0 & 0 & 1 & 0 & \cdots & 0 \\ \vdots & \vdots & \vdots & \ddots & \vdots & \vdots \\ 0 & 0 & 0 & \cdots & 0 & 1 \\ 1 & 0 & 0 & 0 & \cdots & 0 \end{pmatrix}.$$

The eigenvectors of *any* permutation matrix are described by the Fourier matrix \mathbf{E}_f , with

$$E_{fjk} = \frac{1}{\sqrt{n}} e^{i(j-1)(k-1)\theta}, \quad j, k = 1, \dots, n.$$

Because of this, \mathbf{E}_f diagonalises $\mathbf{\Pi}^k$ for any index k as follows

$$\mathbf{P} = \mathbf{E}_f^H \mathbf{\Pi}^k \mathbf{E}_f = \begin{pmatrix} 1 & 0 & 0 & \cdots & 0 \\ 0 & e^{i\theta} & 0 & \cdots & 0 \\ 0 & 0 & e^{i2\theta} & \cdots & 0 \\ \vdots & \vdots & \vdots & \ddots & \vdots \\ 0 & 0 & 0 & \cdots & e^{i(n-1)\theta} \end{pmatrix}, \quad (2.19)$$

where $e^{i(j-1)\theta}$, $j = 1, \dots, n$ is the j -th eigenvalue of $\mathbf{\Pi}^k$ (and also \mathbf{E}_f , because they are similar). From Eqs. (2.18) and (2.19), and the distributive property of the Kronecker product [96]

$$(\mathbf{A} \otimes \mathbf{B}) \otimes (\mathbf{C} \otimes \mathbf{D}) = \mathbf{AC} \otimes \mathbf{BD},$$

it is then possible to prove that any block-circulant matrix \mathbf{M}_b is similar to a block-diagonal matrix $\widetilde{\mathbf{M}}_b$ as follows

$$\begin{aligned} (\mathbf{E}_f^H \otimes \mathbf{I}) \mathbf{M}_b (\mathbf{E}_f \otimes \mathbf{I}) &= \sum_{k=1}^N \mathbf{P} \otimes \mathbf{M}_{bk} = \mathbf{P} \otimes \sum_{k=1}^N \mathbf{M}_{bk} = \\ &= \mathbf{B} \text{diag}[\widetilde{\mathbf{M}}_{b1}, \widetilde{\mathbf{M}}_{b2}, \dots, \widetilde{\mathbf{M}}_{bN}] = \widetilde{\mathbf{M}}_b. \end{aligned} \quad (2.20)$$

The single blocks $\widetilde{\mathbf{M}}_{bk}$ are functions of the blocks of the original matrix \mathbf{M}_b , and can be written as

$$\widetilde{\mathbf{M}}_{bk} = \sum_{j=1}^N \mathbf{M}_{bj} e^{i\theta(j-1)(k-1)}. \quad (2.21)$$

By defining the angle

$$\varphi_k = \frac{2\pi}{N} k = k\theta, \quad k = 0, \dots, N-1, \quad (2.22)$$

the following relationship is easy to prove

$$e^{i\theta(N-(j-1))(k-1)} = e^{i\varphi_k(N-(j-1))} = e^{-i\varphi_k(j-1)}, \quad j = 1 \dots, \lfloor \frac{N}{2} \rfloor,$$

and Eq. (2.21) becomes

$$\widetilde{\mathbf{M}}_{\mathbf{b}k} = \sum_{j=1}^{\lfloor \frac{N}{2} \rfloor} \left(\mathbf{M}_{\mathbf{b}j} e^{i\varphi_k(j-1)} + \mathbf{M}_{\mathbf{b}N-(j-1)} e^{-i\varphi_k(j-1)} \right). \quad (2.23)$$

As the sum of block-circulant matrices is itself block-circulant, it is easy to recognise that the generic matrix $\mathbf{M}_{\mathbf{b}}$ can represent the dynamic stiffness matrix \mathbf{D} as well. Following Eqs. (2.20) and (2.21), thanks to the cyclic-symmetry hypothesis, the original real eigenproblem $\mathbf{D}(\lambda)\Psi = 0$ of Eq. (2.16) can then be transformed into N complex eigenproblems

$$\widetilde{\mathbf{D}}_k \widetilde{\psi} = 0, \quad k = 0, \dots, N-1, \quad (2.24)$$

of dimension n [98], and $\widetilde{\psi}$ is the generic eigenvector of the k -th reduced problem.

If $\mathbf{M}_{\mathbf{b}}$ is symmetric, the property $\mathbf{M}_{\mathbf{b}N-(j-1)} = \mathbf{M}_{\mathbf{b}j}^T$ is easy to prove. Using Euler's formula, Eq. (2.23) can be developed into [99]

$$\begin{aligned} \widetilde{\mathbf{M}}_{\mathbf{b}k} &= \mathbf{M}_{\mathbf{b}1} + \sum_{j=2}^{\lfloor \frac{N-1}{2} \rfloor} \left((\mathbf{M}_{\mathbf{b}j} + \mathbf{M}_{\mathbf{b}j}^T) \cos \varphi_k + i (\mathbf{M}_{\mathbf{b}j} - \mathbf{M}_{\mathbf{b}j}^T) \sin \varphi_k \right) + \\ &+ \begin{cases} \mathbf{0}, & N \text{ odd} \\ (-1)^k \mathbf{M}_{\mathbf{b}N/2}, & N \text{ even.} \end{cases} \end{aligned} \quad (2.25)$$

Since $\mathbf{M}_{\mathbf{b}j} + \mathbf{M}_{\mathbf{b}j}^T$ is the symmetric part of $\mathbf{M}_{\mathbf{b}j}$, and $\mathbf{M}_{\mathbf{b}j} - \mathbf{M}_{\mathbf{b}j}^T$ the antisymmetric part, and $\mathbf{M}_{\mathbf{b}1}$ and $\mathbf{M}_{\mathbf{b}N/2}$ are real and symmetric, $\widetilde{\mathbf{M}}_{\mathbf{b}k}$ is hermitian. This is the case for matrices \mathbf{M} , \mathbf{C} , and \mathbf{K}_{tot} for most linear, non-gyroscopic, traditionally damped structures. With these conditions, Eq. (2.24) becomes

$$\widetilde{\mathbf{D}}_k \widetilde{\psi} = (\lambda^2 \widetilde{\mathbf{M}}_k + \lambda \widetilde{\mathbf{C}}_k + \widetilde{\mathbf{K}}_{tot,k}) \widetilde{\psi} = \mathbf{0},$$

which is itself hermitian. The eigenproblem $\widetilde{\mathbf{D}}_k \widetilde{\psi} = 0$ thus admits n complex-conjugate pairs of eigenvalues and eigenvectors [100].

As $\varphi_{N-k} = -\varphi_k$, it can also be shown that $\widetilde{\mathbf{D}}_{N-k} \widetilde{\psi} = \widetilde{\mathbf{D}}_k^* \widetilde{\psi}$ also admits a complex-conjugate solution, which is in turn the complex-conjugate of the solution of $\widetilde{\mathbf{D}}_k \widetilde{\psi} = 0$. In particular, the j -th eigenvalue $\lambda_{N-k,j}$, corresponding to φ_{N-k} , is equal to the j -th eigenvalue $\lambda_{k,j}$ from φ_k , and is associated to the eigenvector $\widetilde{\psi}_{N-k,j} = \widetilde{\psi}_{k,j}^*$: two different eigenvectors, $\widetilde{\psi}_{k,j}$ and $\widetilde{\psi}_{k,j}^*$ are therefore associated to the same eigenvalue $\lambda_{k,j}$. Non-gyroscopic, proportionally damped cyclic-symmetric structures are thus characterised by *double* eigenvalues for values of the index k between 2 and $\lfloor \frac{N}{2} \rfloor$, and *simple* (unique) eigenvalues for $k = 0$, and, if N is even, $k = N/2$.

The significance of this can be better appreciated by considering the form of the resulting eigenvectors. The set of n eigenvector pairs $\tilde{\psi}_{k,j} \in \mathbb{C}^{n \times 1}$, $j = 1, \dots, 2n$ describes the j -th mode shape of a single sector, corresponding to φ_k . This sector mode shape can then be expanded back to the whole structure. Since the eigenvectors of the Kronecker product of two matrices is equal to the Kronecker product of their respective eigenvectors [96], the global r -th eigenvector ψ_r is, from Eq. (2.20),

$$\psi_r = \mathbf{e}_{f_k} \otimes \tilde{\psi}_{k,j} = \begin{pmatrix} \tilde{\psi}_{k,j} \\ e^{i\varphi_k} \tilde{\psi}_{k,j} \\ \vdots \\ e^{i\varphi_k(l-1)} \tilde{\psi}_{k,j} \\ \vdots \\ e^{i\varphi_k(N-1)} \tilde{\psi}_{k,j} \end{pmatrix}, \quad (2.26)$$

with $r = 1, \dots, nN$, $k = 1, \dots, N$, $j = 1, \dots, n$, and \mathbf{e}_{f_k} is the k -th eigenvector of matrix \mathbf{P} , which coincides with the k -th column of the Fourier matrix \mathbf{E}_f [97].

Eq. (2.26) is equivalent to rotating the sector mode shape $\tilde{\psi}_{k,j}$ around the circumference of the bladed disc by the angle φ_k , which, in the terminology of bladed discs, is called *inter-blade phase angle* (IBPA). The mode shapes of cyclic-symmetric structures are therefore themselves cyclic-symmetric, and the spatial “frequency” at which the sector mode shape repeats itself around the structure is determined by the index k . This leads to the appearance of a set of k zero-displacement nodal lines, which are called *nodal diameters* (ND) [9]. As $\varphi_{N-k} = -\varphi_k$, the maximum number of distinct ND mode families is $\lfloor N/2 \rfloor$. The first 4 ND modes for the first blade bending mode of a 24-sector bladed disc are shown in Fig. 2.2 as an example: nodal diameters, and the modulation of the amplitude of the mode due to φ_k , are well visible. Only the 0ND mode, corresponding to $\varphi_k = 0$, has no nodal diameter, and the blades move in unison.

This highlights the importance of the cyclic-symmetry hypothesis from a computational point of view: thanks to the decoupling introduced by Eq. (2.20), the full eigenproblem for a bladed disc, which, for a detailed model can easily contain more than 1e6 DOFs, can be reduced to $\lfloor \frac{N}{2} \rfloor$ sub-problems containing just the DOFs of a single sector. Only the sub-problems corresponding to the desired ND families can then be actually solved, which usually leads to significant cuts in run-time.

2.3.2 Frequency splits in the gyroscopic eigenproblem

The results of the previous section showed that cyclic symmetric structures are characterised by double eigenvalues for all k ND modes with $k \neq 0, \lfloor \frac{N}{2} \rfloor$, and stemmed from the hypothesis of symmetric system matrices. The Coriolis matrix, however, is skew-symmetric,

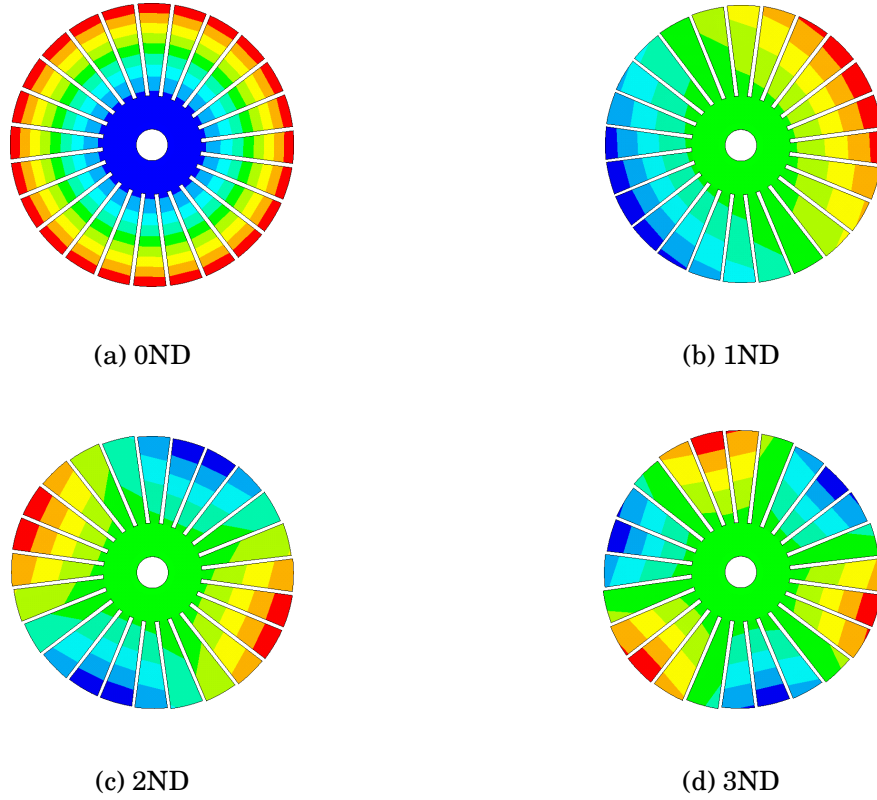


Figure 2.2: First four ND modes of a 24-sector cyclic-symmetric bladed disc. The colour red corresponds to positive displacement, blue to negative, green to no displacement.

i.e. $\mathbf{G}_{N-(j-1)} = -\mathbf{G}_j^T$. For the Coriolis matrix, Eq. (2.25) becomes

$$\begin{aligned} \tilde{\mathbf{G}}_k = & \mathbf{G}_1 + \sum_{j=2}^{\lfloor \frac{N-1}{2} \rfloor} ((\mathbf{G}_j - \mathbf{G}_j^T) \cos \varphi_k + i (\mathbf{G}_j + \mathbf{G}_j^T) \sin \varphi_k) + \\ & + \begin{cases} \mathbf{0}, & N \text{ odd} \\ (-1)^k \mathbf{G}_{N/2}, & N \text{ even.} \end{cases} \end{aligned} \quad (2.27)$$

The skew-symmetric part of \mathbf{G}_j is contained in the *real* part of $\tilde{\mathbf{G}}_k$, while the imaginary part is symmetric. $\tilde{\mathbf{G}}_k$ is therefore non-hermitian, which makes the reduced eigenproblem

$$\tilde{\mathbf{D}}_k \tilde{\boldsymbol{\psi}} = \left(\lambda^2 \tilde{\mathbf{M}}_k + \lambda (\tilde{\mathbf{C}}_k + \tilde{\mathbf{G}}_k) + \tilde{\mathbf{K}}_{tot,k} \right) \tilde{\boldsymbol{\psi}} = \mathbf{0} \quad (2.28)$$

likewise non-hermitian.

Non-hermitian quadratic eigenproblems like Eq. (2.28) admit complex eigenvalues and eigenvectors, which no longer appear as complex-conjugate pairs [100]. The implication for bladed discs is that double eigenvalues cannot exist—unless the sectors exhibit additional symmetry properties, which is not the general case: due to the asymmetry introduced by the Coriolis matrix, the double eigenvalues assume two distinct numerical values. As the eigenvalues represent the natural frequencies of the structure, this phenomenon is called

frequency split [18]. This is an effect of the Coriolis force that can have major consequences, as two distinct resonances can appear where only one would be expected if following the traditional analysis.

It is well known that the real part of the eigenvalue of a damped system is proportional to the damping itself. In a rotating structure, the Coriolis matrix is summed to the damping matrix, and could be expected to affect damping. However, as anticipated, the Coriolis force is not dissipative, and the eigenvalues of an undamped gyroscopic system are purely imaginary [11]. It is then possible to prove that, when damping is added, the eigenvalues take the familiar form

$$\lambda_r = (-\xi_r \pm \sqrt{1 - \xi_r^2})\omega_r, \quad (2.29)$$

where ξ_r is the damping ratio, and ω_r the natural frequency of mode r [101].

2.3.3 Travelling-wave modes

The inclusion of the Coriolis force in the eigenproblem of Eq. (2.16) affects its eigenvectors as well as its eigenvalues. As is well known, the eigenvectors associated to the EOMs of a structure correspond to its mode shapes [21]: the terms mode shapes and eigenvectors will henceforth be used interchangeably. To make the effect of the Coriolis force clear by comparison, the form of the eigenvectors of the non-gyroscopic system will be addressed first.

The eigenvectors ψ_r of Eq. (2.26) for the whole bladed disc apply to both the gyroscopic and non-gyroscopic case, and are generally complex. In the non-gyroscopic case, however, they come from the solution of Eq. (2.16), with $\mathbf{G} = \mathbf{0}$: if then the damping matrix \mathbf{C} satisfies the hypothesis of proportional damping, it is well known that the eigenvectors are purely real [21, 102]. These two statements are not contradictory. As shown previously, each k -index other than 0 and $N/2$ produces a double eigenvalue associated to two complex-conjugate eigenvectors. As these modes belong to the same eigenvalue, say, λ_r , a linear combination of them is still an eigenvector for λ_r . By considering the pair ψ_r and ψ_r^* (where ψ_r^* is the complex-conjugate of ψ_r), a generic combination would be [8]

$$\gamma_r = a\psi_r + b\psi_r^*, \quad (2.30)$$

where $a, b \in \mathbb{C}$ are arbitrary constants. With a and b equal to 1, γ_r would become real-valued: because of the simultaneous existence of two *distinct* eigenvectors for the same eigenvalue, cyclic-symmetric structures admit any kind of mode shape, real *or* complex.

Complex mode shapes are characterised by a relative phase between the DOFs different from 0° or 180° , as is the case for real modes. To better understand the implications, it is necessary to add the time dimension. Assuming single-mode behaviour for simplicity, the displacement response in time $\mathbf{z}_r(t)$, or *operational deflection shape* (ODS), can be obtained by multiplying Eq. (2.30) by $e^{i\omega_r t}$, where ω_r is the natural frequency corresponding to eigenvalue λ_r , and is considered with its sign from Eq. (2.29). A generic DOF j of the

displacement vector can then be expressed as

$$\gamma_{rj}e^{i\omega_r t} = A_j e^{i(\omega_r t + \theta_j)}, \quad (2.31)$$

with

$$\begin{aligned} A_j &= \|\gamma_{rj}\| \in \mathbb{R}, \\ \theta_j &= \arg(\gamma_{rj}). \end{aligned}$$

By taking the real part of Eq. (2.31), it is possible to find the physical ODS, which results in

$$\Re(\gamma_{rj}e^{i\omega_r t}) = z_{rj}(t) = A_j \cos(\omega_r t + \theta_j). \quad (2.32)$$

If γ_r is real, θ_j is either 0 or 180°, depending on the sign of γ_{rj} : the mode shape is locked in place, as the DOFs (or sectors) can only move in or out of phase with each other. For this reason, this type of mode shape is also called *standing wave* (SW) mode.

If γ_r is complex, on the other hand, the phase θ_j changes at every DOF j . Applying this on Eq. (2.26), and considering a single DOF j per sector, the ODS $z_j(t)$ at point j in Eq. (2.32) becomes

$$z_j(t) = A_j \cos(\omega_r t + (j-1)\varphi_k), \quad j = 1, \dots, N, \quad (2.33)$$

where φ_k is the IBPA associated to ND family k (Eq. (2.22)), and $\tilde{\psi}_{rjk}$ is the j -th component of the r -th mode shape $\tilde{\psi}_k$. In this case, each sector reaches its maximum/zero at different times from its neighbours, and fixed nodal lines/diameters cannot exist. Eq. (2.33) represents the equation of a *travelling wave* (TW), and its direction is determined by the relative signs of ω_r from Eq. (2.29), and φ_k . If ω_r and φ_k have the same sign, the TW mode propagates in the direction opposite the rotational speed, and is therefore defined a *backward* (BW) travelling wave. Opposite signs correspond to a *forward* (FW) wave, which moves with the spin speed. For simplicity, in the following, FW TWs will be associated to a negative index k for φ_k , and vice versa for BW TWs. However, in the analysis of gyroscopic structures, it is also conventional to associate FW modes with the frequency ω_r taken with the positive sign, and BW modes with $-\omega_r$. The two conventions can be easily shown to be equivalent, and will be used interchangeably.

Eq. (2.33) is plotted in Fig. 2.3, for the case of an eight-sector blisk (Fig. 2.3a), at the 3ND. As the model is cyclic-symmetric, the mass m_i , stiffness k_i , and damping c_i are the same at all sectors. Each curve represents a different sector, and the displacement $\mathbf{z}(t)$ is plotted in time. The case of a real mode shape is first displayed in Fig. 2.3b. It can be seen that all sectors move either in or out of phase. The displacement amplitude that can be reached is modulated around the circumference of the disc. The maximum amplitude is reached only at sectors 1 and 5, and the displacement at sectors 3 and 7 is zero at all times, indicating that they lie on a nodal diameter: the mode shape is fixed, or locked, in space.

Fig. 2.3c, on the other hand, shows a FW travelling wave. For the FW 3ND mode, φ_{-3}

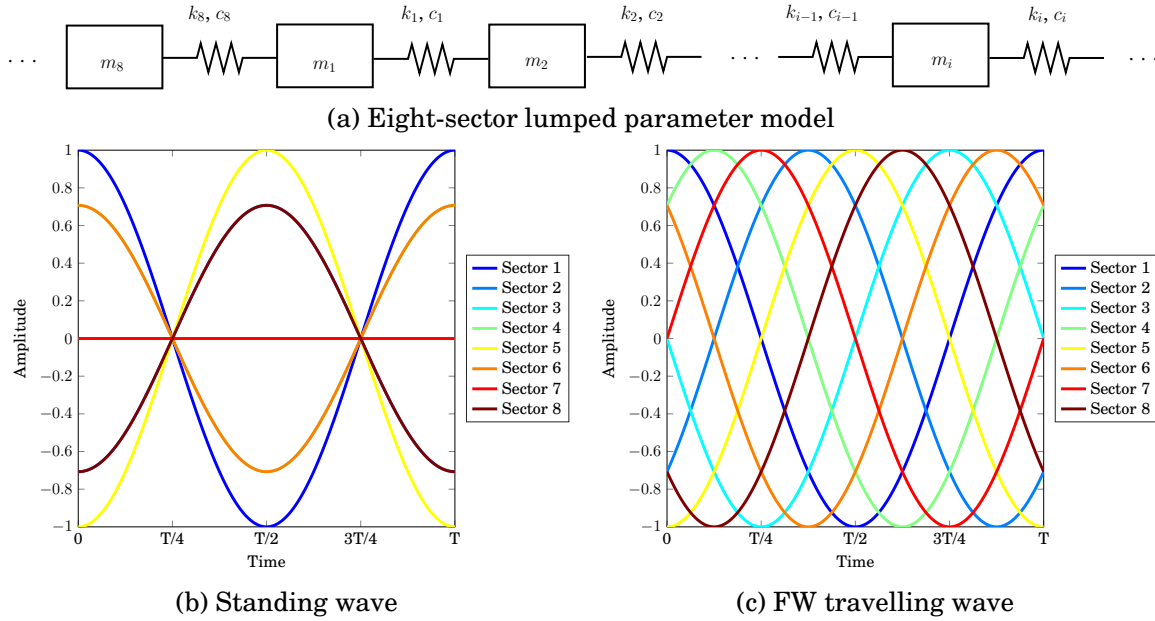


Figure 2.3: Time response of an eight-sector lumped parameter blisk model, 3ND mode.

is equal to -135° . All sectors can be seen to reach the maximum amplitude at some point of the vibration period. The crest of the wave propagates from sector to sector, which means that the nodal diameters are not fixed.

As explained above, non-gyroscopic systems admit SW modes because two distinct eigenvectors belong to the same eigenvalue, and can thus be superposed to yield arbitrary mode shapes. The same does not apply to gyroscopic structures: the Coriolis effect causes a split of the natural frequencies, and a single eigenvector is associated to each of them. Only TW modes are then possible when the Coriolis force is not neglected, and their direction is likewise not arbitrary, but depends on both the sign of φ_k , and that of ω_r . The direction of the mode shape has important consequences on aeroelastic stability: due to the asymmetry of the blades themselves, the aerodynamic forces are influenced differently depending on whether the blades are collectively vibrating with or against the speed of rotation. This in turn affects aerodynamic damping, which can exhibit strong dependence on the direction of the TW mode, and either damp or excite (flutter) the vibration of the blade depending on it [16].

2.3.4 Campbell diagram

The effects of the Coriolis force on both natural frequencies and TW direction can be visualised in a *Campbell diagram* [103]. The Campbell diagram is widely used to display the dependency of the natural frequencies of a rotating structure on rotational speed. Fig. 2.4 shows an example Campbell diagram for a 12-blade disc. It can be seen that the frequencies of most modes tend to increase with rotational speed, due to centrifugal stiffening.

The straight lines in Fig. 2.4 correspond to rotation-dependent excitation sources. Aerodynamic loading is the primary source of dynamic excitation in an aero-engine, and can cause cyclic forcing patterns generated by the rotation of the structure inside the fluid

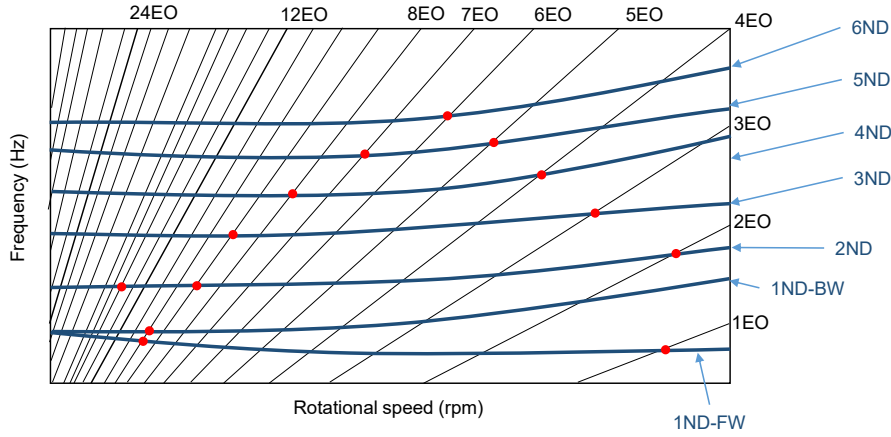


Figure 2.4: Illustrative Campbell diagram for a 12-blade disc.

pressure field: in the internal stages of a turbomachine, the wakes of the stator rows act on the rotating blades as time-periodic excitations [104]. For fans, propellers, or open rotors, which are directly exposed to the external air-flow, even a constant air inflow, if it is angled with respect to the axis of rotation, is seen as a variable force, because the blades change their orientation with respect to it during rotation. Due to their dependence on the rotational speed, this kind of excitation is called *engine order* (EO) excitation, and the order is determined by the spatial periodicity of the excitation along the circumference [105]. A 7EO, for example, corresponds to an excitation that repeats itself seven times per revolution: its excitation frequency is then equal to 7Ω .

The points of intersection between the natural frequencies of the bladed disc of the various ND modes and the EO lines correspond to *critical speeds* of the system: strong resonant behaviour can be expected at these speeds, as the frequency of excitation equals a natural frequency of the system. It can be seen that the EO lines cross most modes: however, EO forces can excite only specific families of ND modes. Considering a forcing vector $\mathbf{f}(t)$ containing the excitation at each sector j , with

$$f_j(t) = f_0(t)e^{i\frac{2\pi m}{N}j},$$

where m is the engine order, and a displacement $\mathbf{z}(t)$, with

$$z_j(t) = z_0(t)e^{i\frac{2\pi k}{N}j},$$

where k is the nodal diameter number, the work done by \mathbf{f} on \mathbf{z} at any time t can then be expressed as [105]

$$\begin{aligned} \mathbf{f}^H \mathbf{z} &\propto \int_0^{2\pi} (\cos m\theta - i \sin m\theta)(\cos k\theta + i \sin k\theta) d\theta = \\ &= \int_0^{2\pi} \cos(m-k)\theta d\theta + i \int_0^{2\pi} \sin(m-k)\theta d\theta = \begin{cases} 2\pi, & m-k = \pm jN \\ 0, & m-k \neq \pm jN, \end{cases} \end{aligned}$$

with $j \in \mathbb{N}$. A critical speed for a k ND mode then appears only at the intersection with engine orders $|m| = jN \pm k$ [106], and the same mode can be excited by different EOs due to spatial aliasing.

The split curves in Fig. 2.4 are caused by the Coriolis effect, as explained in sect. 2.3.2. In a rotating frame of reference, the lower branch is associated to FW TWs, while the upper one to BW TWs [107]. This can be the cause of some confusion, due to the different conventions used in the study of rotordynamics and the dynamics of bladed discs, and should be shortly commented upon.

In rotordynamics, Campbell diagrams are usually derived in the stationary, inertial (or *absolute*) reference frame. Rotordynamics is based on axisymmetric shaft-disc models, which can be solved in either a stationary or rotating frame without significant differences. As rotordynamics is often concerned with rotor-stator interactions, a Campbell diagram in the stationary frame can be directly compared to the dynamics of the stator, which makes the stationary frame more convenient. In the stationary frame, the gyroscopic moment generated in Euler's equations tends to straighten the shaft if it is vibrating in a FW mode: this introduces a stiffening effect, and *increases* the FW frequencies. For BW modes, on the other hand, the gyroscopic moment leads to additional bowing, and the resonance frequencies *decrease* with rotational speed [107].

Fig. 2.5a shows a representative Campbell diagram derived in the stationary frame, which exhibits the characteristics just described. The EO1 line was also added, and its intersection with the FW branch identifies the first critical speed. The first critical speed therefore appears as the rotational speed at which the natural frequency of the rotor equals the rotational speed itself. It thus represents a speed at which the rotor can easily be excited by geometrical imperfections of the rotor itself, i.e. unbalance.

As modes in rotors appear as rotations, or *whirl*, around the spin axis, and as TWs in bladed discs, their natural frequencies in the stationary reference frame ω_{abs} can be correlated to the frequency in the rotating (or *relative*) frame ω_{rel} by applying the galilean transformation

$$\omega_{abs} = \omega_{rel} + \Omega \quad \Leftrightarrow \quad \omega_{rel} = \omega_{abs} - \Omega. \quad (2.34)$$

Here, all frequencies are not simply considered in absolute value, but are signed: a negative sign implies a BW propagation, while a FW mode is associated to a positive frequency.

Through Eq. (2.34), it can then be seen that translating these frequencies into the rotating frame leads to the opposite result to the one obtained in the stationary frame. For a BW mode, ω_{abs} has a negative value, which means that the modulus of ω_{rel} increases if Ω is considered positive, and the frequencies associated to BW modes are larger than those associated to FW modes. This is visible in Fig. 2.5b, where in particular the critical speed is the same as in the stationary frame, but with a corresponding frequency of 0 Hz, as can be found by imposing the condition for the first critical speed of $\omega_{abs} = \Omega$ in Eq. (2.34).

It must also be noted that the lower branches correspond to FW whirl before the critical speed, and BW whirl thereafter. Before the critical speed, the condition $0 < \Omega < \omega_{abs}$ yields a positive ω_{rel} from Eq. (2.34), hence a FW whirl in the relative frame as well. After the

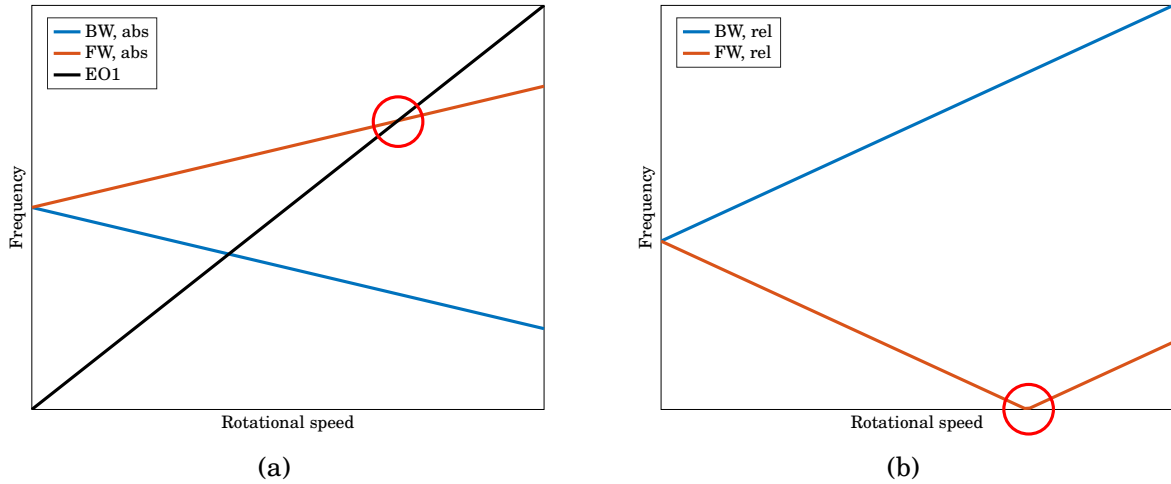


Figure 2.5: Campbell diagram of a gyroscopic system in the a) stationary, and b) rotating frame. The first critical speed is circled in red.

critical speed, on the other hand, the condition $0 < \omega_{abs} < \Omega$ means that the whirl changes direction in the rotating frame, and becomes a BW mode ($\omega_{rel} < 0$).

This is what should be expected for cyclic symmetric structures in general, and bladed discs in particular, as their modal analysis has to be conducted in the rotating frame: as was explained in sect. 2.2.1, solving them in a stationary frame would cause the appearance of time-varying terms in the system matrices, and thus require non-standard solution techniques, which can be avoided in the rotating frame.

2.3.5 Mistuning

The Coriolis force has been shown to affect both natural frequencies and modes of a bladed disc. Another phenomenon, called *mistuning*, is also capable of this. Mistuning has been the subject of much research over the past century, and a thorough treatment of the phenomenon is beyond the scope of this thesis. Its similarities and differences with the Coriolis effect, however, are relevant to this study, and will therefore be explained in more detail.

A structure is defined as *tuned* if it is perfectly cyclic-symmetric. Real structures, however, are rarely tuned, due to the asymmetries introduced by manufacturing tolerances, material defects, micro-cracks, wear, etc. These deviations from symmetry are collectively defined as *mistuning*. The presence of mistuning violates the cyclic symmetry hypothesis on which the results from the previous section were based. In particular, the dynamic stiffness matrix D is no longer block-circulant, as all sectors have different material properties from each other. Its associated eigenvalues do not appear as pairs, but are now, in general, simple. Since the number of eigenvalues is dictated by the dimension of the eigenproblem D , any bladed disc with N sectors described by n DOFs is characterised by Nn natural frequencies. However, a cyclic-symmetric structure has $\frac{n(N+2)}{2}$ unique frequencies, if N is even, or $\frac{n(N+1)}{2}$, if N is odd [99], because of the presence of double eigenvalues. A mistuned system, on the other hand, will have Nn distinct values, since the hypothesis of block-circulant $D(\lambda)$ does not apply any more. This phenomenon is called *frequency split*:

the double eigenfrequencies are no longer coincident, and, with sufficiently low damping, two separate resonances would appear (Fig. 2.6) [108].

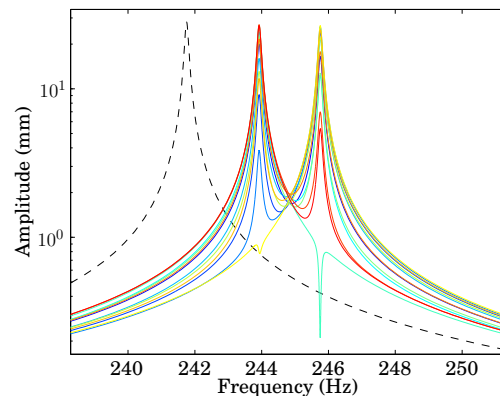


Figure 2.6: Comparison of the dynamic response at the 2ND mode of a 13-sector bladed disc model : ---, tuned case; —, mistuned case. (Adapted from V. Ruffini, “Analisi dinamica di sistemi soggetti a mistuning smorzati per attrito,” Master’s thesis, Università Politecnica delle Marche, 2010.)

Fig. 2.6 shows the amplitude of displacement of representative points at each of the 13 sectors of a bladed disc model subject to stiffness mistuning: besides the already mentioned frequency split, the sectors respond with different amplitude levels, as each of them is characterised by different material properties. This variation in the response depends heavily on the degree of coupling between the sectors. It has been observed [109] that, in strongly coupled systems, the amount of mistuning usually present in bladed discs produces limited deviations from the behaviour of a tuned system, and the associated mode shapes can still be classified in ND families. In weakly coupled systems, on the other hand, strong *localisation* can occur, whereby a few sectors exhibit levels of response much higher than in a tuned system, while others a much lower one. This is accompanied by a strong distortion of the mode shapes [110], which deviate from ND collective behaviour towards a blade-only response mode.

The modes are also affected by the frequency split. In the previous section, it was shown that double modes belonging to the same eigenvalue could be arbitrarily combined to produce either standing or travelling-wave modes. When mistuning is present, the eigenvalues become simple, and they are associated to a single eigenvector, so the mode shapes can no longer be rotated around the structure. If no Coriolis matrix is present, and damping is proportional, the eigenvectors are real [21]. The mode shapes then assume a distinct orientation in the disc, even if they are still arranged in ND configurations, and their nodal diameters are locked in a fixed position [108]. It can therefore be seen that both the Coriolis force and mistuning cause frequency splits, but their effect on mode shapes is opposite.

2.4 Modal testing of rotating structures

2.4.1 Frequency Response Function for rotating systems

Modal testing is an established approach to validate theoretical structural models through experiment: the prediction capabilities of the model can be confirmed by comparing the dynamic properties extracted from experiment to the natural frequencies and mode shapes of the model. In addition, damping, which is essential to predict the maximum vibration levels, and thus assess the risk of fatigue, can only be extracted through testing.

This is most easily and reliably accomplished by forced response analysis: the test structure is subjected to a known excitation, and its response (displacements, velocities, or accelerations) is measured, to obtain the frequency response function (FRF) matrix $\mathbf{H}(\omega)$. The expression for a generic element $H_{jk}(\omega)$ for a linear non-rotating structure is [21]

$$H_{jk}(\omega) = \frac{X_j(\omega)}{F_k(\omega)} = \sum_{r=1}^N \frac{{}_r R_{jk}}{i\omega - \lambda_r} = \sum_{r=1}^N \frac{\psi_{jr} \psi_{kr}}{i\omega - \lambda_r}, \quad (2.35)$$

where N is the number of degrees of freedom in the system, and X_j is the response measured at point j while an excitation F_k is applied at point k . λ_r is the eigenvalue of the r^{th} mode, and ${}_r R_{jk}$ is the *residue* corresponding to mode r , which is proportional to ψ_{jr} and ψ_{kr} , the j -th and k -th components of r -th eigenvector ψ_r , respectively.

Eq. (2.35) shows how the residue ${}_r R_{jk}$ and the eigenvectors of the structure are related. It is therefore possible to obtain the mode shapes from a suitable number of FRF measurements. It is easy to see that, for a system described by Eq. (2.35), the principle of reciprocity applies, as $H_{jk}(\omega)$ is equal to $H_{kj}(\omega)$, i.e. the FRF matrix is symmetric. As a result, the mode shapes could in theory be extracted by either a single column, or a single row of $\mathbf{H}(\omega)$ ². In the first case, this is easily accomplished by applying a known excitation force to a point on the structure, and measuring the response at a number of points corresponding to the number of DOFs required by the target mode shape. In the second, the response at a single location can be acquired, while exciting the structure at the required DOFs [21].

A similar expression for the FRF of a structure in rotating conditions is necessary to allow modal parameter extraction when the Coriolis effects are active, and its derivation is detailed in the following. The quadratic eigenproblem of Eq. (2.16) is usually linearised by recasting it into state-space form [100, 111]. A new vector of unknowns is defined as $\mathbf{z}(t) = |\dot{\mathbf{x}}_d^T \quad \mathbf{x}_d^T|^T$, which yield a first-order representation of the EOMs as

$$\mathbf{A}\dot{\mathbf{x}} + \mathbf{B}\mathbf{x} = \mathbf{0}. \quad (2.36)$$

Assuming a solution of the type $\mathbf{z}(t) = \mathbf{Z}e^{\lambda t}$, and substituting into Eq. (2.36), the generalised eigenproblem

$$(\lambda\mathbf{A} + \mathbf{B})\mathbf{V} = \mathbf{0} \quad (2.37)$$

²In practice, additional components $H_{jk}(\omega)$ may be needed for redundancy, to ensure a more reliable modal parameter extraction process [21].

is found. The matrices \mathbf{A} and \mathbf{B} are defined as

$$\mathbf{A} = \begin{vmatrix} \mathbf{M} & \mathbf{0} \\ \mathbf{0} & \mathbf{K}_{tot} \end{vmatrix}, \quad \mathbf{B} = \begin{vmatrix} \mathbf{C} + \mathbf{G} & \mathbf{K}_{tot} \\ -\mathbf{K}_{tot} & \mathbf{0} \end{vmatrix}.$$

If the damping is not negligible, matrix \mathbf{B} has no particular symmetry structure, and the eigenproblem is defined as *non self-adjoint*, because its adjoint problem

$$(\lambda \mathbf{A}^T + \mathbf{B}^T) \mathbf{L} = \mathbf{0} \quad \Leftrightarrow \quad \mathbf{L}^T (\lambda \mathbf{A} + \mathbf{B}) = \mathbf{0}^T,$$

is different from the original one in Eq. (2.37). While the eigenvalues λ_r remain the same between the two eigenproblems, the solution eigenvectors \mathbf{L}_r ($\mathbf{L} = [\mathbf{L}_1, \mathbf{L}_2, \dots]$), called *left eigenvectors*, do not. The presence of the Coriolis matrix thus generates an additional set of eigenvectors, which are necessary to establish the following orthogonality properties [24]

$$\begin{aligned} \mathbf{L}^H \mathbf{A} \mathbf{V} &= \mathbf{I} \\ \mathbf{L}^H \mathbf{B} \mathbf{V} &= -\mathbf{\Lambda}, \end{aligned} \quad (2.38)$$

where $\mathbf{\Lambda}$ contains the eigenvalues λ_r of \mathbf{D} .

The eigenvector matrices \mathbf{V} and \mathbf{L} of the linearised system are related to the right and left eigenvector matrices $\mathbf{\Psi}_R = [\psi_{R,1}, \psi_{R,2}, \dots]$ and $\mathbf{\Psi}_L = [\psi_{L,1}, \psi_{L,2}, \dots]$ of the original dynamic stiffness matrix by the following relationships [100]:

$$\mathbf{V} = \begin{vmatrix} \mathbf{\Psi}_R \\ \mathbf{\Psi}_R \mathbf{\Lambda} \end{vmatrix}, \quad \mathbf{L} = \begin{vmatrix} \mathbf{\Psi}_L \\ \mathbf{\Psi}_L \mathbf{\Lambda}^H \end{vmatrix}. \quad (2.39)$$

With this notation, the left eigenvectors $\mathbf{\Psi}_L$ are the same as the right eigenvectors $\mathbf{\Psi}_R$ if the system is undamped, but differ if damping is present [111].

Having obtained these relationships, Eq. (2.15) can be translated from the time to the frequency domain by taking its Laplace transform, which yields

$$(s^2 \mathbf{M} + s(\mathbf{C} + \mathbf{G}) + \mathbf{K}_{tot}) \mathbf{X}(s) = \mathbf{F}_{ext}(s) \quad \Leftrightarrow \quad \mathbf{D}(s) \mathbf{X}(s) = \mathbf{F}_{ext}(s), \quad (2.40)$$

where $\mathbf{X}(s)$ and $\mathbf{F}_{ext}(s)$ are the Laplace transforms of $\mathbf{x}(t)$ and $\mathbf{f}(t)$ respectively. The FRF $\mathbf{H}(s) = \mathbf{X}/\mathbf{F}$ is then simply equivalent to the inverse $\mathbf{D}^{-1}(s)$ of the dynamic stiffness. However, this expression does not take advantage of the underlying modal properties of the system like Eq. (2.35) does. It was shown above how the dynamic stiffness can be linearised by recasting it into state-space form. By doing the same in the Laplace domain, $\mathbf{D}(s)$ can be linearised as $s\mathbf{A} + \mathbf{B}$. As these two matrices are equivalent, it can be proved [100] that $\mathbf{D}^{-1}(s)$ can be expressed as

$$\mathbf{D}^{-1}(s) = -\begin{vmatrix} \mathbf{I} & \mathbf{0} \\ \mathbf{0} & (s\mathbf{A} + \mathbf{B})^{-1} \end{vmatrix} \begin{vmatrix} \mathbf{0} \\ \mathbf{I} \end{vmatrix}. \quad (2.41)$$

Remembering Eqs. (2.39), and the orthogonality properties (2.38), and imposing $s = i\omega$ to obtain the Fourier form of \mathbf{H} , the inverse of $(s\mathbf{A} + \mathbf{B})$ can be written as

$$\begin{aligned} (i\omega\mathbf{A} + \mathbf{B})^{-1} &= (\mathbf{L}^{-H}\mathbf{L}^H(i\omega\mathbf{A} + \mathbf{B})\mathbf{V}\mathbf{V}^{-1})^{-1} = \\ &= (\mathbf{L}^{-H}(i\omega\mathbf{I} - \mathbf{\Lambda})\mathbf{V}^{-1})^{-1} = \mathbf{V}(i\omega\mathbf{I} - \mathbf{\Lambda})^{-1}\mathbf{L}^H. \end{aligned} \quad (2.42)$$

From Eqs. (2.41), (2.42), and (2.39), the final expression for the FRF $\mathbf{H}(\omega)$ of a damped rotating system is

$$\mathbf{H}(\omega) = \mathbf{D}(\omega)^{-1} = \mathbf{\Psi}_R(i\omega\mathbf{I} - \mathbf{\Lambda})^{-1}\mathbf{\Psi}_L^H = \sum_{r=1}^{N_m} \frac{\psi_{R,r}\psi_{L,r}^H}{i\omega - \lambda_r} + \frac{\psi_{R,r}^*\psi_{L,r}^T}{i\omega - \lambda_r^*}, \quad (2.43)$$

where N_m is the number of modes, is found. The residue ${}_rR_{jk}$ for mode r , response DOF j and excitation DOF k is then

$${}_rR_{jk} = \psi_{R,rj}\psi_{L,rk}^*. \quad (2.44)$$

The FRF for a rotating system depends on an additional set of parameters, the left eigenvectors. For this reason, it is easy to see from Eq. (2.44) that $\mathbf{H}(\omega)$ is not symmetric in general, and the principle of reciprocity is violated due to the Coriolis effect.

2.4.2 Strain modal analysis

In Chapter 1, the possibility of using strain gauges as sensors was considered. It was therefore necessary to find an analytical expression for the FRF when the output is strain. Strain FRFs (SFRF) have been derived in static cases [78–80, 112], but, to the author's knowledge, not under rotating conditions. An expression for the SFRF for a gyroscopic rotating structure is therefore explicitly derived here, by adapting to strain the analogous procedure outlined in [102] for displacement mode shapes.

Translating Eq. (2.15) into the frequency domain, and state space, the response vector $\mathbf{Z} = \begin{bmatrix} \dot{\mathbf{X}}^T & \mathbf{X}^T \end{bmatrix}$ can be expressed as a linear combination of the right eigenvector basis as

$$\mathbf{Z} = \sum_r Q_r \mathbf{V}_r. \quad (2.45)$$

Assuming the linearised expression of displacement (2.13), the strain induced by the centrifugal force can be considered as a static precondition. The dynamic strain vector \mathbf{E} in generic direction x can then be simply defined as

$$\mathbf{E} = \sum_r Q_r \frac{\partial \mathbf{V}_r}{\partial x} = \sum_r Q_r \mathbf{V}_r^\epsilon, \quad (2.46)$$

where \mathbf{V}_r^ϵ is the right *strain* eigenvector.

Substituting Eq. (2.45) into Eq. (2.37), the expression

$$i\omega \mathbf{A} \sum_r Q_r \mathbf{V}_r + \mathbf{B} \sum_r Q_r \mathbf{V}_r = \begin{vmatrix} \mathbf{F} \\ \mathbf{0} \end{vmatrix} \quad (2.47)$$

is obtained. Pre-multiplying it by the s -th left eigenvector \mathbf{L}_s^H , post-multiplying by the r -th right eigenvector \mathbf{V}_r , and setting $\mathbf{F}' = |\mathbf{F}^T \mathbf{0}^T|^T$, Eq. (2.47) becomes

$$i\omega \mathbf{L}_s^H \mathbf{A} \sum_r Q_r \mathbf{V}_r + \mathbf{L}_s^H \mathbf{B} \sum_r Q_r \mathbf{V}_r = \mathbf{L}_s^H \mathbf{F}',$$

and, for the orthogonality properties (2.38),

$$Q_r(i\omega - \lambda_r) = \mathbf{L}_r^H \mathbf{F}',$$

from which the constant Q_r can be found

$$Q_r = \frac{\mathbf{L}_r^H \mathbf{F}'}{i\omega - \lambda_r}.$$

Substituting into Eq. (2.46), it is possible to find an expression for \mathbf{E} in terms of \mathbf{F}' , as

$$\mathbf{E} = \sum_r \frac{\mathbf{L}_r^H \mathbf{F}' \mathbf{V}_r^\epsilon}{i\omega - \lambda_r}.$$

A generic component j of the strain vector \mathbf{E} is then

$$E_j = \sum_r \frac{L_{kr}^* F'_k V_{jr}^\epsilon}{i\omega - \lambda_r},$$

and the SFRF term between strain output at DOF j and input DOF k can then be found as

$$H_{jk}(\omega) = \frac{E_j}{F_k} = \sum_r \frac{V_{jr}^\epsilon L_{kr}^*}{i\omega - \lambda_r}. \quad (2.48)$$

The SFRF matrix at each frequency ω therefore is

$$\mathbf{H}(\omega) = \sum_r \frac{\mathbf{V}_r^\epsilon \mathbf{L}_r^H}{i\omega - \lambda_r} = \mathbf{\Psi}_R^\epsilon (i\omega \mathbf{I} - \mathbf{\Lambda})^{-1} \mathbf{\Psi}_L^H, \quad (2.49)$$

having substituted the relationships (2.39). It can be seen that the SFRF depends on the (right) strain mode shapes $\mathbf{\Psi}_R^\epsilon$, and on the *left* eigenvectors of the displacement $\mathbf{\Psi}_L$. This differs from the static case, where the SFRF depends on the displacement mode shape itself. For lightly damped systems, it can be shown that the presence of damping only causes first- and second-order perturbations on the eigenvectors of a purely gyroscopic system [101]. This means that the left displacement eigenvectors can be reasonably approximated as their right counterpart.

Until now, the FRF \mathbf{H} has been implicitly assumed as a square matrix. However, in real applications, the number of input DOFs is different (usually, much lower) from the number of outputs. \mathbf{H} is then a $N_o \times N_i$ rectangular matrix, where N_o is the number of outputs, and N_i the number of inputs. This entails that the strain eigenvector matrix Ψ^e_R is a $N_o \times N_m$ complex matrix, where N_m is the number of modes considered. The matrix of left eigenvectors Ψ_L has dimensions of $N_i \times N_m$. It is important to note, then, that Ψ_L contains the left eigenvector components *at the input DOFs*.

2.4.3 Multiple Input Multiple Output (MIMO) testing

From the preceding sections, it was seen that the Coriolis effect can cause the appearance of left eigenvectors that are different from their right counterparts. It was also explicitly proved that this always happens with SFRFs. The extraction of mode shapes, in this case, involves a higher number of unknowns than in traditional modal analysis. In a traditional context, the extraction of a displacement mode shape would require the measurement of N_o FRFs, as the residues ${}_rR_{jk}$ depend only on the N_o components of the right eigenvector $\psi_{R,r} \in \mathbb{C}^{N_o \times 1}$ [21] (see Eq. (2.35)).

However, in the modal analysis of damped gyroscopic systems, or when strain sensors are used, the number of unknowns rises to $N_o + N_i$, as each modal constant is equal to a product of two different entities, right and left eigenvectors. In particular, a generic row of the residue matrix \mathbf{R} , ${}_r\mathbf{R}_j \in \mathbb{C}^{1 \times N_i}$

$${}_r\mathbf{R}_j = \psi_{R,rj} \psi_{L,r}^H$$

contains information on the left eigenvector $\psi_{L,r}$, while a generic column, ${}_r\mathbf{R}_k \in \mathbb{C}^{N_o \times 1}$

$${}_r\mathbf{R}_k = \psi_{L,rk}^* \psi_{R,r}$$

is proportional to $\psi_{R,r}$. If all the modal parameters are to be extracted, at least a column *and* a row of a FRF should be measured, i.e. not only are several sensors needed, but the structure has also to be excited at multiple locations. Multiple-Input Multiple-Output (MIMO) test configurations are therefore necessary in this case.

Fig. 2.7 represents a generic MIMO system. All variables are considered in the frequency domain. The structure is excited by N_i inputs U_k . The measured force F_k differs from the actual input U_k because of noise M_k . Similarly, the true response of the system V_j is contaminated by noise N_j , and the measured signal results in $X_j = V_j + N_j$.

Considering the FRF \mathbf{H} of the system, which also acts as its transfer function, X_j can therefore be written as [113]

$$\begin{aligned} X_j(\omega) &= V_j(\omega) + N_j(\omega) = \sum_{k=1}^{N_i} H_{jk}(F_k(\omega) - M_k(\omega)) + N_j(\omega) = \\ &= \sum_{k=1}^{N_i} H_{jk}F_k(\omega) + E_j(\omega), \end{aligned} \quad (2.50)$$

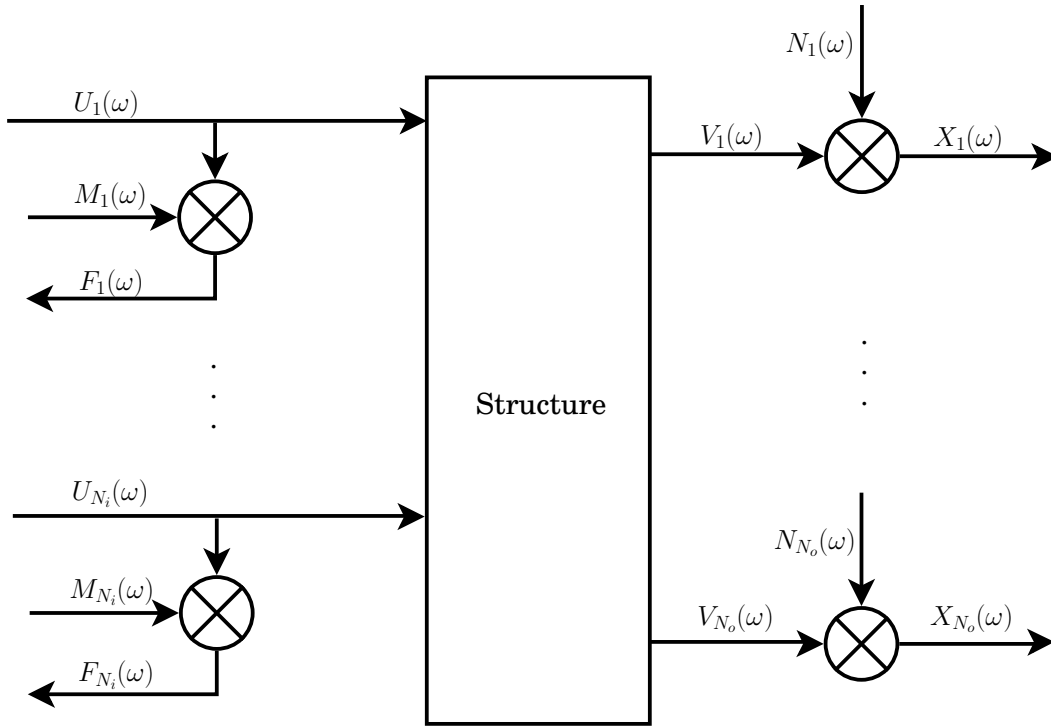


Figure 2.7: Multiple Input Multiple Output system.

where $E_j(\omega)$ combines the noise from the input and output sides. Assuming no input noise, so that U_k and F_k are equal, Eq. (2.50) can be put in vector form as

$$\mathbf{X}(\omega) = \mathbf{H}(\omega)\mathbf{F}(\omega) + \mathbf{N}(\omega),$$

with $\mathbf{X}(\omega) \in \mathbb{C}^{N_o \times 1}$, $\mathbf{F}(\omega) \in \mathbb{C}^{N_i \times 1}$, $\mathbf{H}(\omega) \in \mathbb{C}^{N_o \times N_i}$. Post-multiplying by $\mathbf{F}(\omega)^H$, the equation

$$\mathbf{G}_{XF}(\omega) = \mathbf{H}(\omega)\mathbf{G}_{FF}(\omega) + \mathbf{G}_{NF}(\omega),$$

is obtained. $\mathbf{G}_{XF}(\omega) \in \mathbb{C}^{N_o \times N_i}$ is the single sided cross-spectrum between output and input, $\mathbf{G}_{FF}(\omega) \in \mathbb{C}^{N_i \times N_i}$ is the auto-spectrum of the force, and $\mathbf{G}_{NF}(\omega) \in \mathbb{C}^{N_o \times N_i}$ is the cross-spectrum between force and input noise.

Under the assumption that the output noise is not correlated to the input excitation, an estimate for the FRF $\mathbf{H}(\omega)$ from a MIMO system, called the $\hat{\mathbf{H}}_1$ estimator [114], can be obtained as

$$\hat{\mathbf{H}}_1(\omega) = \hat{\mathbf{G}}_{XF}(\omega)\hat{\mathbf{G}}_{FF}^{-1}(\omega), \quad (2.51)$$

where the symbol $\hat{\cdot}$ signals that the quantity is an estimate. From Eq. (2.51), it is evident that the auto-power spectrum of the force \mathbf{G}_{FF} needs to be invertible. For this to be the case, \mathbf{G}_{FF} needs to be full-rank: its columns, i.e. the inputs, must be linearly independent. A sufficient condition for this (although not necessary [115]) is to have uncorrelated input signals.

Random excitation satisfies this requirement. It is also characterised by a broadband spectrum, which means that $\mathbf{H}(\omega)$ could in theory be obtained from a single test. However,

averaging over a certain number of data records is necessary [115] to obtain a full-rank \mathbf{G}_{FF} matrix, and to reduce the random error affecting the measurements.

An additional bias error ϵ_b in the estimate is introduced by leakage, as the input and output signals are not periodic. This bias can be reduced by the use of a time window. The window forces periodicity within the data record by reducing the signals to zero at the start and end of the blocksize. However, it cannot be eliminated [114, 115], and it can be shown to be equal to [114]

$$\epsilon_b = \frac{(\Delta f)^2}{6} \frac{\mathbf{G}''_{XX}}{\mathbf{G}_{XX}} + \frac{(\Delta f)^4}{72} \frac{\mathbf{G}''''_{XX}}{\mathbf{G}_{XX}},$$

where \mathbf{G}''_{XX} and \mathbf{G}''''_{XX} are the second and fourth derivatives of the auto-spectrum of the output \mathbf{G}_{XX} , respectively. This implies that the error ϵ_b will be larger in regions of fast change in $\mathbf{G}_{XX}(\omega)$, like around resonances. While the FRF estimates will therefore be inevitably biased, the systematic error can still be contained within known bounds, and further limited by reducing the frequency resolution Δf of the measurement.

2.4.4 pLSCF estimation method

MIMO testing provides an estimated FRF matrix $\mathbf{H}(\omega_f) \in \mathbb{C}^{N_o \times N_i}$ at various frequencies ω_f . Several techniques are available to extract the modal parameters [27, 102]. Multi-degree-of-freedom (MDOF) methods stand out because, being based on the data from several locations across a structure, provide more reliable estimates. Poly-reference methods, in particular, allow the full exploitation of MIMO data, because they allow the modal estimation process on the full \mathbf{H} at the same time. They are also the only method that can yield modal participation factors. Modal participation factors provide a measure of the adequacy of a certain forcing distribution to excite a particular mode, and are contained in the matrix \mathbf{L} in the FRF definition [116]

$$\mathbf{H}(\omega) = \mathbf{V}(\mathrm{i}\omega\mathbf{I} - \mathbf{\Lambda})^{-1}\mathbf{L}^H = \sum_{r=1}^{N_m} \left(\frac{\mathbf{R}_r}{\mathrm{i}\omega - \lambda_r} + \frac{\mathbf{R}_r^*}{\mathrm{i}\omega - \lambda_r^*} \right), \quad (2.52)$$

where \mathbf{V} is the mode shape matrix, and $\mathbf{\Lambda}$, as usual, the matrix containing the natural frequencies λ_r of the system. N_m is the number of modes of the system, and \mathbf{R}_r and \mathbf{R}_r^* are the complex-conjugate residues of mode r . In this context, modal participation factors are defined as [27]

$$\mathbf{L}_r = Q_r \mathbf{V}_r,$$

where Q_r is the scaling factor for mode r . However, it can immediately be seen that Eq. (2.52) is identical to Eq. (2.43) or Eq. (2.49): poly-reference methods are thus based on the same FRF representation as the one for rotating structures, or strain modal analysis, with left eigenvectors replacing the modal participation factors. Poly-reference techniques can then be readily applied to these situations, and actually allow the recovery of left eigenvectors alongside all other modal parameters. Among the various methods, the Poly-reference Least-square Complex Frequency domain (pLSCF) was chosen, because it

provides a relatively automatic parameter identification procedure, while at the same time giving the user a measure of its own reliability, the stabilisation diagram [117].

The pLSCF employs a curve-fitting process based on a Right Matrix Fraction Model of the FRF. The FRF is seen as the ratio between a numerator polynomial, represented by matrix $\mathbf{P}(\omega) \in \mathbb{C}^{N_o \times N_i}$, and a denominator polynomial, $\mathbf{Q}(\omega) \in \mathbb{C}^{N_i \times N_i}$, as in

$$\mathbf{H}_o(\omega) = \mathbf{P}_o(\omega)\mathbf{Q}^{-1}(\omega), \quad o = 1, 2, \dots, N_o,$$

with

$$\mathbf{P}_o(\omega) = \sum_{j=0}^M \Xi_j(\omega)\mathbf{B}_{oj},$$

and

$$\mathbf{Q}(\omega) = \sum_{j=0}^M \Xi_j(\omega)\mathbf{A}_j,$$

where $\mathbf{P}_o(\omega) \in \mathbb{C}^{1 \times N_i}$ is the row of matrix \mathbf{P} corresponding to DOF o , and M is the model order, i.e. the maximum order of the polynomial basis $\Xi(\omega)$. There are several possibilities for the choice of polynomial basis $\Xi_j(\omega)$, but the z-transform z was found to guarantee both well-conditioned matrices, and a fast solution [118]. The z-transform maps the FRF onto the unit circle in the complex plane, and yields the orthogonal polynomials [116, 119] $\Xi_j(\omega) = z^j$, with

$$z^j = e^{-ij\omega\Delta t},$$

where $\omega = \omega_f - \omega_0$, and

$$\Delta t = \frac{1}{2(\omega_{N_f} - \omega_0)}.$$

ω , ω_0 , and ω_{N_f} are the generic frequency variable, and the frequency values at the start and end of the analysed frequency range, respectively. It is useful to note here that Δt does not need to coincide with the actual sampling time of the data record, and therefore a variable frequency resolution is allowed during the measurement³. This is particularly convenient when using stepped- or swept-sine testing, as the frequency resolution can be made coarser or finer depending on the position of the resonances without impacting the curve-fitting process.

The parameters to be estimated are \mathbf{B}_{oj} and \mathbf{A}_j , which can be gathered in a matrix of unknowns $\boldsymbol{\theta} = |\boldsymbol{\beta}_1^T, \dots, \boldsymbol{\beta}_{N_o}^T, \boldsymbol{\alpha}^T|^T$, $\boldsymbol{\theta} \in \mathbb{C}^{(M+1)(N_i+1) \times N_i}$, with

$$\boldsymbol{\beta}_o = \begin{vmatrix} \mathbf{B}_{o0} \\ \mathbf{B}_{o1} \\ \vdots \\ \mathbf{B}_{oM} \end{vmatrix}, \quad \boldsymbol{\alpha} = \begin{vmatrix} \mathbf{A}_0 \\ \mathbf{A}_1 \\ \vdots \\ \mathbf{A}_M \end{vmatrix}.$$

³Time and frequency resolution Δt and Δf are linked by the relationship [114] $\Delta f = \frac{1}{N_s \Delta t}$, where N_s is the *blocksize*, i.e. the number of samples in a data record.

Since usually values for \mathbf{H} are available at several frequencies ω_f , the fitting problem can be solved in a least-square sense to obtain the estimated FRF $\hat{\mathbf{H}}(\omega)$ by minimising the error function

$$\epsilon_o^{NLS}(\omega, \boldsymbol{\theta}) = \mathbf{P}_o(\omega, \boldsymbol{\beta}_o) \mathbf{Q}^{-1}(\omega, \boldsymbol{\alpha}) - \mathbf{H}_o(\omega), \quad (2.53)$$

which is a nonlinear function of $\boldsymbol{\theta}$. $\mathbf{H}_o(\omega)$, in this case, is the o -th row of experimental FRF \mathbf{H} . Eq. (2.53) can be linearised by multiplying it by $\mathbf{Q}(\omega, \boldsymbol{\alpha})$, which yields

$$\epsilon_o^{LS}(\omega, \boldsymbol{\theta}) = \mathbf{P}_o(\omega, \boldsymbol{\beta}_o) - \mathbf{H}_o(\omega) \mathbf{Q}(\omega, \boldsymbol{\alpha}). \quad (2.54)$$

While leading to a sub-optimal solution of the minimisation problem, Eq. (2.54) was found empirically to produce excellent fits of the measured FRFs, while avoiding the solution of a fully nonlinear minimisation problem. The details of the solution of Eq. (2.54) can be found in [120].

Once the coefficients \mathbf{A}_j are known, the poles of the denominator polynomial $\mathbf{Q}(\omega)$ are found by solving the equation

$$z^M \mathbf{A}_M + z^{M-1} \mathbf{A}_{M-1} + \dots + A_0 = 0,$$

which is equivalent to finding the eigenvalues of a polynomial eigenproblem of order M . The eigenproblem can be solved through a companion matrix representation [121, 122],

$$\begin{vmatrix} -\mathbf{A}_M^{-1} \mathbf{A}_{M-1} & \dots & -\mathbf{A}_M^{-1} \mathbf{A}_1 & -\mathbf{A}_M^{-1} \mathbf{A}_0 \\ \mathbf{I} & \dots & \mathbf{0} & \mathbf{0} \\ \vdots & \ddots & \vdots & \vdots \\ \mathbf{0} & \dots & \mathbf{I} & \mathbf{0} \end{vmatrix} \mathbf{V} = \mathbf{L} \boldsymbol{\Pi}, \quad (2.55)$$

where $\boldsymbol{\Pi} \in \mathbb{C}^{MN_i \times MN_i}$ contains the poles q_j of $\mathbf{Q}(\omega)$, and \mathbf{L} is the matrix of mode participation factors [27, 116], or of left eigenvectors. The poles q_j have the form $q_j = e^{-\lambda_j \Delta t}$, so that the eigenvalues of the original system can be derived as $\lambda_j = -\ln \frac{q_j}{\Delta t}$, with

$$\begin{aligned} \lambda_j, \lambda_j^* &= -\xi_j \omega_j \pm i \sqrt{1 - \xi_j^2} \omega_j, \\ \omega_j &= \sqrt{(\Re \lambda_j)^2 + (\Im \lambda_j)^2}, \\ \xi_j &= -\frac{\Re \lambda_j}{\omega_j}. \end{aligned}$$

However, the number of poles q_j from Eq. (2.55) is $M^2 N_i^2$, which is in general much greater than the number of modes N_m in the analysed frequency range. This means that some of poles are not physical. A simple first approach to weeding out the computational poles is to discard the unstable ones, with positive real part, which would not appear in most physical passively-damped systems. The rest is sifted through an iterative solution of Eq. (2.55), where the model order M is incremented from one iteration to the other.

By comparing the poles obtained with different model orders, the numerical poles usually undergo large changes, and only the physical poles should stabilise, as they are actual fixed structural properties. This procedure can be presented visually in a *stabilisation diagram*, where the poles at the different model orders are plotted. Poles that have stabilised over a wide range of model orders, both in ω and ξ , within a predetermined tolerance, are usually reliable estimates of the physical parameters [120].

The left eigenvectors \mathbf{L}_r could also be derived at this stage. In the numerical tests of the implementation of the algorithm used for the present work, however, it was found that the eigenvectors \mathbf{L}_r did not stabilise (see also [123]). They can still be extracted, together with mode shapes, from Eq. (2.52), which can be adapted as follows

$$\mathbf{H}(\omega) = \sum_{r=1}^{N_m} \left(\frac{\mathbf{R}_r}{i\omega - \lambda_r} + \frac{\mathbf{R}_r^*}{i\omega - \lambda_r^*} \right) + \frac{\mathbf{R}_L}{\omega^2} + \mathbf{R}_U, \quad (2.56)$$

to take into account the fact that the FRF can only be measured in a limited frequency range, and that the parameter estimation may be further restricted to a subset of this range. For this reason, N_m represents only the modes active in this range, and \mathbf{R}_L and \mathbf{R}_U are the lower and upper residuals, respectively, and allow to simulate the effect of the modes present outside the frequency range considered. After estimating the resonance frequencies and damping factors, the only unknowns are the residues \mathbf{R}_r , \mathbf{R}_L , $\mathbf{R}_U \in \mathbb{C}^{N_o \times N_i}$. This can be done again in a least-square sense. After recognizing that the residues are formed of the multiplication of right and left eigenvectors

$$\mathbf{R}_r = \psi_{R,r} \psi_{L,r}^H,$$

as in Eq. (2.44), it is possible to see that both can be derived by SVD decomposition [120]

$$\mathbf{R}_r = \mathbf{U} \mathbf{\Sigma} \mathbf{W}^H.$$

$\mathbf{U} \in \mathbb{C}^{N_o \times 1}$ corresponds to right eigenvector $\psi_{R,r}$, and $\mathbf{W} \in \mathbb{C}^{N_i \times 1}$ to left eigenvector $\psi_{L,r}$. The singular value matrix $\mathbf{\Sigma} \in \mathbb{C}^{N_o \times N_i}$ can be interpreted as containing the scaling factor Q_r for each mode r [116]. For this reason, it should be of rank 1, as only a single scaling factor per eigenvector can be admitted. As the presence of multiple non-zero scaling factors would imply a deformation of the r -th eigenvector, the rank of matrix $\mathbf{\Sigma}$ provides a final check of the quality of the fitting process.

2.5 Piezoelectric actuation

2.5.1 Piezoelectric materials

The FRF expressions derived so far have been based on the assumption that excitation came from concentrated forces. In Chapter 1, laminar piezoelectric actuators were identified as promising excitation devices, especially in a MIMO testing configuration. This

section therefore aims to introduce their characteristics, and to establish how they can be applied to a modal analysis context.

Piezoelectric materials exhibit coupled electromechanical properties. Under the *direct* piezoelectric effect, an applied stress causes a change in the polarization of the material, and a charge flow. Under the *converse* effect, an electric field generates a strain. Weak piezoelectricity is found in natural crystals, but is enhanced in synthetic materials. Lead-zirconium-titanate (PZT) ceramics are currently the most commonly manufactured piezoelectric material. They are composed of perovskite crystals with an orthorhombic tetragonal structure (Fig. 2.8). The off-centre position of the titanium/zirconium cations produces a spontaneous polarization in the crystals, which behave as dipoles. The orientation of the crystals relative to one another in the material is random, so only weak piezoelectricity can be found in the raw material. Through heating, however, the dipoles can align along the same direction for all the grains if a strong electrical field is added. Once cooled, the material is permanently polarised [124].

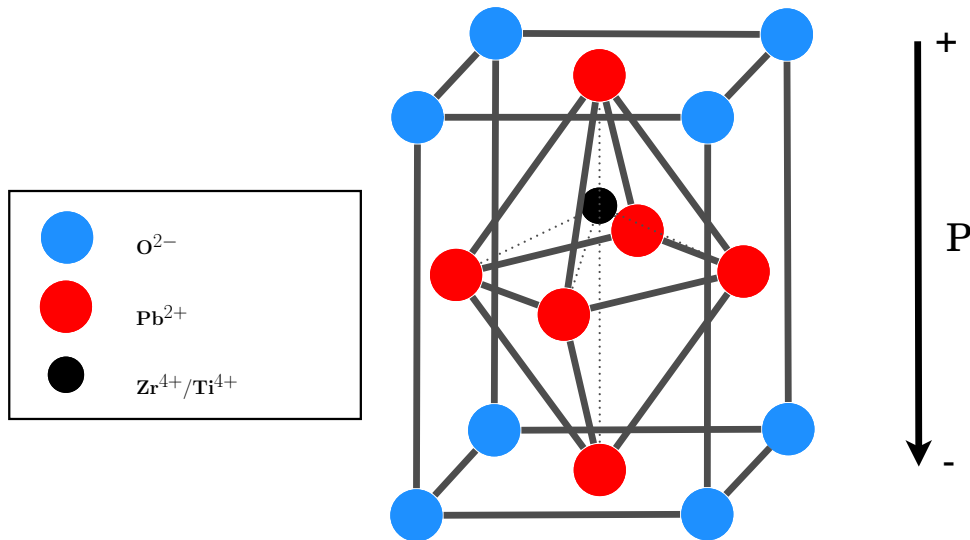


Figure 2.8: Crystal structure of a PZT piezoelectric material.

An applied stress then causes the crystal lattice to deform mechanically, thus increasing the charge asymmetry, and generating a charge flow. An applied voltage, on the other hand, causes an electric field that tends to change the orientation of the dipoles, and thus produces a strain in the material due to the continuum constraint.

These relationships can be formalised in the constitutive equations for piezoelectric materials, which link the strain and charge flow in the form of *electric displacement* \mathbf{D}_e ⁴ with stress and electric field \mathbf{E}_e . It is convenient to exploit the symmetry of the stress and strain tensors, $\boldsymbol{\sigma}$ and $\boldsymbol{\varepsilon}$, and express them as vectors $\mathbf{S}, \mathbf{T} \in \mathbb{R}^{6 \times 1}$ as in sect. 2.2.2. Under the hypothesis of moderate electric fields, these equations are linear, and can be expressed

⁴The *electric displacement* is the charge generated divided by the area of the electrodes, and has units of C/m^2 .

as [45]

$$\begin{vmatrix} \mathbf{S} \\ \mathbf{D}_e \end{vmatrix} = \begin{vmatrix} \mathbf{s}^E & \mathbf{d}^T \\ \mathbf{d} & \boldsymbol{\epsilon}^T \end{vmatrix} \begin{vmatrix} \mathbf{T} \\ \mathbf{E}_e \end{vmatrix}, \quad (2.57)$$

where $\mathbf{D}_e \in \mathbb{R}^{3 \times 1}$ is the electric displacement, and $\mathbf{E}_e \in \mathbb{R}^{3 \times 1}$ the electric field. $\mathbf{s}^E \in \mathbb{R}^{6 \times 6}$ is the short-circuit compliance matrix, which contains the constitutive relationship of the material when the electrodes are short-circuited; $\mathbf{d} \in \mathbb{R}^{3 \times 6}$ contains the piezoelectric strain coefficients, which link strain to electric field, and charge displacement to stress. $\boldsymbol{\epsilon} \in \mathbb{R}^{3 \times 3}$ contains the dielectric permittivity values, and is a diagonal matrix for most piezoelectric materials.

Eq. (2.57) clearly shows that the presence of either a stress or an electric field will generate strain and charge in the piezoelectric material. A common operation mode for a laminar piezoelectric actuator (also called patch, in this case) is the d_{31} mode [45]. The subscripts refer to the conventional reference frame assigned to piezoelectric materials: 3 is the direction of polarisation P , which, in the patch represented in Fig. 2.9, is along the thickness t_p , and 1 and 2 are perpendicular to it. The first subscript refers to the polarisation direction, which is also the direction of application of the input electrical field \mathbf{E}_e . The second reveals the direction of strain. With d_{31} patches, then, the strain is perpendicular to the polarisation axis P , and happens in the plane of the patch.

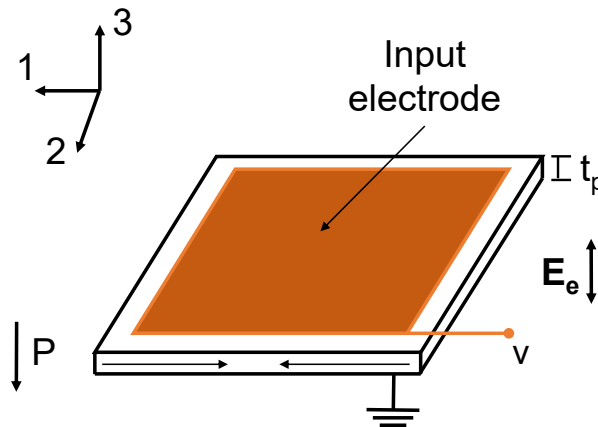


Figure 2.9: Laminar piezoelectric actuator in d_{31} operation mode.

In this mode, the electric field \mathbf{E}_e can be varied to control the patch, and thus provides the actuator capability by inducing a varying strain in the 1 direction. The electrical field is applied at the input electrode on the upper surface of the patch, and is uni-axial, i.e. only the $E_{e,3}$ component is non-zero.

2.5.2 Dynamics of structures with piezoelectric excitation

The previous section has shown that the ability of piezoelectric materials to react with a strain to an applied voltage makes them viable as actuators. In this section, the equations of motion for a piezoelectrically driven rotating structure will be derived to quantify this

capability. Their derivation [94, 125] follows closely the procedure outlined in sect. 2.2.2, and it would be redundant to repeat it. The main difference is the addition of the work of the electrical energy W_e to the Hamiltonian of Eq. (2.4)

$$\int_{t_1}^{t_2} \delta(K - U + W_e + W_{ext})dt = 0, \quad (2.58)$$

with

$$K = \frac{1}{2} \int_{V_s} \rho_s \dot{\mathbf{r}}^T \dot{\mathbf{r}} dV + \frac{1}{2} \int_{V_p} \rho_p \dot{\mathbf{r}}^T \dot{\mathbf{r}} dV \quad (2.59)$$

$$U = \frac{1}{2} \int_{V_s} \mathbf{T}^T \delta \mathbf{S} dV + \frac{1}{2} \int_{V_p} \mathbf{T}^T \delta \mathbf{S} dV \quad (2.60)$$

$$W_e = \frac{1}{2} \int_{V_p} \mathbf{E}_e^T \mathbf{D}_e dV, \quad (2.61)$$

where the subscripts p and s refer to the piezoelectric material and elastic substrate, respectively.

The discretisation for the displacement and strain of the piezoelectric material follows again sect. 2.2.2. The electric field \mathbf{E}_e can likewise be discretised via a shape function \mathbf{N}_v as

$$\mathbf{E}_e = -\nabla \cdot \phi(\mathbf{r}, t) = \mathbf{N}_v \mathbf{v}(t), \quad (2.62)$$

where ϕ is the electrical potential, and $\mathbf{v}(t)$ contains the generalised electrical coordinates at the input DOFs, which can be set to coincide with the voltage applied at the electrodes [125].

The final EOMs for a rotating system excited only by piezoelectric elements can be written as

$$(\mathbf{M}_s + \mathbf{M}_p)\ddot{\mathbf{x}} + (\mathbf{C}_s + \mathbf{C}_p + \mathbf{G}_s + \mathbf{G}_p)\dot{\mathbf{x}} + (\mathbf{K}_{tot,s} + \mathbf{K}_{tot,p})\mathbf{x} = \Theta \mathbf{v}, \quad (2.63)$$

The piezoelectric coupling matrix Θ is equal to [126]

$$\Theta = \int_{V_p} \mathbf{N}_\varepsilon^T \mathbf{d}^T \mathbf{N}_v.$$

Θ represents the electro-mechanical coupling introduced by the piezoelectric effect, whereby an applied voltage translates into a mechanical forcing term.

2.5.3 FRF expression with piezoelectric actuation

An analytical expression for the FRF of a rotating structure under piezoelectric excitation in terms of modal parameters is desirable at this point, to allow the application of modal analysis even with this non-traditional forcing method. By representing $\Theta \mathbf{v}$ with a generic forcing vector \mathbf{F} , it would be possible to obtain an expression identical to Eq. (2.49). However, Θ is in general a full matrix, and therefore each component F_k could depend on the voltage at more than one input DOF. This violates the common interpretation of the FRF

matrix, where each term depends on the response and forcing at one output and one input DOF at a time. Furthermore, since the force generated by a piezoelectric patch cannot be directly measured, it would be convenient to derive a FRF expression dependent only on the input voltage.

Some simplifications can be made. The d_{31} actuators are assumed planar, and their reference frame 1-2-3 aligned with the reference frame of displacement x . If the voltage is applied along direction 3, across the patch thickness, the resulting strain, and excitation, will occur exclusively along direction 1. This means that, with a proper alignment of the reference frames of structure and actuators, no spurious cross-coupling between multiple DOFs takes place.

Under these assumptions, each component of the forcing term Θv depends only on one voltage input, and Θ can be considered a diagonal matrix in this case. A FRF in terms of strain and voltage $H(\omega) = E(\omega)/\bar{v}(\omega)$, where $\bar{v}(\omega)$ is the Fourier transform of the voltage v , can therefore be derived, and is identical to Eq. (2.49), within a constant scaling factor.

2.6 Summary and Conclusions

This Chapter presented the theoretical framework necessary for the quantitative analysis of the Coriolis effect in bladed discs, and the adaptation of the traditional modal analysis methods for the experimental identification of frequencies, mode shapes, and left eigenvectors in rotating structures.

The cyclic-symmetry formalism was used to explain the Coriolis effects in bladed discs. Frequency splits for double modes, and complex-valued mode shapes in the form of travelling-wave modes were shown to derive from the non-hermitian reduced eigenproblem caused by the presence of the Coriolis matrix in the equations of motion. The Coriolis force, depending on the direction of the vibrational velocity, breaks the symmetry of the structure, and thus causes frequency splits much like mistuning, which was briefly treated exactly because it can produce similar effects. However, it was also shown that mistuning generates standing-wave modes, and can thus be discriminated from the action of the Coriolis force.

A FRF expression for strain modal analysis (SFRF) in the presence of the Coriolis effect was derived for the first time, and proven to depend on strain mode shapes, and left displacement eigenvectors. As left eigenvectors can approximate right eigenvectors in lightly-damped structures, it could be proved that both strain mode shapes at the output DOFs, and displacement mode shapes at the input DOFs can be derived, thanks to the combination of the MIMO testing approach and poly-reference modal identification methods.

Finally, piezoelectric actuators, which were identified as ideal candidates to provide multiple-input excitation, were presented, and the derivation of a FRF expression depending on their control voltage was shown and discussed.

Chapter 3

Coriolis effects in current finite element software

3.1 Introduction

The study of the effects of rotation in aero-engine components is usually split in two phases. Since the aerodynamic design of the aerofoils is conducted in operational conditions, thus on the blades as deformed by the centrifugal force, the full FE analysis of the bladed discs is necessary to derive their cold shape, which is the one that will actually be manufactured, and their Campbell diagrams, to identify resonances in the operational range. The Coriolis, or gyroscopic effect, is only considered in a rotordynamics sense: the bladed discs are approximated by full discs, thus neglecting the flexibility of the blades, to focus on the dynamics of their shaft. These simplified models are well suited for the study of whirl modes, and for the derivation of the Campbell diagrams of the disc-shaft assembly, and allow the simulation of the complex, often nonlinear interaction with bearings and stator at reduced computational cost.

However, the new engine architectures are moving towards higher flexibility of all their components, and the fast evolution of the available computational power allows increasingly more realistic models: a comprehensive design and verification process, which is capable of including all the involved physical phenomena, and the interaction between different components, is becoming not only desirable, but also feasible.

The finite element method is particularly suitable for the dynamic analysis of complex structures. The method is well-established for linear and stationary systems, but it is much less clear how accurately the influence of the Coriolis terms is handled. In addition, the simulation of rotating structures involves multiple analysis steps, and, since extended, consistent documentation is frequently lacking, uncertainty in the interpretation of the results can arise, if no reference data is available.

An initial investigation was therefore conducted to verify whether finite element mod-

¹Parts of this chapter have been adapted from [127].

els would be able to predict all the expected phenomena, and to better understand their effective impact on bladed discs, especially with respect to the Coriolis force. Benchmark test cases were created to simulate frequency splits, the appearance of separate forward and backward travelling-wave modes, and the interaction with geometric nonlinearity, and compared to results available in the literature to validate them.

3.2 Finite element analysis

To provide a comprehensive picture of the prediction capabilities available, several FE software packages were tested:

- A proprietary software that will be called “Code A”;
- Abaqus v6.11-13;
- Ansys v12.1;
- NX Nastran v8.5;
- SAMCEF v14.1.

All codes offer advanced modelling functions, and were assessed against a set of features that were identified as essential for the reliable analysis of rotating structures. The first requirement was accuracy in the identification of the speed-dependent natural frequencies of the structures, and in particular, of the splits induced by the Coriolis force. The centrifugal force affects both the frequencies, through the competing centrifugal stiffening and spin softening effects (see sect. 2.2.2), and the mode shapes, by potentially deforming the structure. The way the geometric stiffness matrix (Eq. (2.14)) is calculated in each package was therefore checked. Finally, as all traditional rotating structures exhibit at least cyclic symmetry, the capability of the different pieces of software to exploit said symmetry to improve the computational efficiency of the solution was considered.

All the codes provide the solution features necessary for a realistic simulation of rotation effects, i.e. the addition of the geometric stiffness, spin-softening, and Coriolis matrices. All codes except NX Nastran require a separate preliminary static analysis before the modal step, which allows to take centrifugal stiffening into account via the geometric stiffness matrix. This step applies the centrifugal force as a pre-existing stress state in the structure, and consists in calculating the geometric stiffness matrix of Eq. (2.14).

There are two alternative approaches to this calculation: either the small displacement - large strain, or the more general large displacement-large strain hypothesis. The first is based on the linearisation of the geometric stiffness matrix, and can be applied when the centrifugal force is not expected to cause macroscopic changes in the shape of the structure. The second makes no such assumption, and therefore leads to a fully non-linear form for Eq. (2.14). The subsequent modal analysis step is applied to the deformed geometry. Abaqus, Ansys, NX Nastran, and SAMCEF offer the possibility of choosing between the two different approaches, while Code A always solves the full non-linear problem. While

only this second approach is exact, the small displacements-large strain hypothesis has the advantage of being computationally faster, and is a fair approximation for structures that do not exhibit pronounced radial flexibility.

SAMCEF and NX Nastran offer the possibility of automatically deriving a Campbell diagram by setting a range of rotation speeds. With Abaqus and Ansys, on the other hand, the spin speed has to be changed manually, which means that a new run is required for each spin speed. This increases the computational time, as the system matrices have to be regenerated every time. Further reduction of the computational load is introduced by Code A and SAMCEF, which are the only packages to exploit the cyclic symmetry of a rotating structure when the Coriolis effect is included. In Code A and SAMCEF, a single sector can be modelled, which means that the EOMs can be solved for a reduced number of DOFs, and only for the desired ND families, as explained in sect. 2.3.1.

All codes approach the solution of the unsymmetric eigenvalue problem caused by the presence of the Coriolis matrix G in the same way. The symmetric eigenvalue problem associated with Eq. (2.12) is first solved using the Lanczos algorithm. The resulting eigenvector matrix is used to project the full eigenproblem of Eq. (2.16) into the modal subspace, to reduce the dimension of the problem itself. For the extraction of the complex eigenvalues, every code offers different options: the QR algorithm was used in SAMCEF and Ansys, the Lanczos method in NX Nastran, and the QZ algorithm in Abaqus, and the convergence tolerances were left at the default values for each package.

3.3 Test cases

No extended documentation on the use of the Coriolis option in the chosen FE software was found at the start of this assessment, and only scattered data was available in the literature as validation of the computational results. Test cases were needed to verify the actual capabilities of the codes, and their accuracy. The models to be used as benchmark were selected from the literature according to the availability of analytical solutions or experimental results to provide independent validation. Only models with well-defined data relative to dimensions, material properties, and boundary conditions were used, to eliminate uncertainty in the interpretation of the results due to inconsistent geometries and properties.

Four test cases (Fig. 3.1) were proposed and analysed: the Stodola-Green rotor [128], a rotating thin ring [129], a blisk with swept blades [130], and a simplified blade-disc-shaft assembly. Their dimensions and material properties are summarised in Appendix A. The Stodola-Green rotor (Fig. 3.1a) is a classic model in rotordynamics: it consists of a solid disc at the end of a cantilevered shaft, which exposes it to strong gyroscopic coupling of the DOFs perpendicular to the rotation axis [107]. This causes large frequency splits, and BW and FW whirl modes. It is also insensitive to centrifugal stiffening, as its bulky geometry is not noticeably deformed by the centrifugal force at normal speeds. Since its dynamics are dominated by the action of the gyroscopic moments, a simple lumped-parameter model [128] could be used as reference: the disc was a concentrated mass with rotary in-

ertia, and the shaft was modelled as a pure spring, with linear stiffness terms calculated from beam theory. Stiffness terms coupling displacement and rotations were included.

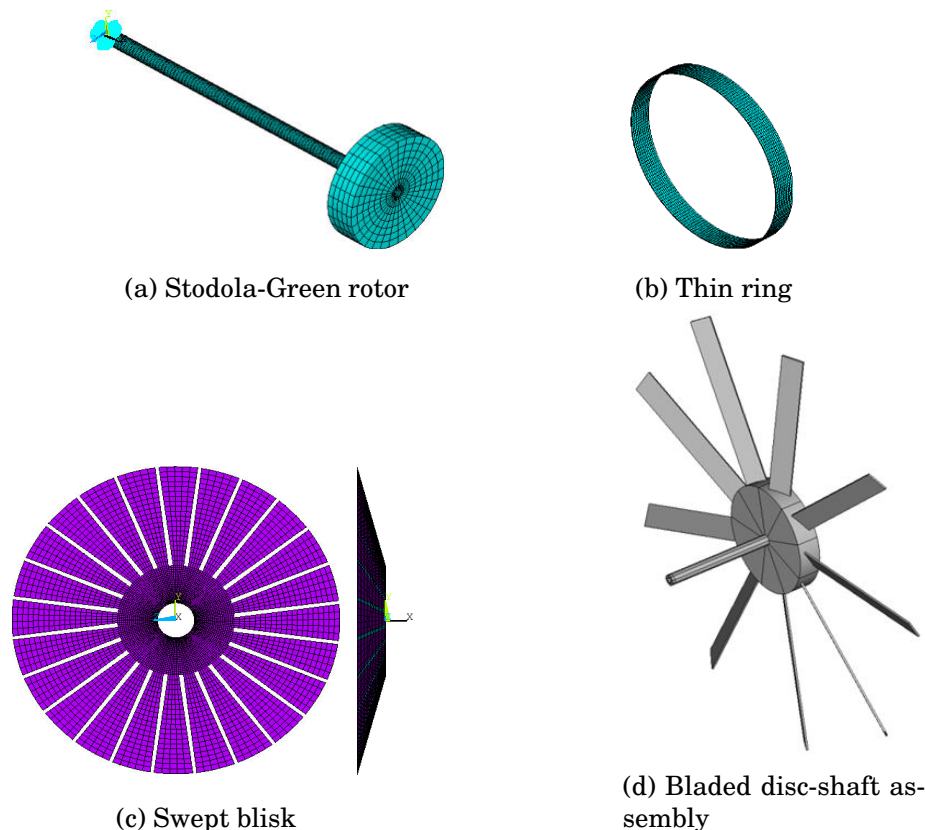


Figure 3.1: Models of the benchmark test cases.

The rotating ring (Fig. 3.1b) was chosen because the dynamics of its in-plane modes can be strongly influenced by the Coriolis effect. With in-plane modes, displacements take place primarily in the plane perpendicular to the rotation velocity, thus displaying only the velocity components to which the Coriolis force is proportional. An analytical formula by Endo *et al.* [129] for the natural frequencies of the in-plane modes under the hypothesis of small displacements was used as reference. The major advantage of this test case was that the formula was validated experimentally by the same authors, with excellent agreement between analytical and experimental Campbell diagrams.

The third model is a blisk¹: it consists of a thin circular plate with the blades bent 15° out of the plane of the disc (Fig. 3.1c). This “sweep”, or pre-cone, angle increases the radial component of the vibrational velocity, thus producing a significant Coriolis force. An analytical solution for its resonance frequencies is not available due to its complex geometry, but the blisk was modelled and analysed through FEA, and its frequency splits were measured experimentally, producing good agreement with the computational results [130, 131].

The fourth model represents a simplified bladed disc-shaft assembly, comprising a solid disc with nine blades mounted on a cantilever hollow shaft (Fig. 3.1d). The dimensions were chosen so that the desired effects could be reproduced and amplified. The blade length

¹A *blisk* is a bladed disc where the blades are integrally connected to the disc, without joints.

was six times the radius of the disc, as a length-to-radius ratio greater than 1 was identified as a condition for instability [132]: with this geometry, it was then possible to verify whether the codes would be able to predict it. The shaft overhung span was deliberately made long and thin to emphasise whirl. Different pitch angles² in the blades were simulated to check the influence of this parameter on the global dynamic behaviour, as open rotors, for example, feature the possibility to change it for optimal efficiency at all flight conditions. Very few analytical models of such structures are available, so the results of the simulations were only compared between the different FE codes.

For all test cases, the same FE models, in terms of constraints, and number and type of elements, were used in all packages. The only exceptions were SAMCEF and Code A, where a single sector was modelled, and Ansys, where, due to license restrictions, beam and shell elements were used instead of solid ones. A modal analysis at different rotation speeds of the FE model of each test case was then run in the software packages listed in the previous section. The small displacements-large strains hypothesis was applied to the Stodola-Green rotor, the thin ring, and the bladed disc-shaft assembly, as the centrifugal force was seen not to modify the shape of the structure for the selected speeds. A fully non-linear step was instead required for the swept blisk, due to its large deflections. The Campbell diagrams were always calculated in the rotating frame of reference, and then compared with the results from the literature and with each other.

3.4 Results

3.4.1 Stodola-Green rotor

The frequency splits induced by the gyroscopic effect are a well-known phenomenon in disc-shaft assemblies, and the derivation of Campbell diagrams is a fundamental outcome of rotordynamic analyses. The Stodola-Green rotor was therefore the first model to be investigated. In dedicated rotordynamics models, rotation DOFs are often used, because they couple with gyroscopic *moments*, as formulated in the laws of rigid-body dynamics, and Euler's rotation equations [107, 133]. This produces orbital vibrations of the rotor called *whirl* modes [39, 134]. Here, however, the rotor was modelled by solid 20-node hexagonal (hex) elements, which are characterised by purely translational DOFs. This would verify whether the Coriolis matrix, which depends on translational velocities alone, would be able to reproduce the gyroscopic effect in a general-purpose FE code.

The resulting Campbell diagram for the first bending mode of the rotor is shown in Fig. 3.2. The diagrams from all codes were found to coincide within 0.05%: for this reason, only the results from Abaqus are shown as reference. This is especially remarkable considering the wide difference in the meshes used in the different codes. In SAMCEF and Code A, the symmetry of the model could be exploited, and the rotor was reduced to a 20° sector, with 9600 20-node hex elements. In Ansys, only 4224 hex elements for the

²The *pitch angle* is the complementary of the stagger angle, which in turn is the angle between the blade chord and the rotation axis.

whole model could be used due to the mentioned license restrictions, and this same mesh was used in the remaining codes for consistency. This confirms that a structure like this, where mass and stiffness properties can be neatly separated between disc and shaft, respectively, is well suited to simplified modelling approaches. Further proof comes from the negligible difference between the frequencies obtained from the FE models and the lumped-parameter model, which amounts to a median of 0.26%.

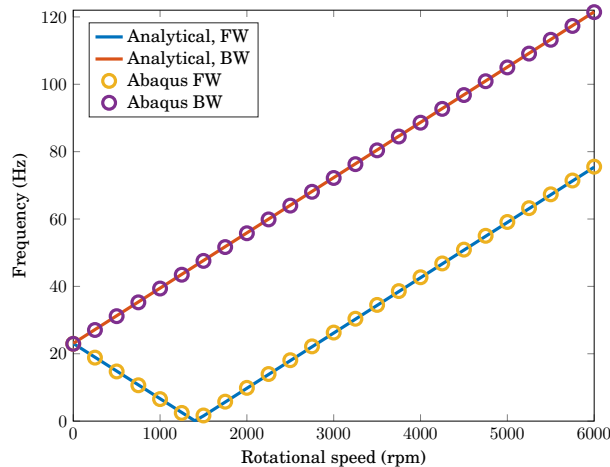


Figure 3.2: Stodola-Green rotor: Comparison of analytical and FE Campbell diagrams for the 1st bending mode. Adapted from [127].

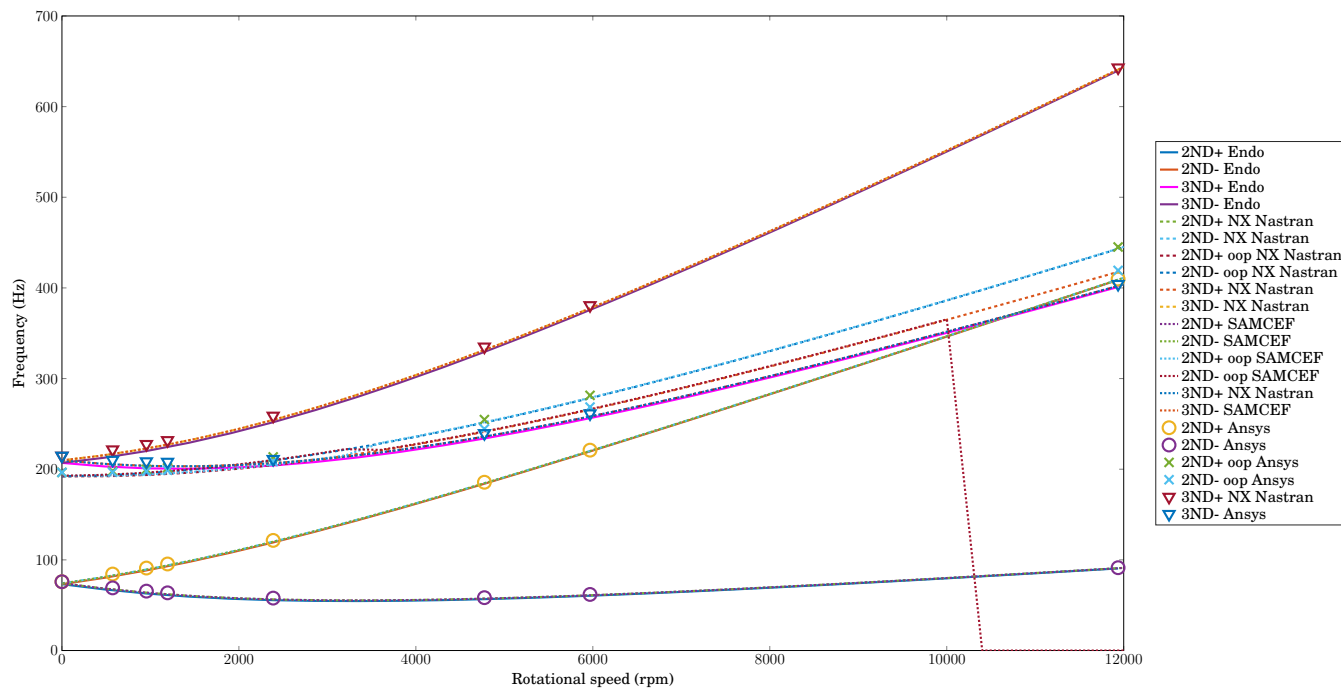
The first critical speed of the rotor is visible at around 1400 rpm. The natural frequency in the Campbell diagram is 0 in this case, because, as explained in sect. 2.3.4, the Campbell diagram was calculated in the rotating frame. All codes dealt with this without issue, and correctly identified the modes corresponding to the rising branches of the diagram as BW whirl, and that of the decreasing line as FW whirl. In this case, then, the modes in Fig. 3.2 were labelled according to their direction in the stationary frame.

3.4.2 Rotating ring

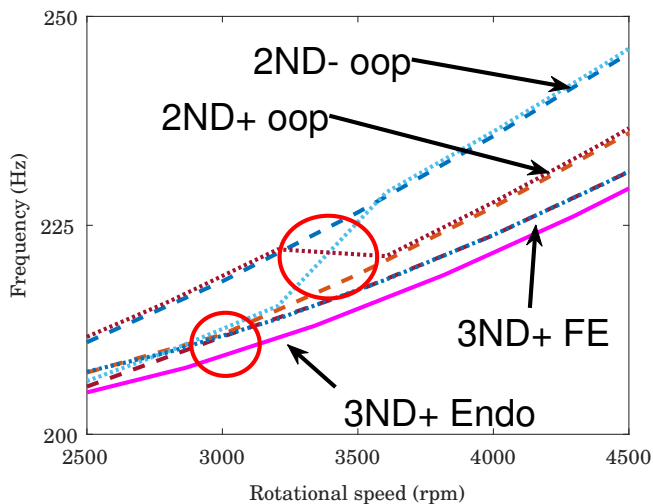
3.4.2.1 Campbell diagrams

The rotating ring was modelled via a 12° sector in Code A and SAMCEF, with 400 20-node hex elements. A 10840-element model was employed for the rest of the codes, except again Ansys, where only 4400 hex elements could be used. The first three modes of the rotating ring are shown in Fig. 3.3a: the 2 and 3ND in-plane modes, corresponding to nodal diameters 2 and 3, and the 2ND out-of-plane (oop) mode. There is very close agreement between the different FE codes. Ansys is the exception with a maximum differences of 2.3%, but, as noted before, the mesh for the Ansys model had to be significantly coarser than for the other codes (normal rules of mesh convergence were observed to apply when the Coriolis effect was added to the simulations). More importantly, all codes show very good agreement with the experimentally validated theoretical model.

Some inconsistencies were also found (Fig. 3.3b). For SAMCEF, the FW branch of the 2ND oop mode was truncated after 10000 rpm, which is a behaviour that was often met



(a)



(b)

Figure 3.3: Thin ring: Campbell diagram comparing different FE codes to analytical formula. (Adapted from [127].)

across all the models, without an apparent explanation. It can be seen that the FW and BW branches switch after 3200 rpm in SAMCEF, and, in NX Nastran, the 3ND-FW (+ in the plot) branch becomes the 2ND-FW branch at 3000 rpm: this switching is a common, and erroneous, occurrence for both SAMCEF and NX Nastran.

3.4.2.2 Mode shapes

The Coriolis force has been shown in Chapter 2 to generate complex mode shapes, which take the form of travelling waves in cyclic-symmetric structures. No quantitative data was available for mode shapes from FE analysis in the presence of the Coriolis force. It was thus important to check how the FE codes would handle the solution. The ring was selected as test model for this case, due to the strong effect the Coriolis force was shown to have on the frequency splits.

The modal constants for 2ND (Fig. 3.4a) were extracted in the radial direction at 20 points spaced 18° from each other along the external circumference of the ring. The modal analysis options used were the same as for the calculation of the Campbell diagrams, and the simulation was carried out in Ansys at rest and at 565.5 rpm (60 rad/s).

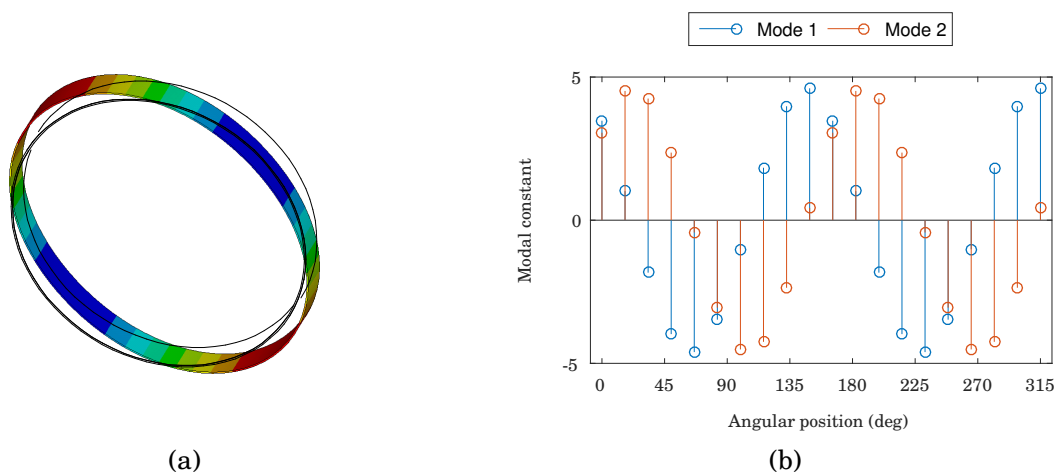
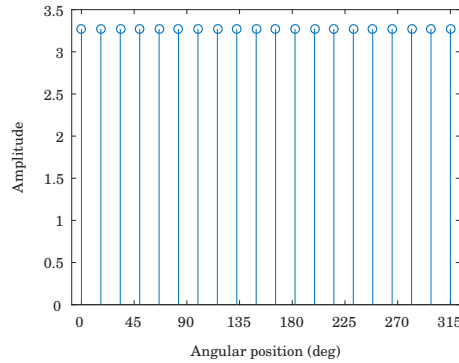


Figure 3.4: 2ND mode shape of the thin ring at rest: a) FE model, and b) modal amplitudes of the double mode at 20 equispaced positions along the circumference at rest.

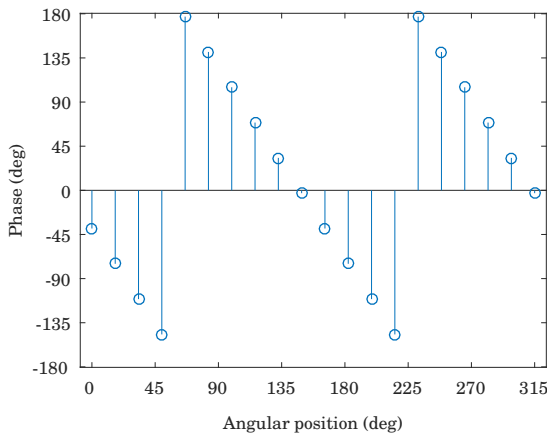
The 2ND mode is a double mode, and the two mode shapes corresponding to the double eigenvalue at rest are shown in Fig 3.4b. The modes are real, and orthogonal to each other. Each DOF has a distinct amplitude, which is modulated along the circumference, and nodal diameters exist at fixed positions. The different points vibrate either in or out of phase with respect to each other: at rest, the 2ND modes are thus typical standing-wave modes.

At 60 rad/s, the Coriolis force splits the frequencies, with resonances at 67 and 83 Hz, and generates complex-valued modes. The amplitude of both modes is shown in Fig. 3.5a. All DOFs now vibrate at the same amplitude, and no nodal diameters appear. The mode shape still takes the form of Fig. 3.4a, but, due to the Coriolis force, the nodal diameters are no longer fixed, but travel around the circumference of the ring, so that all DOFs can

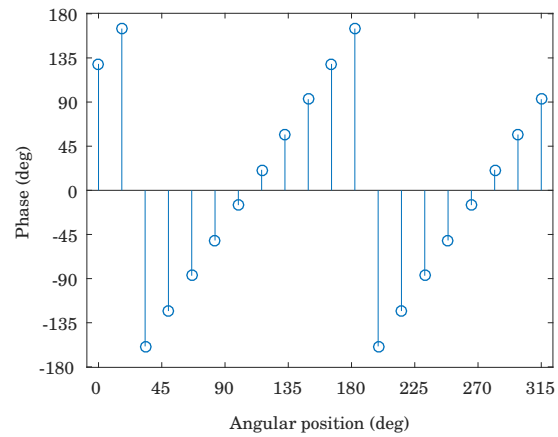
reach maximum amplitude.



(a) Amplitude, FW and BW mode



(b) Phase, FW mode (at 67 Hz)



(c) Phase, BW mode (at 83 Hz)

Figure 3.5: 2ND mode shape of the rotating thin ring at 60 rad/s.

This is confirmed by Fig. 3.5b, which shows the phase of all DOFs for the mode corresponding to the 67-Hz natural frequency. It can be seen that each DOF is, in general, characterised by phase values different from 0° or 180° , and is phase-shifted with respect to the preceding DOF by -36° . Considering the 20 DOFs to divide the ring into 20 sectors, this relative phase difference is correlated to the IBPA φ_k of Eq. (2.22), and can indeed be found as

$$\frac{360^\circ}{20}k\text{ND} = 18^\circ \cdot (-2) = -36^\circ.$$

The mode shape behaves therefore as a FW travelling wave. The opposite happens for the mode at 83 Hz (Fig. 3.5c): the phases are flipped with respect to the x -axis, and the relative phase shift is 36° , showing that the higher frequency is associated to a BW travelling wave.

3.4.3 Swept blisk

The swept blisk was an important test case to verify whether the codes would be able to handle strong interaction between geometric nonlinearity and Coriolis force. Large displacements are caused in this flexible blisk by the centrifugal force, which tends to realign the blades with the radial direction. This leads to a decrease in the sweep angle, which

goes from 15° at rest to around 7° at 1000 rpm [130]. Making the conservative assumption of constant speed $\|\mathbf{v}\|$, the radial component v_r of the vibrational velocity decreases as well to v_r' (Fig. 3.6a).

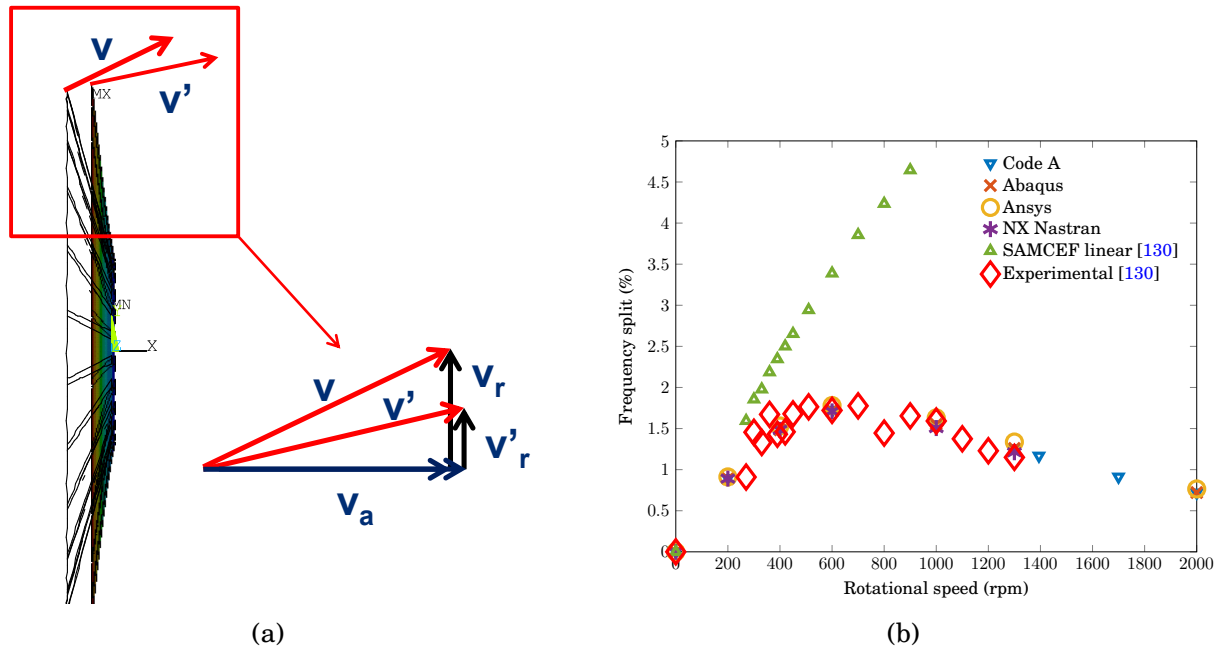


Figure 3.6: Swept blisk: a) Effect of the centrifugal force, and b) Frequency splits.

The effect of this interaction on frequency splits is not obvious, as the Coriolis force is proportional to both Ω and v_r , which follow opposite trends. Measurement data (Fig. 3.6b from [130]) rise sharply up to approximately 600 rpm, after which the frequency split starts to decrease. This effect is due to the interaction between Coriolis and centrifugal forces: the increase in rotational speed at first compensates for the reduction in radial velocity component v_r shown in Fig. 3.6a, leading to an increase in the Coriolis force, but this effect is finally exceeded by the reduction in v_r , and the frequency split drops.

The experimental data at first contradicted the results of the FE simulations. The simulations in the original study, however, were first conducted under the assumption of small displacements (and are therefore referred to here as “SAMCEF linear”), which means that the large modifications in geometry induced by the centrifugal force were not reproduced. In the original study, the change in the shape of the blisk due to the centrifugal force was accounted for by manually creating separate models with different sweep angles, and keeping the analysis linear [130]. For the present assessment, instead, only the original geometry of the blisk was used, and the fully nonlinear static analysis option was activated for all codes.

With this set-up in the analysis, the nonlinear trend of the frequency split is predicted by all codes: the splits from the different packages agree within 0.3%, except for Ansys, which shows a deviation of 6%. This is reasonable, as the Ansys model was meshed with a coarser grid, and with shell elements, instead of solid ones, to keep the number of nodes below the 32000-node threshold imposed by the license. It can also be seen that the FE

curve agrees well with the measured values, thus confirming the validity of the analysis.

3.4.4 Bladed disc-shaft assembly

The Campbell diagram for the bladed disc-shaft assembly at a pitch angle of 90° is shown in Fig. 3.7. In this configuration, the rotor can be subject to instability when the blade length is greater than the disc radius [132] due to centrifugal softening [128]. In this case, the split eigenvalues of the structure appear as complex-conjugates with positive real part, and therefore the FW and BW branches of the Campbell diagrams tend to collapse onto one another.

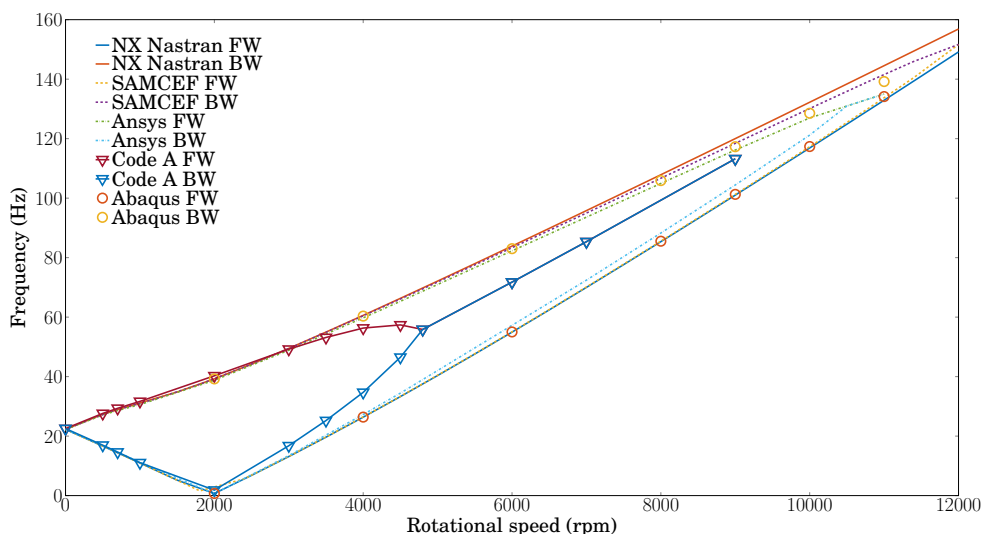


Figure 3.7: Bladed disc-shaft assembly: Campbell diagram for pitch angle 90° . (Adapted from [127].)

All codes predicted this converging trend for the first bending mode of the shaft, but disagreed on the actual position of the onset. Code A produced the lowest threshold, at 4000 rpm. SAMCEF, however, which is the only other code where sector models could be used, predicted instability at 12000 rpm, while the Nastran curves still appeared well-spaced apart at the same speed. Abaqus put the onset at around 11000 rpm. With Ansys, the shaft and blades were modelled as Timoshenko beams, and the disc as a shell with thickness: instability was still predicted, and placed at 10500 rpm. The first critical speed, on the other hand, was identified by all codes at 2000 rpm.

The effect of pitch angle on the frequency split of the first bending 1ND mode of the blades is shown in Fig. 3.8. An increase in pitch angle from 30° to 60° leads to a corresponding increase in split: this can be attributed to the related increase of the in-plane component of the vibrational velocity, which is proportional to the Coriolis force. The curves also appear significantly non-linear, with the split increasing up to about 1200 rpm, and decreasing thereafter. Since no large displacements are modifying the shape of the blades here as opposed to the swept blisk, a possible explanation is the opposing trends caused by the Coriolis effect and centrifugal stiffening. The Coriolis effect tends to enlarge the gap between FW and BW branches in the Campbell diagram with increasing speed. The cen-

trifugal force, on the other hand, does not depend on the direction of rotation of the mode, and thus tends to stiffen both branches, reducing the gap. As the Coriolis force varies linearly with speed, and the centrifugal force quadratically, 1200 rpm in this case represents the speed at which the centrifugal stiffening effect takes over.

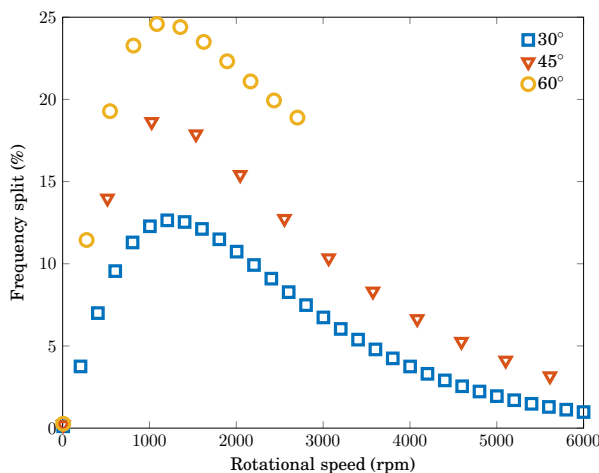


Figure 3.8: Bladed disc-shaft assembly: Frequency split trends at pitch angles 30° , 45° , and 60° (NX Nastran). (Adapted from [127].)

3.5 Discussion of results

3.5.1 Coriolis effects

Predicting frequency splits is essential in analysing gyroscopic systems, and all codes gave consistent results throughout the various test cases. The natural frequencies were nearly coincident for all codes, and, most importantly, the frequencies predicted matched experimentally validated data. The coincidence between the FE Campbell diagrams for the rotating ring and the analytical formula used as reference, which had been validated by the original study [129], offers strong support for the prediction capabilities of the available FE tools. Further confirmation comes from the swept blisk frequency splits, which show excellent agreement between FE and experimental data points. This match is especially significant: it shows that the FE codes are able to deliver reliable predictions not just for simple axisymmetric structures like the ring, but also for cyclic-symmetric bladed discs in the presence of strong geometric nonlinearity.

It is also encouraging that the results from the shell-and-beam blade-disc-shaft assembly in Ansys, while not showing the level of agreement found between the more detailed models, were still adequate, and proved that such simplification can be used in preliminary analyses to reliable outcomes.

The prediction of the instability threshold was the only instance of systematic disagreement between the different packages. The latter issue was particularly evident for Code A. All other codes placed the onset of instability in a range between 10500 and 12000 rpm, which suggests that the differences can be attributed to numerical errors at this extreme

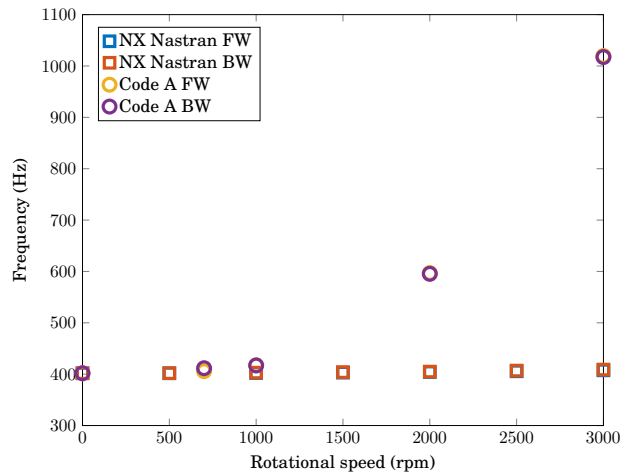


Figure 3.9: Anomalous behaviour of Code A for 1ND modes in cyclic symmetric structures: Campbell diagram for 1ND first torsion mode of the bladed disc-shaft assembly with pitch angle 60° .

condition, since the numerical tolerances could not be set at consistent values across the codes. Code A, however, placed the threshold at 4000 rpm, less than half of what the other codes predicted.

This was not the only discrepancy: Fig 3.9 shows the Campbell diagram for the first torsion 1ND mode of the blade-disc-shaft assembly, at pitch angle 60° . Torsional modes in bladed discs do not usually exhibit significant centrifugal stiffening, as they do not present large radial displacement components, which are what the centrifugal force acts on. Accordingly, the Nastran frequency curves appear flat, while Code A predicts a very sharp increase. No issues were found, however, either for the Stodola-Green rotor or the ring. From the observation of similar non-physical behaviours, it was possible to conclude that issues arise only for the 1ND modes of cyclic symmetric structures. Further investigation revealed that Code A solved the EOMs for 1ND in the stationary frame: while this is acceptable for axisymmetric structures (Ansys and NX Nastran offer the possibility to choose between reference frames in this case, for example), in cyclic symmetric structures this would lead to the appearance of time-dependent coefficients in the eigenproblem [21], which would not be solvable with standard methods.

All codes correctly identified the direction of the travelling wave modes generated by the Coriolis effect. Exceptions are SAMCEF and NX Nastran, the only codes offering automatic Campbell diagram calculations: the eigenvalues are correct in modulus, but the mode tracking algorithm occasionally assigned them to the wrong travelling-wave/whirl direction, and, in some cases, to the wrong mode family altogether. This happened for both the ring and blade-disc-shaft models, but not for the Stodola-Green rotor.

The reason behind this is therefore the high modal density in the speed ranges where these erroneous attributions occur: in the ring model, for example, three different modes (2ND-FW and BW oop, and 3ND-FW in-plane) are contained within 10 Hz at 3500 rpm. The mode tracking algorithm used by NX Nastran is purely based on attempting to match the eigenfrequencies depending on previous results [135], and does not compare the associated eigenvectors. As a result, for the blade-disc-shaft assembly, NX Nastran regularly

mistakes 1ND branches with higher ND curves, and even 0ND at higher speeds, and assigns the direction of the whirl/TW modes incorrectly. No switch, on the other hand, is ever observed when the frequencies are well-spaced apart.

Incomplete Campbell diagrams were another regular problem with SAMCEF (as seen in Figs. 3.3a and 3.8): as no detail about the mode tracking method used was found, it was not possible to determine whether the issue stemmed again in post-processing from the tracking algorithm, or from the solver. This issue, coupled with the fact that, in realistic aero-engine stages, smaller frequency splits, hence higher modal densities, are usually observed, makes current mode-tracking methods for the automatic identification of Campbell diagrams unreliable: the additional implementation of an eigenvector-based tracking algorithm, or visual identification, are still necessary, to assign the mode shapes correctly. The solution of the EOMs at different speeds in a single simulation that is associated to this automatic tracking methods in Nastran and SAMCEF, however, is extremely useful, as all the system matrices, except the geometric stiffness matrix, can be calculated only once, thus allowing a significant cut in computational time.

The second major effect of the inclusion of the Coriolis force in the analysis is the generation of travelling-wave modes in cyclic-symmetric structures. This was confirmed by the model of the rotating thin ring. Ansys predicted a purely real mode at rest, whereas, at 60 rad/s, definite TW behaviour emerged. Fig. 3.5 showed that the Coriolis force causes uniform maximum amplitude at all DOFs around the circumference of the ring, and the phase varies linearly from “sector” to “sector”, as appears in Eq. (2.33). The constant relative phase difference, which is analogous to the IBPA, means that adjacent sectors can never simply vibrate in or out of phase, but are all involved in the global TW motion. Ansys also identified the mode at the lower frequency from the Coriolis-induced split at 60 rad/s as a FW mode, and the higher frequency as a BW mode, confirming that this behaviour is correct for models analysed in the rotating reference frame (cfr. sect. 2.3.4).

3.5.2 Geometric nonlinearity

The inclusion of geometric nonlinearity in the study of rotating structures is essential, as the centrifugal force can modify the shape of the structure itself, and thus its dynamics. It was seen that all commercial codes offer the possibility of choosing between the approximated, but faster, small displacements-large strain solver, and the exact, but fully nonlinear, large displacements-large strain solver. All codes delivered equivalent results when geometric nonlinearity was coupled with the Coriolis effect, both in the linearised, and fully nonlinear case.

The only exception was SAMCEF: it was not possible to use the results of the fully nonlinear pre-stress analysis in the modal analysis step with Coriolis, and, due to a time-limited license, the reason could not be found. An opposite behaviour was found in NX Nastran, and it is appropriate to highlight this peculiarity here: interfacing the nonlinear, large-displacement static solver with other solver modules is officially discouraged [136]. For the present assessment, nevertheless, the deformed shape calculated in the non-linear

step was used in the rotordynamics module to derive the Campbell diagram of the swept blisk, and, as shown in Fig. 3.6b, the process yielded valid results. Both in SAMCEF and NX Nastran, however, the large-displacement pre-stress analysis step prevents the use of the automatic Campbell diagram generation feature: a new analysis must then be started for each rotational speed, with the consequent rise in computation time.

3.5.3 Left eigenvectors

Left eigenvectors were identified in Chapter 2 as a product of the unsymmetric eigenproblem arising in gyroscopic damped structures, and necessary for a full description of the dynamics of such systems. The possibility of extracting them from FE analyses was therefore investigated. Code A, Abaqus and SAMCEF did not provide this feature at the time of the assessment. NX Nastran derives the left eigenvectors during the solution of the unsymmetric eigenproblem [137], but their actual extraction as output requires a user script. Likewise, left eigenvectors are used in Ansys to diagonalise the EOMs for mode-superposition harmonic analysis [95], but no procedure is given to extract them as output.

3.5.4 Cyclic symmetry

The codes were also assessed for their general suitability to the study of bladed discs. An important feature in this context is then the implementation of cyclic-symmetry reduction methods, which allow the same accuracy in the results at a fraction of the computational cost. Surprisingly, only Code A and SAMCEF offer this option natively. Abaqus, Ansys and NX Nastran do have a cyclic-symmetry solver, but it is not available if the Coriolis matrix is included.

Cyclic symmetry would also allow the solution of the eigenproblem only for the desired ND families, as shown in sect. 2.3.1. For this reason, for example, SAMCEF is much less prone than Nastran to the spurious jumps between Campbell branches, as solving for a single ND at a time obviously reduces modal density. Mismatches in SAMCEF were observed only for the 2ND oop mode of the ring after 3500 rpm (Fig. 3.3), where the branches switch between FW and BW.

As the study of gyroscopic effects is particularly relevant in disc-shaft assemblies, computational efficiency is a fundamental feature, as a detailed model can contain millions of degrees of freedom (the simplified bladed disc-shaft model presented above contains more than 750k nodes), and requires significant processing power. The exploitation of cyclic symmetry, where a whole structure can be reduced to a single sector, remains therefore very desirable.

The result of the assessment of the studied FE codes is summarised in Table 3.1.

3.6 Conclusions

The major commercially-available FE software packages have been reviewed to assess their prediction capabilities in the presence of Coriolis and gyroscopic effects. Four bench-

Table 3.1: Summary of software capabilities: ✓✓✓, complete feature support; ✓, partial support; ×, non-native/present but problematic; ×××, unsupported. (Adapted from [127].)

	Code A	Abaqus	Ansys	NX Nastran	SAMCEF
Frequency split prediction	✓	✓✓✓	✓✓✓	✓✓✓	✓✓✓
Cyclic symmetry	✓✓✓	×××	×××	×	✓✓✓
Geometric nonlinearity	✓✓✓	✓✓✓	✓✓✓	✓✓✓	×
Left eigenvectors	×××	×××	×	×	×××

mark test cases, three of them with analytical and/or experimental results available in the open literature, were created and used as reference for the accuracy of the computational output. Close agreement was found for all codes in the Coriolis-induced frequency splits. Discrepancies appeared at high speed in the vicinity of instabilities for the blades-disc-shaft model, due to the different numerical tolerances used by the codes. An inconsistent implementation of the equations of motion, which were solved in the stationary reference frame for 1ND modes, was discovered in the proprietary Code A, and identified as the origin of severe discrepancies with the results from the other codes.

Geometric nonlinearity is handled consistently across all codes, which produce similar results when the nonlinearity is coupled with the Coriolis effect. None of the packages outputs left eigenvectors, which arise from the Coriolis-induced unsymmetric eigenproblem, and are involved in the FRF expression for gyroscopic structures. Cyclic symmetry, an essential feature for the analysis of turbomachinery, is currently missing from all commercial codes, when the Coriolis force is not neglected, except for SAMCEF and Code A.

In conclusion, this review proved that all major FE software packages offer the features necessary for the comprehensive analysis of rotating bladed discs. Their prediction capabilities have been validated with experimental data from the literature, and the codes have thus been shown to be equivalent in terms of results. Differences arise mainly in user experience and computational efficiency: in this respect, no code was found to be optimal for the study of bladed discs with Coriolis effects.

Chapter 4

Rotating test rig: Design and commissioning

4.1 Introduction

The Coriolis force has been shown to affect the dynamics and performance of bladed discs. Frequency splits double the number of resonances, while travelling-wave modes interact with aerodynamic forces, and can produce unstable behaviour in the blades, and high-amplitude vibrations. Both these phenomena can have an impact on fatigue life, and should be taken into account at the design and health-monitoring stage, to ensure maximum performance within clear safety boundaries.

The previous chapter has shown that the FE tools are already in place to analyse the Coriolis effect at the computational level. However, it is also essential to have an experimental framework in place that can detect and identify these effects with accuracy, and generate reliable, high-quality data for model validation and updating.

A test rig that can be applied to the investigation of rotational phenomena in bladed discs was therefore developed, and its design and commissioning will be presented in this chapter. The chosen excitation and measurement systems will be discussed in detail, along with the preliminary tests conducted to verify their reliability. The test piece that was particularly designed for the study of the Coriolis effects will be shown, and the impact of the instrumentation on its mistuning and damping quantified.

4.2 Design requirements

The driving design objective of the test rig was the ability to study the dynamics of bladed discs in near-operational conditions, while at the same time retaining the possibility to focus on particular phenomena. It was thus necessary to introduce variable rotation speeds,

¹Parts of this chapter have appeared in [138].

fully controllable excitation methods, and a vibration measurement system that can operate under rotating conditions. As the phenomena involved are not purely rotordynamic in nature, the response of the rotating test pieces must be monitored along with the shaft.

A set of design criteria was therefore established for the new rotating test rig to meet these requirements:

- **Rotation:** the maximum rotational speed should be at least 6000 rpm, to ensure proper scalability from true operational conditions to test pieces of reduced dimensions. A related requirement is to avoid any major critical speeds for the shaft in the testing range.
- **Excitation system:** it is necessary to not be bound to rotation as a means of excitation, but to have the possibility of exciting the test piece independently, as the application requires. As the first application of the rotating test rig is the modal analysis of bladed disc in the presence of the Coriolis force, it is important to be able to use sine sweep and random excitation to obtain the FRFs of the structure. Arbitrary EO excitation are also required to simulate the forcing patterns present in real aero-engine stages.
- **Measurement system:** the dynamics of bladed discs are dominated by the local and coupled vibration patterns of the blades. Sensors capable of measuring the response of the blades themselves are essential for the comprehensive characterisation of the rotating system and its associated operating deflection shapes.
- **Signal transmission:** the transmission of either excitation or measured signals should maximise data quality, while not interfering with the dynamics of the rig, through friction, unbalance, and/or excessive mass loading.
- **Rig structural design:** the test rig chamber and supports must be capable of withstanding any loading transmitted by the test piece, while providing minimal interference with its dynamic behaviour. The design of the chamber must also provide ballistic protection, to contain any parts that may come loose during high speed testing.
- **Test environment:** the rig must be able to operate as a vacuum chamber if needed, to minimise aerodynamic damping and avoid the risk of flutter.
- **Modularity:** the possibility of easily adapting and modifying the test rig for different test set-ups, and for test piece dimensions, must be guaranteed from the early design stage to ensure a future-proof design.

4.3 Test rig

4.3.1 Test chamber and support components

The test rig and its main components, as designed according to the above criteria, are shown in Fig. 4.1. The technical drawings of its main components are reported in Appendix B for additional details. The core module consists of the support structure, the cylindrical chamber, the shaft, and its bearing housing.

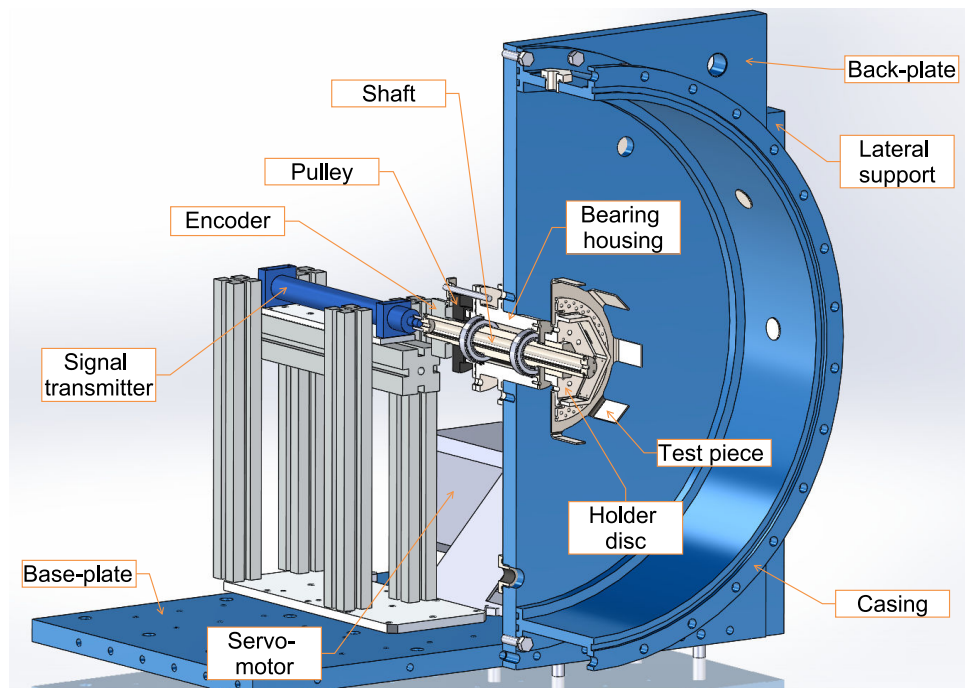


Figure 4.1: 3D CAD drawing of the rig assembly: section view.

The test chamber proper is composed of a flanged cylindrical casing, bolted to a vertical back-plate, and a front cover, which can be mounted at the front flange for safety reasons, or to work in vacuum. The internal diameter of the chamber is 720 mm, thus allowing the study of relatively large scale models of bladed discs, and a thickness of 15 mm, to both prevent caving-in due to atmospheric pressure, and avoid perforation in case of blade-off events. M30 tapped holes are present on both the vertical plate, and the casing. They can act as additional viewports around the casing to allow access for tip timing probes and other instrumentation, and as feedthroughs for the instrumentation cables.

The vertical back-plate and the two lateral triangular mounting plates are the core support components for the rig. They carry the weight of the front casing, and are the main transmission path for any excitation coming from the shaft, as the bearing housing is directly attached to the vertical plate (Fig. 4.1). As a result of this, their design needed to satisfy stringent static and dynamic requirements. On the static side, the vertical plate and the casing have to withstand the atmospheric pressure when working in vacuum. On the dynamic side, it was necessary to avoid major resonances of the rig that could be excited in the operational range of the shaft: as a maximum speed of 6000 rpm was chosen for

the motor, the design target was set to have no resonances below 120 Hz for the entire structure.

A particular focus was on avoiding the first resonance of the rig, associated to the mode shape shown in Fig. 4.2, which could be easily excited by disc unbalance. FE analysis showed that the addition of a 30-mm thick base-plate (Fig. 4.1), to which the lateral supports and the back-plate are bolted, would stiffen the structure enough to move the first resonance frequency to 120 Hz.

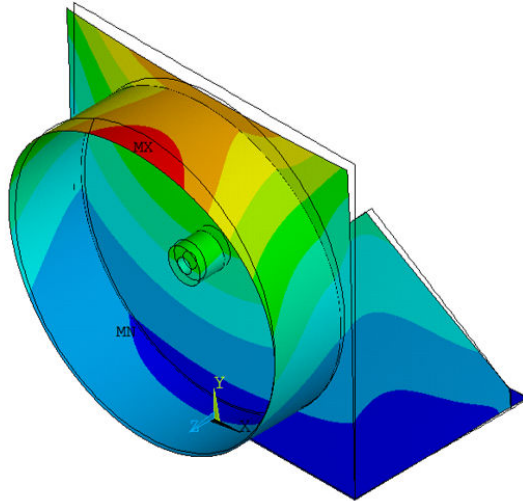


Figure 4.2: First mode of the test rig from FE analysis, at 120 Hz.

4.3.2 Vacuum

The possibility of testing in vacuum conditions is highly desirable in an academic test rig for the study of bladed discs. Vacuum limits the effect of aerodynamic damping on the test piece, and avoids the risk of flutter and galloping, which could damage the blades of the test piece catastrophically [37]. Research has shown [139] that a chamber pressure of 100 mbar (10000 Pa) produces modal damping values roughly equivalent to a much higher vacuum in a radial turbine blisk. Other academic test rigs cite values of internal pressure from 70 Pa [43] to 2000 Pa [31], thus suggesting that only low to medium vacuum levels are necessary. A pressure of 1000 Pa was therefore chosen as the minimum design target, and an Agilent IDP-3A01 dry scroll vacuum pump, capable of reaching a minimum pressure of 40 Pa, was selected for the rig.

To close off the vacuum chamber, and as an additional safety measure, a front cover is bolted to the front flange of the casing. The front cover consists of a 15-mm thick steel plate, which can be replaced with a glass cover to enable optical access for laser Doppler vibrometry or high-speed cameras.

Sealing is ensured by greased FKM O-rings on all flange joints, and by special plugs for the viewports and feedthroughs. A pair of sealed bearings (SKF 6007-2RS1) isolates the

bearing housing from the outside. A lip-seal enclosure has been added on the atmosphere-side of the bearing housing for additional sealing if required.

4.3.3 Drive system

The shaft is made of AISI 1045 stainless steel. It is 365 mm long, with an inter-bearing external diameter of 40 mm. The internal diameter is 20 mm (Fig. 4.3), so the shaft can act as feedthrough for the necessary signal and/or power transmission cables. It is mounted in a cylindrical bearing housing bolted to the vertical backplate via a flange. Considering the expected loads from the belt tension and test piece, and the nominal speed required, two self-lubricated ball bearings with standard clearance were selected (SKF 6007-2RS1).

Both bearings are mounted with transition fits on the shaft, to avoid introducing excessive stresses, and the need for special mounting equipment, while at the same time ensuring a stable connection. The bearing on the atmosphere side of the rig is also mounted with a transition fit in its housing seat: two circlips, one on the outer, and one on the inner diameter of the bearing, are used to prevent relative motion with shaft and seats. The bearing on the vacuum side is mounted with a clearance fit on its outer diameter, which allows thermal expansion of the shaft and avoids over-constraining it. A circlip on the shaft seat prevents the shaft from sliding relative to the bearing, to minimise wear of the bearing seat.

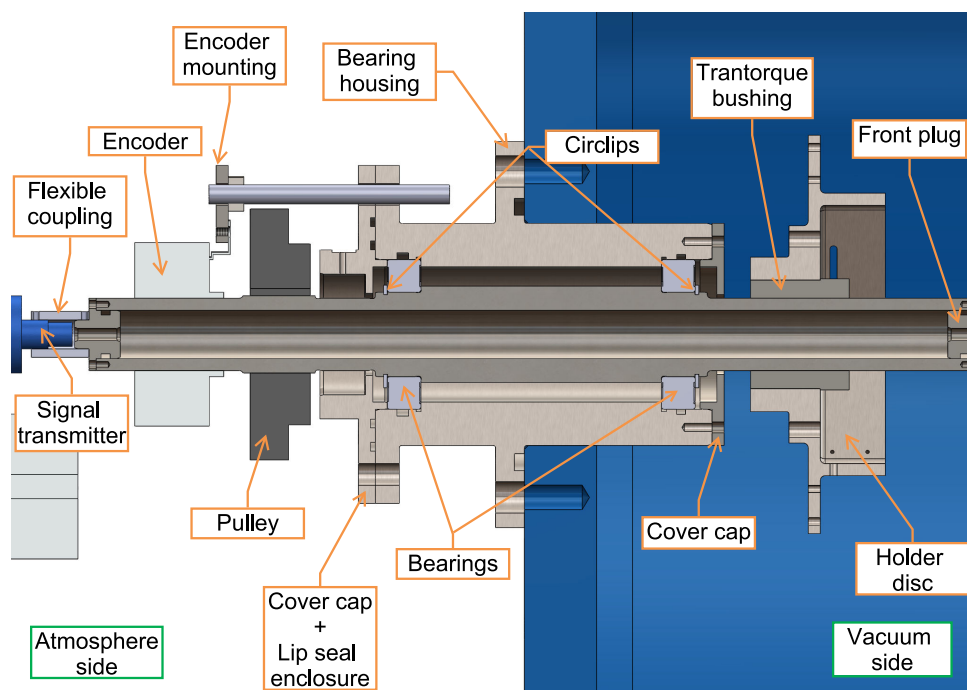


Figure 4.3: Drive system: CAD section view of the bearing housing-shaft assembly

The design of the shaft was targeted towards the minimisation of flexibility and stresses. The dynamics of the final configuration were then checked in a FE analysis, to ensure that no critical speeds occur within the 0÷6000 rpm operational range, and avoid large-amplitude shaft whirling. The shaft was modelled with beam elements, and only transla-

tional degrees of freedom were constrained at the bearing locations: this simulated the fact that ball bearings allow small rotations, and produced a conservative design, as it added flexibility to the system. A mock-blisk with inertial properties representative of a typical test piece (radius 250 mm, thickness 8 mm) was added to the FE model of the shaft: it was thus possible to assess the influence of the additional inertia and flexibility of the blisk on the shaft, which could potentially create disc-shaft coupled critical speeds [140]. Fig. 4.4 shows the Campbell diagram resulting from the FE modal analysis in the fixed frame. It can be seen that, even with the addition of a very flexible, high-inertia disc, no intersection occurs between the synchronous excitation line and the shaft FW and BW resonance branches, indicating that the first forward critical speed is well beyond the operational threshold.

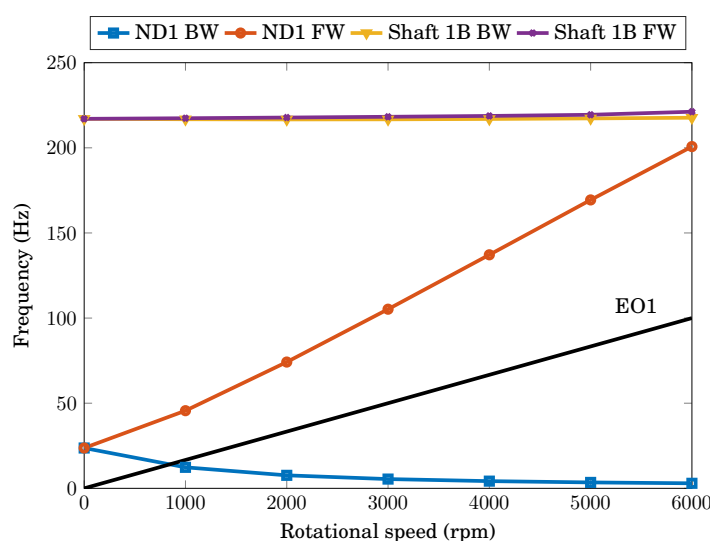


Figure 4.4: Campbell diagram of the driving shaft and mock test piece.

In view of these results, static balancing was considered satisfactory, and a single balancing plane established. To keep the system as compact as possible, it was decided not to have a single-function balancing disc, but to create a disc that could serve multiple purposes, namely hold the necessary electronic components for the measurement system, act as an attachment point for the test piece, and provide a balancing plane.

The resulting multi-function disc is shown in Fig. 4.5. The balancing functionality is fulfilled by two rows of tapped holes in the outer annulus of the disc: balancing weights can then be easily attached and removed during the balancing process. Each row has 36 tapped holes, and the two are shifted by 5° between each other, thus allowing a relatively fine resolution for the optimal positioning of the balancing weights. The assembly is then connected to the shaft via a Trantorque keyless bushing (Fig. 4.3). The other functions of the disc will be discussed in the following sections.

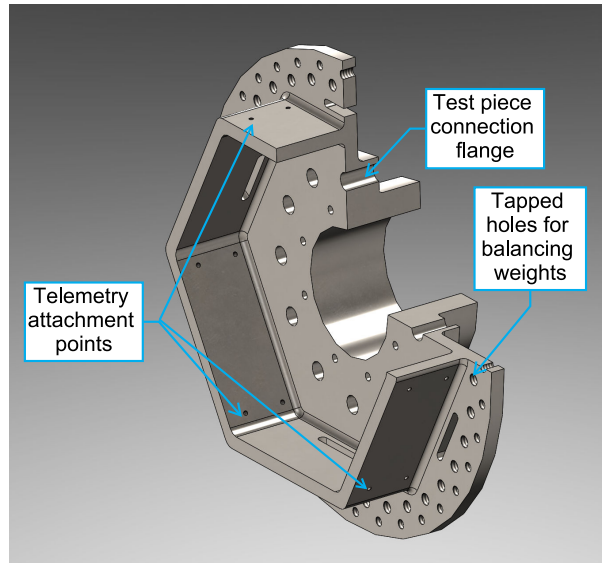


Figure 4.5: Multi-function disc: balancing plane, holder for measurement electronics, and shaft-test piece joint.

4.4 Excitation system

Macro-Fiber Composite (MFC) piezoelectric patches were selected as the excitation system. Despite the difficulty experienced in quantifying the force resulting from the MFC actuator deformation, they are unique in allowing a multiple-input excitation that can be directly attached to the rotating test piece. They are controllable in frequency and amplitude through the driving voltage signal, and can therefore generate both harmonic and random excitation, at adequate levels.

The choice of actuators was based on a compromise between dimensions, which needed to be small to reduce mass loading effects and an excessive impact on the stiffness and damping of the test piece, and attainable maximum force, which increases with increasing dimensions. Due to the flexibility of the planned test piece for this project, the former criterion was considered the most important one, and a very small actuator was chosen in order to minimise the added mass, and the changes to stiffness and damping. The actuators (Smart Material's M-0714-P2 [141]) have an active area of only $7\text{mm} \times 14\text{mm}$, and a thickness of 0.3 mm (Fig. 4.6). They operate in the d_{31} effect, so positive voltages will cause the patch to contract in the 1 direction, while negative voltages to expand. The maximum operational positive and negative voltages are $+360\text{ V}$ and -60 V respectively [141].

To maximize flexibility in the test configuration, it was decided to control each actuator individually, by sending a separate signal to each MFC patch, allowing complete control over the excitation type, frequency, and relative phase. By feeding each actuator with a phase-shifted sinusoid, it is possible to impose arbitrary EO patterns, in particular FW/BW travelling waves, and excite single ND modes, to maximize signal-to-noise ratio (SNR) in the output signal.

To exploit the full operational range of the patches, an amplifier is needed to produce

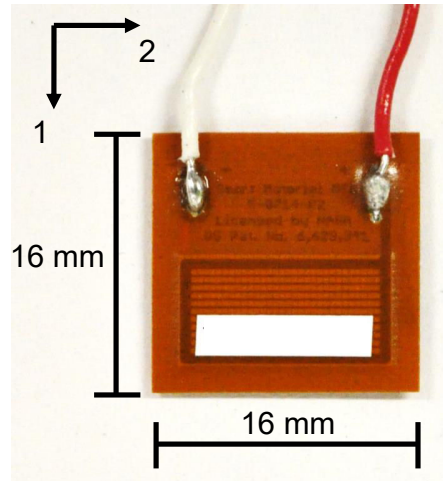


Figure 4.6: MFC actuator: global dimensions and reference frame.

the admissible voltages. An E-835 DuraAct™ piezo-driver module was chosen for the task [142]. It is a semi-bipolar amplifier, accepting an input from -4 V to 10 V. Working in combination with the selected MFC patches, it ensures an unattenuated maximum output across a bandwidth in excess of 4.2 kHz. The amplification factor is 25, which leads to an output range of -100 V ÷ 250 V. This was considered high enough to produce adequate levels of excitation. The amplifiers offer an additional high-impedance output of 1/100th of the high-voltage output, which can be used for monitoring or synchronisation purposes (see sect. 4.7.2).

A Rotrans™ [143] liquid-metal signal transmitter (Figs. 4.1 and 4.3) was chosen for the task of connecting the PC-based signal generator to the MFC actuators attached to the rotating test piece. The transmitter allows the connection of twelve individual wires, rated to 0.3 A. Two wires are needed for the power supply of the on-board electronics, so up to nine MFC actuators can be used, as the last available wire provides the common ground connection for the patches. The transmitter has very low inertia, produces low friction, and is rated up to 42000 rpm, thus ensuring minimum interference with the dynamics of the rig.

4.5 Measurement System

In order to recover the ODSs of the rotating assembly, it was necessary to find a measurement system that could record the response of multiple points on both the bladed disc and the shaft. At the same time, the system should be minimally intrusive, so that the modal parameters of the structure, such as damping, could be retrieved with minimum impact.

Full-field methods, such as Laser Doppler Velocimetry and Digital Image Correlation, are ideal for the acquisition of the displacement of multiple points, and allow the reconstruction of the vibration pattern of the whole structure with minimal interference. However, since they need particular surface characteristics for optimal performance, and direct line-of-sight, they are not well suited to measure complex-shaped specimens like bladed

discs, where high stagger angles limit optical access. Most crucially in the testing of rotating structures, they are also unable to capture constant deformations due to the centrifugal force.

For these reasons, full-field methods were discarded as a possible measurement system for the rotating test rig, and strain gauges were selected instead. They allow moderately fine spatial resolution, irrespective of stagger angle, and the reconstruction of the hot shape of the test piece, as static strain can also be measured. As the test rig is meant to work at ambient conditions, ordinary strain gauges can be used. This means that their influence on the global mass, stiffness, and damping characteristics of the test piece, especially through mistuning, is very small, and can be neglected [76].

The need to minimise the gauge area to measure localised strain led to the selection of the CEA-06-125UN-350 model. The grid length, in the direction of measured strain, is 3.18 mm, and the width 2.54 mm, thus providing a good approximation of point strain [144]. The gauge factor is 2.155, with a maximum transverse sensitivity of 0.5%. The resistance is 350 Ω , to reduce sensitivity to external resistance variations, such as those coming from leadwires or bridge completion circuits [145].

To transmit the voltage signals from the strain gauges, a commercial low-cost modular telemetry system by Transmission Dynamics was selected. The system consists of small transmission modules that sit on the rotating component, and a corresponding static receiver. The transmitter modules provide four strain channels each, with a frequency range of 6 kHz. They incorporate bridge completion (with an excitation voltage of 3.3 V), amplification (300x nominally), and 16-bit digitalisation of the signal. The modules are extremely compact (50×25×5 mm), with a weight of 20 grams, fitting into the holder introduced in sect. 4.3.3 (Fig. 4.5). Receiving antennae are positioned inside the vacuum chamber, and connected to the receivers, where the signal is converted back to analog, and fed into the data acquisition system (see sect. 4.7.1). As a compromise between spatial resolution, which would call for a large number of strain gauges, and added mass loading and damping in the test pieces, three modules are used, allowing a maximum of twelve quarter-bridge strain gauges working in the rig at each time.

Additional sensors are used at other locations in the rig to monitor and control its operation. Shaft vibration is indirectly recorded via two couples of piezoelectric (IEPE) accelerometers (PCB 352B10), glued to the vacuum and air side of the bearing housing in the horizontal and vertical directions. Temperature is monitored via two thermocouples, attached to the bearing housing at the bearing positions, while pressure inside the vacuum chamber is measured by an analogue gauge. Finally, the velocity of the shaft is measured by a 2048-ppr incremental encoder on the shaft itself.

4.6 Test piece design

The test piece was designed to maximize the effects of the Coriolis force. The design effort was therefore driven by the need to make the frequency splits as large as possible, and have distinct TW modes. At the same time, mistuning needed to be limited, since it can

also lead to frequency splits, overshadowing the Coriolis effects.

In order to satisfy these requirements, strong radial components of the vibration are needed during rotation. The simplest way of achieving this is by bending the blades out of the plane of rotation [18]. To maximise the effect over a wide speed range, it was decided to adopt horizontal blades. This would allow to retain large radial motion even at high speeds, where the centrifugal force would tend to straighten them.

The test piece (Fig. 4.7) was conceived as a thin bladed disc (blisk), so that the blades could be easily bent 90° out-of-plane, instead of having to be welded in place, which would introduce unnecessary uncertainties. The test piece was modelled in NX Nastran using 17000 20-node hexahedral elements (121000 nodes), following the approach from Chapter 3. The resulting Campbell diagram calculated for the first four ND modes is shown in Fig. 4.8a, and presents a split of 6 Hz for 2ND and 3ND at 500 rpm. The mode shapes corresponding to the first bending for the 0ND, 2ND, 3ND, and 4ND families are shown in Fig. 4.8b.

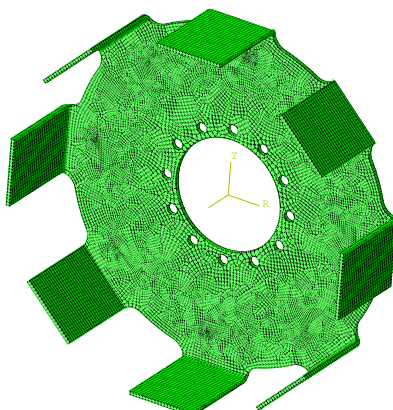


Figure 4.7: FE model of the test piece.

The peculiarity of this design lies in these large splits even at higher ND modes, which, being decoupled from the shaft whirl modes, are usually less affected by gyroscopic splitting. At the higher NDs, the horizontal leaning causes the vibrational velocity to still have a predominant radial component, thus increasing the Coriolis force [6]. Due to the horizontal leaning of the blades, centrifugal stiffening is not noticeable, as demonstrated by the 0ND curve, which shows a 1-Hz frequency increase over a 2000 rpm velocity span. The principal geometric and material parameters are summarized in Table 4.1.

4.7 Data acquisition and processing

4.7.1 Data acquisition system

The data acquisition (DAQ) system comprises a PC, the DAQ cards, the telemetry system (sect. 4.5), and other sensors. The PC runs the LabView software needed for the generation of the excitation signals for the MFC actuators and the motor target speed as outputs, and the recording of the measured data. The PC is also connected to a NI cDAQTM-9178 8-slot

Table 4.1: Main dimensions and material characteristics of the test piece.

Disc diameter	200 mm
Disc thickness	2 mm
Blade width	40 mm
Blade length	54 mm
Number of sectors	8
Material	304 stainless steel
Density	7850 kg/m ³
Young's modulus	194 MPa

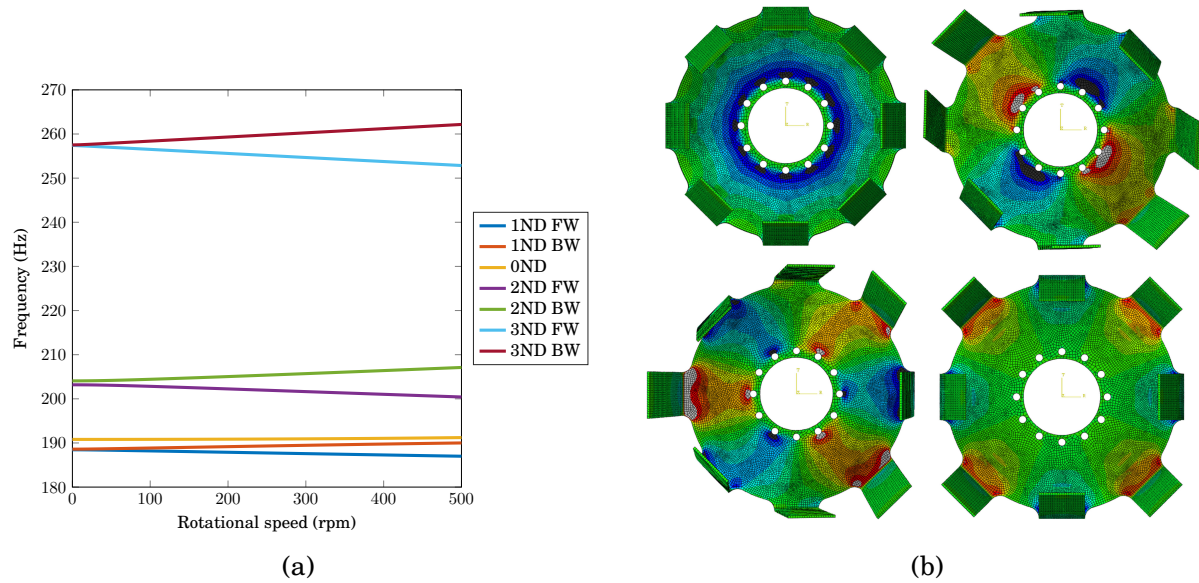


Figure 4.8: Dynamic FE analysis of the test piece: a) Campbell diagram for the first four ND modes from NX Nastran, and b) 0ND, 2ND, 3ND, and 4ND radial strain mode shapes.

chassis, which hosts the different acquisition and signal generation cards. The layout of the system and its connections is shown in Fig. 4.9.

The main acquisition card is the NI 9220, a 16-bit analog input module. It has 16 channels, which are sampled simultaneously (without multiplexing) at a maximum programmable sampling rate of 100 kHz per channel. It was used to acquire the voltage signals from the telemetry receivers, and the monitor signals from the piezo-drivers for synchronisation purposes.

The NI 9234 is a 24-bit analog input module. As it is able to generate excitation currents for IEPE sensors, it was used to acquire acceleration data from the accelerometers on the bearing housing. The temperature signals are processed by a NI 9211 24-bit thermocouple input module, while the encoder is interfaced with a NI 9401 TTL digital/input output module to recover shaft speed information.

The signal generation is handled by a NI 9264 analog voltage output module. It has 16 channels, a resolution of 16 bits, and a simultaneous sampling frequency of 25 kHz per channel. The generated voltage range is ± 10 V, which allows the exploitation of the

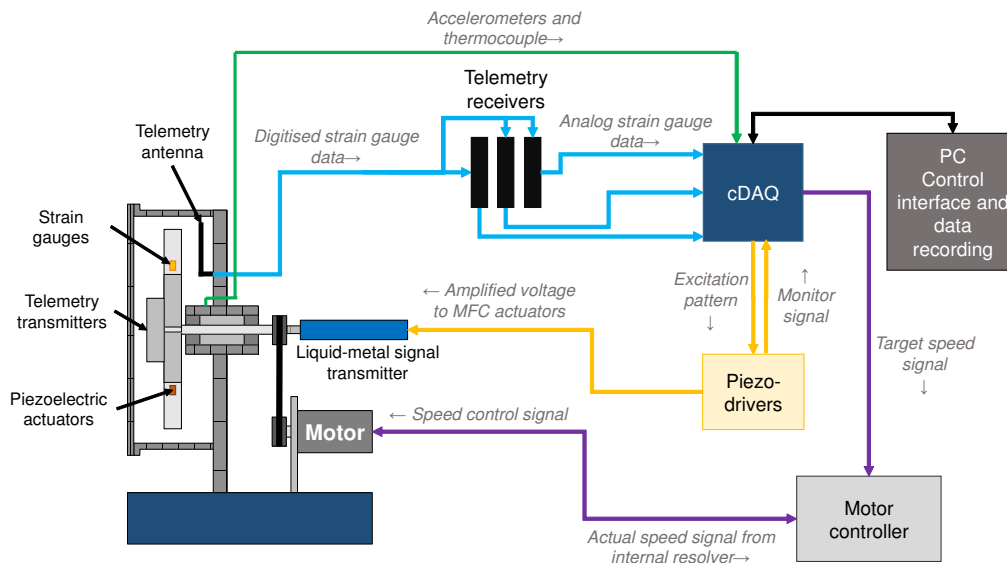


Figure 4.9: Layout of the data acquisition system.

full range of the piezo-driver amplifier range. Eight channels are connected to the piezo-drivers, and thus produce the excitation signals for the MFC actuators on the test piece. One channel sends the ON/OFF signal to the motor controller, and another the target rotation speed.

All parameters needed to control the test rig and acquire the data can be set through a newly developed LabView control program (VI). The user interface allows to specify excitation type (sine, stepped sine, random, etc.), its amplitude, frequency, and phase, and to set the speed of the motor, besides turning it on and off. On the measurement side, sampling frequency, frequency resolution, and the time length for the test can also be set, enabling a fully automated test once the rig is running.

4.7.2 Synchronisation of the strain gauge data

The three telemetry transmitter/receiver pairs described in sect. 4.5 operate independently of each other. This means that synchronisation between the acquired strain gauge data is not guaranteed, and the signals can experience a certain spurious relative delay. To help with the synchronization of the signals, a digital tacho channel is present on all transmitters, which sends a reference signal with the same delay as the strain information.

The name "tacho" comes from the synchronisation method recommended by the manufacturer: a Hall sensor mounted on the test piece records a pulse when it rotates past a small permanent magnet glued to the static part of the rig, thus providing a 1/rev signal as a simple tachometer would. This signal is then fed to the tacho channel of each transmitter module. Once the tacho signals are acquired by the DAQ, the strain gauge data can be synchronised by shifting them in time by the relative delay of the tacho pulses.

This suggested approach allows to retrieve the relative phase of the strain gauges between themselves, but since the fundamental aim of this project is the acquisition of FRFs from the measured data, the phase between output *and* input is also required. For this

reason, it was decided to use the voltage signal to the MFC actuators as reference for the synchronisation. A 0.1 V square wave signal is generated by the analog output card in sync with the voltage waveform used to drive the active MFC patch (in a MIMO test, one of the patches is taken as reference, and the square wave synchronised with it. The phase difference with the voltages of the other actuators is then known, as it is pre-set in the control software). This square wave is then fed to the piezo-drive amplifier, so that it follows the same path as the excitation signals.

Here, the information is split: the amplified square wave is sent simultaneously to the tacho channels via the Rotrans signal transmitter, while the output of the monitor channel (sect. 4.4) goes back to the analog input DAQ card. This signal, and not the voltage generated at control software level, is then used as reference. In this way, any delay introduced by the piezo-driver electronics can be ignored, as the signal is measured after the amplifier: this reference signal and the control voltage for the MFC patches can then be considered in sync. Once the data (from the strain gauges and tachos) has been acquired, the signals are again synchronised by shifting them by the relative delay of the tacho pulses with the reference signal. Fig. 4.10 illustrates the concept.

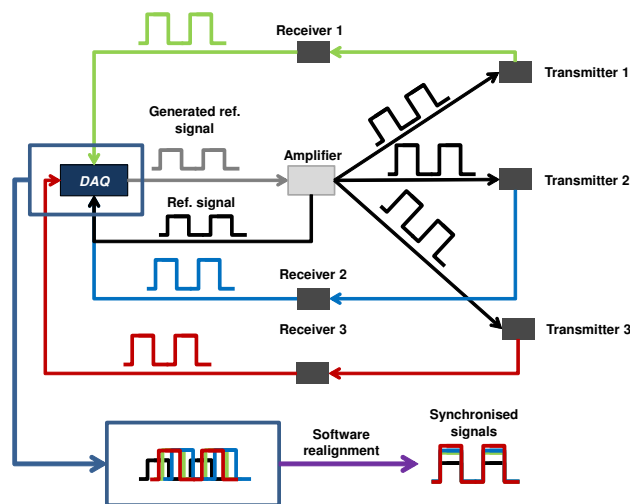


Figure 4.10: Synchronisation process.

4.7.3 Data processing

The strain gauge data goes through a first round of processing in the telemetry modules (sect. 4.5), where the signals are amplified by a factor of 300, and offset by a constant value of 2.5 V. Together with the rest of the measurement inputs from the accelerometers, thermocouples, etc., the raw data are then subjected to further manipulation during post processing in a newly-developed Matlab code to transfer them from the time to the frequency domain.

The recorded time-domain data were first subdivided into potentially overlapping datablocks, which are processed separately, and then averaged. The length N_s of each datablock was determined by a trade-off between the need for a high number of averages from short datablocks, and that for a fine frequency resolution, which would require long blocks, and so long measurement times. The block length was varied according to the requirements of each experiment, but a minimum frequency resolution of 0.15 Hz was always enforced, allowing the identification of relatively close modes, and the minimisation of bias error ϵ_b (sect. 2.4.3). Each block was de-trended by removing any offset from the time domain signals, and a Hanning window was applied to minimise leakage. The Discrete Fourier Transform (DFT) for each pre-processed channel in the block could then be calculated, leading to a clear indication of the frequency content in the signal.

The \hat{H}_1 estimator of the frequency response function (Eq. (2.51)) was selected for both the stepped-sine, and random excitation tests. The use of this estimator is based on the hypothesis of no input noise, i.e. no noise in the forcing of the test piece. The excitation, which in this case is introduced through a voltage signal applied to piezoelectric patches, was considered to satisfy this assumption.

The autospectrum of the input \hat{G}_{FF} , necessary for the calculation of \hat{H}_1 , is defined as

$$\hat{G}_{FF}(\omega) = \frac{2A_w^2}{N_s^2 N_{av}} \sum_{j=1}^{N_{av}} \mathbf{F}_{w,j}^H \mathbf{F}_{w,j}, \quad (4.1)$$

where A_w is the amplitude correction factor associated with the particular window used, N_{av} the number of averages (number of datablocks), and $\mathbf{F}_{w,j}$ is the DFT of the j -th windowed datablock of input vector $\mathbf{F} \in \mathbb{C}^{N_i \times 1}$. The cross-spectrum is determined through

$$\hat{G}_{XF}(\omega) = \frac{2A_w^2}{N_s^2 N_{av}} \sum_{j=1}^{N_{av}} \mathbf{X}_{w,j} \mathbf{F}_{w,j}^H, \quad (4.2)$$

where $\mathbf{X}_{w,j} \in \mathbb{C}^{N_o \times 1}$ is the DFT of the spectrum of the windowed response. For stepped-sine tests, Eqs. (4.1) and (4.2) are applied at each excitation frequency. The amplitude at the forcing frequency ω is then obtained by extracting the maximum value in a neighbourhood $\omega - \delta < \omega < \omega + \delta$ of ω , where δ is a small value, dependent on the frequency resolution. Having thus obtained $\hat{G}_{XF}(\omega)$ and $\hat{G}_{FF}(\omega)$, Eq. (2.51) can be applied to derive the corresponding value of $\hat{H}_1(\omega)$ at the given excitation frequency. Once the data for all excitation frequencies has been processed, the FRF response of the system can be derived.

4.8 Commissioning

4.8.1 Test rig and drive system

The assembled test rig is shown in Figs. 4.11, and what follows is a description of tests that were conducted to commission it. To ensure that the basic design criteria were met, a hammer test was performed on the main components to identify their resonance frequen-

cies. In the first test, an accelerometer was glued to the tip of the shaft (with no test piece mounted), and the hammer hit at the top right corner of the rig backplate (Fig. 4.11). The resulting FRF is shown in Fig. 4.12a: it can be seen that the first resonance frequency occurs at 84 Hz, which places a resonance within the operational range of the rig (0÷100 Hz, see sect. 4.3.1). However, its corresponding acceleration is only 0.0023 g/N, indicating that it does not constitute a major resonance for the rig. The second resonance is at 112 Hz, which, while lower than the 120-Hz limit targeted during the design phase, is outside the operational range of the shaft.

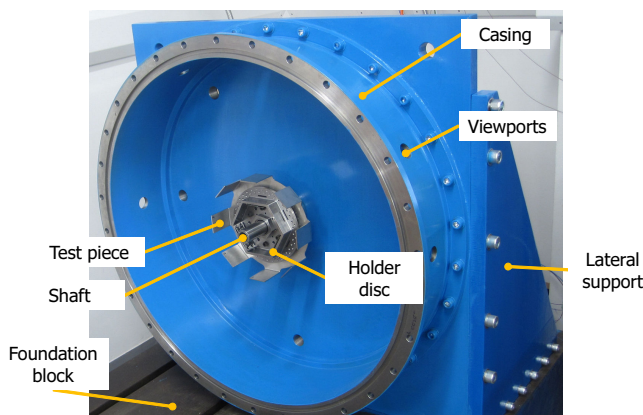


Figure 4.11: Front view of the test rig: chamber and support [138].

More tests were conducted on the shaft, by hitting it directly with the modal hammer next to the accelerometer, to check whether lower localised modes could be found. Three different configurations were tested: in the first, no disc was mounted; in the second, the telemetry holder disc was installed near the tip of the shaft; in the third test, the disc was shifted back towards the bearing housing, which is where the test piece would normally sit. As can be seen in Fig. 4.12b, the presence and position of the test piece have a strong impact on the shaft response: when no disc is mounted, the first natural frequency can be found at nearly 350 Hz, while with the disc at the shaft tip, a peak can be seen at 187 Hz, and a smaller resonance is placed at 109 Hz. No real peak, on the other hand, is visible once the disc is mounted at its designed location, indicating that the system is sufficiently damped. More importantly, there is no trace of the 84 Hz resonance when exciting the shaft directly: this indicates that dynamic loading on the shaft (e.g. unbalance) would not easily excite the rig at this frequency. As no other excitation sources are present elsewhere, this resonance was not considered a major risk for the operation of the rig.

The shaft is powered by a Siemens 1FT6082-8AK71 brushless synchronous servomotor through a belt and pulley system (Fig. 4.13). The motor has a rated speed of 6000 rpm, a torque of 5.5 Nm, and a stall torque of 13 Nm, providing satisfying power characteristics over the entire speed range. An internal high-accuracy 4-pole resolver measures the motor speed and transmits it to the motor control unit. This module (a Sinamics CU310-2 DP model) performs the closed-loop control of the motor speed, and only receives the ON/OFF

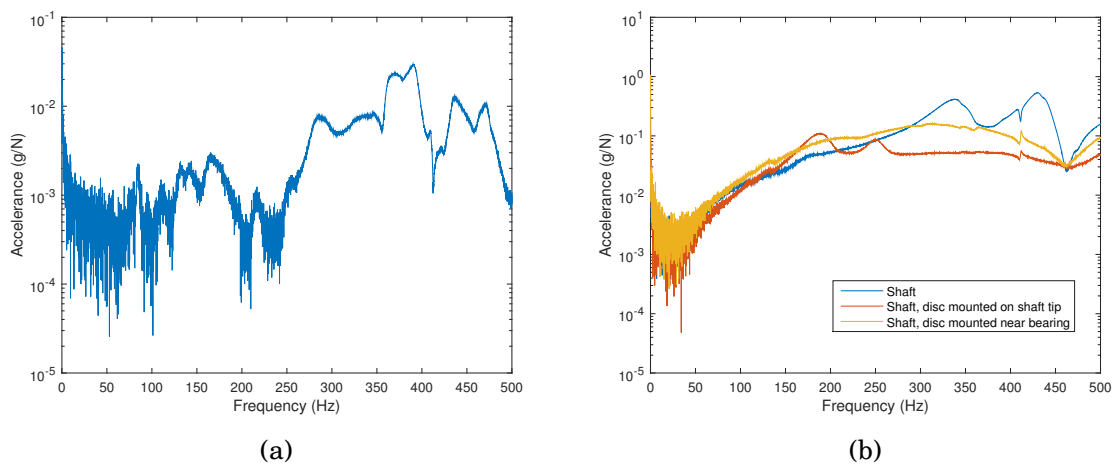


Figure 4.12: Dynamics of the test rig: Accelerance of the shaft from hammer tests by hitting a) on the top right corner of the rig backplate, and b) on the shaft, with and without a representative disc mounted on it

signal and target speed value from the DAQ system (sect. 4.7.1) through one of its analog ports.

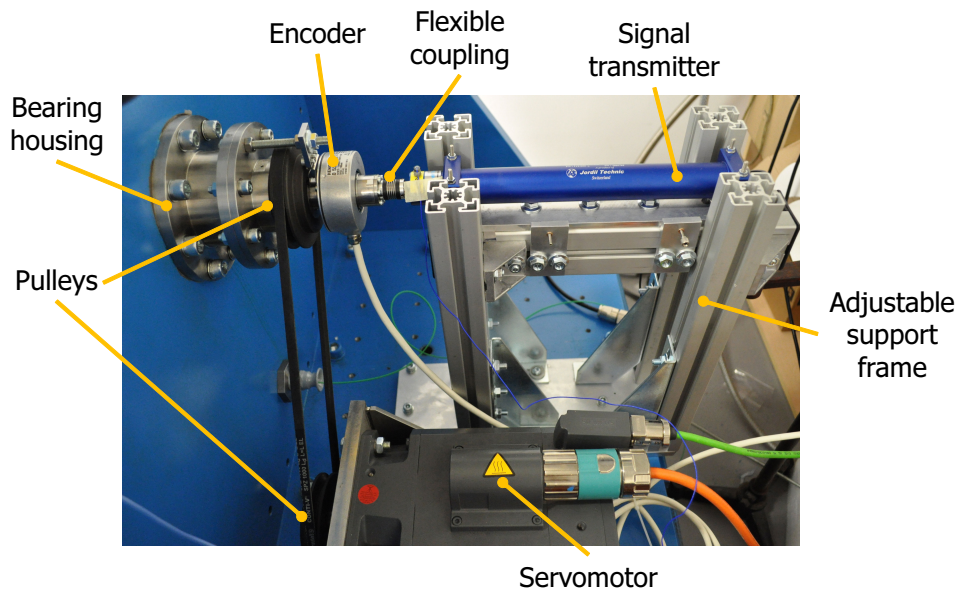


Figure 4.13: Drive system and signal transmitter [138].

The characteristics of the motor allow the use of a 1:1 transmission system. A belt and pulley system was chosen for this purpose, so that the signal transmitter (Fig. 4.13) and its cables could be installed in line with the shaft, and the motor support could be securely bolted to the base-plate of the rig. The chosen V-belt ensures smooth operation with minimal slippage. Synchronisation between the motor and rig shaft was checked by measuring their respective speeds with a tachometer and a higher-resolution stroboscope. The results are shown in Table 4.2. The nominal speed (in Hz) was set from the analog

output card of the DAQ, and the motor and shaft speed were measured separately. It can be seen that, even if the absolute value of the slip increases with speed, it stays constant in percentage, at 1%, which was considered acceptable.

Table 4.2: Measurement of the speed difference between motor and shaft due to the belt slip.

Nominal (Hz)	Motor (Hz)	Shaft (Hz)	Slip (Hz)	Slip (rpm)	Slip (%)
15	15.04	14.89	0.15	9	1.01
20	20.02	19.82	0.21	12.3	1.03
25	25.02	24.77	0.25	15	1.01
30	30.02	29.70	0.32	19.2	1.08
35	35.02	34.65	0.37	22.2	1.07
40	40.00	39.58	0.42	25.2	1.06

The Rotrans signal transmitter, finally, is connected to the back end of the shaft via a flexible coupling, thus minimising interference with the dynamics of the shaft itself, and is grounded to a stiff frame made of 60mm×60mm aluminium profiles (Fig. 4.13). The transmitter is bolted to an aluminium base, which is equipped with a total of eight ThorLabs M3×0.2 fine-adjustment screws to correctly align it with the shaft.

4.8.2 Test piece

The test piece was laser-cut from a flat plate, and the blades were subsequently bent. Laser-cutting was used to minimise mistuning in the blisk, but the bending process, with its relatively large tolerances, was another potential source. A qualitative assessment of the angles of the blades with a straight edge showed minor deviations from the ideal 90° value for nearly all blades. Hammer tests were therefore performed on the blisk to determine its natural frequencies and damping, and to identify its inherent mistuning before instrumenting. All tests were conducted in a free-free configuration: the blisk was suspended with fishing wire by two of its flange holes, and hit in a direction perpendicular to the wire itself to minimize its influence on the response.

The blisk was then instrumented. The number of strain gauges was dictated by a compromise between the need to reduce mass loading, the number of available channels, and spatial resolution on the blisk. The telemetry modules allowed a maximum of 12 gauges at a time, to which four more were added to increase resolution if required. Two sectors, Sector 1 and 4 (Fig. 4.14a), were completely instrumented, with six and four gauges each. A single strain gauge was glued at the top right corner of the remaining sectors, to allow the measurement of phase differences between sectors, and thus detect the propagation of Coriolis-induced travelling waves. No gauges were attached to the blades because this configuration would have required longer wire lengths, and therefore add more damping, without providing significantly different information.

During measurements, the gauges were divided into two groups, as the number of available channels was reduced to eight after one telemetry module broke. One was therefore dedicated to the measurement of the global TW behaviour of the blisk, and comprises SGs

3, 7, 8, 10, 13, 14, 15, 16, and will henceforth be referred to as “circumferential SGs”. The other was used to detail the sector response, and includes SGs 1, 3, 4, 5, 6, 9, 10, which will be referred to in the following as “sector SGs”.

All strain gauges were aligned along the radial direction, as radial strain is the principal strain component on the disk. Their position was optimised for the validation of the first 3ND mode shape (Fig. 4.14b), which the previous simulation results showed to be strongly affected by the Coriolis effect (sect. 4.6).

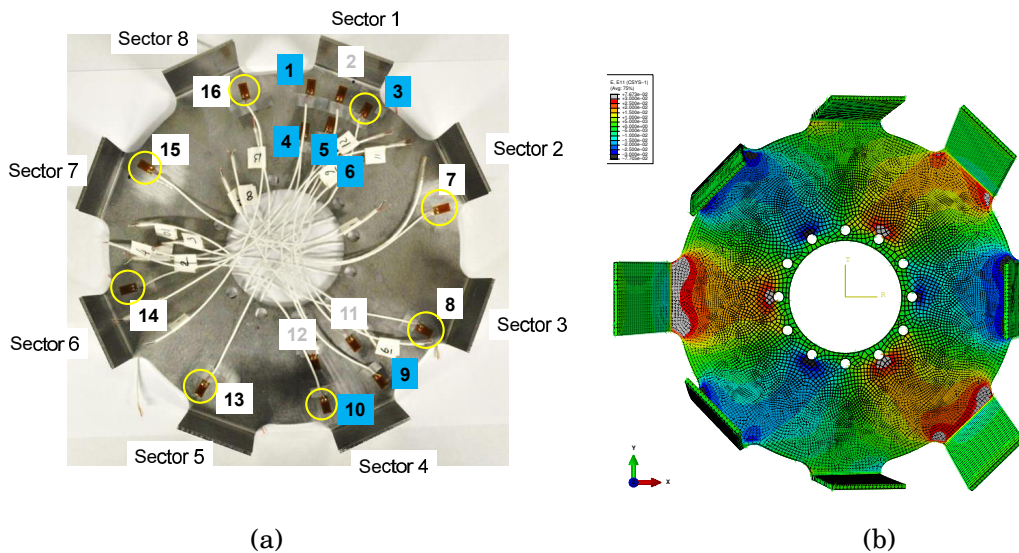


Figure 4.14: Strain gauges on the test piece: a) position of the strain gauges on the test piece (the sector SGs are highlighted in blue, while the circumferential SGs are circled in yellow); b) radial strain for the first 3ND mode shape from FE modal analysis.

To maximise flexibility of the forcing configuration, each sector of the blisk was equipped with one MFC actuator on its rear face (Fig. 4.15). Their angular and radial position was located at a point of medium/high strain for the first 5 nodal diameter modes, based on the finite element evaluation, to ensure effective excitation of all of them. Before applying the MFC, the surface was sanded and thoroughly cleaned. A two-component epoxy (3M DP 460), as recommended by the manufacturer [141], was used, and left to cure under the pressure applied by spring clamps at ambient temperature for 24 hours to develop its maximum strength properties.

The FE analysis and test results for frequency, damping (loss factor η) and mistuning behaviour of the blisk before and after instrumenting are reported in Table 4.3. It can be seen that there is fair agreement between the computational and experimental resonance frequencies, in the case of the non-instrumented blisk: a maximum difference of 5.3% between the 0ND frequencies, and 4.2% for the 1ND mode, while all the rest fall within 1%. Mistuning of the non-instrumented disk is also limited, with a maximum split of 3.16%, again for the first 1ND mode. All other values are below 1%.

Addition of the MFC actuator and strain gauges (with their cables) does not seem to drastically change the dynamic response of the blisk. Natural frequencies are mostly unaffected (maximum difference -0.341%), with only very small splits in frequency appearing,

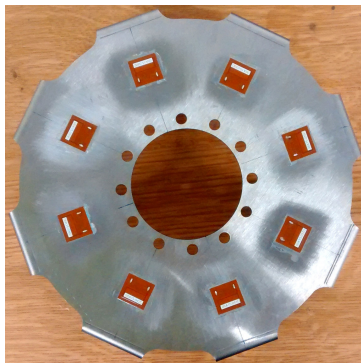


Figure 4.15: MFC actuators installed on the rear face of the test piece.

all below 1%. Existing mistuning is only marginally increased (in the case of the 3ND-III mode, it is actually halved, the patches and strain gauges having acted as tuning masses). While mass loading seems thus to have been effectively minimised, damping increases somewhat, but the resulting loss factors of less than 0.3% can still be considered as very low, and are not expected to impact the FRF measurements during testing.

Another impact test was performed on the instrumented blisk after it was installed on the shaft via the holder disc, to evaluate its dynamic behaviour in its final test configuration. Table 4.4 shows that the only mode to be significantly affected by mistuning is 1ND (2.7% frequency split), while 3ND shows a split of only 0.6 Hz (0.2%). This was considered acceptable due to the much larger expected splits caused by the Coriolis effect. Based on these results it was concluded that the manufacture and instrumentation of the blisk had a minimal effect on its dynamic behaviour, and it would provide an excellent test piece for the measurement of mode shapes under rotation conditions.

The FE model of the blisk was updated with the results of the hammer tests to match the measured frequencies with those predicted by the FE analysis. The mass of the blisk was obtained by weighing it, so the density of the material was treated as a known quantity. The only parameter subject to updating was therefore the Young's modulus of the 304 stainless steel used to manufacture the blisk, which was set at 194 MPa (Table 4.1). The procedure resulted in a maximum discrepancy of 8% between simulated and measured average frequencies of the 1ND mode in the assembled configuration. This error is relatively high, and is likely due to the coupling between the 1ND mode and the shaft dynamics, which was not modelled. Since the error for the other modes goes from 0% for the 3ND mode, to 2% for the 2ND mode, the results were considered acceptable, and no further updating was pursued.

4.8.3 Characterisation of the piezoelectric actuators

4.8.3.1 Excitation configuration

To test the accuracy and effectiveness of the piezoelectric excitation, two different forcing signals were generated. Both were single-frequency sine waves, but while the first was applied to only one MFC actuator, the second was a travelling wave. In the latter case, all

Table 4.3: Natural frequencies and damping of the test piece: Comparison between the results from the FE simulations, and the actual blisk, before and after instrumenting. Mistuning values for the two configuration are also shown.

Mode	f FE (Hz)	f original		f after		η original blisk (%)	η after instrumenting (%)	Δf after/ before instrumenting (%)		Mistuning	
		blisk (Hz)	instrumenting (Hz)	blisk (Hz)	instrumenting (Hz)			original blisk (%)	after instrumenting (%)	original blisk (%)	after instrumenting (%)
2ND	119.4	111.0	111.0	0.04	0.19	0.04	0.19	-0.01	3.16	3.18	0
0ND	180.5	114.6	114.6	0.03	0.11	0.03	0.11	0.02	0	0	0
3ND	239.1	190.6	190.8	0.02	0.35	0.02	0.35	0.11	0	0	0
		236.7	236.6	0.018	0.05	0.018	0.05	-0.04	0	0.12	0
4ND	302.1	300.1	300.3	0.02	0.03	0.02	0.03	0.10	0	0	0
1ND	318.8	316.0	315.8	0.001	0.06	0.001	0.06	-0.07	0.79	0.86	0
		318.5	318.5	0.001	0.26	0.001	0.26	0.01	0	0	0
2ND-II	358.7	352.5	350.2	0.02	0.04	0.02	0.04	-0.71	0	0.69	0
			352.6		0.04		0.04	0.04	0	0	0
4ND-II	356.4	354.4	354.7	0.02	0.03	0.02	0.03	0.10	0	0	0
3ND-II	371.0	363.3	363.6	0.02	0.04	0.02	0.04	0.08	1.04	1.03	0
		367.1	367.3	0.03	0.03	0.03	0.03	0.07	0	0	0
0ND-II	548.6	556.3	555.8	0.03	0.19	0.03	0.19	-0.09	0	0	0
3ND-III	657.7	647.5	647.5	0.02	0	0.02	0	0.00	0.6	0.25	0
		651.4	649.2	0.02	0.05	0.02	0.05	-0.38	0	0	0
2ND-III	659.9	653.8	651.62	0.02	0.04	0.02	0.04	-0.36	0	0.38	0
			654.1		0.035		0.035	0.06	0	0	0
4ND-III	657.9	656.9	657.2	0.019	0.038	0.019	0.038	0.05	0	0	0

Table 4.4: Natural frequencies of the mounted blisk: frequencies from finite element simulation, experimental frequencies, and their mistuning

	f FE (Hz)	f blisk (Hz)	Mistuning (%)
1ND	194.8	177.5 182.4	2.7
0ND	196.4	199.6	0
2ND	209.4	205.8 209.8	1.9
3ND	261.3	260.7 261.3	0.2
4ND	305.4	301.9	0

actuators were excited by the same phase-shifted sinusoidal signal.

As explained in sect. 2.3.4, engine order excitation is a cyclic forcing pattern generated by the rotation of a bladed disc inside a fluid pressure field due to variations in its distribution. The order depends on the spatial periodicity of the excitation. This type of loading is the main source of dynamic excitation in a bladed rotor, and it is thus important to be able to reproduce it in an experimental setting for forced response investigations. EO forcing tends to excite the corresponding ND mode, which, in a structure where the Coriolis effect is present, manifest itself as a travelling wave. An EO forcing pattern reproducing itself a travelling wave is particularly effective in selectively exciting only one particular ND mode during a test. The travelling wave is obtained by phase-shifting the forcing signal by the IBPA φ_k (Eq. (2.22)) between one sector and the other, and the excitation voltage $V_j(t)$ to each piezoelectric actuator j can thus be expressed as

$$v_j(t) = A \sin(\omega t + \varphi_k) = A \sin\left(\omega t + \frac{2\pi k}{N} j\right),$$

where A is the excitation amplitude, which is the same for all sectors.

Initial tests to assess the effectiveness of the MFC actuation were performed with the rotor at rest. In this case, a single-point laser Doppler vibrometer was used to measure the response of the blisk. Several checks were conducted. The first aimed at establishing whether the actuators could generate a clean sinusoidal response of sufficient strength off resonance, to ensure the measurement of well-defined FRFs. One single patch was therefore excited at 230 Hz (around 30 Hz far from the 3ND resonance). Ten acquisitions of the response measured by the laser were made, and the signals were processed with a Hanning window to minimise leakage. Single-sided spectra for all samples were obtained, and the resulting average is shown in Fig. 4.16a. It can clearly be seen that the maximum peak of -2 dB occurs at the excitation frequency, with only two additional, much smaller harmonics (second and third) at -40 dB and -34 dB respectively. This strong amplitude from a single MFC patch indicated a good forcing level, and provided confidence that an acceptable excitation under rotating conditions could be achieved.

The travelling-wave excitation pattern was tested next. The target mode was the first

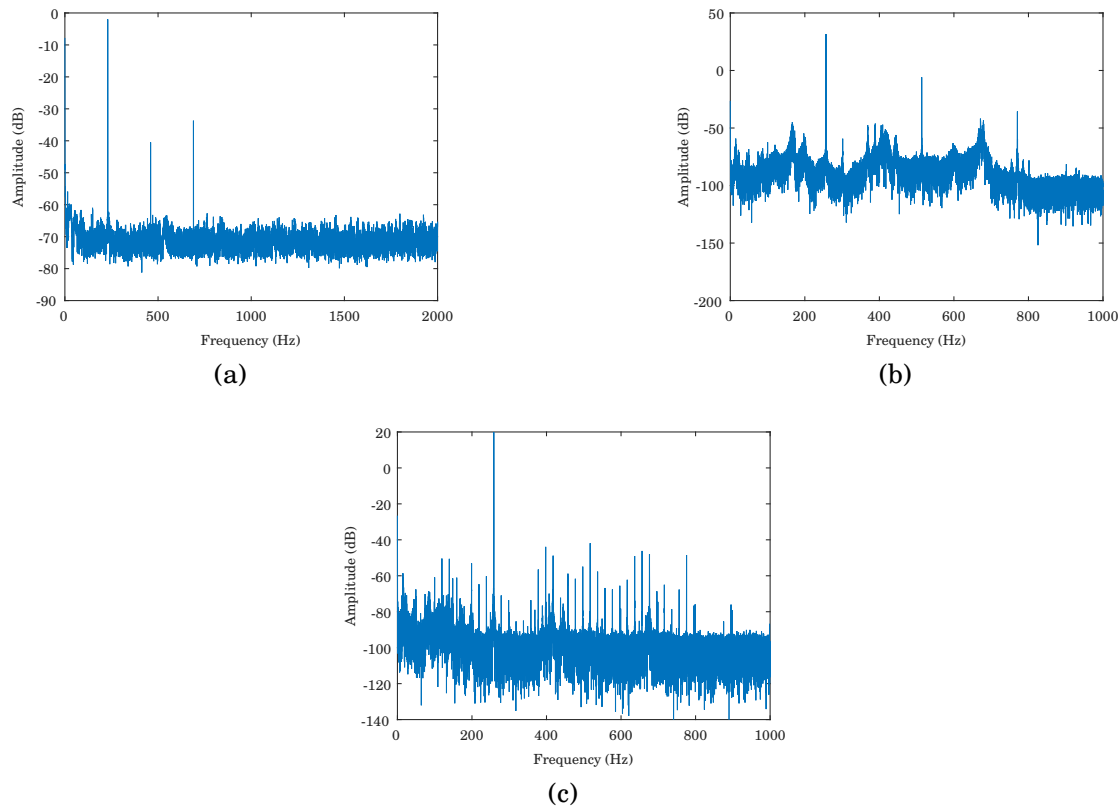


Figure 4.16: Spectral amplitude of blisk response from MFC actuators: a) single actuator, far from resonance (230 Hz), b) 3EO TW pattern at resonance (260 Hz), and c) 3EO TW pattern off resonance (262 Hz) [138].

3ND at 260 Hz (Fig. 4.14b). Each actuator was excited by a sinusoid of the same amplitude (350 V p-p), but with a relative sector-to-sector phase shift of 135° to reproduce a 3EO forcing. The spectrum obtained following the same procedure as above is shown in Fig. 4.16b. The peak amplitude of the response is much higher than in the single-actuator case (+32 dB), which clearly shows that the actuation in eight locations can significantly increase the forcing in the structure. The two higher harmonics show values of -6 dB and -36 dB, and are once more smaller than the amplitude at the main forcing frequency. Some other NDs are also excited, but their amplitudes are all below the -40 dB threshold, making their impact on the response negligible. The same excitation pattern was applied off-resonance, at 262 Hz (Fig. 4.16c), to investigate the capability for targeted FRF measurements. Once more, the maximum response occurs at the excitation frequency, with an amplitude of 20 dB, while all other peaks are below -40 dB.

The results showed that the chosen actuators, with their small active area, provide sufficient excitation strain to reach a high-amplitude response in the lightly damped test piece. On- and off-resonance responses could be obtained with satisfactory amplitudes, enabling frequency response measurement. The targeted 3ND mode could be excited cleanly even though the placement of the patches was not optimised for this particular nodal diameter.

4.8.3.2 Linearity

The actuators were finally tested for linearity. This test was also performed directly on the test blisk. The patch attached to the first sector was excited at various voltage levels with a sine signal, and the response measured by an accelerometer positioned on the disc, at the blade root, close to strain gauge (SG) 3. To exploit the full range allowed by the patch and amplifier, the voltage was also biased. With no bias, the maximum voltage amplitude would be 60 V, as -60 V is the minimum voltage allowed by the MFC actuators in order to avoid depolarisation. Applying a constant voltage offset equal to the mean between the two limits, +250 V and -50 V¹, on the other hand, would allow a maximum oscillating amplitude of 150 V (300 Vp-p). Five bias levels were tested, from 0 V to 100 V, to check whether the bias itself would affect the response. The maximum oscillating amplitude of the voltage signal was adjusted according to the level allowed by the bias: for the 0 V bias, the driving voltage was varied from 4.8 V to 52.8 V, while for the 100 V bias, the range was 4.8 ÷ 144 V. At least 11 oscillating voltage values were tested for each bias level.

Fig. 4.17a shows the measured values of the acceleration at the different excitation voltages, for each bias level. The acceleration amplitudes at the various bias levels are very close to each other, indicating that the presence of a constant voltage offset in the piezoelectric actuators does not affect the dynamics of the structure. Fig. 4.17b offers a closer look at how the measured acceleration varies with the excitation voltage, at 100 V bias. The experimental acceleration data points show a systematic deviation from the regression line, and follow a slightly parabolic nonlinear trend. However, assuming a linear relationship would lead to a mean error of only 0.07 g, or 5% for an excitation voltage of 60 V. This was considered acceptable, and a bias level of 100 V was adopted for all tests, so that the maximum excitation level allowed by the actuator-amplifier combination could be exploited.

4.8.4 Measurement system

4.8.4.1 Calibration

The telemetry transmitter/receiver pairs, as introduced in sect. 4.5, supply bridge completion, anti-alias filtering and amplification, ADC and DAC, providing all the necessary processing for the strain gauge signals. This made them a black box system, which called for a proper calibration procedure to verify the accuracy of the gain data supplied by the manufacturer. To eliminate unnecessary sources of uncertainty in the procedure, a simple mild steel beam (70×505×3 mm) was chosen as test piece, and suspended by thin fishing wires in free-free configuration. A CEA-06-125UN-350 strain gauge was attached at one of the anti-nodes for the third bending mode (3b) of the beam (115 mm), and an electromagnetic shaker connected to the beam through a stinger at the same longitudinal position.

Despite its simplicity, it was not possible to eliminate the influence of the set-up, as lightly-damped, flexible system are inevitably very sensitive to even minor changes (ad-

¹A safety factor was applied to the minimum voltage, as depolarisation of the piezoelectric actuators had to be avoided. The minimum voltage for all tests was therefore always set at -53 V.

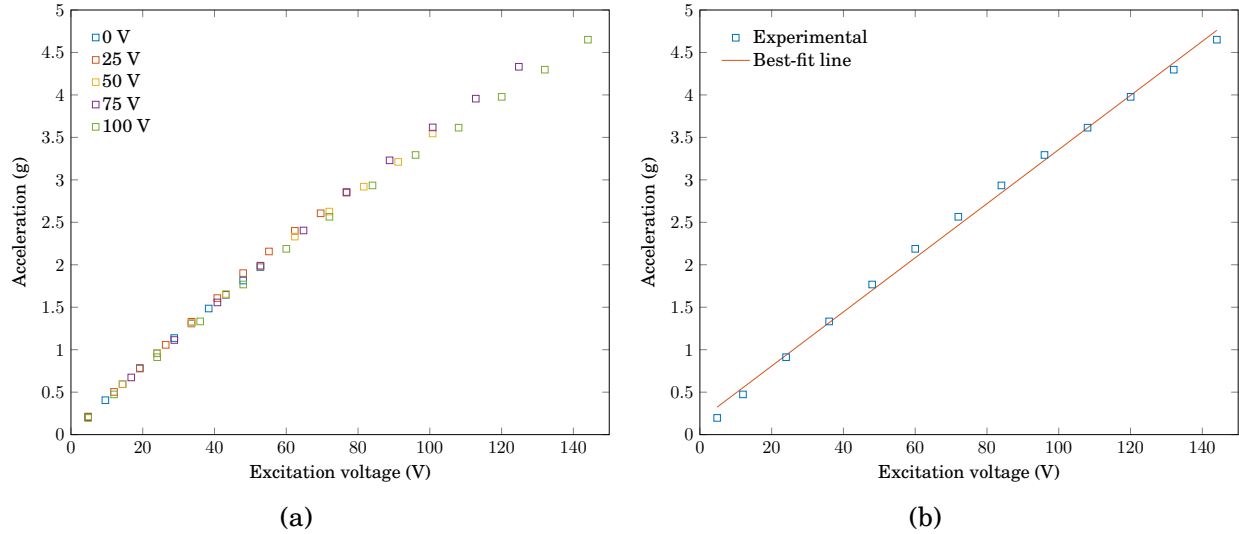


Figure 4.17: Linearity check on the piezoelectric excitation: a) Experimental acceleration data points at different excitation levels, for different bias voltages; b) Dependence of acceleration on excitation amplitude, and best-fit regression line, for 100 V bias.

justments in the position of the shaker, or of the supporting wires, etc.). It was therefore decided not to use FRFs for the calibration, because they could exhibit large variations from one test to the next. It was decided instead to take advantage of the linear kinematic relationship between acceleration and strain in the neighbourhood of resonance. Considering steady-state, mono-harmonic response at resonance frequency ω_r , the displacement u_j at the output DOF j can be written as $u_j = a\psi_j \cos \omega_r t$, where a is a scaling factor, and ψ_j the j -th component of the mode shape ψ corresponding to resonance ω_r . The corresponding acceleration is $\ddot{u}_j = -a\omega_r^2 \psi_j \cos \omega_r t$. The amplitude of the strain in the longitudinal direction z ε_z is then equal to

$$\varepsilon_{z,j} = \frac{\partial u_j}{\partial z} = a \frac{\partial \psi_j}{\partial z} = \frac{\ddot{u}_j}{\omega_r^2 \psi_j} \frac{\partial \psi_j}{\partial z} = \frac{\ddot{u}_j}{\omega_r^2 \psi_j} \psi_j^\varepsilon.$$

Under the stated hypotheses, which can be considered reasonable with fixed-frequency shaker excitation at resonance, it can be seen that strain amplitude and acceleration amplitude are proportional.

The calibration procedure was then set as follows. An IEPE accelerometer was glued to the beam next to the strain gauge, and the shaker was then driven at the 3b resonance, 327 Hz, with linearly varying voltage amplitudes (from 0.2 V to 1.4 V). Acceleration and strain data were acquired for 90 seconds, and processed as described in sect. 4.7.3. The voltages from the strain measurement devices were plotted against the corresponding acceleration. A linear regression procedure was applied to these experimental data, and the values for the slope m and intercept q of the best-fit line were obtained [146].

To provide a reference for the calibration process, the strain gauge was initially connected through a NI 9944 bridge completion module to a NI 9237 24-bit bridge analog input acquisition card, which was known from past experience to provide noiseless and

accurate strain readings. The resulting acceleration/strain data are plotted in Fig. 4.18a, together with the corresponding linear regression line. It can be seen that a linear relationship exists between strain and acceleration levels, with a correlation coefficient of 1. The calibration relationship thus obtained from the NI system between strain and acceleration is

$$q_\varepsilon = m_\varepsilon q_{acc} + q_\varepsilon = 173.98 q_{acc} - 0.11 \quad (4.3)$$

where q_ε is the measured strain in $\mu\varepsilon$, q_{acc} the acceleration in g , and m_ε and q_ε are the slope and intercept of the regression line, respectively.

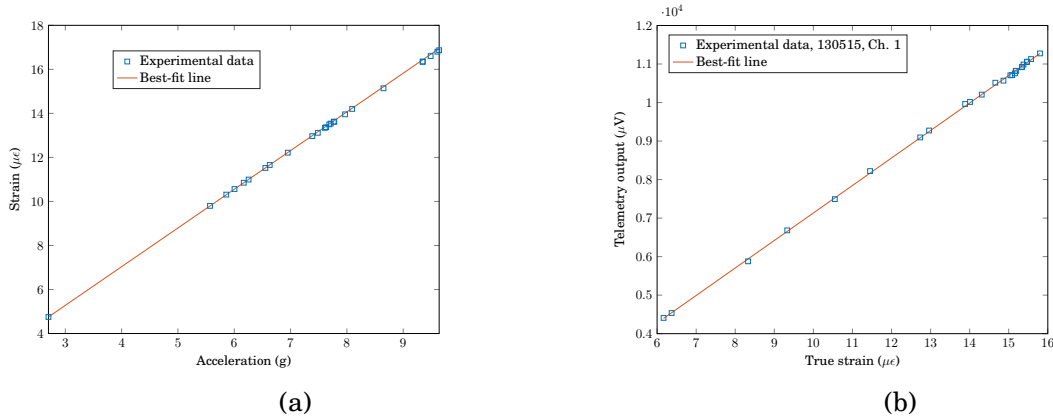


Figure 4.18: Calibration of the telemetry modules: a) Preliminary calibration using NI bridge completion system; b) Calibration plot for the telemetry system.

Eq. 4.3 was then used in the following tests with the telemetry system: the measured accelerations were substituted in Eq. 4.3 to derive the corresponding “true strain” values q_ε ; these calculated strains were then plotted against the voltage output from the telemetry, and again a best-fit line was obtained. The results of the procedure are shown in Fig. 4.18b for one of the modules. Values for slope m and intercept q were calculated and are shown in Table 4.5 for all modules. They provide the calibration data for the telemetry outputs with regards to each channel, according to the calibration relationship

$$q_{\mu V} = m q_\varepsilon + q,$$

where $q_{\mu V}$ is the voltage output from the telemetry, and q_ε the calculated “true strain”.

While these two parameters allow to eliminate the measurement bias of each module, random error also needs to be quantified to verify the repeatability of the measurements. The chosen parameter is the standard deviation of the value of the true strain s_{q_ε} . Assuming a Gaussian distribution for the error, taking a value equal to three times the standard deviation of q_ε as the error measure means that the true value of the strain will be obtained 99.7% of the time [146]. The maximum measurement error in this case can then be quantified as $0.3 \mu\varepsilon$ ($3s_{q_\varepsilon}$) from Table 4.5.

Fig 4.19a shows the spectrum of the response of the beam in one of the calibration tests presented above (single-frequency shaker excitation at 327 Hz). It can be seen that the spectrum contains several frequency components. However, as the test piece is a slender

Table 4.5: Calibration parameters for the telemetry modules.

	\mathbf{m} ($\mu\text{V}/\mu\epsilon$)	\mathbf{q} (μV)	$\mathbf{s}_{q\epsilon}$ ($\mu\epsilon$)
130515 Ch. 1	713.79	-5.03	0.047
130515 Ch. 2	710.00	-111.68	0.024
130515 Ch. 3	708.99	-61.89	0.025
130515 Ch. 4	693.61	56.03	0.10
130516 Ch. 1	704.37	-25.69	0.014
130516 Ch. 2	693.17	-89.97	0.027
130516 Ch. 3	701.91	-98.34	0.031
130516 Ch. 4	704.37	-25.69	0.014
130521 Ch. 1	1149.02	97.80	0.067
130521 Ch. 2	1147.25	-11.50	0.043
130521 Ch. 3	1144.37	50.63	0.054
130521 Ch. 4	1145.12	-80.77	0.023

linear beam excited in pure bending, only one frequency line would be expected at 327 Hz, which is confirmed by the measurement performed with the NI system described above (Fig. 4.19b). Comparison with further experiments indicates that most of the frequencies are electronic noise in the telemetry system, as they are very coherent (the two highest lines always appear at 2327 Hz and 4654 Hz). Since it was not possible to eliminate this noise on the hardware side, it was decided to neglect all frequency lines besides the one corresponding to the excitation. This was considered acceptable, as the noise appears only at very specific, well spaced frequencies, and can be separated clearly from the excitation signal.

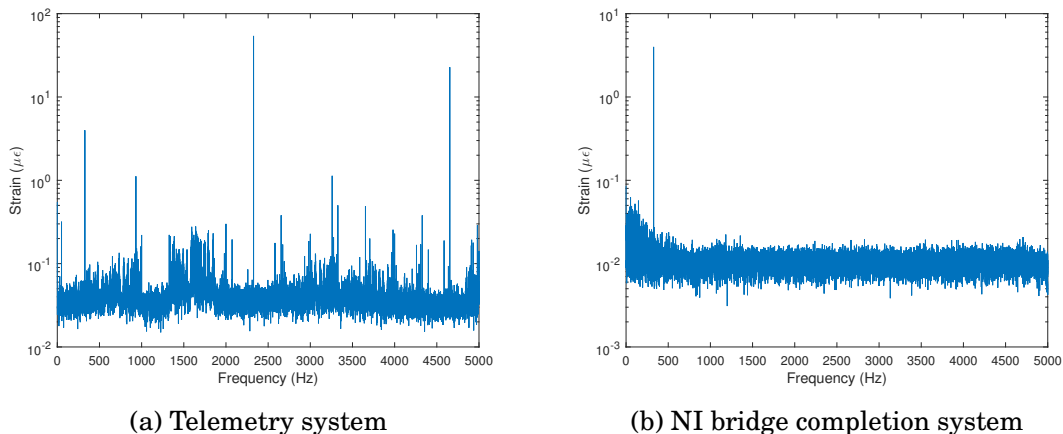


Figure 4.19: Comparison between the strain spectra in the calibration beam with single-frequency excitation (327 Hz).

4.8.4.2 Interaction between strain gauges and MFC actuators

MFC patches operate at voltages in excess of 100 V, and are a potential source of spurious voltages by electrostatic/electromagnetic induction. Large errors in the strain gauges, which typically produce output voltages in the order of microvolts, can therefore be introduced. To ensure the accuracy of the strain measurements, the issue was thoroughly investigated in a simple test configuration.

A mild steel beam (70 mm×505 mm×3 mm) was equipped with two M-2814-P2 MFC actuators, placed at a line of high strain for the the first five bending modes ($z=212$ mm). Three strain gauges were attached to the beam (Fig. 4.20) at the same longitudinal position z , one on the same side as the MFC patches, on the mid-line of the beam, and the other two in line with the midpoint of the patches, on the opposite side. The beam was suspended in free-free configuration by fishing wires, and grounded via a copper wire. The strain gauges were connected to one of the telemetry modules.

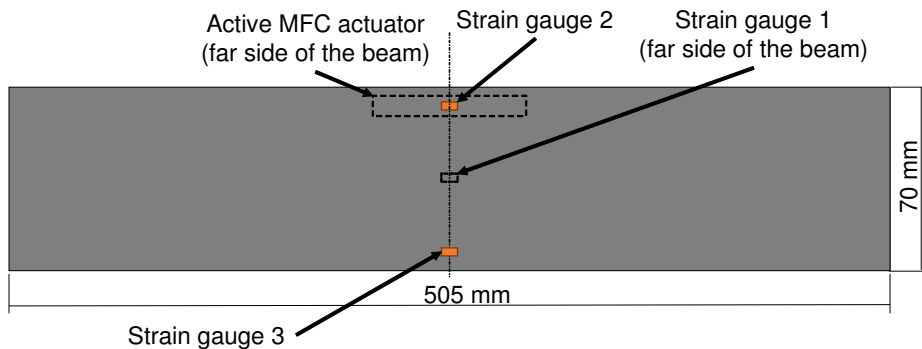


Figure 4.20: Test beam and positions of strain gauges and MFC actuator (dimensions not to scale) for the study of electrical interference in the strain gauges from the piezoelectric actuators.

Stepped-sine sweeps around the 3b resonance were performed by using first an electromagnetic shaker to provide reference data, without the influence of the driving voltage for the MFC patch. The resulting FRFs are shown in Fig. 4.21a. The three strain gauges, placed at the same position along the length of the beam, produce the same amount of strain as expected.

In the second test set-up, the MFC patch and strain gauges were both connected to their respective instrumentation via plain hookup wires. The gauge wires were tightly braided to protect them against electromagnetic interference, as equal and opposite voltages tend to be induced in the gauge leadwires, thus cancelling each other out [147]. The beam was excited via the MFC patch at the full range allowed by its amplifier, -50 V to +250 V. As can be seen in Fig. 4.21b, the three FRFs are widely different. FE simulations showed that the localised strain introduced by the piezoelectric patch would not be high enough to cause significant differences between the gauges. This pointed to a pronounced influence of electrostatic or electromagnetic noise, either in the wires, or the beam itself.

To minimise this effect, the plain MFC actuator wires were replaced by a shielded cable: the leadwires, which are twisted, are also wrapped in aluminium foil. The foil acts as a

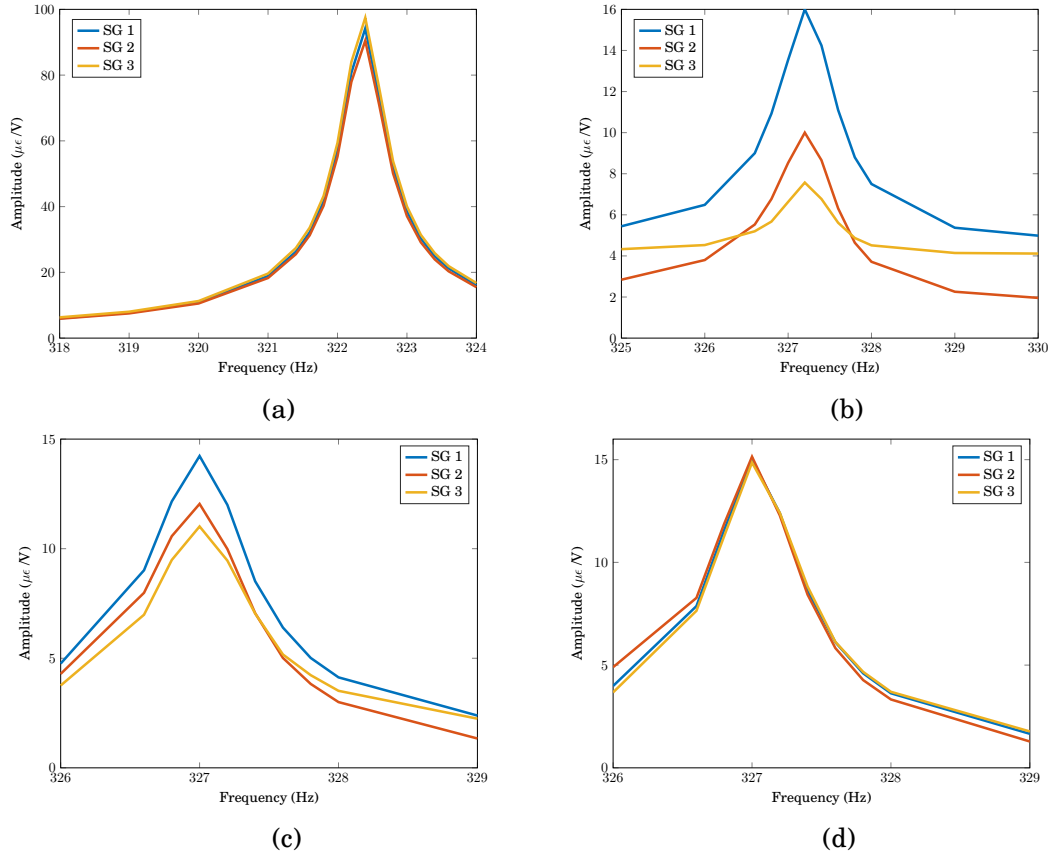


Figure 4.21: Investigation of the interaction between piezoelectric patches and strain gauges. FRFs around the resonance frequency for the third bending mode of the test beam: a) shaker excitation; b) MFC actuator, plain twisted wires; c) shielded cable for the MFC patch, shield not grounded; d) shielded cable for the MFC patch, shield grounded.

Faraday cage, where the charges induced by electrostatic fields accumulate, and can then be discharged to ground, thus shielding the wires inside and outside. For the third test, however, the shield was not connected to ground. In this case, the FRF of strain gauge 1, which is glued on the same side as the MFC patch, is again much larger than the other two (Fig. 4.21c). Strain gauge 2 and 3, both located on the other face of the beam from the patch, show remarkably closer values, suggesting that the actuator noise seems to display a surface effect. As a last step, the cable shield was connected to ground. Fig. 4.21d shows that the three FRFs finally overlapped.

This test campaign highlighted that piezoelectric patches constitute a strong noise source when used in combination with strain gauges. In particular, no noise relief was found by simply twisting the leadwires, which is the standard method to cancel electromagnetic interference. Perfect results, on the other hand, were achieved by simply shielding the actuator leadwires, and grounding the shield itself. This suggests that most of the noise was actually electrostatic.

For these reasons, special cables (Industriafil TAU UAA3407 and UBA3219) were used for the final test piece, both for the strain gauges and the MFC actuators. They are twisted and shielded by a silver-plated copper braid. They are also extremely compact, with a

maximum diameter of 1.43 mm, and a linear density of 3.9 g/m, minimising mass loading of the specimen.

4.9 Summary

A new test rig has been developed to study the effects of rotation on bladed discs, and to provide validation data with regards to the Coriolis effect. The acquisition of operational deflection shapes is guaranteed by an array of strain gauges, whose signals are transmitted via wireless telemetry to the data acquisition system. Excitation is provided by MFC piezoelectric actuators that can be individually controlled, thus allowing the generation of arbitrary forcing patterns, including engine-order travelling waves. The rig can operate in vacuum to avoid undesired aerodynamic excitation and damping, and the risk of flutter.

A test piece, in the form of a laser-cut blisk, with eight blades bent 90° out-of-plane, was designed to enhance the frequency splits and travelling-wave modes produced by the Coriolis force. Modal tests showed that the chosen manufacturing method successfully minimised mistuning for the 3ND mode, and that mistuning itself was not significantly modified by the addition of the piezoelectric actuators and strain gauges. Damping was affected, but low values were still measured.

A series of commissioning tests were conducted to ensure the safe and accurate operation of the rig. The rig itself does not exhibit dangerous resonances in the operational speed range of the motor. It was verified that piezoelectric actuators can induce high-level responses in a linear range, and selectively excite the wanted modes. The strain gauges and telemetry system were calibrated, and the electrostatic interference they suffered from the high-voltage excitation signal for the piezoelectric patches was successfully eliminated by employing shielded leadwires.

Chapter 5

Frequency Response Function measurement in rotating bladed discs

5.1 Introduction

The capability of MFC actuators to produce responses with good SNR has been shown in the previous chapter. One outstanding question is whether they are usable in a modal analysis context, where knowledge of the excitation is the foundation for the derivation of FRFs and the extraction of damping, natural frequencies, and mode shapes.

The methods of Operational Modal Analysis (OMA), where these same variables are extracted from the response alone, have gained robustness and reliability in recent years. It could be reasonably argued that OMA could be applied with piezoelectric actuators, as the real value of the excitation they introduce can only be known indirectly. Mounting parameters that can only be controlled within the relatively loose tolerances of manual application, such as the thickness of the adhesive layer, and the orientation of the patch, can also affect the efficacy of the applied forcing.

However, the control voltage to the piezoelectric patches can be accurately known, both in amplitude and phase, thanks to the synchronisation procedure described in sect. 4.7.2. This gives an important piece of information on the excitation level, which cannot be dismissed. Furthermore, in sect. 2.5.3, it was found that, with reasonable assumptions, a FRF expression where voltage behaves as a traditional force can indeed be found.

The possibility of using the input voltage to the piezoelectric actuators as a forcing term was therefore investigated, and will be presented in this chapter. Several different forcing patterns will be explored, with a special emphasis on MIMO random excitation, and the quality of the FRFs and the extracted modal parameters assessed. The measured FRFs will also be used to discuss the dependence of their characteristics on rotational speed.

5.2 Piezoelectric excitation for modal analysis in rotating structures

5.2.1 Stepped sine excitation

Sinusoidal excitation is one of the principal means of modal analysis, thanks to the high-energy forcing it can provide, and its consequent high SNR, and was tested first. The blisk presented in sect. 4.8.2 was excited by a single MFC patch at sector 1, and the response was acquired in different conditions, i.e. at rest and under rotation. The excitation frequency was incremented in steps around the first 3ND resonance frequency, and the signals were recorded after any transients due to the step change had died out.

Fig. 5.1 shows the derived FRF characteristics at rest using three different sensors: an accelerometer attached on top of the active piezoelectric patch; a LDV pointed to the right of SG 3; and SG 3 itself (Fig 4.14a). As expected, the amplitude of all FRFs shows a peak at resonance. Perhaps more interestingly, the phase of the FRFs (Fig. 5.1b) displays exactly the behaviour that would be expected with a traditional excitation source: the phase of the acceleration FRF starts at 180° off resonance, decreases to 90° at resonance, and stabilises at 0° . The velocity FRF, on the other hand, varies from -90° to 90° . Finally, the SFRF goes from 0° to 180° .

This is confirmed by the Nyquist plots of Figs. 5.1c–5.1d, where the FRF from the accelerometer is contained in the first and second quadrant, as the real part changes sign at resonance. For the velocity, it is the imaginary part to do so, and its Nyquist plot is contained in the second and third quadrant.

5.2.2 Multiple-Input Multiple-Output random excitation

Random excitation is widely used in modal analysis: it is relatively easy to produce, and with its broadband characteristics, can yield a complete spectrum in a comparatively short time. It also lends itself to multiple-input configurations, as it is easy to generate uncorrelated input signals, and obtain a well-conditioned form for the FRFs. One known issue with random excitation is the leakage due to the non-zero signal levels at the start and end of the acquisition: this introduces a bias in the FRF estimation that only a large number of averages and a fine frequency resolution can limit, without eliminating it (sect. 2.4.3). Other broadband forcing types, such as burst random and chirp, are therefore normally preferred.

In the present case, however, due to the background noise already present in the strain gauge telemetry, and the decision to limit the use of filters, leakage would not be avoided by any alternative means. Pure random excitation was therefore used to drive all the eight MFC actuators, while the response signals were acquired by both strain gauges, and, at rest, by LDV. The input voltage signal was offset so to exploit the full range offered by the chosen MFC patches and amplifiers ($-50 \div 250$ V, see sect. 4.8.3.2), and maximise the forcing energy. In every test, the acquisition length guaranteed a frequency resolution in

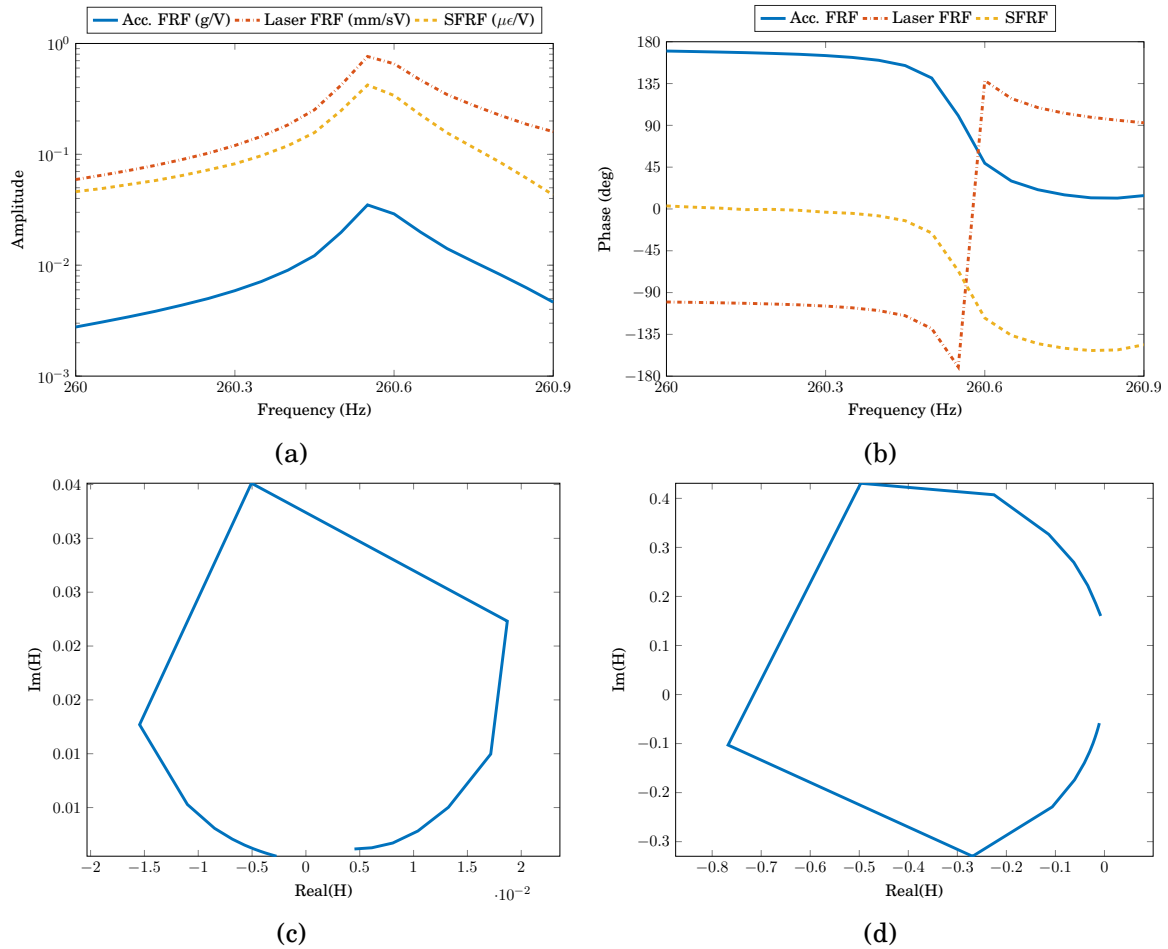


Figure 5.1: Characteristics of the response of the blisk in static conditions with sinusoidal single-input piezoelectric excitation: a) amplitude of the velocity and acceleration FRFs, and SFRF; b) phase; c) Nyquist plot of the velocity, and d) of the acceleration FRFs.

the resulting spectrum of at least 0.15 Hz, and 100 averages were taken. This led to a maximum measurement time of 50 minutes at each speed for a 5-kHz frequency range, against the 45 minutes required in the stepped-sine test for a maximum range of 10 Hz.

Fig. 5.2 shows the resulting FRFs, and the curve-fitting process used to extract natural frequencies and damping. LDV data was used to both provide an upper boundary to the accuracy of the curve-fitting procedure, due to their high quality, and to compare the modal data derived from a traditional acquisition method to the strain data, which are rarely used for modal analysis purposes.

Fig. 5.2a shows the stabilisation diagram (sect. 2.4.4) for the MISO test, where all the MFC patches are active, and velocity at point 3 (Fig 4.14a) is measured via LDV. The frequency range of interest is 160 ÷ 320 Hz, where the first four nodal diameter modes lie. The diagram is remarkably clear, with no spurious computational poles found. Stable poles are identified only at the actual resonance frequencies of the blisk, and stability in both frequency and damping is reached at very low model orders (below 10) for the lightly damped modes (2ND ÷ 4ND), and after order 20 for the 1ND and 0ND modes.

This can be better appreciated in Fig. 5.2b: modes 2ND ÷ 4ND all exhibit sharp peaks,

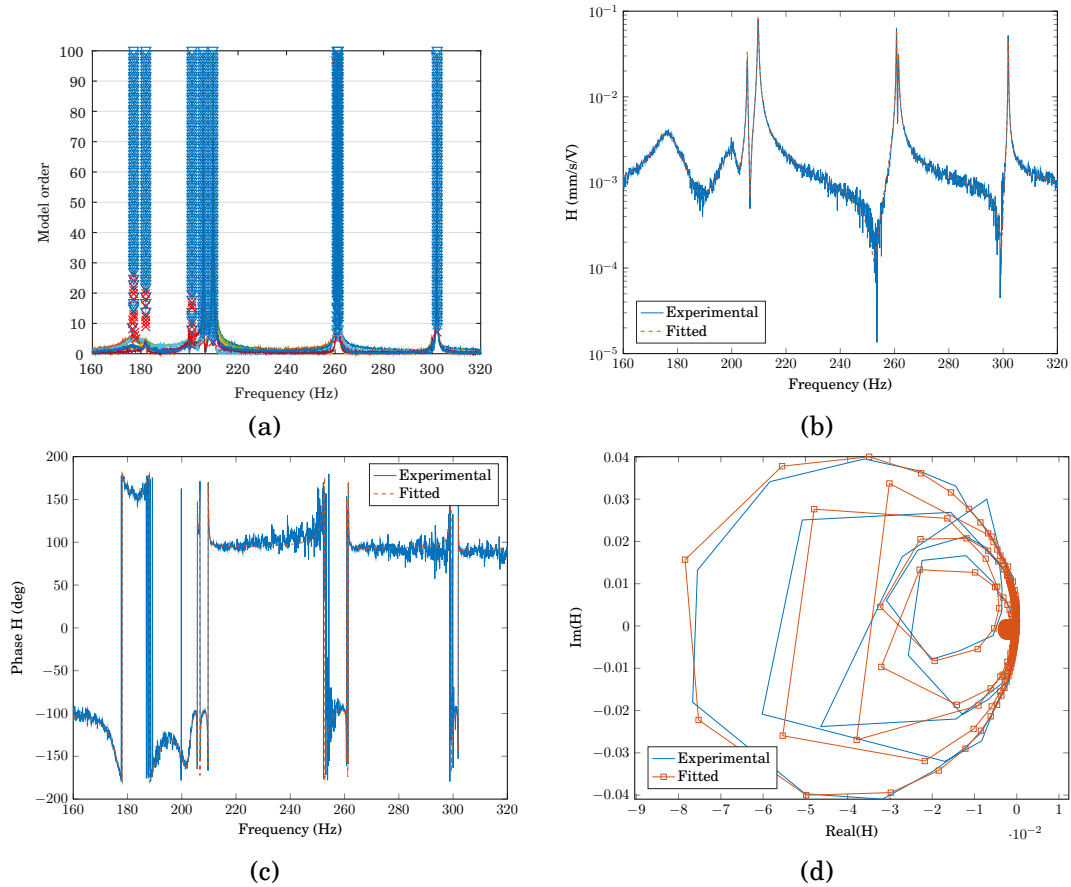


Figure 5.2: Curve-fit results with laser and MIMO random excitation: a) stabilisation diagram; b) magnitude of the velocity FRF in the 160÷320 Hz frequency range at rest; c) phase, and d) Nyquist plot

while 1ND and 0ND are still well visible, despite being noticeably more damped. The FRF captures the frequency splits due to mistuning (Table 4.4) in the 2ND and 3ND modes, where the difference in frequency is just 0.7 Hz, as opposed to the 4 Hz of the 2ND peaks. The features of the FRF are also well-defined, both in amplitude, and in phase (Fig. 5.2c), with noise mainly concentrated close to anti-resonances, which are still clearly identifiable. The FRF data resulting from the poly-reference curve fit are overlaid on the experimental data, and show very good agreement. In particular, the areas of the fitted circles in the Nyquist plots (Fig. 5.2d) closely match those of the experimental FRFs, which indicates a good estimation of damping.

The same procedure was followed with the strain gauge data, and a representative stabilisation diagram and FRF fit appear in Fig. 5.3. The stabilisation diagram is still very clean: poles are again only found at the actual natural frequencies of the system. Because of the lower SNR, however, they stabilise at higher orders with respect to the laser data, with stable values for both frequencies and damping at orders above 40 for all modes. As better seen in Fig. 5.3b, the 0ND mode is barely visible in the noise, but it is still identified by the poly-reference algorithm, although its modal parameters only stabilise at very high model orders.

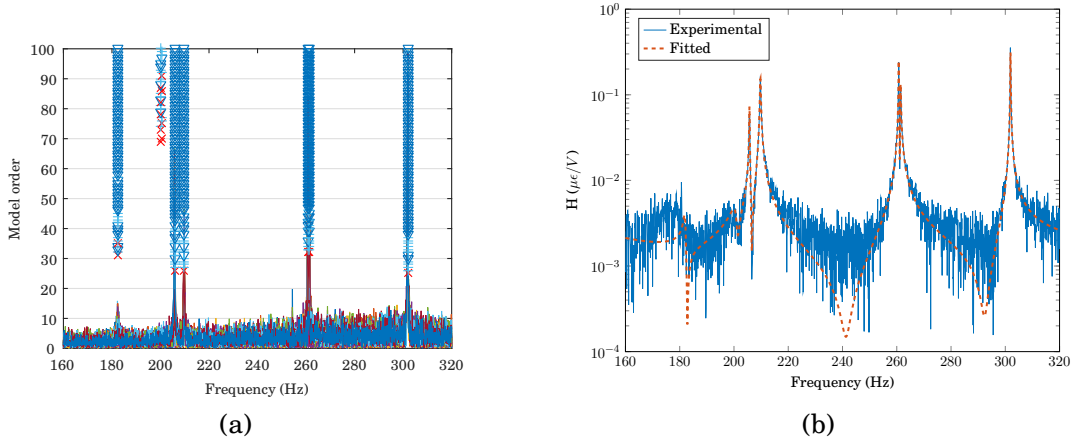


Figure 5.3: a) Stabilisation diagram from strain gauge data at rest, and b) representative SFRF and fit.

Due to the significant noise levels, it is now difficult to identify features in the FRF besides the resonance peaks, and anti-resonances disappear under the noise floor. However, around resonance, the fitted FRF still follows the experimental data, and the curve-fit process manages to discriminate the two close 3ND modes. A clearer indication of the quality of the FRFs comes from assessing its multiple coherence. The multiple coherence $\gamma_{X_i:F}^2$ is a measure of the quality of a FRF estimate, and describes the correlation between each output X_i and all the inputs F . Using the symbols of sect. 2.4.3, the $\gamma_{X_i:F^2}$ is defined as [113]

$$\gamma_{X_i:F}^2(\omega) = \frac{\sum_{j=1}^{N_i} H_{ij}(\omega) G_{X_i F_j}(\omega)}{G_{X_i X_i}(\omega)}$$

where $G_{X_i F_j}$ and $G_{X_i X_i}$ are the cross-spectrum between the measured, noise-contaminated, output X_i and j -th input F_j , and the auto-spectrum of the output X_i , respectively, at each frequency ω .

The multiple coherence between the laser velocity output and the input voltage to the MFC actuators is plotted in Fig. 5.4a. The coherence values are nearly always above 0.7, which indicates a fair quality of the overall FRF, even far from resonance. Very low coherence can be found only at discrete frequencies, namely 200 Hz, where a spurious peak appears in the FRF of Fig. 5.2b, indicating interference from mains noise, and around 300 Hz, where both mains noise and an anti-resonance are present.

The multiple coherence for the strain gauge data appears in Fig. 5.4b. Coherence values above 0.8 can be observed even for the 400-Hz frequency cluster, where the SNR is lower than in the 160÷320 range. As could be anticipated from Fig. 5.3b, the coherence drops below 0.2 everywhere else, making the SFRF data outside the resonance regions unusable. Fig. 5.4c shows a magnified view of the coherence in a close neighbourhood of the 3ND split resonance for SG 3: coherence is above 0.7 in the whole range, and reaches 0.9 at the resonance peaks. These data indicate that reliable modal analysis can still be conducted from these SFRFs, as the useful range for the extraction of modal parameters is usually limited to the resonance regions.

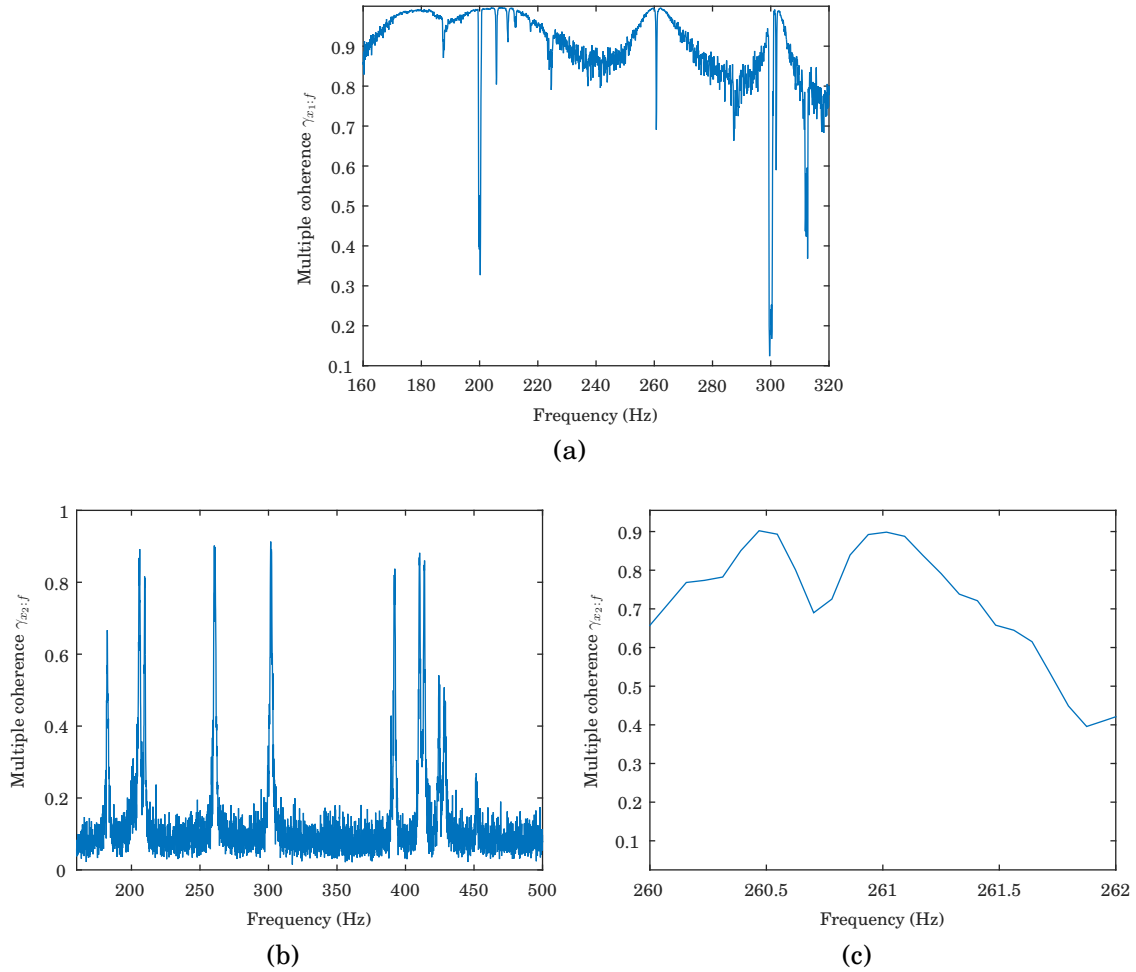


Figure 5.4: Multiple coherence at rest: a) laser data, b) SG3 3, and c) zoom on the frequency range around the 3ND split resonance for SG 3.

The modal parameters extracted from the SFRFs were then compared to those extracted from the laser velocity FRF data. This comparison serves two main purposes: on the one hand, it is necessary to verify that the modal model developed in sect. 2.4.2 is indeed correct; on the other, that the noise in the strain FRFs does not invalidate the modal parameter extraction.

The values of the resonance frequency and damping for the first 4 nodal diameter modes, as extracted from the laser and strain data, is reported in Table 5.2. First of all, it can be seen that the laser frequencies agree very closely with the ones found from traditional hammer tests in Table 4.4. As anticipated, the 2ND, 3ND, and 4ND modes are very lightly damped, with a maximum ξ of 0.075%. The 1ND-1 and 0ND modes, on the contrary, exhibit high values, with 2.077% and 1.377% respectively. The coupling of these two mode families with the shaft dynamics is probably the origin of this behaviour, as the shaft is heavily damped by the greased bearings.

The frequencies found using the strain gauge MIMO data coincide nearly perfectly with the laser ones, although they do not allow the identification of the 1ND-1 mode frequency, due to the high noise levels. In spite of these, however, the damping values agree closely.

Table 5.1: Comparison of frequency and damping values from laser and strain gauges data at rest (MIMO).

	Laser		Strain gauges	
	Frequency (Hz)	ξ (%)	Frequency (Hz)	ξ (%)
1ND	177.0	2.08	-	-
	182.0	0.28	182.0	0.23
0ND	200.9	1.38	200.8	0.51
2ND	205.7	0.04	205.7	0.04
	209.7	0.08	209.7	0.08
3ND	260.7	0.03	260.7	0.02
	261.4	0.04	261.4	0.04
4ND	301.9	0.02	301.9	0.02

The only significant difference is the 0ND mode, where the SFRFs predict nearly a third of the ξ found from the laser FRF. This is again predictable, since the 0ND mode has very little SNR. This comparison thus shows that, with the present test set-up and SFRF model, strain gauges can be reliably used to extract frequency and damping data for lightly damped modes.

The quality of the raw SFRFs and curve-fit in rotating conditions was verified next, to check the effect of the additional noise coming from the bearings, interaction with the test rig, aerodynamic excitation, etc. For brevity, only the frequency range around the 3ND mode is shown in Fig. 5.5, as it will be the main focus of the mode shape validation in the next chapter. The SFRFs shown were derived at 300 rpm, which, belonging to the high end of the rotational speeds tested for this project, could provide a representative lower bound for the SFRF quality.

Contrary to what observed in Fig. 5.3b, however, not only the resonance peaks, but also the inner anti-resonance are visible already in the raw SFRF (Fig. 5.5a). The curve-fit approximates both amplitude and phase (Fig. 5.5b) very closely, as shown by the Nyquist plot (Fig. 5.5c).

It may seem counter-intuitive that data from a noisier environment (rotating configuration) should be of better quality than those measured in an “ideal” set-up (still configuration). A possible explanation comes from the different frequency bandwidth of the excitation in the two configurations. During the stepped-sine tests, the sampling frequency of the analog output card used to generate the control voltage to the piezo was set at 20 kHz, to maximise the smoothness of the excitation signal, and avoid jerk. This setting was kept during the first random tests, and was later halved because the DAQ PC started having difficulties keeping such a high output generation rate for eight channels simultaneously. Since the maximum allowed amplitude of the voltage was not changed, the same excitation power was now spread across half the bandwidth, thus producing a more effective forcing, hence better quality SFRFs.

The Frequency Response Assurance Criterion (FRAC) provides a more quantitative

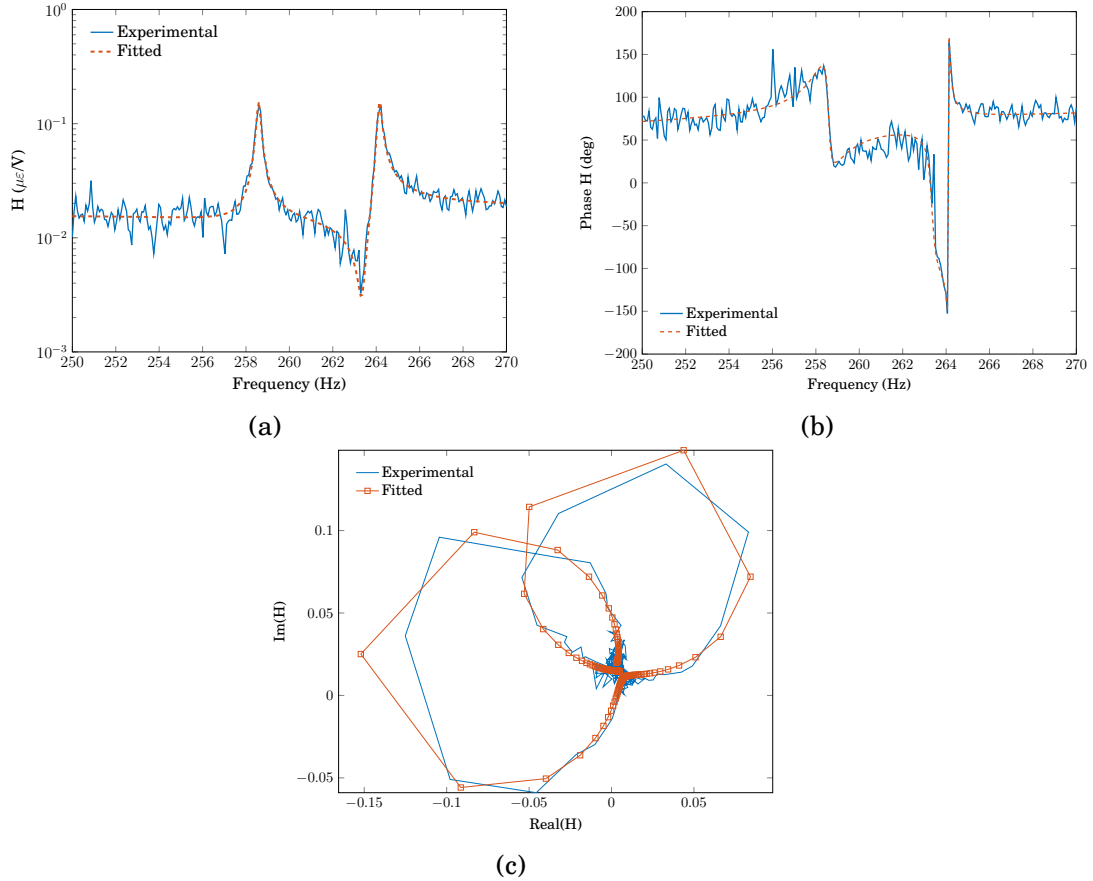


Figure 5.5: Curve-fit results from strain gauge data at 300 rpm: a) magnitude of the SFRF in the 250÷270 Hz frequency range, b) phase, and c) Nyquist plot.

evaluation of the goodness of the fit. The FRAC is defined as [27]

$$FRAC_{ij} = \frac{\left(\hat{H}_{ij}^H(\omega) H_{ij}(\omega) \right) \left(\hat{H}_{ij}^H(\omega) H_{ij}(\omega) \right)^*}{\left(\hat{H}_{ij}^H(\omega) \hat{H}_{ij}(\omega) \right) \left(H_{ij}^H(\omega) H_{ij}(\omega) \right)},$$

where $\hat{H}_{ij}(\omega)$, $H_{ij}(\omega) \in \mathbb{C}^{N_f \times 1}$ are the estimated and measured FRFs, respectively, at output DOF i and input j , and N_f is the number of frequency lines. It is easy to see that the FRAC is analogous to the MAC, and is a measure of the correlation between different sets of FRFs, in this case, the experimental and fitted ones: while less straightforward to interpret than the MAC, a FRAC close to 1 is still evidence of good correlation. Usually the FRAC compares the FRFs at different output DOFs (different lines of the FRF matrix): here, the FRAC is presented as a matrix in Fig. 5.6, to take into account the different *input* DOFs (different rows of the FRF matrix), and extend it to a MIMO context. The colour scale was limited to the 0.8÷1 range to enhance contrast.

The FRAC is above 0.8 for all input/output combinations, which indicates a good level of fit. This is especially important since it was not calculated just around resonances, where SFRF quality has been shown to be acceptable, but along the whole 190÷305 Hz range, thus taking into account regions of very low SNR.

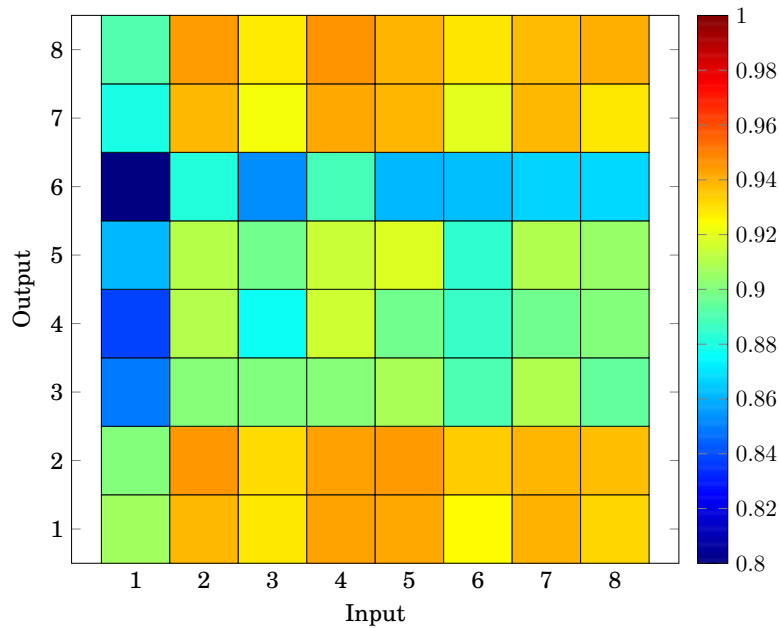


Figure 5.6: Frequency Response Assurance Criterion (FRAC) between the experimental MIMO random SFRFs and the fitted ones at 300 rpm, in the 190÷305 Hz frequency range.

It is interesting to notice a rather stark contrast between two groups of SGs, belonging to sector 1÷2 and 7÷8 on one side, and sectors 3÷6 on the other. In the first case, the FRAC is included between 0.92 and 0.95, while in the second, between 0.86 and 0.92. Since these two groups of SGs were connected to different telemetry modules, it is plausible that differences in their noise levels affected the resulting SFRFs, since noise would be the primary reason for a small, yet noticeable, deviation between real and fitted SFRFs.

Similarly, a lower FRAC for input 1 (MFC actuator nr. 1) indicates a possible issue in its mounting or electrical connection. From this point of view, however, it is reassuring to see that all other inputs show very similar FRAC values, suggesting that overall the differences between the MFC patches do not affect significantly the quality of the SFRFs.

Multiple Coherence was calculated in this rotating case as well, and is shown in Fig. 5.7. On average, coherence is higher than 0.4 in the whole 160÷500 Hz range, and peaks higher than 0.8 around resonances are visible. Zooming in around the 3ND frequency split, it is possible to see that coherence stays above 0.6 even at the anti-resonance between the peaks.

5.2.3 Impulse excitation

Hammer testing is one of the most used forms of modal testing due to its simplicity, and quickness: the hit of the hammer approximates a Dirac pulse, which can excite a large frequency range, allowing the recovery of a full spectrum with a very short test. When executed manually, however, uncertainties arise from the inevitable imprecision in the location, orientation, and energy of the impact: this lowers the precision of the FRF estimates, and obtaining precise results can become time-consuming. Piezoelectric actuators, on the other hand, have the potential to produce high-coherence results, as they are permanently

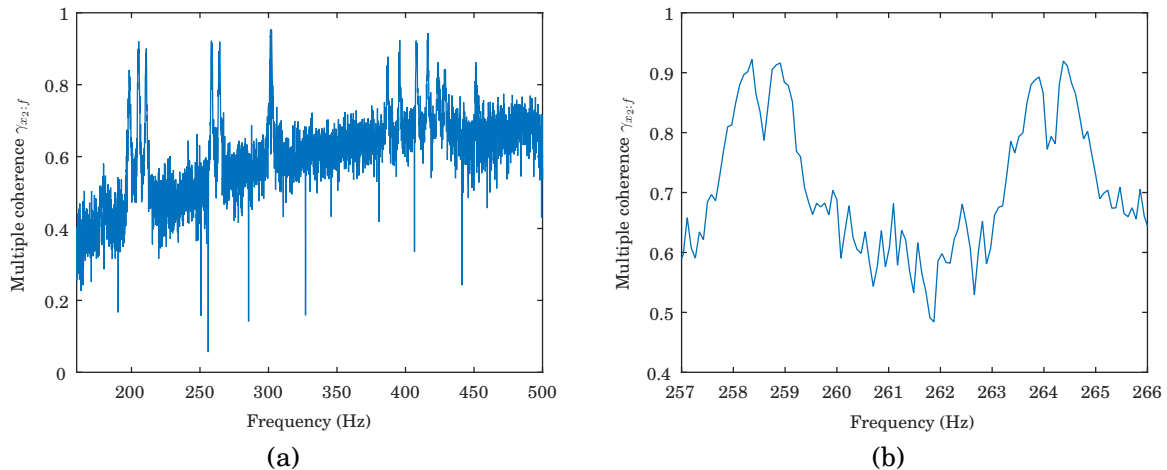


Figure 5.7: Multiple coherence for strain gauge data at 300 rpm: a) 160 ÷ 500 Hz frequency range, and b) zoom on the frequency range around the 3ND split resonance.

attached to the structure under test. In this section, the possibility to generate an impulse with the MFC actuators to conduct a transient measurement on the blisk will be explored.

In this case, the “impact” would actually consist in a strain pulse induced by a voltage impulse signal in the patch. This set-up was put to the test by producing a half-sine impulse at one of the patches. Its duration was kept at 4 ms, simulating a rather soft impact hammer tip, to avoid harmfully exciting the dynamics of the amplifier electronics. The maximum amplitude was kept at 190 V, below the 250 V limit, to protect the MFC patches in case of large oscillations of the signal from the amplifiers.

Fig. 5.8a shows the actual time signal at the amplifier output, and Fig. 5.8b its frequency spectrum. Due to the characteristics of the chosen impulse, it can be seen that the excitation starts at a low level (-70 dB ca.), and decreases quite quickly, although the whole usual frequency range of interest (160 ÷ 320 Hz) is covered by the main lobe. While the low excitation problem may yield SNR issues, it also means that the blisk could be excited in the linear range.

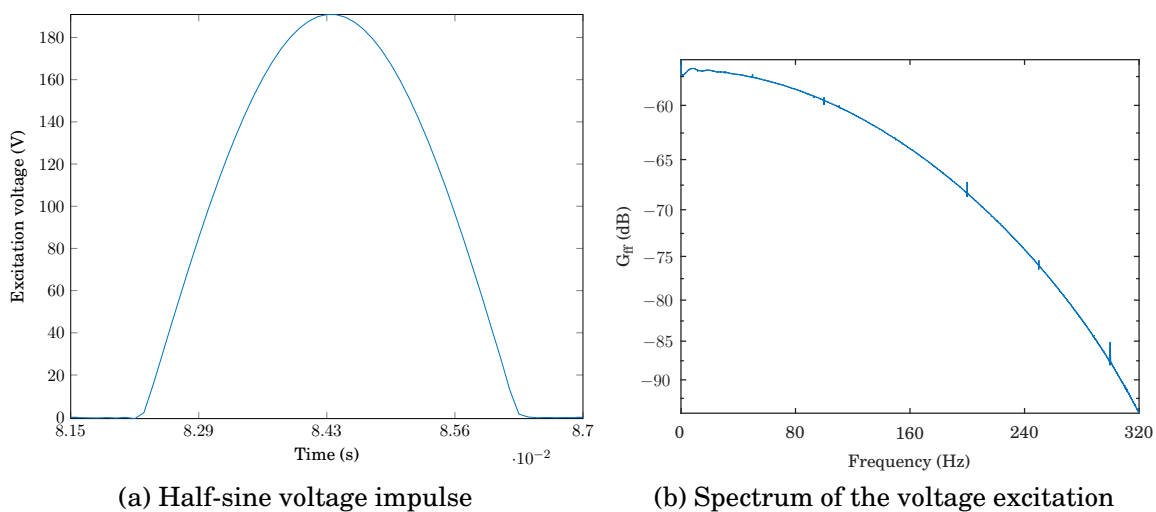


Figure 5.8: Impulse voltage excitation to the MFC actuators. The pulse width is 4 ms.

Because of the limited energy that could be introduced in the system, strain gauges could not be used for this test, and measurements were taken only by LDV, to exploit its high sensitivity. Fig. 5.9 shows a typical raw velocity time signal: a very clear decaying pattern is present in the response, even when not using the maximum sensitivity level allowed by the available LDV (25 mm/sV instead of 5 mm/sV).

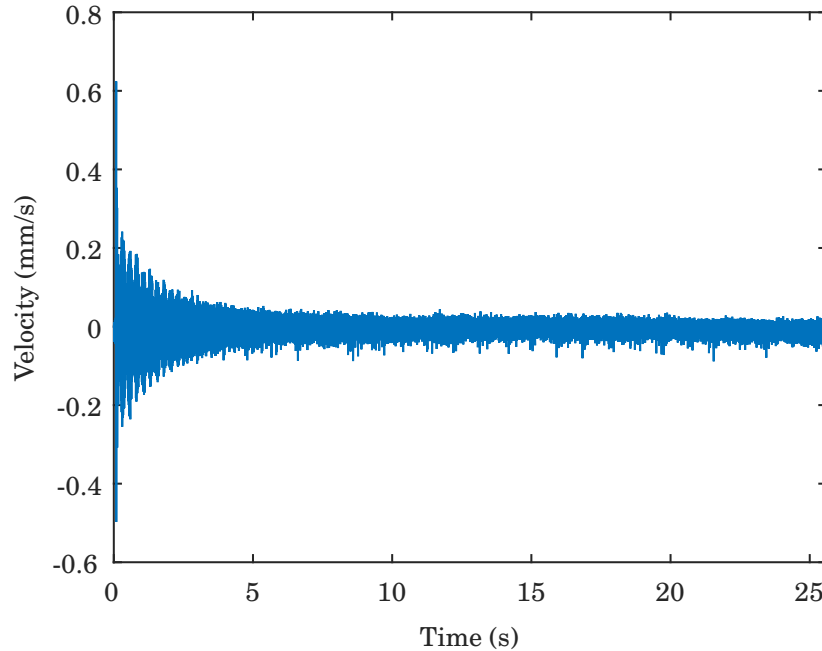


Figure 5.9: Time signal of the laser response with impulse excitation (no window applied).

A mix of residual vibration and noise is present up to and after the end of the blocksize. To avoid leakage, an exponential window was applied to the raw time signals. It is important to note that this window was applied to both the response and the input, so that the additional damping introduced by the window could be eliminated, and the true damping ξ retrieved according to the following formula [114]

$$\xi = \xi_{win} - \frac{1}{2\pi f_r \tau},$$

where ξ_{win} is the damping obtained from the windowed FRF, f_r is the corresponding resonance frequency, and τ is the window time constant (in this case, 12.8 s).

The FRFs from seven tests were thus processed and averaged, and the result is shown in Fig. 5.10a. The FRF displays distinct resonance peaks and anti-resonances, where the major influence of the noise is concentrated. Spurious peaks at 200 Hz, 250 Hz and 300 Hz are also present, and derive from electrical noise (50-Hz noise and its higher harmonics are visible in the input voltage spectrum in Fig. 5.8b).

These characteristics are reflected in the coherence (Fig. 5.10b). Its value stays above 0.9 in the whole 160÷240 Hz range, and drops significantly only around the 3ND and 4ND resonances, where the low response levels, accentuated by anti-resonances, and electrical noise predominate.

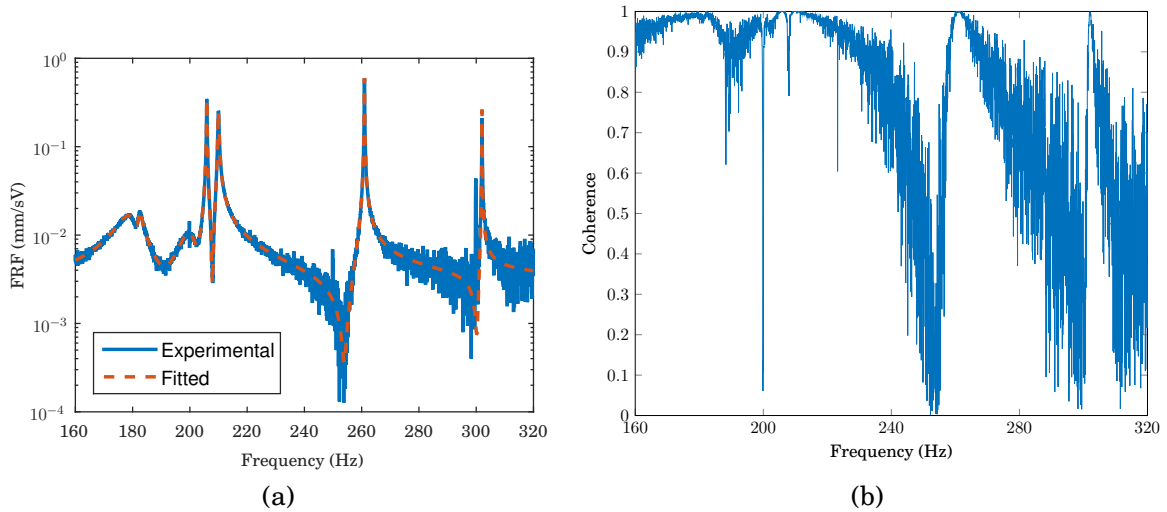


Figure 5.10: Impulse excitation: a) Amplitude, and b) coherence from seven averages of the SFRF of the blisk.

To provide an independent reference for the accuracy of this new application of piezoelectric actuators, the frequency and damping data extracted from the voltage impulse tests were compared to those from a traditional manual impact test, and are reported in Table 5.2. The maximum discrepancy in the extracted frequencies is 1.1%, and it is interesting to notice that, while the piezo-impulse test fails to identify the 3ND-2 frequency, so does the hammer test, as in both cases the excitation point was close to a nodal diameter.

Table 5.2: Comparison of frequency and damping values from traditional hammer and piezoelectric impulse testing.

	Hammer		MFC impulse	
	Frequency (Hz)	ξ (%)	Frequency (Hz)	ξ (%)
1ND	177.5	2.45	179.4	2.26
	182.6	0.16	182.3	0.34
0ND	199.6	1.16	200.6	1.55
2ND	205.8	0.04	205.9	0.03
	209.8	0.08	210.0	0.08
3ND	260.7	0.02	261.0	0.01
4ND	301.9	0.01	302.0	0.01

There is also fair agreement between the damping values, with major differences only for the 1ND-2 and 4ND modes. In the first case, the reason is that the location of the hammer hit/actuator was not optimal for that particular mode, while the second shows that the force input for that particular frequency (-85 dB) was too low for the reliable extraction of modal parameters.

5.2.4 Travelling-wave excitation

As was argued in sect. 4.8.3.1, travelling-wave excitation can be an important forcing pattern in the experimental investigation of bladed discs. A 3EO pattern was therefore reproduced using all the eight MFC actuators installed on the blisk to test its effects and potential, and to analyse the interaction between an external TW excitation, and the TW modes naturally induced by the Coriolis effect.

The 3EO excitation was obtained by driving all the patches with the same sinusoidal voltage amplitude, but the signal to each patch was phase-shifted by

$$\varphi_{exc} = \pm \frac{2\pi EO}{N} = \pm 135^\circ$$

with respect to the preceding sector. A $+135^\circ$ phase shift corresponds to a BW travelling wave, while -135° to a FW wave. The response was measured by the eight circumferential SGs to be able to acquire both the amplitude and the direction of the resulting wave. The tests were conducted at 300 rpm, and the same frequency range ($258 \div 264.4$ Hz) was swept for both wave directions.

While all actuators are active at the same time, the forcing functions are perfectly correlated, and therefore the TW excitation method cannot be considered a proper MIMO configuration. It is possible to reduce the analysis to a SIMO configuration [148], but since this would not lead to a substantially different configuration than the SIMO stepped-sine modal testing described in sect. 5.2.1, only the amplitude spectra were calculated, and they appear in Figs. 5.11a and 5.11b. The relative phases of the SG signals (Figs. 5.11c and 5.11d) were then simply taken as the phase difference between one SG and the one on the immediately preceding sector.

From Figs. 5.11a and 5.11b, it can be seen that the two resonance peaks behave very differently. At the peak corresponding to the TW mode coinciding with excitation direction (henceforth, coincident mode), the amplitude of all the responses is nearly exactly the same. This is a very strong indication that a TW mode has indeed developed: since all DOFs have the possibility of reaching maximum amplitude, it means that the nodal diameters are not fixed in space, and actually travel around the blisk following the excitation. At the coincident mode, the amplitude reached by the strain response is also very high, exceeding $250 \mu\epsilon$: as a reference, the typical strain reached with single-input excitation is around $45 \mu\epsilon$, nearly 6 times smaller.

Theoretically, the peak corresponding to the the TW mode not matching the excitation direction (non-coinciding peak) should be cancelled, since the excitation (proportional to $\cos(\omega t \pm k\theta)$) and response (proportional to $\cos(\omega t \mp k\theta)$) would be orthogonal. The peak, however is still visible (at 258.5 Hz and 264.2 Hz for the $+135^\circ$ and -135° phase, respectively), due to mistuning in the blisk and excitation. However, it is 15 times smaller than the coinciding peak, which proves that TW excitation is highly selective, and can be used to magnify the target mode in regions of high modal density.

This is confirmed by the behaviour of the relative phase between the sectors, as can be

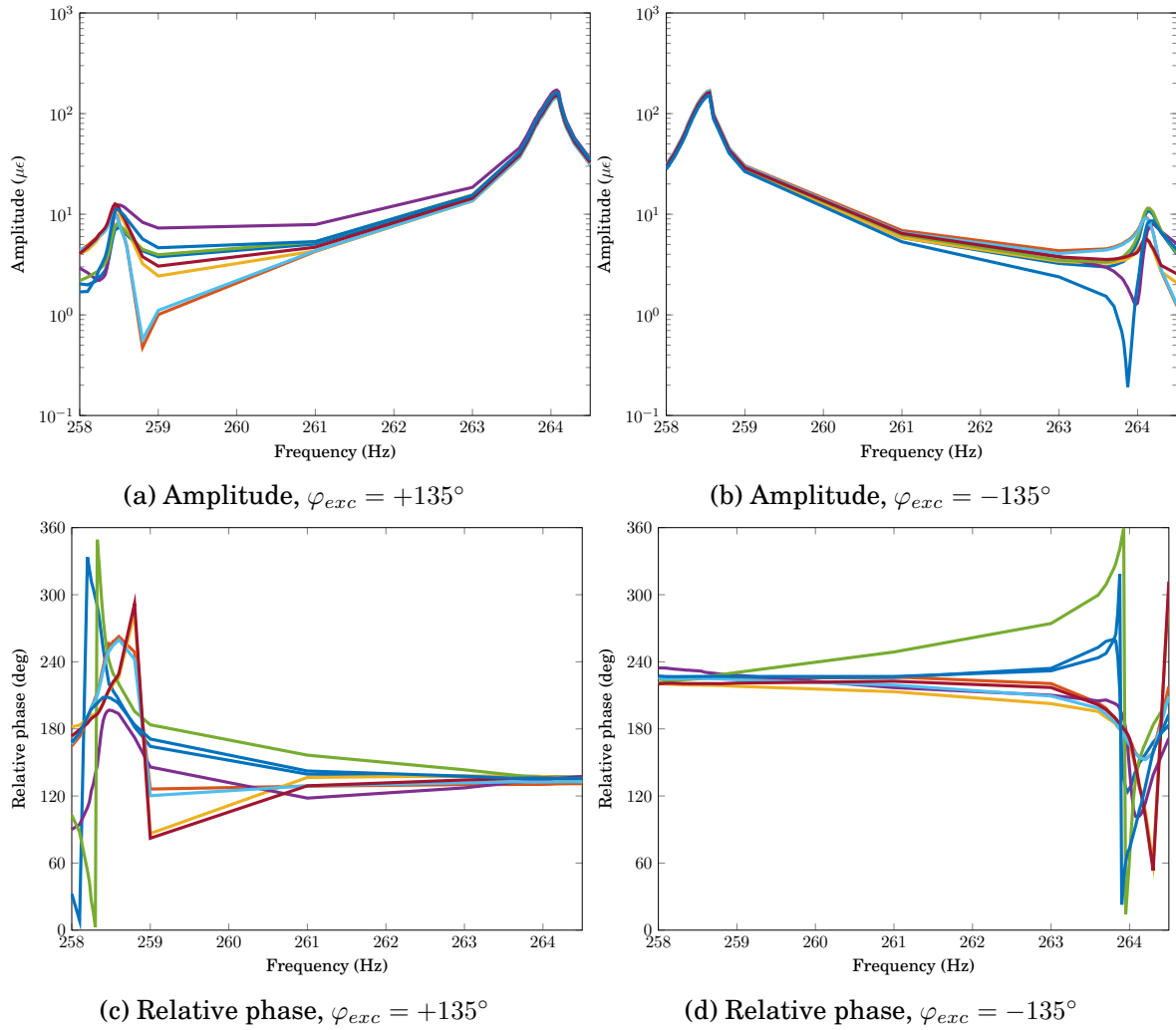


Figure 5.11: 3EO travelling-wave excitation: Strain amplitude and inter-sector angle for the two opposite excitation directions at 300 rpm. Each line corresponds to a different sector.

seen in Figs. 5.11c–5.11d). In both cases, the phase at the non-coinciding peak is scattered around $\pm 135^\circ$, because the TW cannot be properly excited by a non-matching pattern. Far from it, on the other hand, the phase starts converging towards the phase of the excitation, and reaches exactly this value at the coinciding peak. This shows that a full TW has developed, and that it is not simply due to the excitation, but to the Coriolis effect. Without it, it would not be possible to induce a TW behaviour artificially, as demonstrated by the inability of the excitation to cause it at the non-coinciding peak.

5.2.5 Comparison of SIMO stepped-sine and MIMO random excitation

Both the presented piezoelectric impulse and TW excitation methods offer interesting features for modal analysis or the testing of rotating structures in general. However, the impulse excitation cannot be used in conjunction with the used SGs and telemetry modules, as their noise threshold is too high to detect the response generated by the chosen MFC actuators. The TW excitation, on the other hand, can cause very high levels of response, but does not present significant advantages over a standard stepped-sine method

in a strict modal analysis context.

For this reason, only the stepped-sine and MIMO random excitation techniques were employed in this project, and their results are here compared to check their relative quality, and ensure that they can be used interchangeably. It is especially important to prove this particular implementation of the MIMO random excitation against the golden standard of stepped-sine testing, to ensure that the new application of MIMO with random is as robust as it promises to be.

Partial validation was provided by the data reported in Table 5.2, which showed good agreement between LDV and the comparatively noisier SG/telemetry system, both in terms of frequencies and damping values. The LDV results, however, could only be obtained at rest, and data is needed at different speeds, as rotation inevitably induces additional measurement noise sources. Fig. 5.12 shows the natural frequencies extracted at various speeds from SIMO sine and MIMO random tests for the 3ND mode. Only the 3ND mode was used for this comparison because, due to the length of the stepped-sine tests, just one mode could be extensively tested. Fig. 5.12a shows the frequencies for the FW mode, while Fig. 5.12b the BW mode.

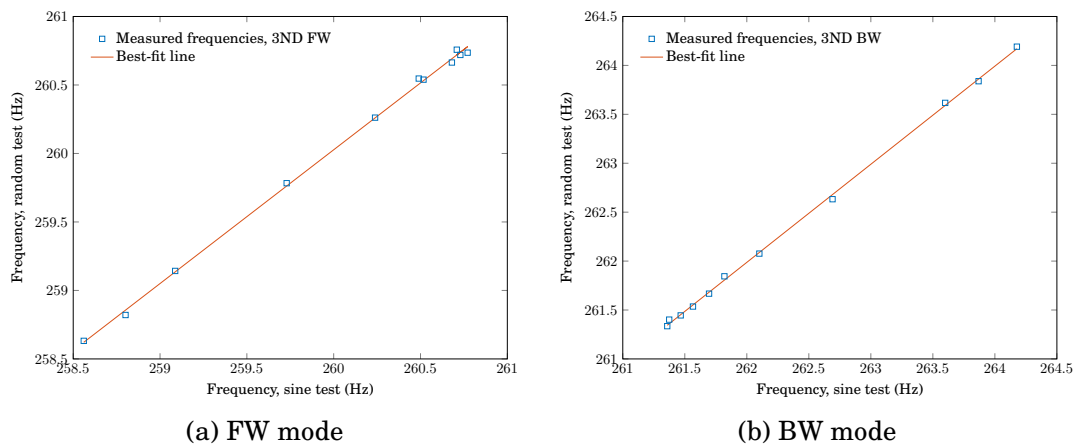


Figure 5.12: Comparison between resonance frequencies extracted from SIMO stepped-sine and MIMO random-excitation tests at various speeds, and best-fit lines of the 3ND mode.

In both cases, a linear relationship (regression coefficient 1.0) was found between the two testing methods. In the FW case, the slope of the regression line fitted to the experimental frequency points is 0.976 ± 0.03 , which indicates a minor tendency of the MIMO random to underestimate the resonance frequencies with respect to sine. In the BW case, the slope is 1.003 ± 0.024 . This proves that both methods provide essentially the same frequencies, with no evident bias.

Damping, in the form of critical damping ratio ξ , was always extracted alongside frequencies using the pLSCF method. The values for both the 3ND-FW and 3ND-BW modes at speeds from 0 to 450 rpm appear in Fig. 5.13. Random gives very similar values for both the FW and BW modes. They are very stable, with relatively low scatter around the 0.02% mean, and show no obvious dependency on speed. This is reasonable, since the the blisk, with its thin horizontal blades, is relatively aerodynamic, thus not producing a high

amount of drag. The rotational speed range is also not wide enough to contain a large variation in aerodynamic damping.

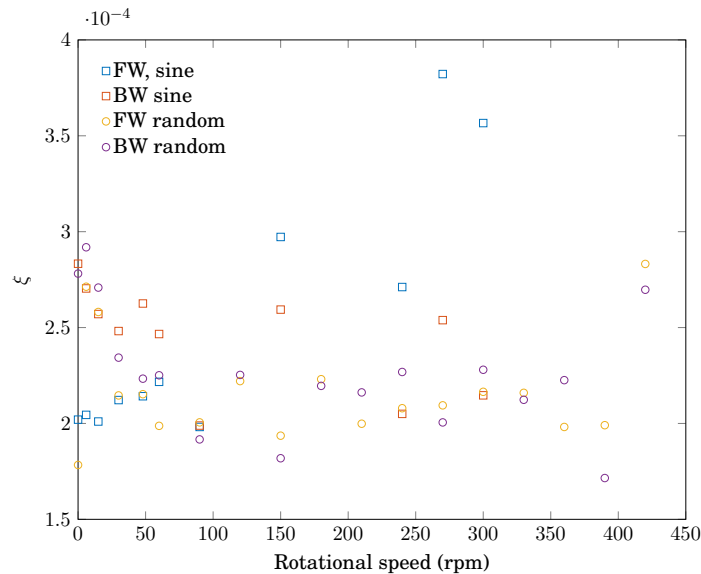


Figure 5.13: Comparison of damping extracted from SIMO stepped-sine and MIMO random excitation tests against speed.

The damping from the sine data follows the same pattern, and shows the same values as random for the BW mode. The FW mode, instead, shows a quite clear increasing trend, and reaches values nearly twice as high as the BW mode. The cause of this is not entirely clear. It stands to reason that the sine method, concentrating the excitation at one specific frequency at a time, thus producing larger responses, could trigger additional, potentially nonlinear, damping sources (e.g. friction in the flange joint). The interaction between the single active MFC patch and the induced TW mode, which would be different depending on the direction of the wave, could explain the asymmetry in behaviour between FW and BW modes. However, as only two anomalous values were measured, and the resulting damping was still in the same range as all the others, the two methods were considered equivalent with respect to damping as well.

Mode shapes will be discussed in the next chapter, but, since the reliability of their extraction depends heavily on the quality of the measured FRFs, the used stepped-sine and MIMO random methods will be compared here with regards to the produced mode shapes as well. The principal tool to assess the correlation between two sets of vectors (mode shapes, in this case) is the Modal Assurance Criterion (MAC). As is well known, it is defined as [21,27]

$$MAC = \frac{(\mathbf{u}^H \mathbf{v})^* (\mathbf{u}^H \mathbf{v})}{(\mathbf{u}^H \mathbf{u}) (\mathbf{v}^H \mathbf{v})}, \quad (5.1)$$

where \mathbf{u} and \mathbf{v} are two generic vectors. As it is fundamentally equivalent to the square of the cosine of the angle between the two vectors, a value of 0 indicates no correlation (the vectors are orthogonal), while a value of 1 is a sign of coincident vectors. The MAC is a global quality indicator, and as such does not give a direct indication of the relative

error between the DOFs of the different vectors. For this reason, the Normalised Modal Difference (NMD) was used as an additional measure of the similarity between the mode shapes obtained from the stepped-sine and MIMO random methods. The NMD can be expressed as

$$NMD = \sqrt{\frac{1 - MAC}{MAC}}, \quad (5.2)$$

and represents the average percentage difference of the single DOFs between the two modes [102]. Table 5.3 reports the MAC and NMD values for the 3ND modes at rest, and at two additional speeds. Since more measured DOFs lead to more reliable MACs, the modes compared are in the form of the reconstructed mode shapes, which will be presented in more detail in sect. 6.2.1. Due to the limited amount of telemetry channels, the strain data were acquired in two separate tests: one set of strain gauges was connected first, followed by the other. The mode shapes extracted from the two measurements were then recombined, so that the data from all the strain gauges installed on the blisk could be used.

Table 5.3: Comparison between different excitation methods: MAC and Normalised Modal Difference (NMD) for the reconstructed 3ND mode between SIMO sine and MIMO random excitation.

Speed (rpm)	Mode number	MAC	NMD (%)
0	3ND-1	0.9993	2.71
	3ND-2	0.9984	3.96
60	3ND-1	0.9997	1.82
	3ND-2	0.9992	2.78
300	3ND-1	0.9998	1.53
	3ND-2	0.9997	1.71

It can be seen that MAC values are very close to unity were obtained, indicating very high correlation between the modes, especially since the NMD is simultaneously very low. The two mode shape sets are thus essentially equivalent. Together with the frequency and damping data, this contributes to show that the MIMO random method for rotating structures, which has been developed here, leads to reliable measurements in the rotating frame. This allows an accurate modal analysis of the blisk system in a significantly shorter amount of time than with the traditional stepped sine approach.

5.3 FRF behaviour in the rotating blisk

5.3.1 Effect of rotation

Having confirmed the capability of piezoelectric actuation to produce consistent data for use in modal analysis, the resulting SFRFs and their characteristics in rotating conditions will be presented here. All SFRFs shown in this section were derived from SIMO stepped-sine tests to maximise visual clarity, especially in the phase plots.

Fig. 5.14 gathers the SFRFs for a single output SG (SG 3) at different rotational speeds for the 3ND mode. The excitation was provided by the MFC actuator at sector 1. It can be

seen how the small frequency split due to mistuning at 0 rpm widens progressively with increasing speed, revealing the effect of the Coriolis force. At the same time, the amplitude varies as well. The first peak (henceforth, 3ND-1) at 260.74 Hz is more than twice the second (3ND-2) at 261.41 Hz. This is to be expected from the presence of position-locked mode shapes, which causes a variation in the amplitude of the FRFs along the blisk: at the nodal diameters, the strain is always going to be zero, for example.

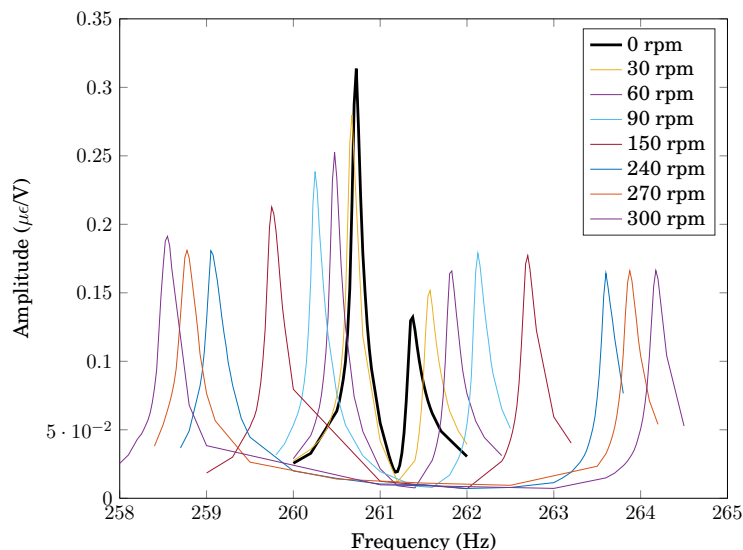


Figure 5.14: Evolution of the SFRFs with speed (SG3, input 1, SIMO stepped-sine).

When the speed increases, however, the amplitude of 3ND-1 starts decreasing, while 3ND-2 increases. They both tend to level off after 240 rpm, and stabilise at a very similar amplitude level. As explained before, this indicates the progressive development of a TW in the blisk. While at rest, the maximum amplitude that can be reached at each point of the structure is dictated by the corresponding mode shape; in rotating conditions, the Coriolis effect causes the modes to rotate, so that any point can reach maximum strain.

It can also be seen that the maximum amplitude decreases quite sharply for 3ND-1, while the expected behaviour would be for it to stay constant, and for 3ND-2 to increase to its level. This is associated to the increasing damping trend with speed that was found for the stepped-sine excitation (Fig. 5.13), and not to any particular rotational effect.

The development of the 3ND TW pattern is confirmed, and better visualised, in the phase plots of Fig. 5.15. At rest (Fig. 5.15a), the phase at the different sectors neatly divides into two groups, shifted by 180° : this means that the sectors move either perfectly in phase, or perfectly out of phase, which indicates that the deflection shape (and its associated mode) is locked in a SW. At 300 rpm (Fig. 5.15b), however, the phase of each sector is different, and the difference between adjacent sectors is equal to $\mp 135^\circ$, depending on the mode. It is also possible to see that in between the resonances, the phases tend to regroup into two separate phase levels, suggesting that in this frequency range the coexistence of the two opposite TW can generate a SW.

The SFRFs presented are the basis of the modal parameter extraction procedure. The

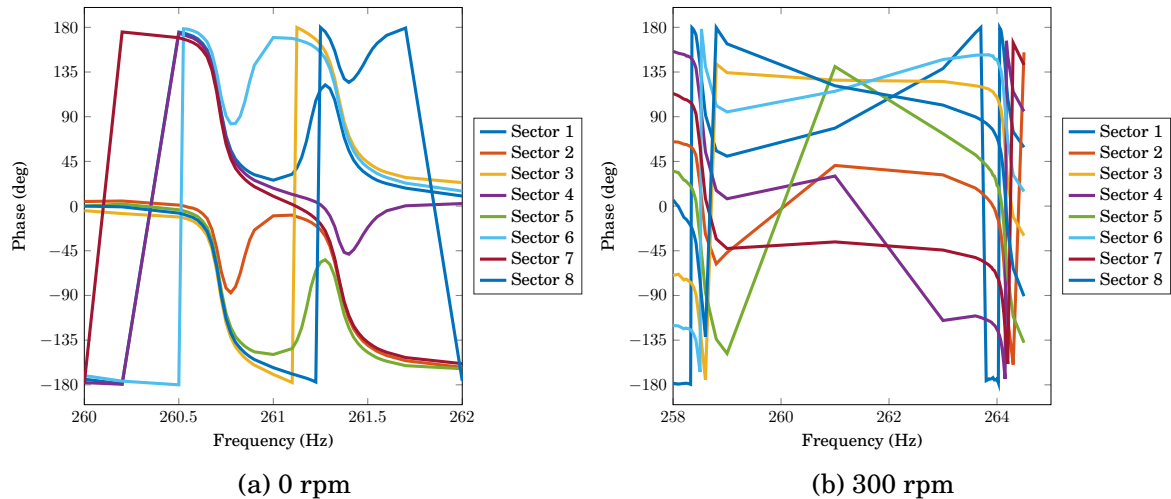


Figure 5.15: Effect of rotational speed on the phase of the SFRF.

frequencies for 3ND are reported in the Campbell diagram of Fig. 5.16a. The decreasing branch is associated with the FW mode (see sect. 2.3.4), and the increasing one to the BW mode. Both branches can be accurately represented by straight lines, as can be expected in the used test piece, where the horizontal blades cause negligible centrifugal stiffening.

Fig. 5.16b displays the split. A split is present already at rest, and is due to mistuning, as previously noted. A purely mistuning-induced split would have no dependence on speed, while here the Coriolis effect causes the FW and BW frequency to diverge, and the split increases linearly with rotational speed, as the Coriolis force is linear itself.

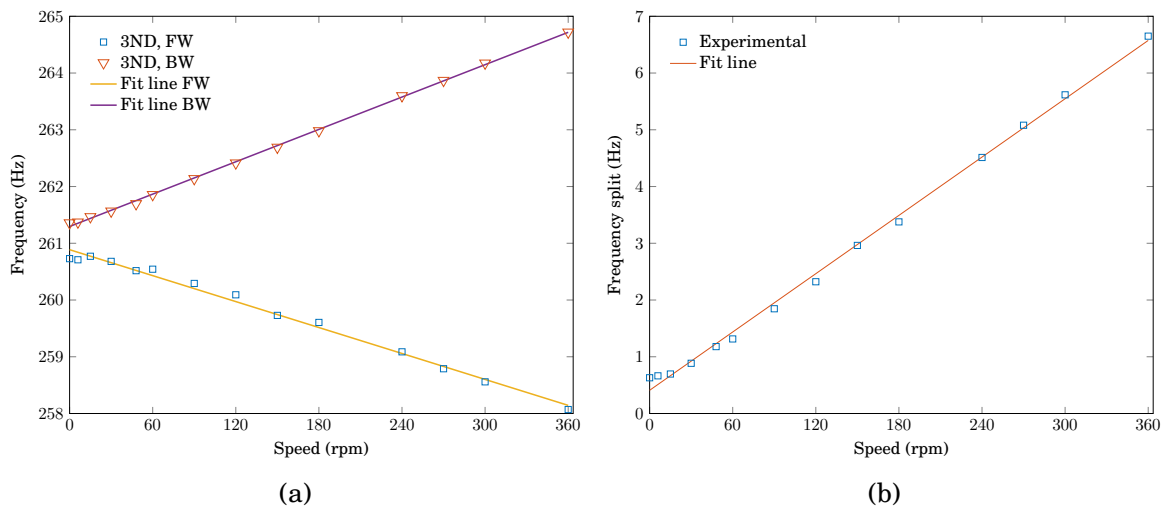


Figure 5.16: SIMO sine experimental frequency results for 3ND with best-fit lines: a) Campbell diagram, and b) frequency split curve.

5.3.2 Effect of mistuning

As shown in Table 4.4, the 2ND mode is affected by a high degree of mistuning, with a frequency split of 4 Hz (2%) already at rest. If only the Coriolis effect were active, this level of split would be reached only at 300 rpm (Fig. 4.8a). The question then arises as

to how the Coriolis and mistuning-induced split would interact. The Campbell diagram of Fig. 5.17a offers a partial answer. There is a speed range, approximately between 0 and 60 rpm, where the FW and BW branches are horizontal. This is better visible in Fig. 5.17b, as the reported frequency split is constant. After 60 rpm, the branches slowly start diverging, as is reflected in the frequency split plot, which increases quadratically in this speed range. There thus seems to be a mixed behaviour: at low speeds, the blisk seems to respond as a stationary mistuned blisk, and the Coriolis effect seems to start being active only after a certain threshold, when the characteristic speed-dependent split appears.

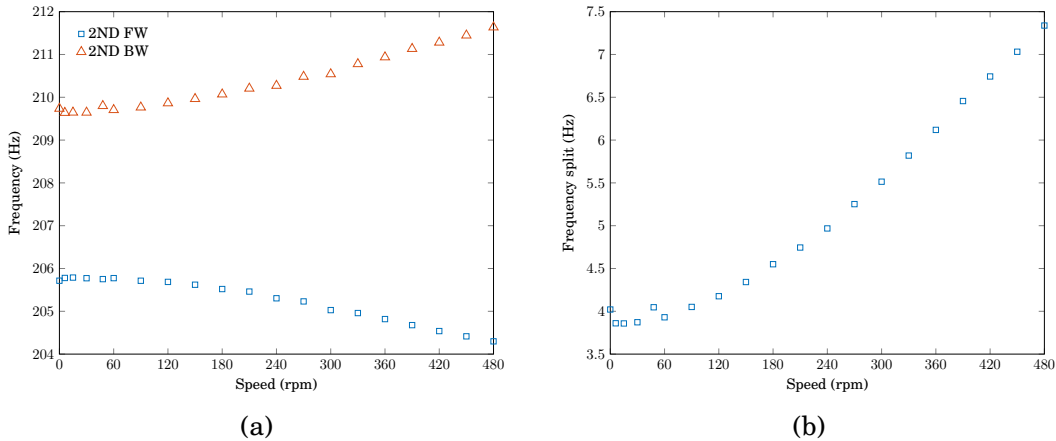


Figure 5.17: MIMO random experimental frequency results for 2ND: a) Campbell diagram, and b) frequency split curve.

The SFRF phase plots of Fig. 5.18 offer more insight. It can be seen that, at rest (Fig. 5.18a), the different sectors show again a relative phase of either 0° or 180° , which confirms that the blisk is vibrating in a SW. At 60 rpm (Fig. 5.18b), if indeed mistuning were the only active phenomenon, we would expect the same phase pattern as for the locked SW mode. This is only partly true: the sectors are still divided into two main phase groups, but the phase values start to scatter around 0° or 180° , indicating that the SW is no longer pure. Stronger signs of a TW developing are shown at 300 rpm (Fig. 5.18c), where the sectors tend to group at four distinct phase levels, as would be expected for a 2ND mode (a 2ND mode corresponds to an IBPA of $360^\circ \text{ND}/N = 90^\circ$, so four different phase values can appear around the blisk).

This behaviour shows that the Campbell diagram is misleading, and that the Coriolis effect can be actually active, and cause deviations from pure SW response patterns, even if no change in frequency can be detected, as happens in the 0–60 rpm. These features will be discussed in more detail in sect. 6.2.3.

5.4 Discussion of results

The overarching question behind this work is the identification of effective testing methods for the modal analysis of rotating bladed discs. Piezoelectric patches were found to be able to introduce adequate excitation levels in the test pieces in Chapter 4, and their full poten-

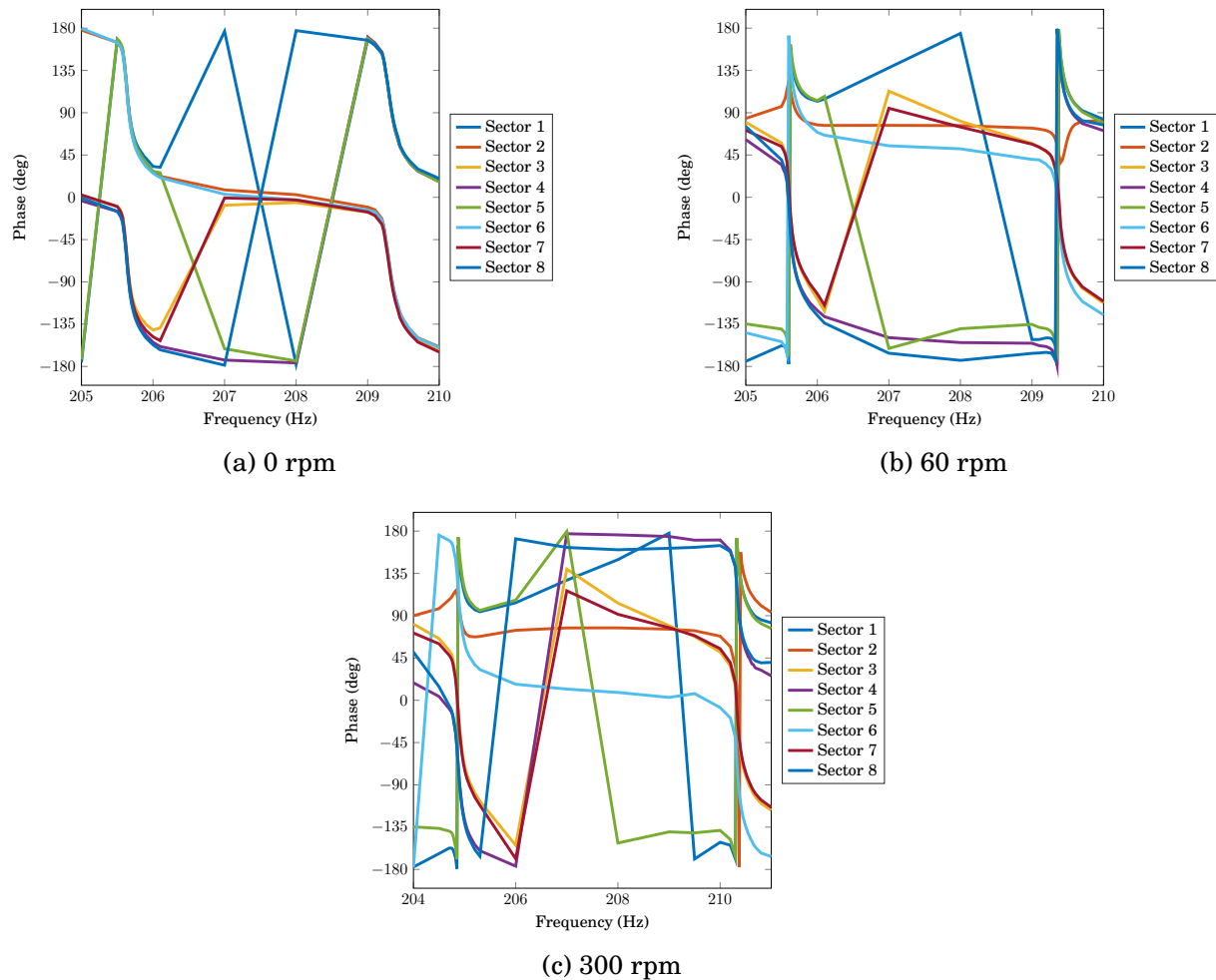


Figure 5.18: Evolution of the phase of the SFRF with rotational speed at the 2ND mode.

tial as actuators in the context of EMA was investigated here. The main drawback of MFC patches is that they do not produce a directly measurable force: due to their piezoelectric properties, they react to an applied voltage with a strain, which is then transmitted to the structure by bonding the two. The induced strain can be known, but only through the piezoelectric constants of the material (Eq. (2.57)). These are usually supplied by the manufacturers, and are subject to variable levels of uncertainties. The bonding process adds to these unknowns: the thickness of the adhesive layer cannot be accurately controlled in a standard lab environment, and the correct positioning, especially in terms of orientation relative to the test piece reference frame, of the actuators can be challenging. The development of a repeatable bonding technique helped to minimise these uncertainties in this work, but the excitation cannot be directly measured.

The control voltage to the MFC patches, on the other hand, can. The first target of the experimental campaign was therefore to assess if this voltage could be considered an excitation term, how it would behave, and if FRFs could be built from it. Sect. 5.2.1 dealt with this question explicitly at the start. When the blisk was subject to sinusoidal excitation, and the response measured by LDV or accelerometers, the resulting velocity and acceleration FRFs behaved just as they would with a traditional force excitation, by displaying

peaks at resonance, and especially the signature 180° phase shift through it. The same behaviour was found for all main excitation techniques investigated, namely stepped-sine, MIMO random, and impulse, and it is followed by strain as well.

It was therefore established that piezoelectric actuators can be appropriately used as excitation sources, and their potential applications further explored. Piezoelectric patches can be driven by arbitrary control voltages, and lend themselves very well to MIMO set-ups. They can be attached to the structure directly at the input locations of choice, even ones that would be inaccessible to standard shakers or magnet arrays (e.g. the side of a blade in a staggered cascade): this allows a fine tailoring of the distribution of the exciters to optimise response quality. MIMO works particularly well with broadband excitation, where the input energy is spread across a wide frequency range: multiple exciters then allow to introduce higher and more targeted forcing levels. This helps counteract the main disadvantage broadband excitation has with respect to sinusoidal testing, where forcing is concentrated at one frequency at a time, thus causing larger response, and larger SNR.

Care must be taken with the leakage caused by the non-zero signals at the start and end of each measurement, as it introduces a bias in the estimation of the FRFs, and inaccuracies in the modal parameters. Alternative broadband signal types, like burst random, or chirp, that were developed to eliminate this issue, could not really be used in this work, due to the high noise background of the telemetry system, and the decision to limit the use of filters: even if the forcing voltage could have been made to start and end at zero, the response would have still suffered from leakage because of the noise components. Pure random excitation was therefore used. Bias minimisation was sought by increasing the frequency resolution, and using a relatively high number of averages, while leakage was contained by applying a Hanning window to the raw measurement data.

Good-quality FRFs were obtained when measuring with LDV (Figs. 5.2 and 5.4a). Sect. 5.2.5 showed that, even for the noisier strain data, MIMO random is essentially equivalent to the SIMO stepped-sine testing method. Both yielded the same frequencies and mode shapes. It is particularly noteworthy that not only the MAC between the eigenvectors extracted from the two set-ups is nearly exactly 1, but the NMD values, which give a more local estimation of the difference between the individual DOFs, is concurrently very low (Table 5.3). This also demonstrates that, while the telemetry noise did not allow the recovery of all the features of the strain FRFs, so that some important indicators of FRF quality (e.g. anti-resonance vs. minimum behaviour) are lost, the signals are still good enough around resonance (as visible in the coherence plots of Figs. 5.4c and 5.7) to produce consistent values for all modal parameters.

The main highlight of this newly-proposed MIMO random excitation in this section is the possibility to measure the response spectrum of a structure in a fraction of the time required by a stepped-sine, or even swept-sine, test. The Z-mod plot in Fig. 5.19 shows the amplitude of the strain response over the 160–440 Hz frequency range, at different speeds. It is very useful in visualising the most dangerous resonance frequencies over the whole operational range. The resonances corresponding to the various ND families are clearly visible, as are the Coriolis-induced frequency splits. The plot was acquired by using

the MIMO random excitation at different speeds. Due to the discussed need for small frequency resolution and high number of averages, the measurement at each speed took 45 minutes, so the acquisition of the whole plot required nearly 13 hours. However, a stepped-sine measurement would take between 30 and 45 minutes for a maximum frequency range of 10 Hz. This highlights the significant time saving allowed by random testing, especially in spinning conditions, as measurements are necessary for different speeds to tests the effects of rotation.

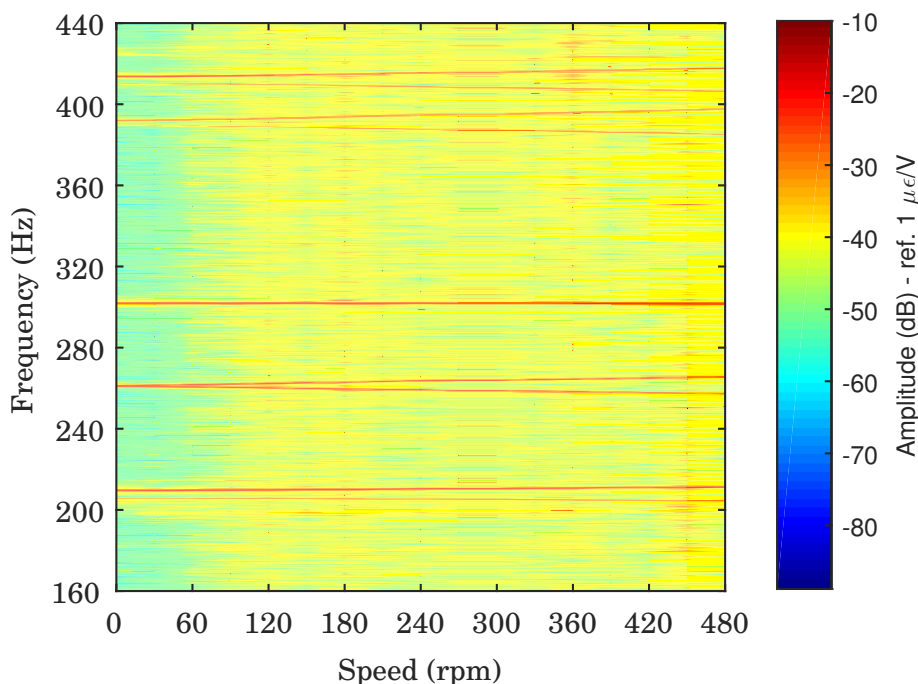


Figure 5.19: Z-mod plot for MIMO random excitation in the 160÷440 Hz frequency range, from strain gauge data.

Impulse excitation is characterised by a broadband input spectrum as well. Sect. 5.2.3 demonstrated for the first time, to the author's knowledge, that MFC actuators can be used to produce this forcing function, and meaningful results. This is a promising approach, as exploiting an actuator that is permanently attached to the structure under test could provide significant improvements in quality, and speed, over traditional impact testing. The permanent location would get rid of most of the variability afflicting manual impact testing, like the inevitable changes in the position and orientation of the hammer relative to the structure, and the force of the hit itself, from test to test.

While the piezoelectric impulse excitation was not shown, in the tests conducted, to be better than manual hammer testing (Fig. 5.10b), it proved itself at least as good, yielding frequencies and damping values very close to those of the traditional impact test (Table 5.2), which highlights its potential. However, considering that over most of the frequency range, dips in coherence occur around anti-resonances, it can be argued that noise would be the main reason. As shown in Fig. 5.8b, the energy that could actually be introduced in the blisk was extremely low. This is due to both the characteristics of the impulse, and the actuator model. The length of the impulse was kept relatively long, its shape

smooth, and its amplitude only 75% of the maximum attainable to not endanger the piezoelectric patches with amplitude overshoots, since the dynamics of the amplifier electronics were not known. As for the actuator model, the one chosen is in a way ideal, as, thanks to its small dimensions, it approximates well a point excitation, but it is possible that a slightly larger/thicker actuator could be more effective in producing good levels of forcing.

As a last proof of the versatility of piezoelectric patches as actuators, travelling-wave excitation was also tested. While effectively functioning as a multiple-input system, TW excitation is actually equivalent to a single-input configuration, due to the fact that the control signals to the different actuators is perfectly correlated. As such, there is no particular advantage in using it over a single actuator, also considering that an additional step is required to reduce the data to a proper single-input configuration to be processed with the usual modal analysis techniques [148]. However, TW forcing patterns are very effective in exciting a large response at the frequencies matching the mode shapes associated with that pattern. This could be exploited to simply improve SNR, or, even more effectively, to enhance selectivity, i.e. to discriminate between closely-spaced modes, as only the mode corresponding to the TW direction will respond with any consistence, as shown in Fig. 5.11.

Of the excitation types presented that could be efficiently applied to modal analysis, the impulse was not usable in conjunction with SGs due to the low SNR of the telemetry system. Stepped-sine and MIMO random were found to be able to produce good quality data, but ultimately, MIMO random was the excitation method of choice, and used to derive all the experimental data from which the mode shapes of Chapter 6 were extracted.

5.5 Summary and Conclusions

The possibility of using piezoelectric actuators in a modal analysis context was successfully demonstrated in this chapter. In particular, the FRFs and SFRFs measured exhibited the same amplitude and phase characteristics as with traditional excitation sources, proving that the voltage excitation signal sent to the actuators acts as the forcing term in standard modal analysis.

An in-depth investigation into the capabilities of MIMO random excitation was conducted for the first time on a rotating blisk, and showed that it can be used in combination with the pLSCF method to extract consistent modal parameters. Despite drops in coherence at resonance, excellent agreement was found for frequencies and mode shapes between the results of MIMO random and stepped-sine data, both at rest, and in rotation. This was a particularly important finding, as it showed that MIMO random is essentially equivalent in this application to stepped-sine testing in terms of quality of results. In addition, it was able to provide broad-band data, and thus Campbell diagrams and z-mod plots, at a fraction of the time necessary for stepped-sine.

The versatility of piezoelectric actuators was further explored, and the patches were used to provide impulse excitation. This set-up was tested at rest to allow comparison with the standard transient excitation provided by a modal hammer. The small actuators installed on the blisk resulted in a very low-amplitude response, but the extracted fre-

quencies and damping values showed good agreement with the hammer test, and proved the potential of this novel application.

Travelling-wave excitation patterns were also successfully introduced, and resulted in high-level response, and mode selectivity. This suggests that this forcing type could be suited for testing in the nonlinear range, as amplitude-dependent nonlinearities could be excited, and for fast mode identification in high modal density regions.

The effects of the Coriolis force on the measured SFRFs was shown, with clear frequency splits developing. A first indication of the generation of travelling-wave modes was also measured in the phase of the SFRFs, which went from fixed $0^\circ/180^\circ$ values at rest to the IBPA determined by the ND family at high speed. This contrasted with the behaviour of modes with mistuning, where the split remained closer to the value induced already at rest by mistuning itself, and travelling-wave behaviour developed later than in tuned modes.

Chapter 6

Mode shapes and left eigenvectors: Experiments and validation

6.1 Introduction

The MIMO experimental approach tested in the previous chapter, coupled with a full poly-reference identification method, produced consistent results for resonance frequencies and damping values. The Coriolis force caused large frequency splits, and its effect on mode shapes will be examined in this chapter, with two main aims: a closer understanding of the Coriolis effects themselves, and a thorough validation of the proposed testing framework.

Very few studies address the generation of travelling-wave modes in bladed discs due to the Coriolis force, and most are based only on measurements at a limited amount of speeds. However, precise knowledge of mode shapes is essential in aeroelastic analyses to maximise performance and stability. The complex mode shapes of the test blisk will therefore be studied at a large number of speeds, to gain further insight into how rotational speed itself influences modes via the Coriolis effect.

The identification powers of the developed experimental methodology will be put to the test with mistuned modes, as mistuning causes frequency splits like the Coriolis force, but standing-wave modes instead of travelling-wave ones. The measurement of left displacement eigenvectors will also be presented for the first time in a rotating blisk, and its reliability will be discussed.

As a final step, the experimental Campbell diagrams for the test piece, its mode shapes, and left eigenvectors, will be compared to their FE counterparts, to produce a comprehensive validation of the identification capabilities and accuracy of the developed testing methodology.

6.2 Experimental mode shapes

6.2.1 Complex mode shapes

The mode shapes of any physical system can be represented as complex variables, and thus be characterised by an amplitude and a phase. In the case of normal modes, the phase reduces to 0° or 180° , as they are purely real, while, for complex mode shapes, the imaginary part is not negligible. To illustrate this difference, the strain mode shapes were extracted from the FRFs at the eight circumferential SGs (SGs 3, 7, 8, 10, 13, 14, 15, 16, Fig. 4.14a) at rest and at 390 rpm. The target mode shape was the third nodal diameter (3ND), and its modal amplitudes at rest are plotted in Fig. 6.1. Because of a small amount of mistuning, two distinct modes, corresponding to two separate frequencies, are visible already at rest, and are 90° out-of-phase.

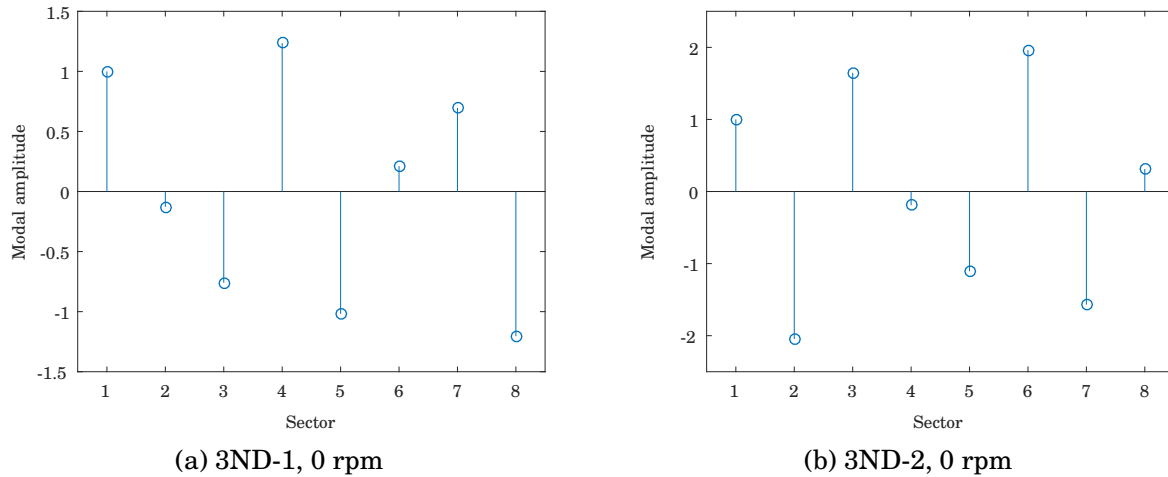


Figure 6.1: Modal amplitudes from MIMO random at rest of the a) 3ND1, and b) 3ND2 modes. The modes are normalised so that sector 1 has an amplitude of 1.

The elements of the modal vectors at 0 and 390 rpm are shown in Fig. 6.2 on the complex plane as phasors. To provide a consistent representation, the modes were normalised so that the strain modal constant for the first sector would always be equal to 1 (and thus have a phase of 0°). The modal constants at the various DOFs at rest neatly align along the real axis both for the 3nd1 (Figs. 6.2a) and the 3ND2 mode (6.2b): the phase only assumes values very close to 0° and 180° as anticipated, since the damping is not high enough to cause the occurrence of complex modes at rest. The fact that adjacent sectors can move out of phase also confirms the presence of nodal diameters in the blisk.

Figs. 6.2c and 6.2d show the modal constants at 390 rpm. Here the constants are fully complex, and the phase difference between adjacent sectors is -135° for the 3ND-1 mode (which corresponds to a FW travelling wave), and $+135^\circ$ for the 3ND-2 mode (which corresponds to a BW travelling wave): it is easy to notice that the phasors are flipped with respect to the real axis between 3ND-1 and 3ND-2. It is also possible to see how the amplitudes of the modal constants are nearly the same in the rotating case, while there are noticeable differences at rest.

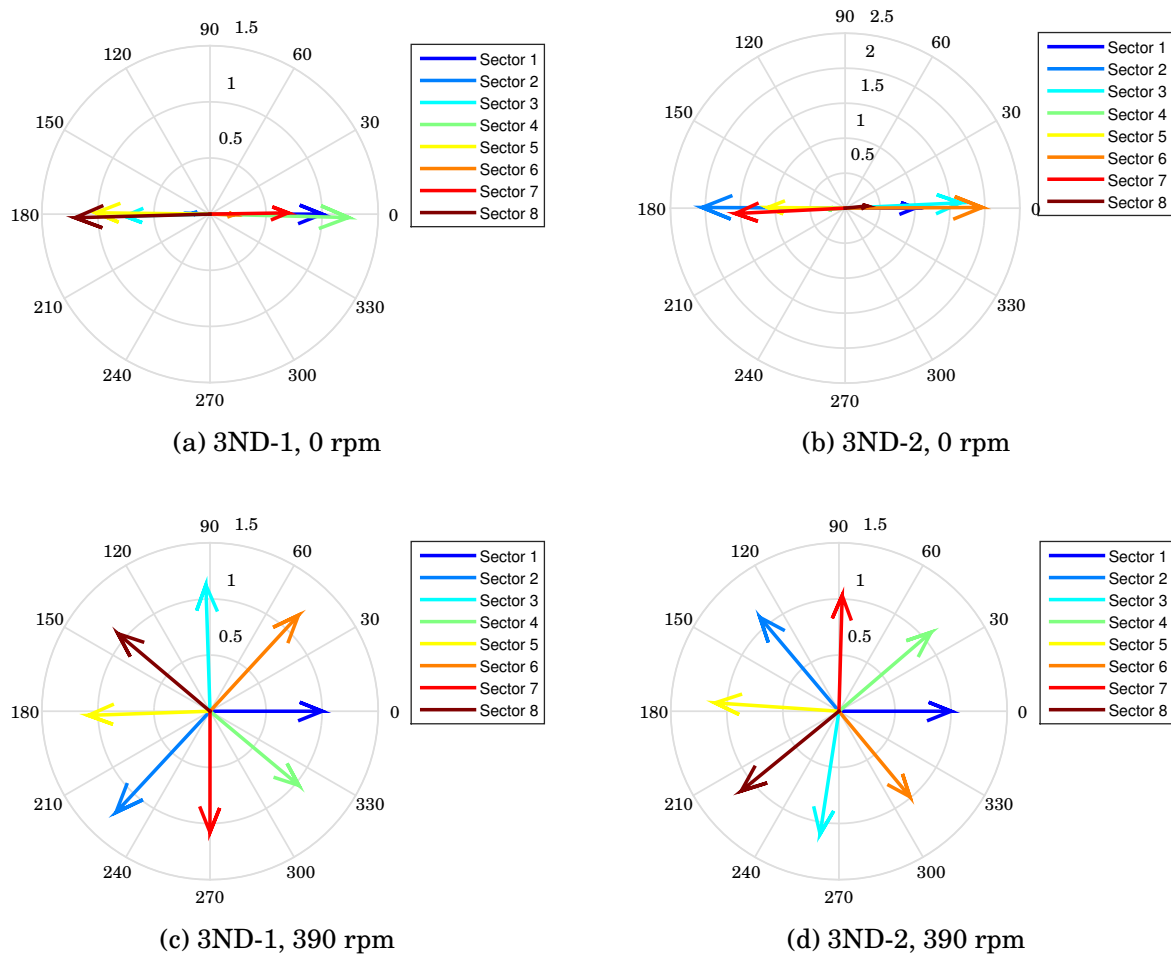


Figure 6.2: Phasor plot of the 3ND mode shape pair at 0 and 390 rpm, from MIMO random. The modes are normalised so that sector 1 has zero phase, and acts as reference.

To get a clearer picture, the amplitudes of the modal constants are plotted in Fig. 6.3 for all modes at 0 and 300 rpm. The two single modes, 0ND and 4ND, are reported first in Figs. 6.3a and 6.3b. These modes can only present a relative phase between adjacent sectors of 0° and 180° , and are therefore always real. Due to the absence of nodal diameters, in the 0ND case, and the presence of $N/2$ diameters, in the 4ND case, the amplitudes of the strain modal amplitudes at all sectors should be the same. While this is true for the 4ND mode, the 0ND shows a clear modulation, and a small variation with speed. This modulation shows the characteristics of both a 1ND and 2ND shape. The 1ND modulation can be explained by considering that the flange joint between the blisk and the telemetry holder (Fig. 4.5) is slightly off-center due to a mismatch between the tolerances in the bolt holes on the two components. The annulus that is constrained by the bolts is thus slightly skewed, so that half of the blisk is effectively stiffer than the other. The 2ND modulation can be ascribed to the vicinity of the 0ND and 2ND-1 modes (200 Hz and 204 Hz), and the noisiness of the FRFs around the 0ND frequency: it is then possible that in these conditions, the mode extraction algorithm failed to properly discriminate between the two.

The modal amplitude for the 2ND (Figs. 6.3c–6.3d) varies at 0 rpm, confirming the presence of nodal diameters. As at rest the modes are real, the nodal diameters are also fixed in space, and it can be seen that the mode shape is rotated by 90° between modes 2ND-1 (at 205.7 Hz) and 2ND-2 (at 209.7 Hz), as translating the amplitudes by two sectors (amounting to 90°) would lead to a perfect coincidence of the two. At 300 rpm, the amplitudes display the same modulation as the ones at rest, and the modal constants at each sector show only a slight reduction in their relative difference (a maximum difference of 0.45 vs. 0.6 at 0 rpm). This behaviour is consistent with the presence of a standing-wave mode even at 300 rpm due to mistuning, and will be treated in more detail in sect. 6.4.2.

This contrasts starkly with the 3ND modes (Figs. 6.3e–6.3f). At rest, the amplitudes still show the presence of nodal diameters, and the 3ND-1 and 3ND-2 mode shapes are rotated by 90° as well. At 300 rpm, on the other hand, the modal constants have nearly the same amplitude. The data then suggests that, for the 3ND mode, the TW mode that would be expected from the Coriolis effect has developed, and all DOFs can reach maximum amplitude as the wave propagates through them.

The TW behaviour is better explained through Figs. 6.4a and 6.4b. To show the propagation of the TW, the time dimension was added as in Eq. (2.31) by multiplying the experimental mode shapes by a generalised coordinate $q(t) = e^{\lambda_{+/-}t}$, with $\lambda_{+/-} = (-\xi \pm i\sqrt{1 - \xi^2})\omega$, where the sign and frequency depend on the TW mode (sect. 2.3.3). The variable strain amplitude was then derived for each SG position along the circumference as a time-dependent variable $z = \Re(\psi q(t))$, where ψ is the 3ND mode shape. These discrete strain values were interpolated along the external rim and captured at distinct time instants in $\pi/6\omega$ increments to provide a continuous representation of the strain varying through the sectors.

The first feature of Figs. 6.4a and 6.4b are that the different sectors never go through zero at the same time, which is the most obvious signal of the presence of a travelling wave. By fixing on any point of maximum strain in Fig. 6.4a at time 0, it is possible

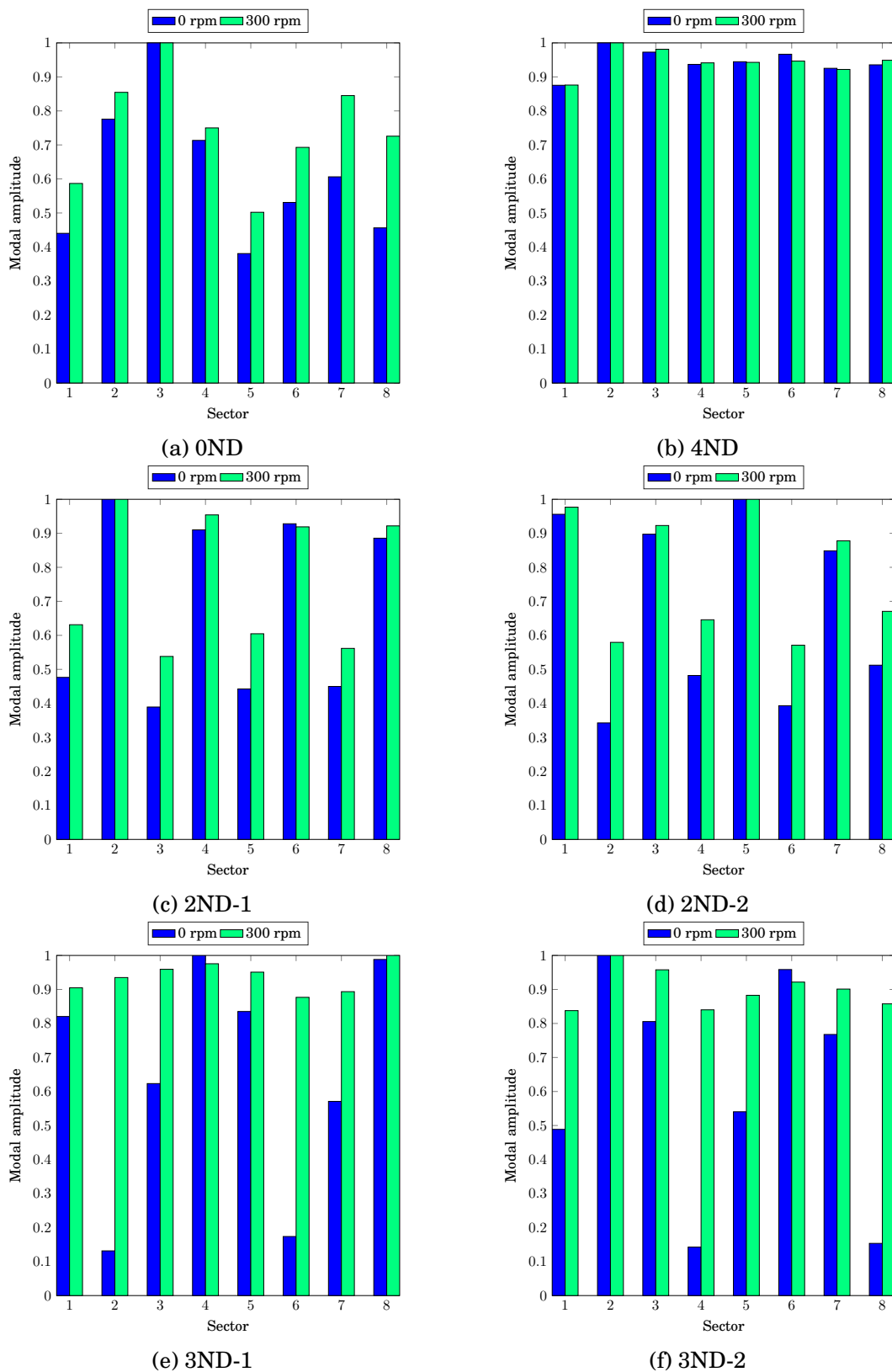
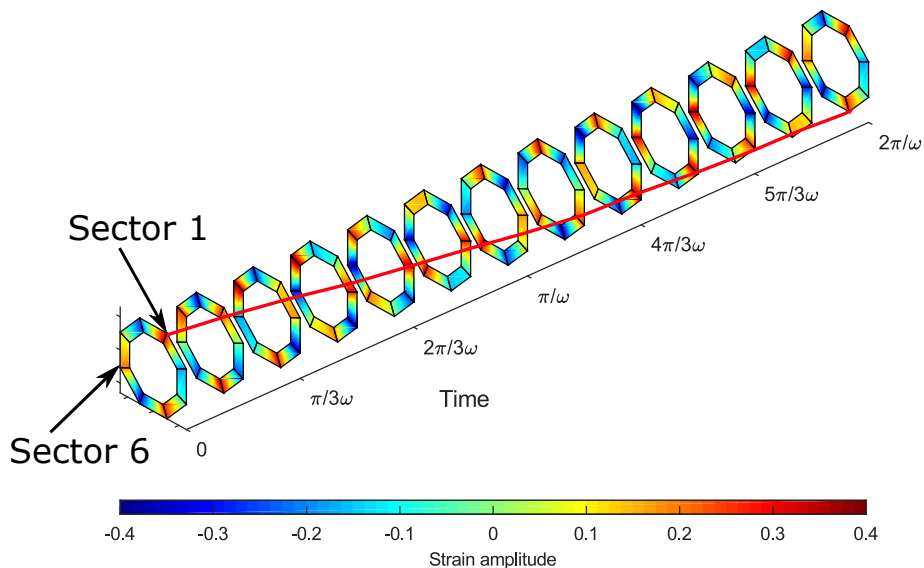
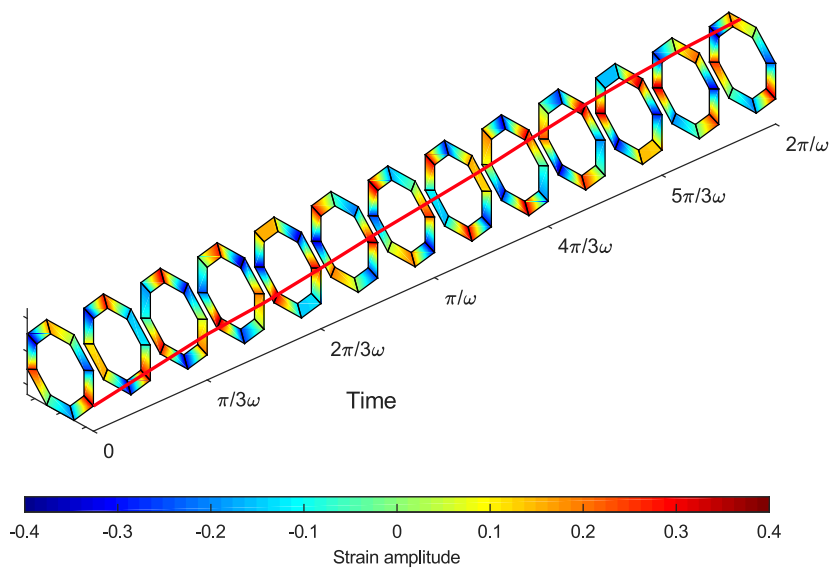


Figure 6.3: Comparison of the absolute value of the modal amplitudes normalised to unity, at rest and at 300 rpm.



(a) 3ND-FW mode, 259 Hz



(b) 3ND-BW mode, 264 Hz

Figure 6.4: Time visualisation of the strain travelling wave for the 3ND FW and BW modes at 300 rpm.

to see that this maximum gradually rotates from one sector to the next in a clockwise direction, along with the spin speed, as this is a FW mode. Each sector goes through a full vibration cycle at frequency ω , as can be seen by noticing that the strain configuration at time $t = 0$ is the same as at time $t = 2\pi/\omega$. During the same time, however, a single crest of the wave has travelled only three sectors. This is because the presence of multiple nodal diameters causes an apparent spatial aliasing: the TW only moves by an angle of $2\pi/k$, where k is the number of nodal diameters, and the speed of the TW is ω/k [149, 150]. These same considerations apply to Fig. 6.4b, with the only difference that the TW is against the rotation speed, as characteristic of a BW mode.

After presenting the complex mode shapes as extracted from the experimental data, the accuracy of these modes should be treated. The autoMAC is simply a MAC where the vectors come from the same set (in this case, they are both experimental mode shapes). The autoMAC is a good way of assessing how different the mode shapes are between themselves. This, indirectly, also indicates the resolution power allowed by the applied sensors. It is an important check especially when only a few DOFs can be measured: a limited number of DOFs is often insufficient to properly discriminate between different mode shapes, which undermines the possibility of meaningful mode shape validation [151].

This effect is illustrated in Fig. 6.5a. Here, the data comes from seven sector SGs (SGs 1, 3, 4, 5, 6, 9, 10, see Fig. 4.14a). Perfect mode shape resolution would lead to an autoMAC matrix with values of 1 only on the diagonal. It can be seen that, instead, there is a high degree of correlation between a large number of modes. The 0ND and 2ND-1 modes, in particular, are highly correlated, with an autoMAC of 0.85. This is confirmed by Fig. 6.5b, which shows the autoMAC for the same DOFs from mode shapes computed in Abaqus, and is very similar to the one of Fig. 6.5a. This agreement proves that this autoMAC does not derive from bad-quality measurements, but by the similarity of the mode shapes at the sector DOF level.

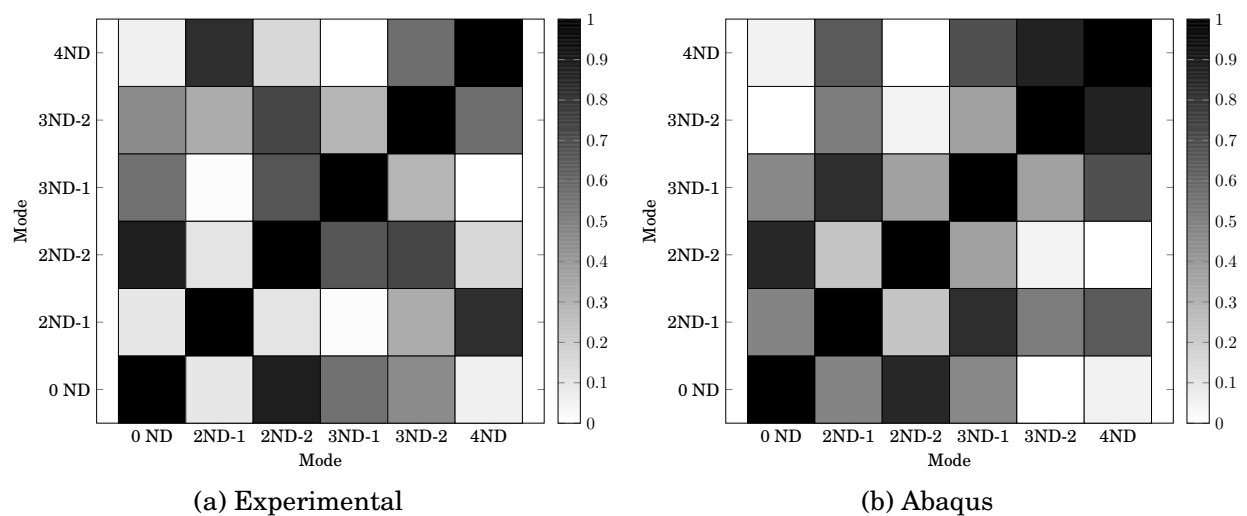


Figure 6.5: Auto-Modal Assurance Criterion (autoMAC) plot of the strain data from a single sector at rest.

The circumferential DOFs (SGs 3, 7, 8, 10, 13, 14, 15, 16, Fig. 4.14a) yield a very

different result: the autoMAC matrix is purely diagonal, both at 0 (Fig. 6.6a), and 300 rpm (Fig. 6.6b). The circumferential DOFs are highly selective, as they can precisely resolve different nodal diameter modes, and between different TW directions. Since this work is particularly concerned with the Coriolis effect on TW modes, these eight measurement DOFs would therefore be sufficient.

However, as an additional check, the sector and circumferential mode shapes were merged to provide more significant MAC values, leading to a total DOF number of 13. The modes had to be merged *a posteriori*, as only eight SG channels were available at any one time in the telemetry system, after one of the transmitters broke. The mode shapes were extracted from different experiments sets conducted in the same configurations, and, in merging them, normalised so to equalise the modal constants for SGs 3 and 10, which were common to the two sets. The autoMAC for the reconstructed modes is shown in Fig. 6.7, for the 0 and 300 rpm. The selective effect of the circumferential SGs shows itself in the drastic reduction of the off-diagonal terms. Since the addition of the sector DOFs does not have a large impact on the autoMAC, with respect to the matrices in Fig. 6.6, this also shows that the eight circumferential DOFs are adequate for the study of the TW form of the examined modes (2ND and 3ND).

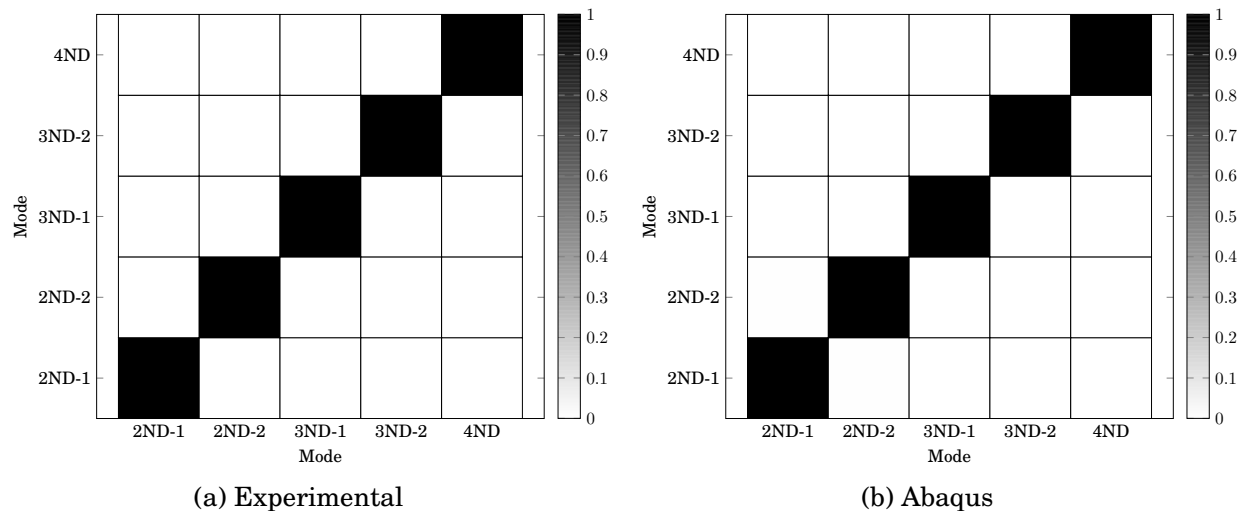


Figure 6.6: AutoMAC plot of the strain data from the eight strain gauges attached to each sector.

6.2.2 Coriolis effect

The effect of the Coriolis force, namely the appearance of TW mode shapes in rotating conditions, has been shown in the previous section. The evolution of the mode shapes with rotation speed remains to be assessed. As explained in sect. 6.2.1, the MAC is the most common used tool in modal analysis to highlight correlation in different sets of modes. It thus provides the means to evaluate the influence of rotation on the *shape* of the modes, since it has never been verified experimentally whether the Coriolis force affects the mode shapes differently at different speeds.

The 3ND strain modes at increasing rotational velocities, as extracted from the circum-

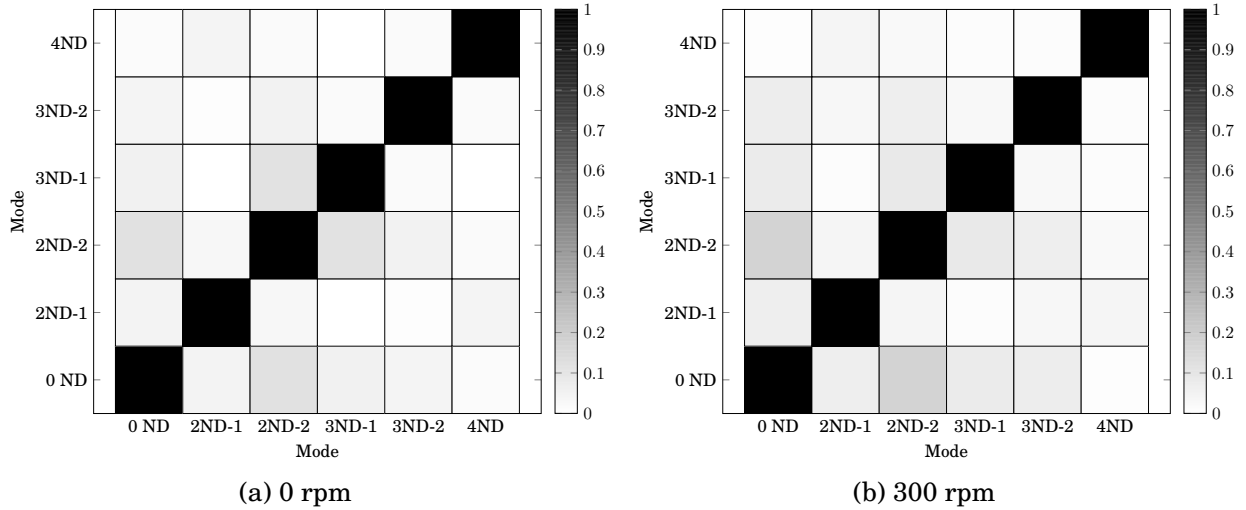


Figure 6.7: AutoMAC plot of the experimental strain data from the reconstructed SG mode (13 SGs).

ferential DOFs, were used for the first comparison: the very limited amount of mistuning of the 3ND mode would allow to observe the Coriolis effect with minimal interference from extraneous phenomena.

To maximise resolution, a slightly modified version of the MAC was used, the Linearised MAC (LMAC) proposed by Morales [152]. This formulation allows to bypass the flattening effect at low and high MACs that is caused by its being equivalent to $\cos^2 \alpha$, where α is the angle between the compared vectors: in a neighbourhood of $\alpha = 0$ and $\alpha = 1$, the traditional MAC remains nearly constant, and it is thus not possible to distinguish small differences between the vectors, which would yield small values of α . The LMAC is defined as

$$LMAC = 1 - \frac{2}{\pi} \alpha = 1 - \frac{2}{\pi} \arccos \sqrt{MAC} = 1 - \frac{2}{\pi} \arccos \left| \frac{\mathbf{u}^H \mathbf{v}}{\|\mathbf{u}\| \|\mathbf{v}\|} \right|,$$

where \mathbf{u} and \mathbf{v} are two generic vectors, and the symbol $\|\cdot\|$ indicates the Euclidean norm.

This linearisation produces a larger gradient in the correlation values, and thus a greater resolution power. The resulting multi-speed LMAC matrix is shown in Fig. 6.8. In it, the FW and BW 3ND modes are present side-by-side at each spin speed, so that the two opposite TW can also be compared between themselves. The most prominent feature is the presence of an area of low correlation (LMAC below 0.5) at the bottom of the matrix (autoMAC matrices are symmetric). This indicates that the low-speed mode shapes (0, 6, 15, 30 rpm), while reasonably similar between themselves, are significantly different from the high-speed ones.

The 48 ÷ 90 rpm range sees a gradual transition to higher values of the LMAC, indicating that the TW is gradually evolving, and the modes in this range exhibit a higher degree of correlation (LMAC above 0.8) with the modes at larger speeds. The 120 rpm speed constitutes a threshold, as the LMAC between the modes at any speed larger than 120 rpm is above 0.9, which is traditionally the MAC value at which certain correlation is assigned to

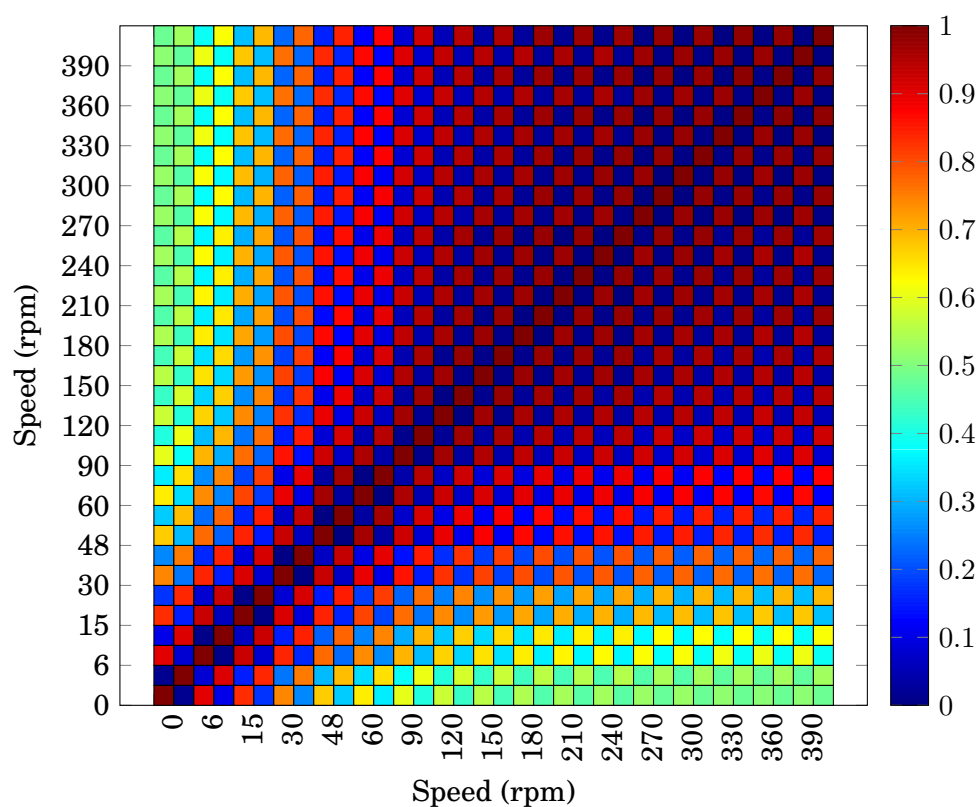


Figure 6.8: Linearised Modal Assurance Criterion (LMAC) matrix between 3ND mode pairs at different speeds, MIMO random excitation, circumferential SGs. Two modes are present at each speed side by side, as the 3ND mode is a double mode.

the compared mode shape pairs. At this point, the corresponding MAC would already be above 0.96, and after 180 rpm, the LMAC too reaches values close to 1, which means that at high speeds, the first 3ND strain modes become virtually undistinguishable. The reason for the existence of this transition region is attributed to mistuning, and will be discussed in more detail in sect. 6.2.3. It is important to note, too, that this high correlation level only applies to modes with the same TW direction, i.e., the 3ND-FW and 3ND-BW always show LMAC values of 0 at all speeds, as they are orthogonal.

The LMAC was calculated for the reconstructed (13 DOFs) strain mode as well, and is shown in Fig. 6.9. Since fewer speeds were used, the contrast between the modes at rest and in rotation is even starker. The same LMAC trends as in Fig. 6.8 can be seen, with the 60-rpm modes still in the transition region, while the modes at 180 and 300 rpm are virtually the same.

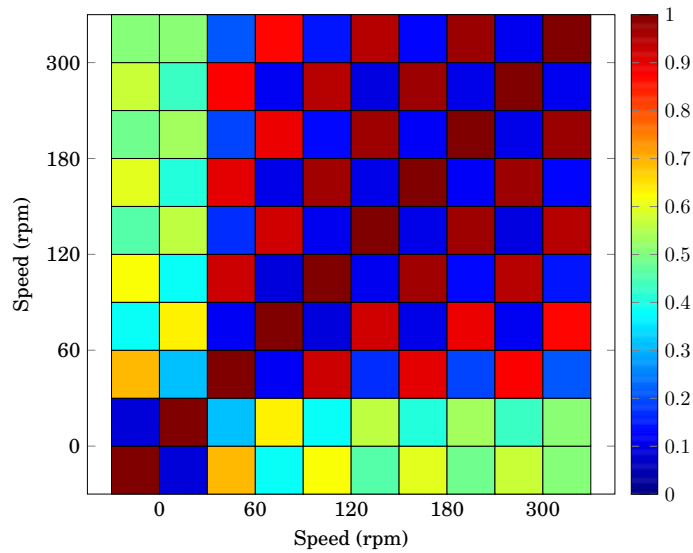


Figure 6.9: LMAC of the reconstructed strain gauge data (13 SGs), MIMO random, at different speeds, for the 3ND mode pair.

A more quantitative estimation of this evolution to complexity is the Mode Phase Collinearity (MPC) index. While it can be variously defined [27], a simpler formulation poses it as the MAC between a vector and its complex-conjugate [153]. A value of 1 is therefore expected only for real mode shapes, as their imaginary part is zero. The MPC matrix in Fig. 6.10a shows a similar pattern as the LMAC, as the modes at 0 and 6 rpm have near-unity MPC values, after which a transition region appears, indicating the emergence of complexity. After 60 rpm, the MPC “flips”, i.e. the MPC on the diagonal becomes 0, which indicates that the modes are no longer similar to their own conjugates. What happens instead is that the 3ND-FW modes become correlated to the complex-conjugate of the 3ND-BW mode. This is consistent with the fact that the complex-conjugation operator can be seen as changing the phase of the original vector to $2\pi - \varphi$ (φ being the phase of the original vector): in terms of TW representation, this consists in the inversion of the travelling speed (see sect. 2.3.3).

Fig. 6.10b shows the MPC through a wider range of rotational speeds, to give a clearer

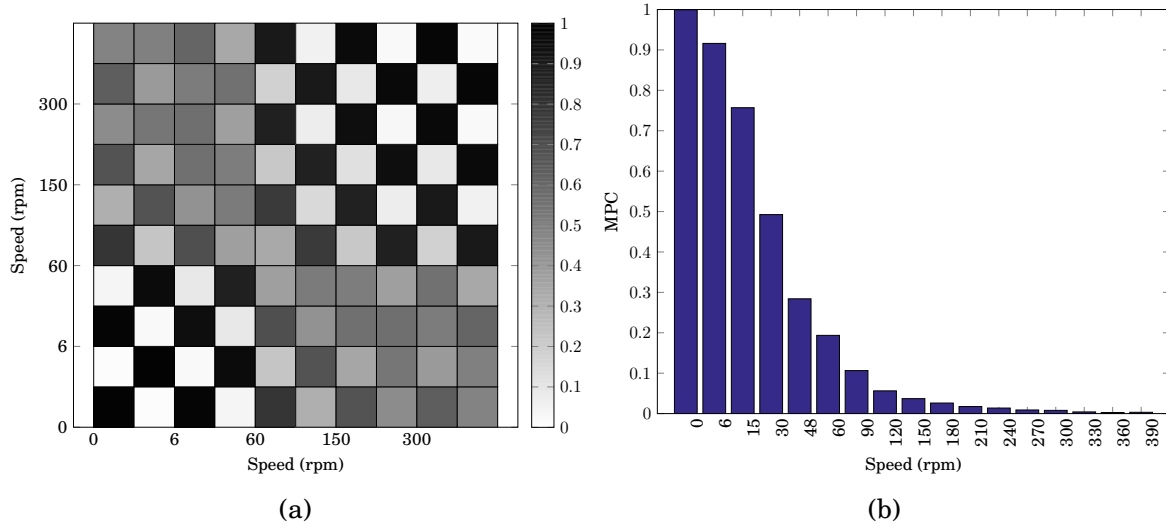


Figure 6.10: Mode Phase Collinearity (MPC) plot for the 3ND modes at different speeds. a) Comparison between 3ND-1 and 3ND-2 at different speeds. Two modes are present at each speed, as the second and third nodal diameters are double modes. b) MPC for 3ND-1 alone at different speeds (the 3ND-2 mode shows the same behaviour).

appreciation of its gradual variation, and of the appearance of fully complex behaviour. This is better quantified by looking at the actual complex form of the mode shapes, which is easily done by performing a DFT operation on them [20]. ND mode shapes, when sampled at each sector as with the eight circumferential SGs, are ultimately a periodic sequence of complex numbers. The modal constants ψ_j , with $j = 1, 2, \dots, N$, can be expressed as

$$\psi_j = \sum_{k=-\frac{N}{2}}^{\frac{N}{2}-1} X_k e^{i2\pi jk/N}. \quad (6.1)$$

This is equivalent to an IDFT performed between $-N/2$ and $N/2 - 1$, which corresponds to the number of signed NDs present in a cyclic-symmetric structure. The mode shapes can then be represented by a sum of DFT coefficients X_k corresponding to the various ND components. Coefficients with negative k indices correspond to FW components (negative ND), and positive k indices to BW components (positive ND). For a physical explanation of how this relates to travelling waves, it is necessary once again to add the time dimension, by multiplying eq. (6.1) by the generalised coordinate $q(t) = e^{i\omega t}$. Taking the real part of the result yields the following expression:

$$x_j(t) = \sum_{k=-N/2}^{N/2-1} X_k \cos(\omega t + k\varphi),$$

with φ equal to the usual interblade phase angle. When considering pure ND modes, $|k|$ reduces to the respective ND number, which translates to

$$x_j(t) = X_{-k} \cos(\omega t - k\varphi) + X_k \cos(\omega t + k\varphi). \quad (6.2)$$

Eq. (6.2) represents a generic wave. The relative amplitude of the DFT coefficients X_{-k} and X_k therefore determines whether standing waves, travelling waves, or a mixture of the two will occur. Since for the 3ND mode no significant contribution from other NDs was present, only the 3ND-FW and 3ND-BW components are shown in Fig. 6.11.

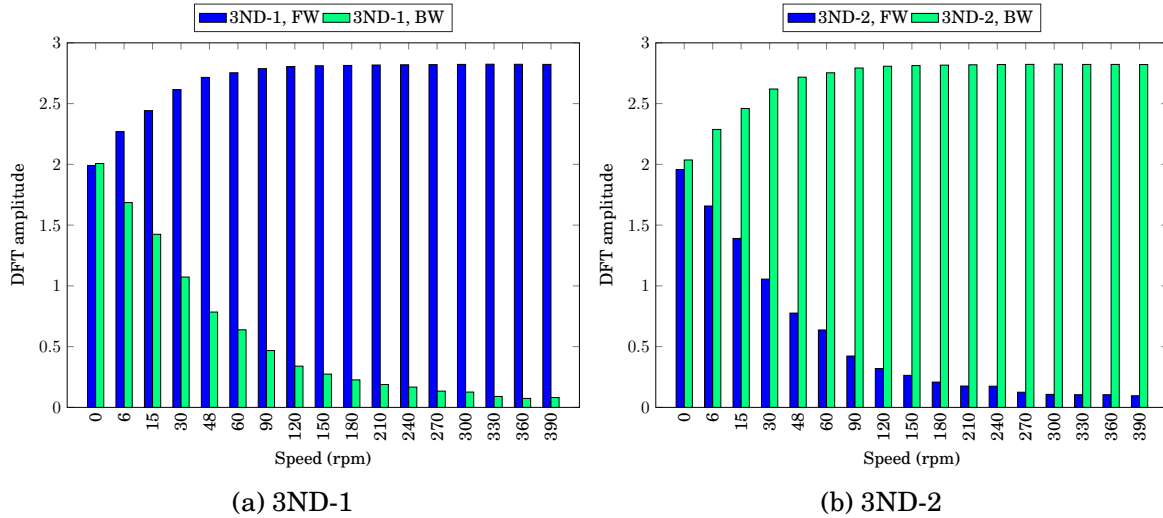


Figure 6.11: Evolution of the spatial DFT components of the 3ND modes with speed.

The spatial components for the 3ND-1 mode appear in Fig. 6.11a. At rest, the DFT amplitudes are equal, which results in a standing wave, as demonstrated by the real mode shapes identified above. As speed is increased, it can be seen that the two BW and FW components start to diverge, with the FW ($k = -3$) increasing, and the BW ($k = 3$) decreasing. The BW component becomes negligible only after 180 rpm, which means that a full FW-TW mode has developed, while at lower speeds, standing and travelling waves coexist. The same, and opposite, behaviour applies to the 3ND-2 mode (Fig. 6.11b), where it is the FW component to gradually disappear, while the BW-TW progressively predominates. The presence of a SW component would not be caused by the Coriolis effect: as explained in sect. 2.3.3, the Coriolis effect inevitably causes the appearance of complex modes, regardless of the value of the rotational speed. The coexistence of TW and SW characteristics is due instead to mistuning, and will be treated in the next section.

6.2.3 Effect of mistuning

While the 3ND mode is affected by a low degree of mistuning, the 2ND has a 2% frequency split already at rest. The full Campbell diagram, extracted from MIMO random data, is in Fig. 5.17a. The FW and BW branches are separated from start by a 4 Hz split, and maintain a near flat trend until 90 rpm, as confirmed by the frequency split plot in Fig. 5.17b. After 90 rpm, the curves slowly start diverging, and the split widens. The rotational speed range appears thus divided into two areas, one in which the Coriolis effect is absent, and the split is purely due to mistuning, and one in which it is active.

This is only partially confirmed by analysing the harmonic components in the 2ND mode shapes (Fig. 6.12). The two figures show, as before, the DFT components of the 2ND-

1 and 2ND-2 mode shapes at different speeds. In both cases, the FW and BW components are equal at 0 rpm, which produces a standing wave. A standing wave is also present at 6 rpm, while for the 3ND, at this point a weak TW was already developing (Fig. 6.11). After this, however, a difference between the two coefficients starts appearing, which means that a small TW components has formed. This gap widens progressively in a non-linear way, and predictably reaches a maximum at the maximum velocity, 390 rpm, where a definite TW is present. The SW contribution is far from negligible, while in the 3ND case it had basically disappeared at 210 rpm.

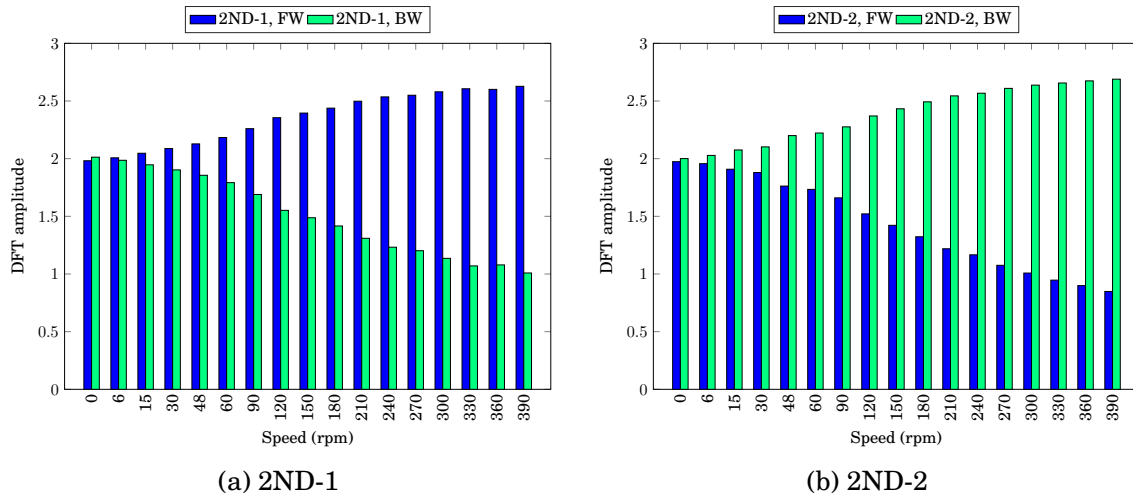


Figure 6.12: Evolution of the spatial DFT components of the 2ND modes with speed.

The relative importance of SW and TW components can be appreciated qualitatively in Fig. 6.13. Fig. 6.13a shows the evolution of the strain amplitude for the 2ND-2 mode shape (the 2ND-1 follows the opposite pattern), as derived in sect. 6.2.1. The SW can be recognised in the presence of distinct time instants ($0, \pi/\omega$) when *all* sectors go through zero strain at the same time, and the points of maximum and minimum strain remain fixed in space. At 300 rpm (Fig. 6.13b), the behaviour is only slightly different: the maximum and minimum strain levels are fixed at the same sectors (1, 3, 5, and 7) through the whole vibration cycle, but the instants of global zero strain have disappeared. While sectors 2, 4, 6, and 8 never reach the actual maximum strain values of the others, neither are they true nodal diameters, and a faint rotation can be seen between $\pi/6$ and $\pi/3$: the SW pattern is still strong, but a TW (BW in this case) is present.

The LMAC was again used (Fig. 6.14) to assess the self-correlation of the mode shapes with increasing speed. As in Fig. 6.8, both 2ND-1 and 2ND-2 were included at each speed. A high degree of correlation is present between the modes at all speeds: the lowest LMAC that is reached between two 2ND-1 modes is between the mode at 0 and 390 rpm, and is still above 0.6. This indicates that the presence of the SW keeps the modes similar in a wide speed range. The LMAC between the modes at 210 rpm and 390 rpm is only 0.9, which, while still being a sign of high correlation, shows that significant differences are present.

The MPC (Fig. 6.15) provides an even more definite interpretation: the mode shapes

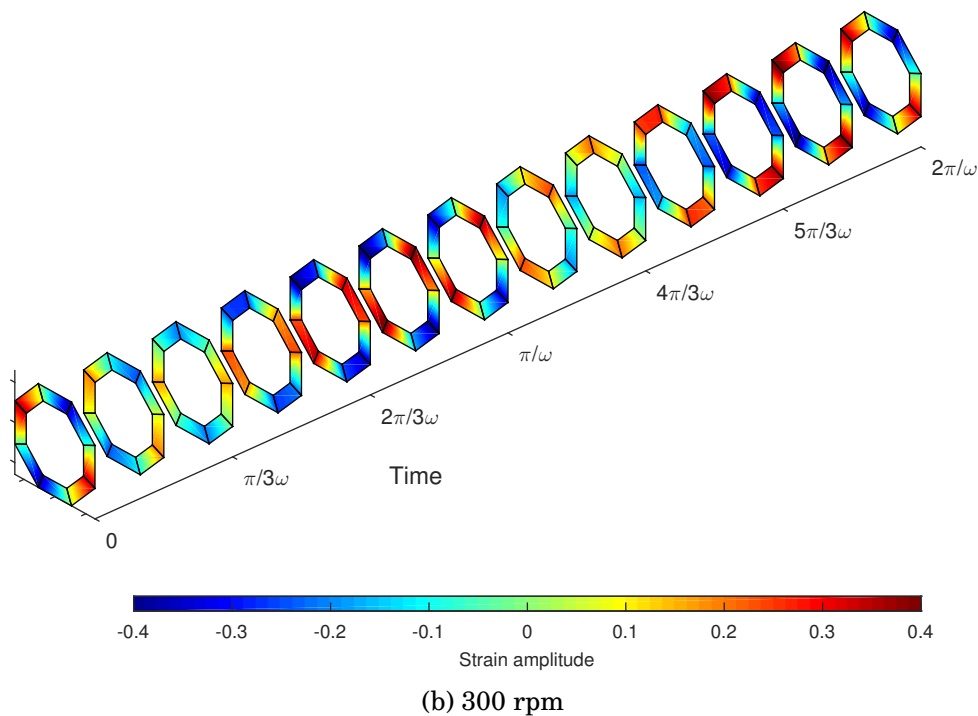
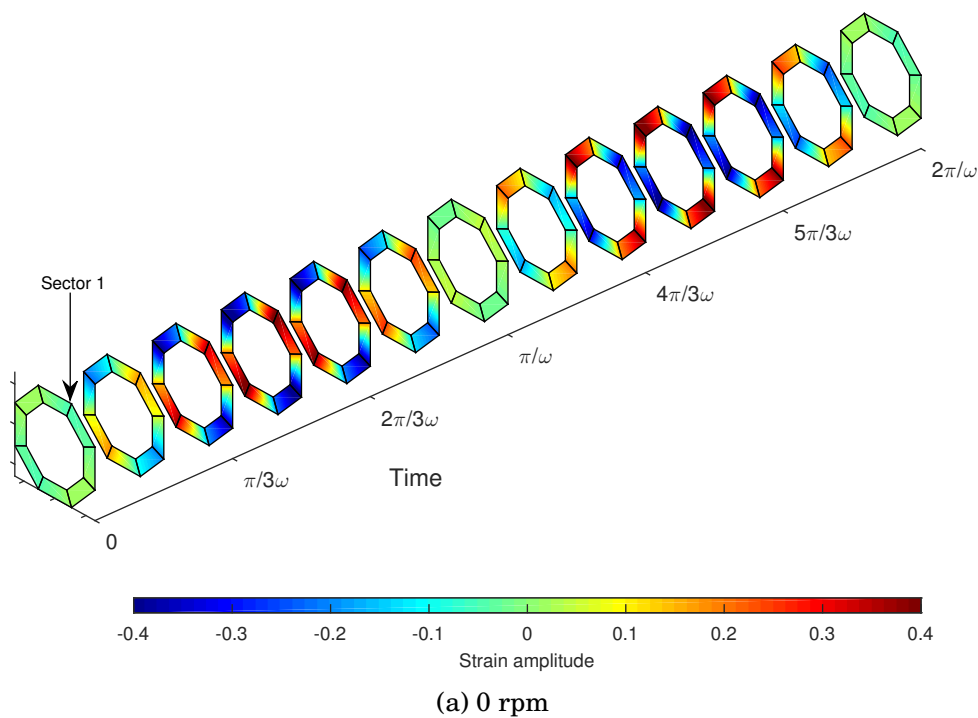


Figure 6.13: Strain travelling wave for the 2ND-BW mode at different speeds.

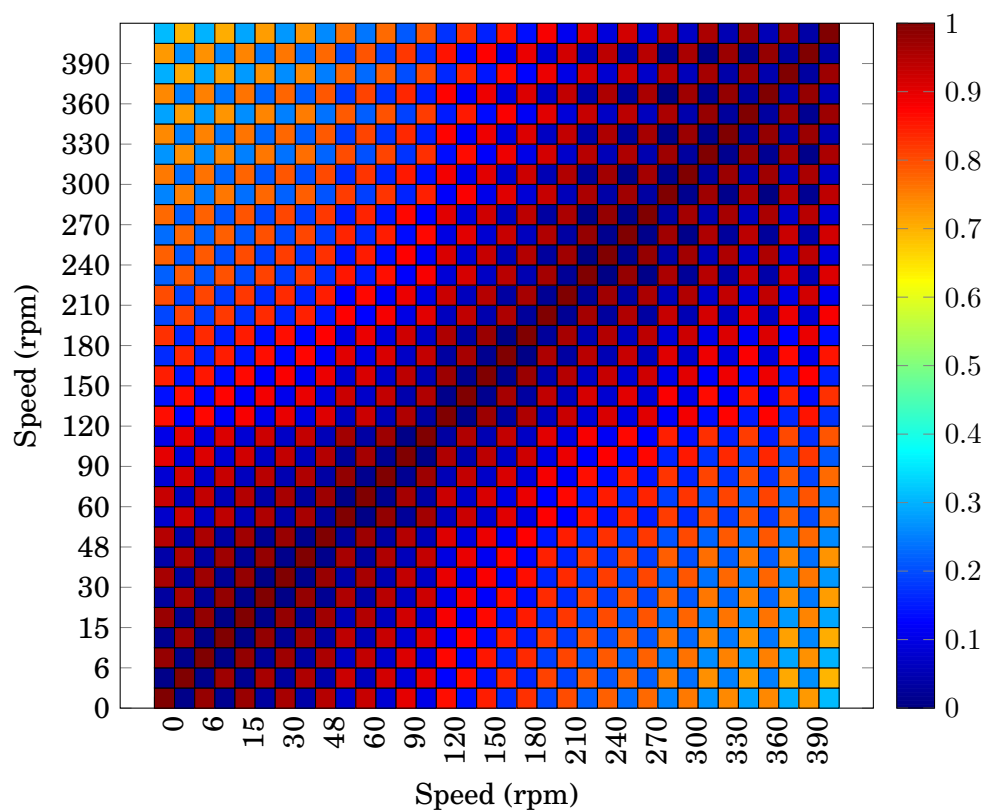


Figure 6.14: Linearised Modal Assurance Criterion (LMAC) matrix between 2ND mode pairs at different speeds, MIMO excitation. Two modes are present at each speed, as the second and third nodal diameters are double modes.

stay fundamentally real up until 150 rpm, and seem to develop a significant complex character only at 300 rpm (Fig. 6.15a). This is confirmed by the results in Fig. 6.15b, where the modes show near-perfect correlation with their complex-conjugates up until 60 rpm. After this, the rate at which complexity develops increases, and finally seems to stabilise at 300 rpm. This suggests that the SW component would fade very slowly, even though the Coriolis effect is active enough to both cause an increase in the frequency split, and the formation of travelling waves.

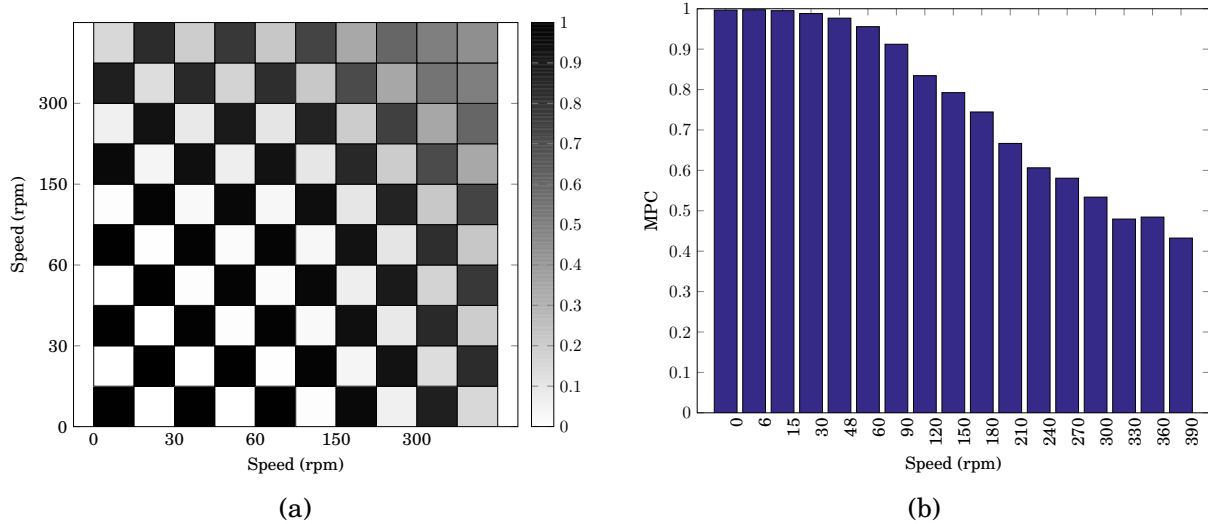


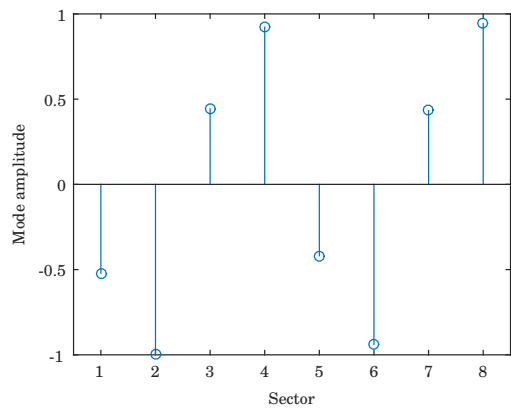
Figure 6.15: MPC plot for the 2ND modes at different speeds. a) Comparison between 2ND-1 and 2ND-2 at different speeds. Two modes are present at each speed, as the second and third nodal diameters are double modes. b) MPC for 2ND-1 alone at different speeds (the 2ND-2 mode shows the same behaviour).

6.2.4 Left eigenvectors

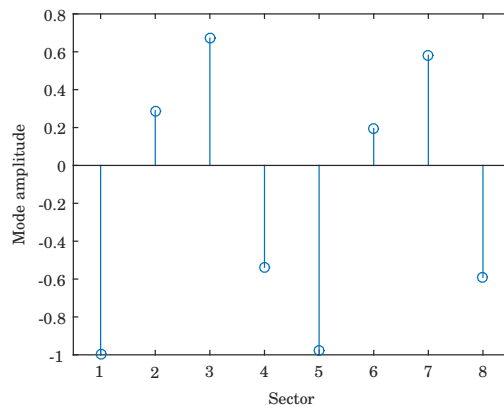
As explained in sect. 2.4.2, when using strain gages, the FRFs of rotating structures depend on the strain mode shape components at the output DOFs, and on the left *displacement* eigenvector components at the *input* DOFs. In this case, the input DOFs correspond to the positions of the MFC actuators at each sector. The left displacement eigenvectors for the 2, 3, and 4ND modes at rest are plotted in Fig. 6.16. It can be seen that the left eigenvectors are characterised by nodal diameters, and are real-valued at zero speed, just as mode shapes would be.

Left displacement eigenvectors have never been extracted in rotational conditions before. It was therefore decided to seek further proof that the extraction method, based on the pLSCF method described in sect. 2.4.4, was valid. In particular, it was important to show that the left eigenvectors are entities in their own right, and their measured components depend only on the locations of the actuators, and not on those of the sensors.

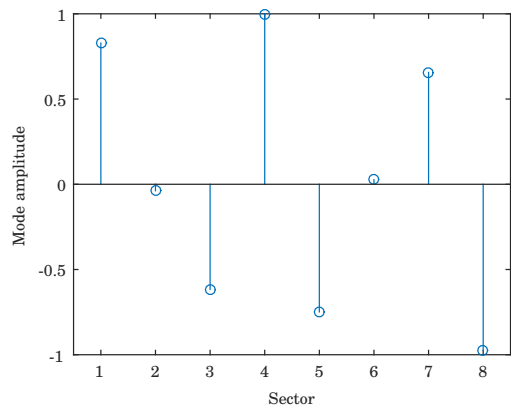
Two different sets of measurement strain DOFs were then used to extract the left eigenvectors: in one case, the eight circumferential SGs were used for the FRFs, and, in the other, the seven sector SGs. The left eigenvectors were then compared with a MAC for the first 6 nodal diameter modes, and the diagonal of the matrix is shown in Fig. 6.17. The use



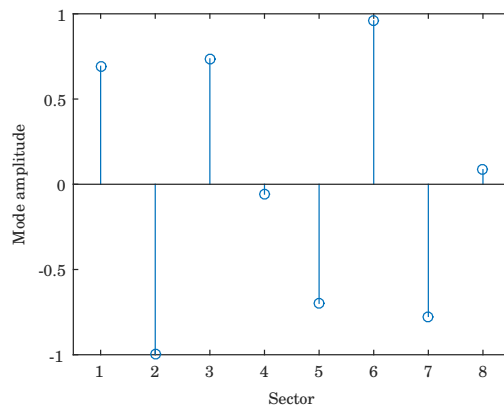
(a) 2ND-1



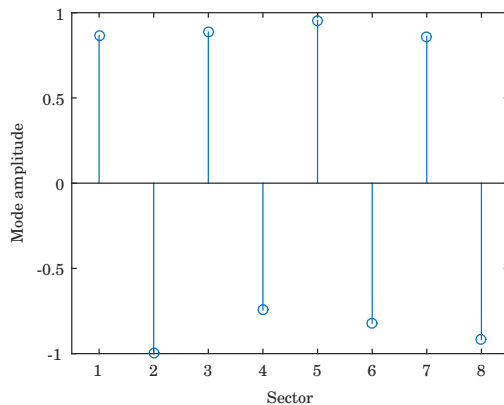
(b) 2ND-2



(c) 3ND-1



(d) 3ND-2



(e) 4ND

Figure 6.16: Modal amplitudes of the left displacement eigenvectors at the eight MFC locations, at rest, normalised to unity.

of different output DOFs yields widely different FRFs and strain mode shapes, but the resulting left eigenvectors consistently have MACs above 0.95, and for the most part higher than 0.98. This shows a very good level of agreement, and proves that the extracted left eigenvector components are independent of the strain mode shape DOFs.

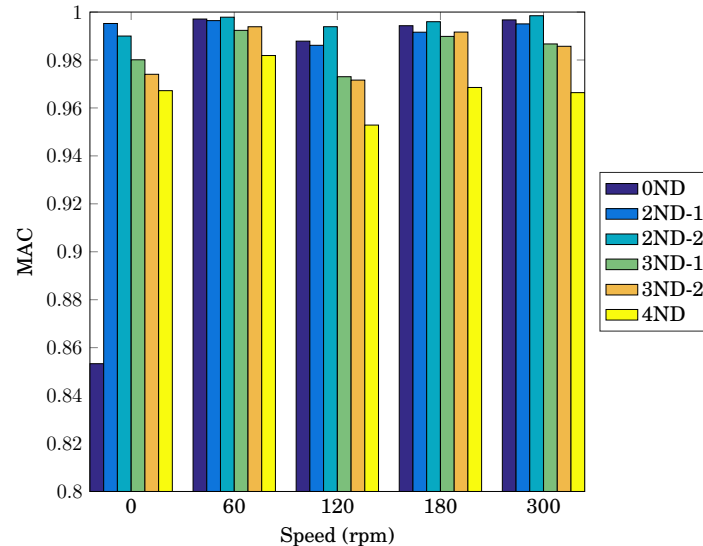


Figure 6.17: MAC between left eigenvectors extracted for the first 6 modes, at different speeds, from two different strain gauge configurations: only the eight circumferential SGs, and only the seven sector SGs.

6.3 Validation

6.3.1 Campbell diagrams

The experimental findings of the test campaign have been presented in the previous sections. General agreement has been found between the results and the theory behind the Coriolis effect, but quantitative validation is still needed to define the adequacy of the new testing methodology. The experimental results were therefore compared to the frequencies and mode shapes obtained from FEA. As explained in sect. 4.8.2, the FE model used during the design phase of the test piece was updated using the natural frequencies extracted at rest. The updating process was aimed at reaching perfect agreement for the frequency at rest of the 3ND modes, as they were chosen to be the main focus of the validation process, and the only updated parameter was the Young's modulus of the steel. This proved enough to ensure a very good agreement between the experimental Campbell diagram, and the one calculated in NX Nastran for the first 6 modes is shown in Fig. 6.18. In this case, NX Nastran was chosen for its convenient automated Campbell diagram generation feature, which shortened the simulation times considerably.

Perfect overlap between the 3ND measured and FE frequencies was reached. For the other modes, the discrepancy is visible, but it amounts to a maximum difference of only 2% for the 2ND modes (error for 0 and 4ND modes being 1%). This was due to mistun-

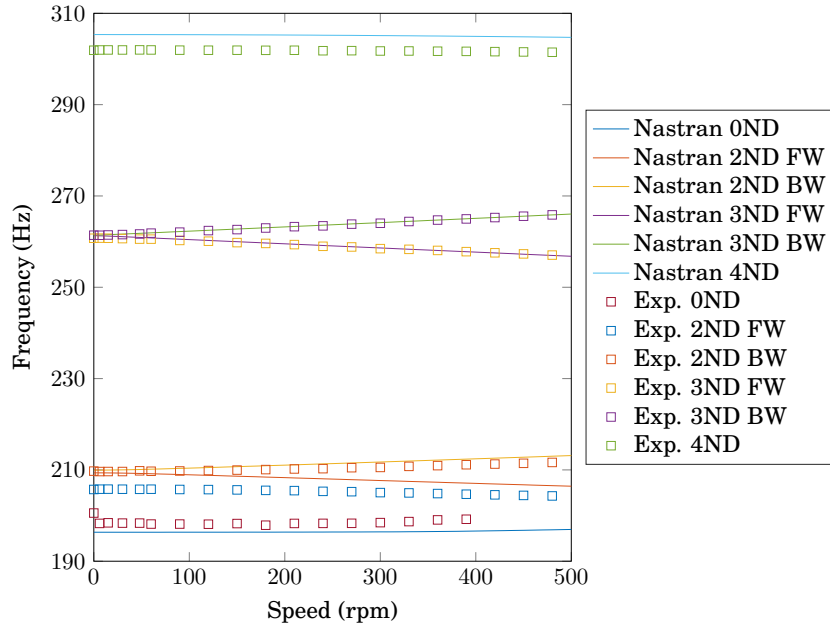


Figure 6.18: Comparison of the experimental and computed (NX Nastran) Campbell diagrams for the first six modes of the test piece.

ing: a mistuning pattern was introduced to provide a better match for the 2ND modes, in the form of different Young’s moduli for the blades, but it was not possible to reproduce computationally the large frequency split observed experimentally.

The splits were then checked, and are reported in Fig. 6.19 for the 2ND and 3ND modes. It can be seen that the split for the 3ND mode is linear (Fig. 6.19a), which reflects the linearity of the Coriolis force itself. Experimental and FE data show excellent agreement in this case.

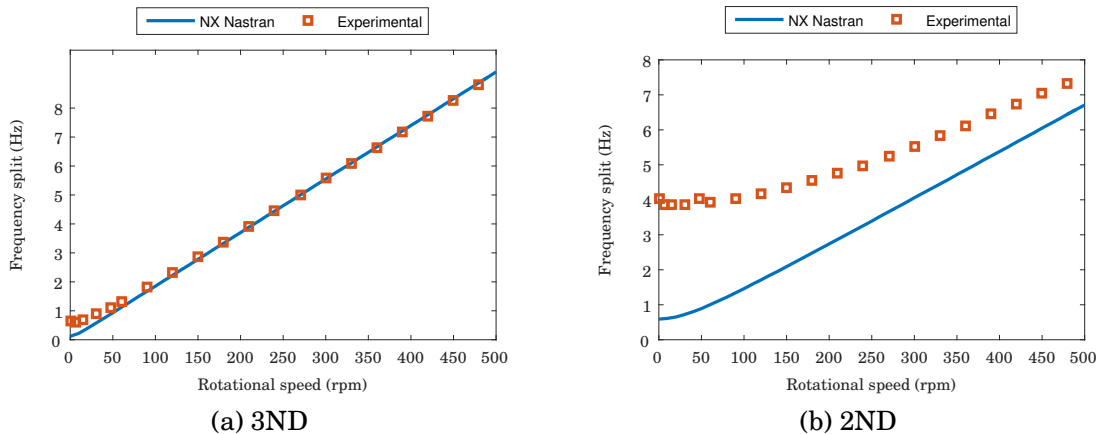


Figure 6.19: Frequency split curves: Comparison between the experimental and NX Nastran data.

For the 2ND split (Fig. 6.19b), a wide difference exists between FE and experimental splits, as the real mistuning pattern could not be reproduced. However, the Nastran split shows a small speed range, between approximately 0 and 60 rpm, where the split varies nonlinearly, which mirrors the behaviour of the experimental data. The experimental split

stays close to the one induced by mistuning up until 120 rpm, after which it varies nonlinearly before becoming linear, and approaching the FE split nearly asymptotically.

6.3.2 Strain mode shapes

With an updated model available, mode shapes were then verified, and Abaqus used as the main validation tool. To compare the experimental and Abaqus mode shapes, it was necessary to normalise the two sets. In particular, it is essential to remember that, with complex mode shapes, even two mode shapes with identical amplitudes would yield low MACs, if the two are rotated with respect to each other [153]: since eigenvectors (hence, mode shapes) are defined within a multiplication factor, multiplying a complex mode by a complex number would still yield the same mode, but phase-shifted (rotated along the circumference, in case of a bladed disc).

For this reason, it was decided to normalise the two mode shapes by finding the complex constant that would minimise the norm of the difference between the Abaqus and experimental mode vectors, in a least-square sense. The Abaqus modes were taken as reference, and the complex constant was then used to multiply the experimental mode shapes. This complex constant thus acts purely as a scaling factor, to rotate the mode shapes so that they can be compared reliably.

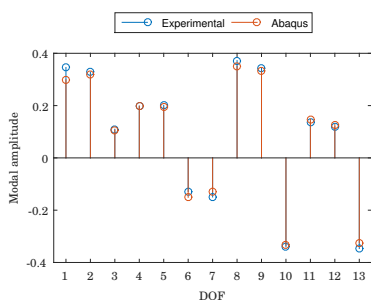
The individual modal constants for the reconstructed (13 SGs) mode shape at 300 rpm from experiment and Abaqus are superposed in Figs. 6.20–6.21. For the 3ND modes (Fig. 6.20), the experimental real and imaginary parts are nearly coincident with their computational counterpart. It is noticeable that the imaginary part is not negligible, indicating the presence of a TW component.

This does not apply to the 4ND mode, which is a single mode, and always purely real. Abaqus correctly predicts a null imaginary part, while in the experimental data, the modal constants have non-zero imaginary components. However, they amount to 10% at most of the real part values, whereas for double modes they reach the same values as the real parts. These spurious components can therefore be considered a negligible product of the inevitable inaccuracies rising from mode shape extraction from noisy data.

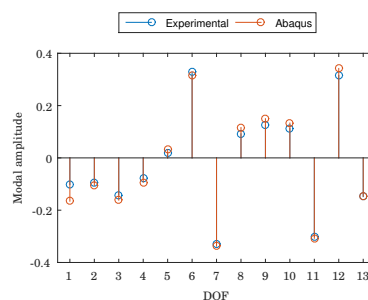
Agreement is mixed for the 2ND modes (Fig. 6.22): the real and imaginary parts of the Abaqus and experimental modal constants do tend to follow the same amplitude variation pattern across the DOFs, but their amplitudes do not match. The disagreement, in particular, comes from the ratio between real and imaginary parts: the real part is always underestimated, while the opposite applies to the imaginary part.

A MAC was also derived between the first 6 modes from Abaqus and experiment (Fig. 6.23). The MAC matrices are strongly diagonal, proving that computational and experimental modes are well matched. At rest (Fig. 6.23a), the MAC diagonal values are greater than or equal to 0.98, proving excellent correlation between computational and experimental modes.

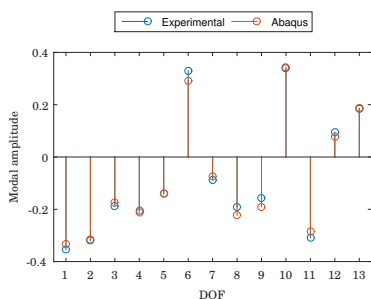
The exception is the 0ND, with a MAC of 0.79. As explained above, it was decided to attempt to mistune the model to reach more realistic results for the 2ND modes. The



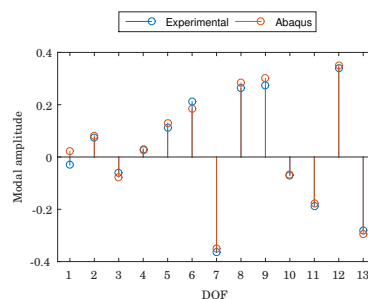
(a) 3ND-1, real part



(b) 3ND-1, imaginary part

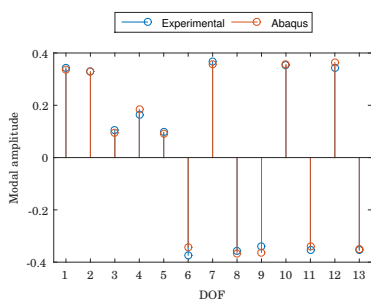


(c) 3ND-2, real part

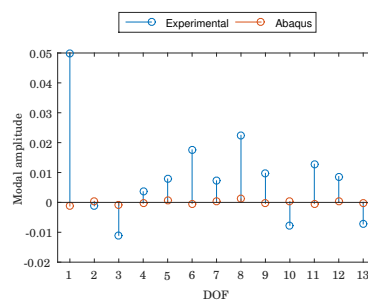


(d) 3ND-2, imaginary part

Figure 6.20: Comparison between the experimental and Abaqus reconstructed 3ND mode shapes at 300 rpm.



(a) 4ND, real part



(b) 4ND, imaginary part

Figure 6.21: Comparison between the experimental and Abaqus reconstructed 4ND mode shapes at 300 rpm.

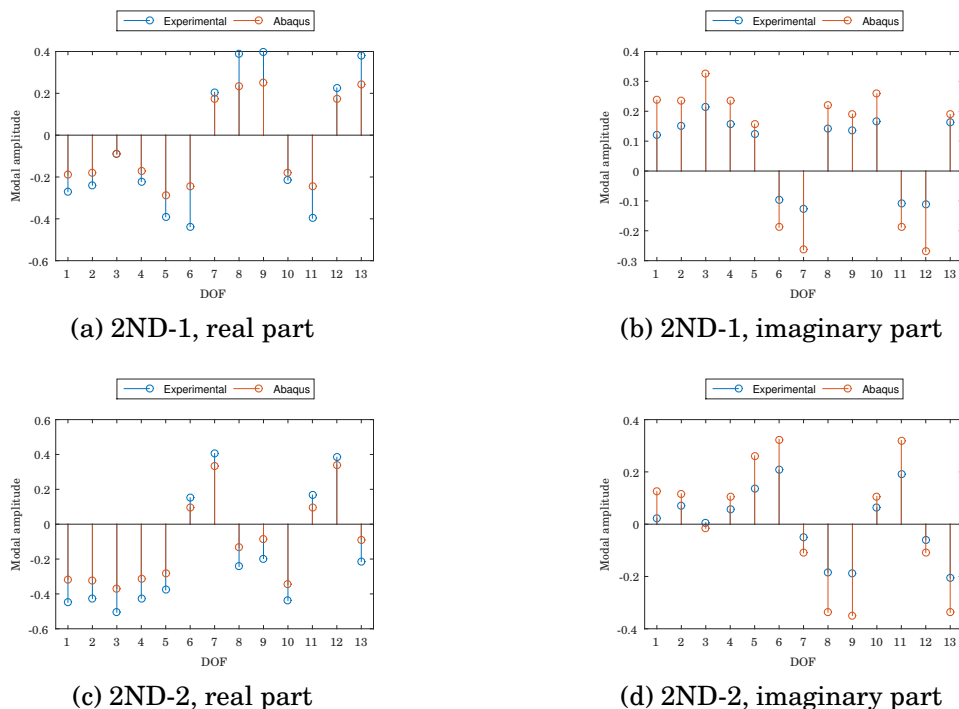


Figure 6.22: Comparison between the experimental and Abaqus reconstructed 2ND mode shapes at 300 rpm.

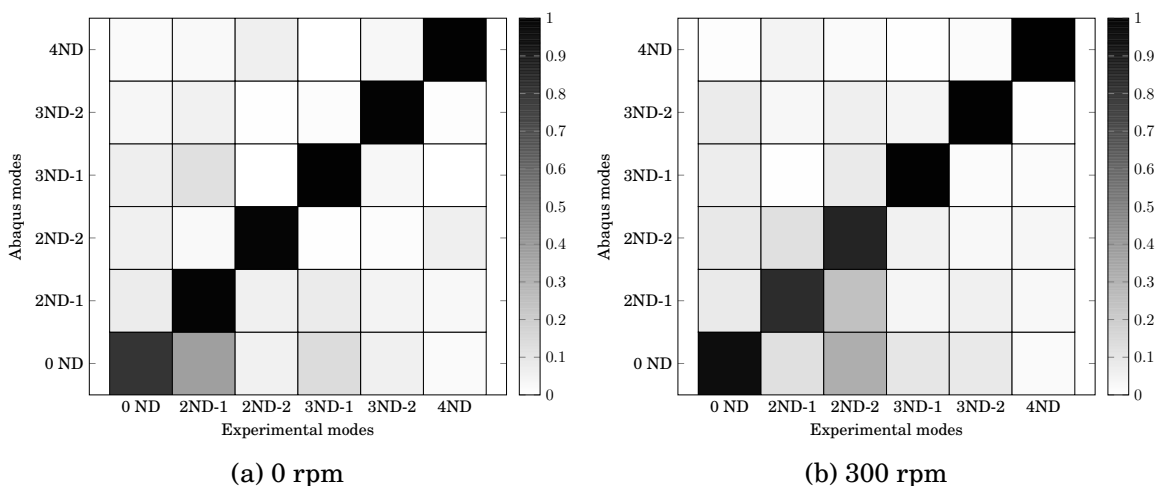


Figure 6.23: MAC between the reconstructed strain mode, MIMO random, and the Abaqus modes.

added mistuning pattern allowed an increase in the MAC at rest to 0.98 both for 2ND-1 and 2ND-2, but significantly deformed the 0ND mode, leading to the corresponding 0.79 MAC.

This mistuning pattern, despite having a large impact on the mode shape, produced a very small increase in the frequency split, as shown in Fig. 6.19b. From the experimental data, this suggests that the Coriolis effect would cancel the mistuning-induced standing wave already at low speeds in the FE model, whereas sect. 6.2.3 proved that a strong standing wave is present throughout all the investigated range of rotational speeds in the real test piece. This discrepancy causes the low MAC value of 0.85 for the 2ND modes at 300 rpm (Fig. 6.23b): the applied mistuning pattern in the FE model is not strong enough, and still allows a fully-developed TW mode, which does not match the coexistence of SW and TW of the experimental modes.

This is even clearer in the NMD values, which are reported for the same modes in Table 6.1. Besides the very large errors for 0ND, it can be seen that all the other modes show relatively low average discrepancies with the computational ones at rest. The situation changes at 300 rpm, where the 2ND modes have errors of 46% and 41% due to the absence of a SW component in the Abaqus modes. The 3ND modes, on the other hand, are only marginally affected by mistuning, and they display low average discrepancies both at rest and at higher speed.

Table 6.1: NMD between the reconstructed strain modes, MIMO random, and the Abaqus modes, at rest, and at 300 rpm.

Mode number	NMD (%)	
	0 rpm	300 rpm
0ND	50.68	50.39
2ND-1	13.79	45.72
2ND-2	13.06	40.65
3ND-1	8.69	9.34
3ND-2	10.37	9.25
4 ND	9.45	7.35

6.3.3 Left eigenvectors and displacement mode shapes

It was remarked in sect. 6.2.4 that, in the case of strain modal analysis, the mode participation factors take the form of the left displacement eigenvectors. In sect. 2.4.2, it was also noted that, for lightly damped structures, left eigenvectors can be approximated by right eigenvectors [101, 154], i.e. the displacement mode shapes, in this case. As the extraction of left eigenvectors is not a standard feature of current FE software packages, the experimental left eigenvectors as derived through the pLSCF method had to be compared to the FE displacement mode shapes from a standard Abaqus modal analysis. Having reached at this point a good level of confidence in the modal identification process, this could be used to validate the accuracy of this approximation.

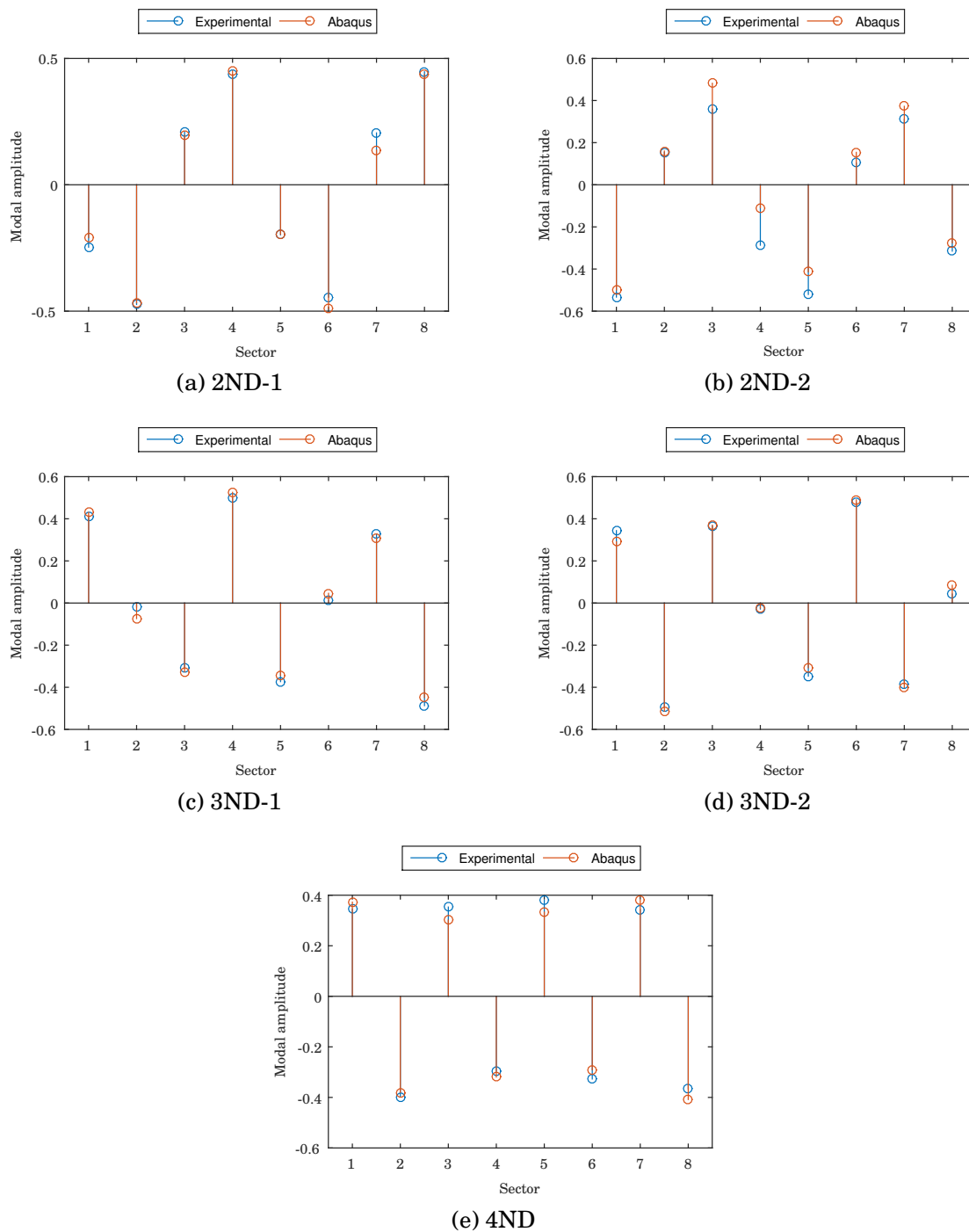


Figure 6.24: Left eigenvectors at rest, extracted from the SFRFs at the sector SGs, normalised to unity.

The components of the FE and experimental left eigenvectors at rest are compared in Fig. 6.24. At rest, the left eigenvectors extracted through the pLSCF method are the actual radial displacement modes at the input DOFs. This is reflected in the very close agreement between the two data sets.

The real and imaginary parts of the left eigenvectors/displacement mode shapes at 300 rpm, and the comparison between Abaqus and experiment, are reported in Figs. 6.25–6.27. As seen for the strain mode shapes (Fig. 6.20), agreement is only qualitative for 2ND (Fig. 6.25). It can be seen that the imaginary components predicted by Abaqus (Figs. 6.25b and 6.25d) are up to twice as large as the measured ones: this is again due to the strong SW present in the real blisk, and not reproduced in the FE model.

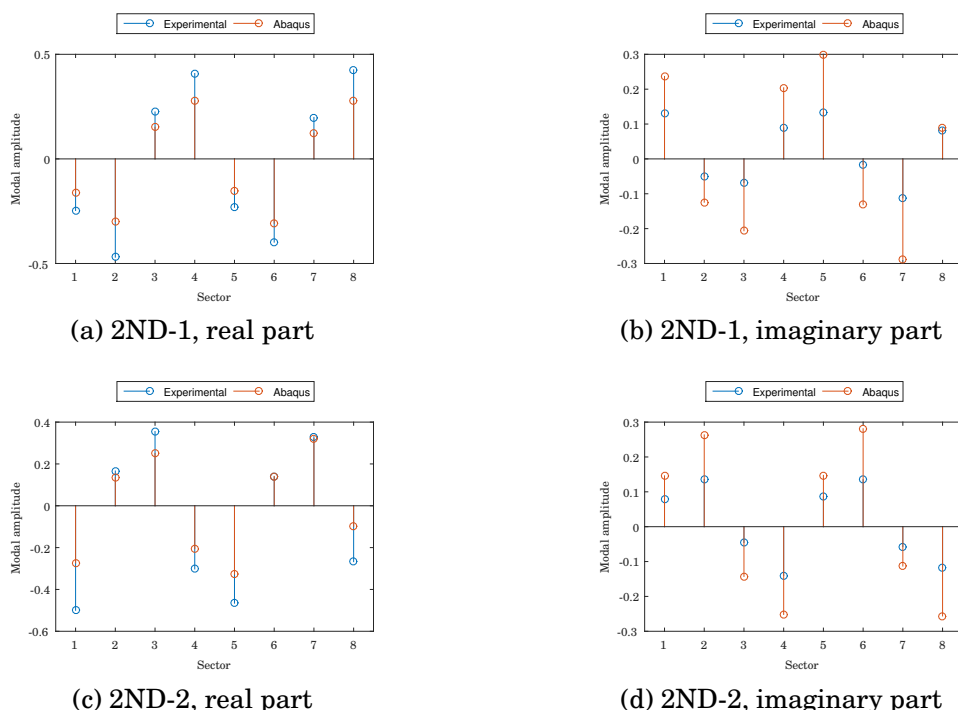
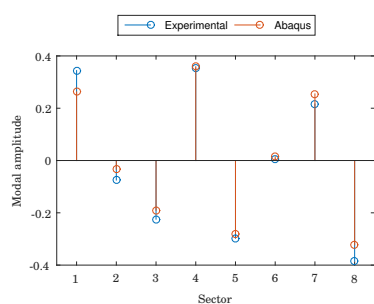


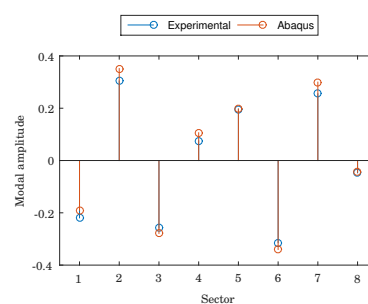
Figure 6.25: Comparison between the experimental left eigenvectors and Abaqus displacement mode shapes at 300 rpm, for the 2ND mode.

Much closer correspondence is found for 3ND (Fig. 6.26) and 4ND (Fig. 6.27) modes. An imaginary component is still detected in the latter (Fig. 6.27b), but is again comparatively negligible.

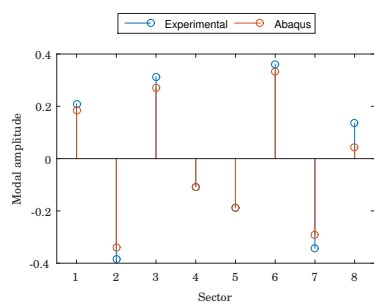
A more quantitative assessment of these results is shown in Table. 6.2, with the MAC and NMD values for the comparison between computational and experimental values at 0 and 300 rpm. The 0ND is not shown because, as discussed above, its MAC would not be representative, as the FE mistuning pattern was not updated for optimal match with all modes. MAC values are very high at rest, indicating a good similarity between the two sets of modes, and the relative error is acceptable. The MPC was also added, only for the experimental data, to provide an idea of the degree of complexity of the relative mode. It can be seen that, at rest, the MPC is always very close to 1, confirming that all experimental modes were correctly extracted as real.



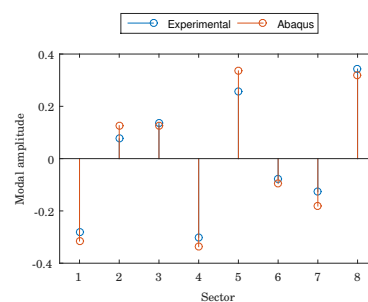
(a) 3ND-1, real part



(b) 3ND-1, imaginary part



(c) 3ND-2, real part



(d) 3ND-2, imaginary part

Figure 6.26: Comparison between the experimental left eigenvectors and Abaqus displacement mode shapes at 300 rpm, for the 3ND mode.

Results vary with mode shape family at 300 rpm. For the 2ND family, MAC is relatively low, at around 0.78 for both modes, with a corresponding high NMD. This highlights once again the discrepancy between experiment and model, where mistuning was not properly captured. This is suggested by the corresponding MPCs, which, at 0.74 and 0.67 respectively, show that the two 2ND left eigenvectors are still very close to real, and no proper TW has developed. The 4ND mode appropriately shows a high MPC, as it stays real at all speeds. The low NMD also proves the good match between experimental eigenvectors and Abaqus model.

For the 3ND modes, the MAC is still very high, and the NMD values are also acceptable, indicating good correspondence between data and model. Fittingly, the MPC is very low, as the 3ND displacement mode shapes, like their strain counterparts, are expected to be fully complex at this speed.

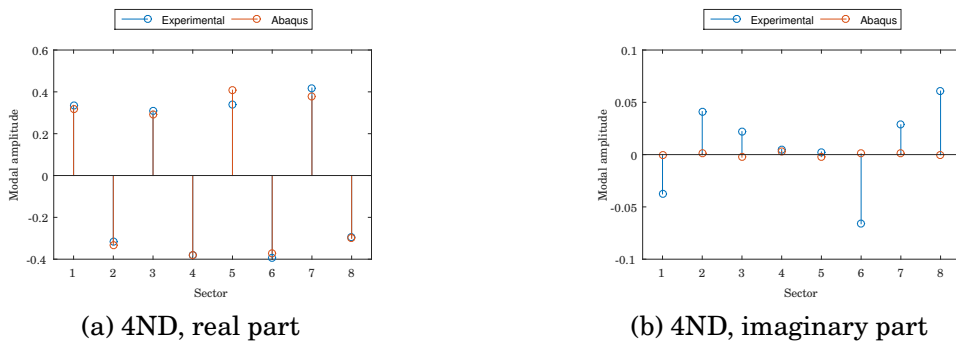


Figure 6.27: Comparison between the experimental left eigenvectors, and Abaqus displacement mode shapes at 300 rpm, for the 4ND mode.

6.4 Discussion of results

6.4.1 Mode shapes

This chapter offered three main results: further insight into the effects of the Coriolis force on mode shapes, in tuned and mistuned conditions; a validation of the developed experimental framework; and finally the identification and validation of the left eigenvectors arising in rotating structures.

Table 6.2: Comparison between the experimental and Abaqus displacement mode shapes (left eigenvectors) at rest, and at 300 rpm.

Mode	0 rpm			300 rpm		
	MAC	NMD (%)	MPC	MAC	NMD (%)	MPC
2ND-1	0.9905	9.80	0.9962	0.7798	53.13	0.7432
2ND-2	0.9493	17.58	0.9864	0.7897	51.61	0.6746
3ND-1	0.9897	10.21	0.9912	0.9776	15.14	0.0272
3ND-2	0.9887	10.70	0.9824	0.9692	17.83	0.0402
4ND	0.9831	13.11	0.9764	0.9803	14.19	0.9506

The data gathered in Figs. 6.2, 6.3e, 6.3f, and 6.4a showed that complex mode shapes develop in rotation, and they take the form of a travelling wave in the blisk, so that all sector can experience maximum-amplitude oscillations. These results confirm that the poly-reference modal identification method described in sect. 2.4.4 has no difficulty handling either real mode shapes, or the highly complex eigenvectors caused by the Coriolis effect.

The effect of rotational speed on the mode shapes could then be investigated reliably. The two 3ND mode shapes (FW and BW) at each speed were compared between themselves, using the LMAC tool. The greater resolution power of the LMAC allowed to distinguish small variations in the mode shapes from speed to speed, and conclude that, after 180 rpm, the 3ND mode shape, as measured by the eight circumferential strain gauges, is virtually independent from rotational velocity (Fig. 6.8). This is predictable, as, once the TW behaviour has fully developed, all DOFs at corresponding locations on each sector will reach the same amplitude, and have a phase determined by the IBPA. In this configuration, with only one DOF per sector, all fully complex mode shapes belonging to the same ND family are inevitably identical, as the spatial vibration pattern is proportional to $\cos \varphi_k$, and is thus determined by the IBPA, which does not depend on speed.

To gain a better understanding of the evolution of the modes with speed, it was therefore necessary to add the data from the sector DOFs. The sector DOFs are not correlated by the IBPA, and thus add information about the mode shape. It was therefore interesting to see that, in Fig. 6.9, the LMAC of the mode shape, reconstructed from strain data from the circumferential and sector DOFs, exhibits the same behaviour as Fig. 6.8. This suggests that the Coriolis force has no further effect on the mode shapes beyond causing them to assume TW form, if no significant centrifugal stiffening is present.

This is further confirmed by the MPC calculated for the 3ND mode pair. Fig. 6.10a shows that, at high speeds, where the TW behaviour has fully developed, the 3ND-FW mode becomes progressively closer to simply being the complex-conjugate of the 3ND-BW, as the MPC between the two approaches unity. If indeed the Coriolis effect only causes the appearance of a travelling wave, the spatial form of the vibration pattern would be identical for both FW and BW modes, provided the nodal diameter is the same: the sector mode shape $\tilde{\psi}_k$ in Eq. (2.26) would then stay constant. The resulting FW or BW direction of propagation of the pattern is simply determined by a negative or positive value of the IBPA φ_k , respectively. From Eq. (2.26), it can be seen that, if the sector mode shape $\tilde{\psi}_k$ is not affected by the Coriolis force, FW and BW modes do become complex-conjugates due to the factor $e^{i\varphi_k}$.

6.4.2 Mistuning

Multiple indications have been found from the experimental results that TW behaviour does not develop as soon as the blisk starts rotating. For the 3ND mode pair, the multi-speed LMAC of Fig. 6.8 showed a transition zone at lower speeds, where the mode shapes exhibit low degrees of correlation with the higher-speed modes. This indicates that a pure

TW cannot be present, since, as argued above, corresponding TW modes at different speeds are the same. Fig. 6.11 confirms that a large standing wave component is present up to 60 rpm. Eq. (2.26) showed that cyclic-symmetric structures always admit TW modes, but a SW mode can be obtained via linear superposition of the BW and FW waves corresponding to the same eigenvalue. Considering that the Coriolis effect does not allow the existence of standing waves, a complex mode should appear as soon as the rotational speed is increased from zero, if the structure is truly symmetric.

These transition zones coincide with the speed ranges of different frequency split behaviour identified in Fig. 6.19: a low speed range, where the split stays constant at the level set at rest by mistuning, an intermediate range of nonlinear variation, and a high-speed range of linear increase. The only plausible source for the SW components is thus mistuning, which, violating the cyclic symmetry hypothesis, causes the modes to be locked in place: since each sector of a mistuned blisk has different physical properties (mass, stiffness, . . .), the modes can no longer be arbitrarily rotated around the structure.

This is supported by the coupled results from the 3ND and 2ND mode pairs, which are similar in behaviour, but different in scale. The 3ND mode is affected by a very low degree of mistuning, as evidenced by a frequency split at rest of 0.3%. The 3ND mode thus shows a transition zone, with coexistence of TW and SW modes, and near-constant frequency split, but it is very narrow: the dynamics of the blisk can be considered exclusively dominated by the Coriolis effect after 48 rpm.

The split for 2ND modes at rest, on the other hand, is 2%. The range of constant split (within 4%) goes from 0 up to 120 rpm, after which it starts slowly increasing as would be expected for a structure subjected to the Coriolis effect. Likewise, the SW component is dominant for more than half the speed range. This is confirmed by Fig. 6.14, which shows that the 2ND mode shapes remain similar over a wider speed range, and are nearly perfectly real-valued up to 90 rpm (Fig. 6.15b).

A significant SW participation remains even after the Coriolis-induced frequency split starts displaying a consistent increase. At the same time, a small TW component (5% of the SW amplitude) is present for the 2ND mode already at 15 rpm, and increases steadily even within the constant-split range. Mistuning, therefore, counteracts the Coriolis effect, by delaying the appearance of a widening frequency split, and the development of full TW modes, but does not cancel it. In particular, the value of the frequency split is not necessarily a reliable indicator of whether the Coriolis effect is active: even in speed ranges where the frequency split remains constant at the level caused by mistuning, the Coriolis effect is already originating TW modes in the blisk.

The latter phenomenon has an important consequence. As discussed in Chapter 1, previous studies found that the Coriolis force leads to an increase in mode localisation caused by mistuning [17, 19], so a few sectors are characterised by much higher modal amplitudes than the rest. The results of this chapter, on the other hand, suggest the opposite: Figs. 6.3c and 6.3d show that the amplitude difference between adjacent sectors tends to decrease with speed, due to the presence of the TW component. This global mode shape, which comes from the propagation of the TW that only the Coriolis effect can generate in

this context, thus tends to act as an additional coupling mechanism between the sectors. Strong coupling has been identified as a condition for reduced mode localisation [109, 155], and, in this sense, the Coriolis force would help in preventing rogue-blade behaviour. In a way, the frequency split behaviour of Fig. 6.19b seems to suggest that the Coriolis effect would cancel mistuning at some speed, as the measured frequency split curve approaches the line from the low-mistuning FE model at higher speeds.

It should be noted, however, that the cited studies were based on models where very weak structural coupling was present between the sectors, whereas the test piece used throughout this work has a very strong coupling medium in the thin and flexible disc. Evidence for this is given by the fact that even the noticeably mistuned 2ND modes do not exhibit major differences in their amplitudes—besides, of course, those due to the SW mode shape pattern itself. These results should therefore be seen as complementary to the previous investigations, and further study is needed to reach a definite conclusion.

6.4.3 Validation

The mode shapes that were presented in this chapter were based on a series of steps that, taken collectively, constitute a novel approach to the modal testing of bladed discs in rotating conditions. The FRFs obtained from a combination of strain gauges and piezoelectric actuators were shown in the previous chapter to yield accurate values for frequency and damping at rest, but a formal validation of the mode shapes was still needed to ensure the reliability of the whole testing and identification method, especially in rotation.

The validation was then conducted on two fronts: frequencies and modes. Excellent agreement was found between the experimental Campbell diagram of the 0, 2, 3, and 4 ND modes of the blisk and the one calculated by NX Nastran. A maximum difference of 2% was found for the 2ND mode, and 1% or less for the remaining modes.

The frequency split curve was found to be linear for the 3ND mode, reflecting the linearity of the Coriolis force, and the absence of centrifugal stiffening or geometric nonlinearity at the speeds studied. The experimental data points showed near coincidence with the FE line, proving the reliability of the modal parameter extraction method in rotating conditions as well.

Good agreement could not be reached for the frequency split of the 2ND mode. This, however, is due to the high mistuning level present in the structure, and which could not be captured exactly in the FE model. It is therefore important to note that, even if the FE split starts at 0.6% instead of 4%, the behaviour of the frequency split curve mirrors the real trend, and displays a constant-split range at low speeds before starting to increase. Considering also that the experimental data tend to approach the FE line at high speeds, this highlights how the application of a realistic mistuning pattern is essential to model regions of mixed mistuning-Coriolis behaviour.

For the validation of the strain mode shapes, Abaqus was the FE code of choice, as the extraction procedure for the strain mode shapes is particularly easy. Excellent agreement between FE and experimental strain mode shapes was found for the 3ND mode augmented

pairs (13 DOFs), both at rest, and at 300 rpm. It is also interesting to notice that the NMD is relatively low, at around 10%, indicating that the single modal amplitudes at each DOF are very close. These values do not change much at 300 rpm (+0.65% for the FW mode, and -1.12% for the BW), which confirms the soundness of the testing methodology, as no significant degradation of the identified modal parameters is visible. This also suggests that 10% is the accuracy allowed by the present combination of sensors, actuators, and curve-fitting method.

Lower MAC values at 300 rpm were found for the 2ND mode pair. As was discussed above, this mode is affected by high mistuning. The focus of this work not being mistuning identification, the mistuning pattern that provided the highest MAC between FE and experimental data was chosen to have a more representative model, which produced a MAC for the 2ND mode pair higher than 0.98 at rest. This mistuning pattern however, introduced a frequency split of only 0.6 Hz, one order of magnitude less than the real one. As a consequence, once rotation was added, the FE model developed full TW modes already at speeds as low as 6 rpm. Qualitative agreement remained between the experimental and FE strain mode shapes in the real and imaginary parts, but the NMD was more than 40%. These results prove once again that a correct mistuning model is essential for realistic analyses, as the Coriolis effect and mistuning have been shown to be competing mechanisms in the dynamics of bladed discs.

6.4.4 Left eigenvectors

Finally, thanks to the MIMO testing approach, the left displacement eigenvectors at the actuators' positions could be identified using the pLSCF method. The extraction process itself proved to be reliable. Two different sets of data were used, to confirm that the left eigenvectors are independent entities, and not a simple by-product of the pLSCF method. This doubt could arise by noting that the left eigenvectors behave just as the strain mode shapes, with nodal diameters that are fixed at rest, and rotate as TW when the structure is spinning. For this reason, the left eigenvectors were extracted from a completely different test set-up as well, where only the seven sector SGs, as opposed to the eight circumferential ones, were used. The very high correlation obtained between the component of the left eigenvectors identified from the two different SG sets proved the reliability of the method.

The left displacement mode shapes were then themselves validated. As explained in sect. 2.4.2, in a non-rotating structure, the mode participation factors L_r assume the form of the r -th displacement mode shape (r -th right displacement eigenvector). These could then be directly compared to the displacement mode shapes from FE analysis. The displacement, in this case, was in the radial direction. At rest, the MAC values between experimental and FE displacement mode shapes was above 0.98 for all modes, with low values of NMD (10%), which are compatible to those characterising strain mode shapes. The only exception was the 2ND-2 mode, with a MAC value of 0.94, but a relatively high NMD (18%), which was again due to the non-representative mistuning pattern.

In rotating conditions, on the other hand, the mode participation factors become the

left displacement eigenvectors. No FE code provides direct access to them, to the author's knowledge. For this reason, the assumption was made, following [101, 154], that, since the blisk was found to be lightly damped, the left eigenvectors could be reasonably approximated by the right, i.e. the displacement mode shapes. The measured left eigenvectors at 300 rpm were therefore again compared to the radial displacement mode shapes from Abaqus, calculated at the same speed. For the 3ND modes, the MAC is very high, at 0.99 and 0.98 for the FW and BW modes, respectively. This suggests that the approximation made is valid, as the measured *left* displacement eigenvectors and the FE *right* ones show a high degree of correlation. This validation then shows that, for lightly damped systems, the use of a MIMO approach in combination with SGs can lead to the recovery of the displacement mode shape components at the input locations, which can be used as additional data for model validation and updating.

However, there is a noticeable increase in the NMD (from approximately 10% to 15% and 17%), which was not seen for the strain mode shapes (Table 6.1). This may indicate that extracted left eigenvectors are more sensitive to increased noise under rotating conditions than right eigenvectors. However, it is also possible that, while the hypothesis of coinciding left/right displacement eigenvectors is clearly warranted by the high MAC values, the left eigenvectors do start diverging from the displacement mode shapes due to the interaction between damping and Coriolis effect, which would cause an increasing asymmetry in the structural eigenproblem (sect. 2.4.1).

6.5 Summary and conclusions

The novel modal testing and identification framework developed throughout this work was successfully validated. Excellent agreement of the Campbell diagrams, within 2%, was obtained between experimental and FE data. Mode shapes were also compared, and several quality measures were given to support the validation process. Very high MAC values were found for the low-mistuning modes, both at rest and under rotation. For these modes, the NMD, which was used to assess the average error between FE and experimental modes at DOF level, was consistently around 10%, which could be considered as the accuracy allowed by the method with the current transducer configuration.

Lower MACs were found for the modes more sensitive to mistuning, as it was not possible to reproduce the correct mistuning pattern in the FE model. Mistuning and Coriolis effects were indeed found to be competing physical phenomena. At lower speeds, the frequency splits tend to stay at the value imposed by mistuning at rest, and start increasing under the Coriolis effect only after a certain speed threshold, which increases with mistuning level. At the same time, mistuning delays the development of full travelling-wave modes with strong standing-wave components, but, after the Coriolis effect becomes dominant, no further change in the mode shapes was detected, as the test piece was not significantly affected by centrifugal stiffening.

On the other hand, non-negligible travelling-wave behaviour was found to be present even in the speed range where frequency split stayed constant. This showed that frequency

splits, while being the most obvious and easily measured sign of the presence of the Coriolis effect, are not a reliable indicator of whether it is active or not: travelling waves can develop even in conditions when mistuning is the only apparent phenomenon. This should be taken into account in aeroelastic simulations, as mistuning is considered to increase flutter stability, but the travelling waves originated by the Coriolis force may counteract this positive effect.

Left displacement eigenvectors were successfully extracted thanks to the combined use of MIMO testing and pLSCF identification process. Their extraction was proven to be independent of the output configuration, which confirmed that the measured components of the left eigenvectors depend only on the input locations, and that the identification method is reliable. Further proof came from the high MAC values at rest obtained between the experimental left eigenvectors, and the FE displacement mode shapes: with strain modal testing at rest, left eigenvectors coincide with displacement mode shapes.

Under rotating conditions, left eigenvectors can only be approximated by displacement mode shapes. This was reflected in the MAC values, which were still high, but accompanied by higher NMD values, i.e. larger errors. Since the NMD values at rest were in line with those associated to strain mode extraction, it is thought that this increase in error depends on the progressive divergence between right and left eigenvectors with speed: the Coriolis effect, itself increasing with speed, would increase the degree of asymmetry of the structural eigenproblem, and thus enhance the difference between left eigenvectors and mode shapes.

Chapter 7

Conclusions

7.1 Main contributions

7.1.1 Summary

This section summarises the original contributions of this work, which will be discussed in more detail in the following.

- Modal testing and identification methodology for rotating structures
 - This thesis work provided a novel test framework that enables full modal analysis of bladed disks under rotating conditions. It is based on a multi-input multi-output testing approach, using piezoelectric excitation and strain measurements, to extract the full set of modal parameters: resonance frequencies, damping, and right and left eigenvectors.
 - An FRF expression in terms of strain mode shapes and the left eigenvectors of displacements was derived for the first time to account for the effects of the Coriolis force.
 - A poly-reference modal analysis method was applied for the first time in this context to extract both modal strain and displacement properties during rotation.
 - A new application of piezoelectric actuators was developed to simulate impact testing.
- Coriolis effects and mistuning
 - The interaction between Coriolis effects and mistuning was investigated in great detail, by considering both frequency splits and mode shapes. A gradual transition from mistuning-dominated behaviour at low speed to Coriolis-dominated features at higher speeds was identified.
- FE modelling of rotating bladed discs

- A thorough assessment of the prediction capabilities of FE codes in the presence of all major rotational effect was conducted, and demonstrated that all commercial packages produce equivalent and valid results.
- Validation of Coriolis effects in bladed discs
 - A full model validation could be provided with the test data obtained with the developed technique and the FE analysis results, establishing confidence in the modelling and testing methods to be applied on future engine architectures.
 - The developed techniques was demonstrated to generate reliable strain and approximated displacement mode shapes, which can be used for strain- or displacement-based model validation.

7.1.2 Modal testing and identification methodology for rotating structures

This thesis work has developed a coherent framework for the investigation of rotational phenomena in multi-component structures like aero-engine stages. A new rotating test rig was designed and built to provide the experimental capabilities to investigate rotational effects in general, and enable high-quality modal analysis in rotating conditions. The MIMO testing approach was identified as the only capable of the extraction of the complete set of modal parameters—damping, frequencies, mode shapes, left eigenvectors—necessary for the full characterisation of damped gyroscopic structures, and was successfully translated to rotating conditions for the first time for bladed discs.

The need for controlled multiple inputs for the extraction of modal information required the development of an excitation system based on a set of laminar piezoelectric actuators attached directly at all the sectors of the blisk. The actuators were individually driven to provide uncorrelated forcing, and the control voltage was found to produce FRFs displaying the same behaviour as with traditional force inputs, i.e. response amplification and phase transition at resonance. Combined with the derivation of the equations of motion of a piezoelectrically actuated system, this showed their suitability for modal analysis purposes.

To minimise testing time and increase efficiency, random signals were used for the excitation, which led to the acquisition of Campbell diagrams over a wide frequency range in a fraction of the time required by the stepped-sine method. MIMO random excitation was proved to be equivalent to single-input stepped-sine, producing very good agreement in the values of frequencies and damping, and near-identical mode shapes. It also proved superior to standard single-input methods in identifying close modes, especially since its full potential could be exploited by coupling it with a poly-reference modal identification technique.

A novel concept in the use of piezoelectric actuators was also developed to simulate impact testing. Transient excitation was produced by driving the actuators with an electric pulse. Excellent agreement with the results of a traditional hammer test was obtained for

the resonance frequencies, and a good match for the damping values reached for most modes. This would offer the possibility of performing quick modal testing on a structure with high repeatability, due to the permanent position of the photoelectric patch, and even in rotating conditions.

The versatility of the actuation system was confirmed by generating travelling-wave excitation to reproduce arbitrary EO patterns. This led to high response levels and mode selectivity. This excitation form is therefore particularly suitable to reproduce realistic conditions in the testing of rotating blisks, as both excitation and response take the form of travelling waves in turbomachinery, and to study nonlinear effects, thanks to the large forcing levels allowed by the synchronised action of the actuators. It was possible to demonstrate that, as the travelling-wave excitation greatly enhances only the modes matching its phase and direction, it can be used to quickly identify modes hidden in zones of high modal density.

To allow multiple-output measurements, strain gauges were selected. The expression for FRFs with strain as output in rotating conditions was derived for the first time. It could be demonstrated that strain FRFs in rotating conditions are dependent on strain mode shapes, and the left displacement eigenvector components at the input DOFs. With the developed approach, left eigenvectors could be extracted, and their measured components were proven to be independent of the measurement set-up, which confirmed that the modal extraction technique is able to identify them as separate physical entities from the standard mode shapes.

The poly-reference method, combined with the MIMO approach, was also found to adapt well to the requirements of modal analysis in rotating structures, and there was no issue in identifying the complex mode shapes originated from the Coriolis effect. The developed technique allows to extend the use of strain gauges, the sensors most widely employed in the testing of turbomachinery components, from forced response measurements to full modal analysis. It also enabled the acquisition of an additional set of data, left eigenvectors, which approximate displacement mode shapes in light damping conditions.

7.1.3 Coriolis effects and mistuning

The main driver of the developed modal testing techniques was the investigation of the effects of the Coriolis force on the modal properties of bladed discs, i.e. the generation of frequency splits and complex mode shapes in the form of travelling waves. A very detailed experimental analysis at several different speeds was conducted to gain in-depth understanding of how the Coriolis effects evolve, to provide additional understanding of their impact on rotating structures and ensure that the testing methodology can correctly identify them, to provide reliable validation data.

The resulting behaviour was found to depend on mistuning levels. Large frequency splits were observed experimentally on a thin blisk with eight horizontal blades for the 1ND, 2ND, and 3ND mode families, which confirmed the observations from the literature. Three speed ranges characterised by different behaviours were identified at a high level of

detail for the first time thanks to the large number of investigated speeds. At low speeds, the frequency split remained nearly constant at the value determined by structural mistuning at rest. At medium speeds, the frequency split started increasing, with a markedly nonlinear trend. At the high end of the operational speed range, the split settled on a linear increase, and tended towards the values it would have assumed without mistuning.

The level of sensitivity of the different modes affected the relative extension of the speed ranges. Thanks to the newly developed testing framework, strain modes were measured under rotation, and their evolution with rotational speed was quantified through different indicators. At rest, all modes are real-valued, and they are locked at specific angles around the circumference of the blisk due to mistuning. With increasing speed, it was possible to see that the modes progressively develop imaginary components. The low-mistuning modes become full travelling waves at low speeds, and corresponding modes at high speeds are virtually identical. It could therefore be concluded that the Coriolis effect, in structures with low centrifugal stiffening, only causes the appearance of travelling-wave modes, without deforming them.

The modes with a high degree of mistuning remained quasi-real for half of the rotation speed range, and a noticeable SW component was present at maximum speed. It was seen, however, that even in the constant-speed range, small TW components are present. It could also be observed that the Coriolis effect, creating TWs, tends to even out the modal amplitudes at the various sectors. It thus provides a further coupling mechanism in the blisk (besides structural and aerodynamic coupling), and could therefore contribute to lessen the danger of mode localisation caused by mistuning, where a few blades respond at much higher amplitudes than the others.

The Coriolis effect is often neglected in the analysis and design of real aero-engines because of the small frequency splits it generates, which means that it causes no truly separate resonance frequencies. The experimental results have shown that even in the absence of a variation in the frequency split, the Coriolis effect can still be active, and force the existence of TW vibration in a specific direction in the blisk. The presence of travelling-wave modes, which can lead to unstable response, is often taken for granted in aeroelastic studies, while at the same time mistuning is considered to increase flutter stability. The impact of the coexistence of the two behaviours, which is induced by the action of the Coriolis force, needs therefore to be taken into consideration in detailed aeroelastic analysis.

7.1.4 FE modelling of rotating bladed discs

A systematic assessment of the most used commercially available, and one proprietary, FE software packages was conducted to identify the capabilities available to model and predict rotational effects, and to highlight potential deficiencies. Rotational effects like geometric nonlinearities, centrifugal stiffening and spin softening are included in standard design practices, and are therefore well-documented features in FE software. Coriolis effects, on the other hand, are usually considered only in purely rotordynamic analyses, which are

based on axisymmetric disc-shaft models. Bladed discs, as *cyclic*-symmetric structures, require particular features: the possibility of doing modal analysis in a rotating frame, for example, is necessary to avoid the appearance of time-varying terms, and the capability of reducing the model to a single sector would significantly cut computational time.

A set of benchmark test cases was therefore created, so that the results from the FE analyses could be compared to analytical solutions, and experimental data, for a wide variety of geometries. This study showed that all commercial codes produced compatible Campbell diagrams, and all were able to identify FW and BW travelling-wave modes, and to assign them to the correct frequency. All codes provided the ability of combining the Coriolis effect and centrifugal stiffening. The interaction between the two phenomena, Coriolis and geometric nonlinearities, was studied consistently for the first time, and it was possible to observe the heavily nonlinear variation of the frequency split due to the large-displacement deformations caused by the centrifugal force. Large discrepancies between the assessed codes could be found only at high speeds close to instability conditions, which is arguably due to differences in the default numerical tolerances used by the different codes. This indicates that particular care must be taken when modelling high rotor speeds with Coriolis effects.

From the comparison of these computational results to experimental data available in the literature, it was possible to conclude that all codes are able to produce reliable results, and are equivalent in terms of prediction capabilities. The sole exception was the proprietary “Code A”: a major finding of the evaluation was that wrong values for the frequencies were calculated for the 1ND modes of cyclic-symmetric structures using this code, due to the erroneous implementation of the equations of motion, and the assessment resulted in its correction.

7.1.5 Validation of Coriolis effects in bladed discs

MIMO testing techniques have never been exploited to the fullest of their potential for the modal identification of rotating bladed discs. In particular, the use of strain gauges in a structure subject to the Coriolis force causes FRFs that depend on an additional set of parameters, the left displacement eigenvectors, which have never before been identified experimentally in bladed discs. All of this, coupled with the non-standard use of strain gauges with piezoelectric actuators, required a formal validation of the testing approach through a comparison with FE results. As the FE codes were shown to be equivalent in terms of prediction capabilities, the validation was carried out in NX Nastran and Abaqus alone, and involved both frequencies and mode shapes to ensure the highest possible level of confidence in the experimental results.

The measured strain mode shapes were compared to the computational ones through MACs, which revealed high degrees of correlation. Further confirmation was offered by the localised error measured by the NMD, which was of the order of 10% for the low mistuning modes.

Large discrepancies were found only for the high-mistuning modes, as it was not pos-

sible to reproduce the correct mistuning pattern present in the blisk used as test piece: in this case, large differences arose in rotation, as the relatively low mistuning added to the FE model allowed the early development of travelling-wave modes, while, in the real test piece, a strong SW component remained at all measured speeds due to the higher mistuning levels. However, the close match between FE and experimental modes at low mistuning allowed the successful quantitative validation of the Coriolis effect on mode shapes. It also showed that the developed technique is capable of detecting the Coriolis effects even in cases where they are mixed with competing phenomena like mistuning.

The full MIMO testing technique, coupled with the pLSCF modal identification method for rotating structures, also allowed the recovery of left displacement eigenvectors at the input DOFs. None of the FE codes natively provides left eigenvectors as outputs, so the validation was conducted by comparing the measured eigenvectors to the displacement mode shapes. At rest, where the left eigenvectors do coincide with the right, excellent agreement was found, which confirmed the validity of the testing and identification method. In rotation, where the left eigenvectors are only approximations of the actual mode shapes, close agreement was still found, but associated to larger errors. This proved that left eigenvectors can reasonably be approximated by the mode shapes proper in lightly-damped rotating structures: in these conditions the developed test set-up and techniques can be successfully applied to derive both strain and displacement information, allowing the validation of both.

7.2 Suggestions for future work

Based on the experience accumulated during this thesis work, and the results already reached, the following topics have been identified as potential areas for further research:

- This work has shown that the modelling features necessary for bladed discs are in place. However, the exploitation of cyclic symmetry to reduce computational costs, while well established for non-rotating structures, is nearly never implemented when the Coriolis force is added. This implementation is absolutely essential for an uptake from the industry, so that accurate analyses can be efficiently conducted on FE models that regularly feature hundreds of thousands of DOFs.
- The drive for increasing performance in aero-engines requires ever greater realism at the model level, to reduce the need for expensive testing campaigns. This in turn is leading towards whole-engine modelling, where several stages of bladed discs are coupled with their shafts, and the stator through bearings. This study produced a conclusive validation of the capabilities of FE codes to predict the influence of the Coriolis effect in rotating bladed discs, at component level. It thus provides a first step for the evolution of rotordynamics from axisymmetric models to complete bladed disc-shaft models. The simultaneous study of multiple components interacting in different reference frames poses challenges both on a computational and experimental level. The development of experimentally validated model reduction techniques, in particular, is essential considering the present state of computing power, and would

also allow the addition of nonlinear effects from bearings and rotor-stator interaction at a reasonable computational cost.

- Piezoelectric actuators have been shown to produce reliable results, but they remain a source of uncertainty, as it is difficult to quantify the actual forcing they introduce in a structure. The knowledge of the excitation amplitude levels is especially important in a multiple-input context, where precise amplitude patterns may be needed. A calibration technique capable of identifying, directly or indirectly, the strain levels the actuators actually produce, and of separating its effect from the inherent mistuning of the structure, would therefore help in increasing accuracy. For an indirect calibration, a method based on a combination of testing and modelling, to identify equivalent forcing levels, could be the first step. For a direct evaluation, self-sensing circuits, which allow the exploitation of piezoelectric patches as both actuators and sensors, should be explored.
- The Coriolis effect was found to interact with mistuning, and lead to operational zones of mixed behaviour. The identification of geometrical factors that influence the relative importance of the two (structural coupling, stagger angle, blade stiffness, etc.) could be the basis of a systematic parametric study, to highlight the conditions at which one of the two effects becomes prevalent.
- This work has shown that the generation of travelling waves from the Coriolis force tends to even out the mode amplitudes at the different sectors, which suggests that it would have a beneficial effect on the mode localisation induced by mistuning. Results from the literature in this regard, all computational, reach mixed conclusions, with some researchers witnessing too a reduction in amplitude localisation, and others an increase. An experimental study, or an extended computational one, where controlled mistuning patterns could be introduced, is needed to gain a clearer understanding.

References

- [1] S. Hashemi and M. Richard, “Natural frequencies of rotating uniform beams with Coriolis effects,” *Journal of vibration and acoustics*, vol. 123, no. 4, pp. 444–455, 2001.
- [2] K. B. Subrahmanyam, K. R. V. Kaza, G. V. Brown, and C. Lawrence, “Nonlinear vibration and stability of rotating, pretwisted, precone blades including Coriolis effects,” *Journal of Aircraft*, vol. 24, pp. 342–352, 1987.
- [3] R. Kar and T. Sujata, “Dynamic stability of a rotating, pretwisted and precone cantilever beam including Coriolis effects,” *Computers & Structures*, vol. 42, no. 5, pp. 741 – 750, 1992.
- [4] T. G. Carne, D. W. Lowitz, A. R. Nord, and R. A. Watson, “Finite element analysis and modal testing of a rotating wind turbine,” Tech. Rep. SAND82-0345, Sandia National Laboratories, October 1982.
- [5] J. H. Argyris and H. P. Mlejnek, *Dynamics of structures*. Texts on computational mechanics, North-Holland, 1991.
- [6] R. M. Laurenson, “Modal Analysis of Rotating Flexible Structures,” *AIAA Journal*, vol. 14, pp. 1444–1450, Oct. 1976.
- [7] L. Meirovitch, “A new method of solution of the eigenvalue problem for gyroscopic systems,” *AIAA Journal*, vol. 12, no. 10, pp. 1337–1342, 1974.
- [8] D. L. Thomas, “Dynamics of rotationally periodic structures,” *International Journal for Numerical Methods in Engineering*, vol. 14, no. 1, pp. 81–102, 1979.
- [9] D. J. Ewins, “Structural dynamics characteristics of bladed assemblies,” *AGARD Manual on aeroelasticity in axial-flow turbomachines*, vol. 2, 1988.
- [10] J. Padovan, “On gyroscopic problems in elasticity,” *International Journal of Engineering Science*, vol. 16, no. 12, pp. 1061 – 1073, 1978.

- [11] J. Wildheim, "Vibrations of rotating circumferentially periodic structures," *The Quarterly Journal of Mechanics and Applied Mathematics*, vol. 34, no. 2, pp. 213–229, 1981.
- [12] N. Khader and R. Loewy, "Shaft flexibility effects on the forced response of a bladed-disk assembly," *Journal of Sound and Vibration*, vol. 139, no. 3, pp. 469 – 485, 1990.
- [13] M. Nikolic, D. J. Ewins, E. P. Petrov, and D. Di Maio, "The effects of Coriolis forces on vibration properties of bladed discs," in *7th IFToMM Conference on Rotor Dynamics*, September 25–28, 2006, Vienna, Austria.
- [14] C. Gibert, V. Kharyton, F. Thouverez, and P. Jean, "On forced response of a rotating integrally bladed disk: Predictions and experiments," in *ASME Turbo Expo 2010: Power for Land, Sea, and Air*, pp. 1103–1116, American Society of Mechanical Engineers, 2010.
- [15] M. Imregun and D. J. Ewins, "Complex modes—Origins and limits," in *13th International Modal Analysis Conference*, February 13–16, 1995, Nashville, Tennessee.
- [16] F. Barbarossa, A. B. Parry, J. S. Green, and L. di Mare, "An aerodynamic parameter for LP turbine flutter," *Journal of Turbomachinery*, Forthcoming 2016.
- [17] B. Huang and J. Kuang, "Mode localization in a rotating mistuned turbo disk with Coriolis effect," *International Journal of Mechanical Sciences*, vol. 43, no. 7, pp. 1643 – 1660, 2001.
- [18] M. Nikolic, E. P. Petrov, and D. J. Ewins, "Coriolis forces in forced response analysis of mistuned bladed disks," *Journal of turbomachinery*, vol. 129, no. 4, pp. 730–739, 2007.
- [19] J. Xin and J. Wang, "Investigation of Coriolis effect on vibration characteristics of a realistic mistuned bladed disk," in *ASME 2011 Turbo Expo: Turbine Technical Conference and Exposition*, pp. 993–1005, American Society of Mechanical Engineers, 2011.
- [20] P. Almeida, C. Gibert, X. Leblanc, J.-P. Ousty, and F. Thouverez, "Experimental and numerical investigations on a rotating centrifugal compressor," in *ASME Turbo Expo 2012: Turbine Technical Conference and Exposition*, pp. 1133–1142, American Society of Mechanical Engineers, 2012.
- [21] D. J. Ewins, *Modal testing: Theory, practice and application*. Research Studies Press Ltd., 2nd ed., 2000.
- [22] J. J. Kielb and R. S. Abhari, "Experimental study of aerodynamic and structural damping in a full-scale rotating turbine," in *ASME Turbo Expo 2001: Power for Land, Sea, and Air*, pp. V004T03A028–V004T03A028.

- [23] J. H. Ginsberg and B. B. Wagner, "On the use of modal parameters as metrics for condition-based monitoring of rotating machinery," in *ASME Turbo Expo 2005: Power for Land, Sea, and Air*, pp. 871–882, American Society of Mechanical Engineers, 2005.
- [24] C.-W. Lee, "A complex modal testing theory for rotating machinery," *Mechanical Systems and Signal Processing*, vol. 5, no. 2, pp. 119 – 137, 1991.
- [25] H. Irretier, "Mathematical foundations of experimental modal analysis in rotor dynamics," *Mechanical Systems and Signal Processing*, vol. 13, no. 2, pp. 183 – 191, 1999.
- [26] C. Kessler and J. Kim, "Complex modal analysis and modal superposition for rotating machinery," in *IMAC XVII - 17th International Modal Analysis Conference*, pp. 1930–1937, Society for Experimental Mechanics, 1999.
- [27] W. Heylen, S. Lammens, and P. Sas, *Modal analysis Theory and testing*. Katholieke Universteit Leuven, Departement Werktuigkunde, 1998.
- [28] R. Nordmann, "Identification of modal parameters of rotors," in *Dynamics of rotors: stability and system identification* (O. Mahrenholtz, ed.), Springer, 1984.
- [29] D. J. Ewins, "Modal analysis for rotating machinery," in *Modal analysis and testing*, 1998.
- [30] E. S. Gutierrez-Wing, *Modal Analysis of Rotating Machinery Structures*. PhD thesis, Imperial College London, 2003.
- [31] I. A. Sever, *Experimental Validation of Turbomachinery Blade Vibration Predictions*. PhD thesis, Imperial College London, 2004.
- [32] S. A. Russell, "Strain gauge measurements of blade resonance using eddy current excitation in a vacuum spin pit," Master's thesis, Monterey, California. Naval Postgraduate School, 2002.
- [33] T. Berruti and V. Maschio, "Experimental investigation on the forced response of a dummy counter-rotating turbine stage with friction damping," *Journal of Engineering for Gas Turbines and Power*, vol. 134, no. 12, 2012.
- [34] D. Di Maio and D. J. Ewins, "Applications of continuous tracking SLDV measurement methods to axially symmetric rotating structures using different excitation methods," *Mechanical Systems and Signal Processing*, vol. 24, no. 8, pp. 3013 – 3036, 2010.
- [35] C. Furrone and T. Berruti, "An electromagnetic system for the non-contact excitation of bladed disks," *Experimental Mechanics*, vol. 52, no. 5, pp. 447–459, 2012.

- [36] J. Chang and J. Wickert, "Measurement and analysis of modulated doublet mode response in mock bladed disks," *Journal of Sound and Vibration*, vol. 250, no. 3, pp. 379–400, 2002.
- [37] N. Anegawa, H. Fujiwara, and O. Matsushita, "Vibration diagnosis featuring blade-shaft coupling effect of turbine rotor models," *Journal of Engineering for Gas Turbines and Power*, vol. 133, no. 2, 2011.
- [38] E. F. Crawley, E. H. Ducharme, and D. R. Mokadam, "Analytical and experimental investigation of the coupled bladed disk/shaft whirl of a cantilevered turbofan," *Journal of Engineering for Gas Turbines and Power*, vol. 108, no. 4, pp. 567–575, 1986.
- [39] I. Bucher and D. J. Ewins, "Modal analysis and testing of rotating structures," *Philosophical Transactions of the Royal Society of London A: Mathematical, Physical and Engineering Sciences*, vol. 359, no. 1778, pp. 61–96, 2001.
- [40] C. R. Morrison, A. Provenza, A. Kurkov, G. Montague, K. Duffy, O. Mehmed, D. Johnson, and R. Jansen, "Fully suspended, five-axis, three-magnetic-bearing dynamic spin rig with forced excitation," *Experimental mechanics*, vol. 45, no. 3, pp. 226–237, 2005.
- [41] N. Anegawa, H. Fujiwara, and O. Matsushita, "Blade-shaft coupled resonance vibration by using active magnetic bearing excitation," in *ASME Turbo Expo 2008: Power for Land, Sea, and Air*, pp. 1183–1190, American Society of Mechanical Engineers, 2008.
- [42] A. Okabe, T. Kudo, K. Shiohata, O. Matsushita, H. Fujiwara, H. Yoda, and S. Sakurai, "Reduced modeling for turbine rotor-blade coupled bending vibration analysis," *Journal of Engineering for Gas Turbines and Power*, vol. 134, no. 2, 2012.
- [43] A. J. Provenza and K. P. Duffy, "Experimental methodology for determining turbomachinery blade damping using magnetic bearing excitation and non-contacting optical measurements," in *ASME Turbo Expo 2010: Power for Land, Sea, and Air*, pp. 739–747, American Society of Mechanical Engineers, 2010.
- [44] E. F. Crawley and J. De Luis, "Use of piezoelectric actuators as elements of intelligent structures," *AIAA journal*, vol. 25, no. 10, pp. 1373–1385, 1987.
- [45] D. J. Leo, *Engineering Analysis of Smart Material Systems*. John Wiley & Sons, Inc., 2008.
- [46] N. Jalili, *Piezoelectric-Based Vibration Control: From Macro to Micro/Nano Scale Systems*. New York: Springer, 2010.
- [47] X. Wang and J. Mills, "Experimental modal identification of configuration-dependent vibration using smart material transducers with application to a planar parallel robot," in *Robotics and Biomimetics (ROBIO). 2005 IEEE International Conference on*, pp. 234–239, 2005.

- [48] F. Charette, C. Guigou, A. Berry, and G. Plantier, "Asymmetric actuation and sensing of a beam using piezoelectric materials," *The Journal of the Acoustical Society of America*, vol. 96, no. 4, pp. 2272–2283, 1994.
- [49] M. Porfiri, C. Maurini, and J. Pouget, "Modal analysis of stepped piezoelectric beams," 2007.
- [50] R. L. Clark, C. R. Fuller, and A. Wicks, "Characterization of multiple piezoelectric actuators for structural excitation," *The Journal of the Acoustical Society of America*, vol. 90, no. 1, 1991.
- [51] G. Park, M. Sausse, D. J. Inman, and J. A. Main, "Vibration testing and finite element analysis of an inflatable structure," *AIAA journal*, vol. 41, no. 8, pp. 1556–1563, 2003.
- [52] E. J. Ruggiero, G. Park, and D. J. Inman, "Multi-input multi-output vibration testing of an inflatable torus," *Mechanical Systems and Signal Processing*, vol. 18, no. 5, pp. 1187 – 1201, 2004.
- [53] J. J. Hollkamp and R. W. Gordon, "Modal testing of a bladed disk," in *Proceedings of IMAC XVII: 17th International Modal Analysis Conference*, pp. 826–832, Society of Photo-Optical Instrumentation Engineers, 1999.
- [54] T. Jeffers, J. Kielb, and R. Abhari, "A novel technique for the measurement of blade damping using piezoelectric actuators," in *ASME Turbo Expo 2000: Power for Land, Sea, and Air*, 2000.
- [55] A. Kammerer and R. S. Abhari, "Experimental study on impeller blade vibration during resonance—Part II: Blade damping," *Journal of Engineering for Gas Turbines and Power*, vol. 131, no. 2, p. 022509, 2009.
- [56] J. Belz, M. May, J. Siemann, J. R. Seume, C. Voigt, H. Böhmer, and B. Grüber, "Excited blade vibration for aeroelastic investigations of a rotating blisk using piezoelectric macro fiber composites," in *ASME Turbo Expo 2013: Turbine Technical Conference and Exposition*, American Society of Mechanical Engineers, 2013.
- [57] P. Beuseroy and R. Lengell, "Nonintrusive turbomachine blade vibration measurement system," *Mechanical Systems and Signal Processing*, vol. 21, no. 4, pp. 1717 – 1738, 2007.
- [58] V. Kharyton, C. Gibert, L. Blanc, and F. Thouverez, "Elements of dynamic characterization of a bladed disk by using the tip-timing method under vacuum conditions," in *ASME 2011 Turbo Expo: Turbine Technical Conference and Exposition*, pp. 1127–1135, American Society of Mechanical Engineers, 2011.
- [59] M. Martarelli, *Exploiting the Laser Scanning Facility for Vibration Measurements*. PhD thesis, Imperial College London, 2001.

- [60] D. Di Maio and D. J. Ewins, "CAISER MYMESIS: a new software platform for virtual and actual vibration testing on rotating structures using a continuously scanning LDV technique," in *Proc. SPIE 6345, Seventh International Conference on Vibration Measurements by Laser Techniques: Advances and Applications*, 2006.
- [61] U. Schmidt Paulsen, O. Erne, T. Möller, G. Sanow, and T. Schmidt, "Wind turbine operational and emergency stop measurements using point tracking videogrammetry," in *SEM Annual Conference and Exposition on Experimental and Applied Mechanics, Albuquerque, NM (US), 1-4 Jun, 2009*.
- [62] P. N. Bansal, P. J. Arseneaux, A. F. Smith, J. E. Turnberg, and B. M. Brooks, "Analysis and test evaluation of the dynamic response and stability of three advanced turboprop models," Tech. Rep. NASA-CR-175026, NASA, December 1985.
- [63] E. Ducharme, D. Mokadam, and E. Crawley, "Forced rotating whirl tests on a cantilevered turbofan," Tech. Rep. GTL Report No. 182, Gas Turbine Laboratory, MIT, March 1985.
- [64] G. Jacquet-Richardet, G. Ferraris, and P. Rieutord, "Frequencies and modes of rotating flexible bladed disc-shaft assemblies: A global cyclic symmetry approach," *Journal of Sound and Vibration*, vol. 191, no. 5, pp. 901–915, 1996.
- [65] A. Srinivasan, "Flutter and resonant vibration characteristics of engine blades," *Journal of Engineering for Gas Turbines and Power*, vol. 119, no. 4, pp. 742–775, 1997.
- [66] E. Seinturier, J.-P. Lombard, M. Berthillier, and O. Sgarzi, "Turbine mistuned forced response prediction: Comparison with experimental results," in *ASME Turbo Expo 2002: Power for Land, Sea, and Air*, pp. 943–952, American Society of Mechanical Engineers, 2002.
- [67] W. Ning, S. Moffatt, Y. Li, and R. G. Wells, "Blade forced response prediction for industrial gas turbines: Part 2—verification and application," in *ASME Turbo Expo 2003, collocated with the 2003 International Joint Power Generation Conference*, pp. 415–422, American Society of Mechanical Engineers, 2003.
- [68] H. Schönenborn and T. Breuer, "Aerodynamic and mechanical vibration analysis of a compressor blisk at surge," in *ASME Turbo Expo 2004: Power for Land, Sea, and Air*, pp. 517–526, American Society of Mechanical Engineers, 2004.
- [69] D. Frank, A. Kleinfeldt, U. Orth, and W. Cline, "Investigation of blade and disc vibrations on the upgraded power turbine for the thm 1304 gas turbine," in *ASME Turbo Expo 2004: Power for Land, Sea, and Air*, pp. 349–355, American Society of Mechanical Engineers, 2004.

- [70] J. S. Green, “Forced response of a large civil fan assembly,” in *ASME Turbo Expo 2008: Power for Land, Sea, and Air*, pp. 685–692, American Society of Mechanical Engineers, 2008.
- [71] S. Pavone, *Design and development of a spin test rig for turbine disks*. PhD thesis, Politecnico di Torino, 2010.
- [72] T. C. Allison, A. H. Lerche, and J. J. Moore, “Experimental validation of empirical methods for dynamic stress prediction in turbomachinery blades,” in *ASME 2011 Turbo Expo: Turbine Technical Conference and Exposition*, pp. 121–131, American Society of Mechanical Engineers, 2011.
- [73] A. Batailly, M. Legrand, A. Millecamps, and F. Garcin, “Numerical study of a rotor/stator interaction case experimentally simulated with an industrial compressor,” in *ASME Turbo Expo 2012: Turbine Technical Conference and Exposition*, pp. 1053–1062, American Society of Mechanical Engineers, 2012.
- [74] T. Giersch, F. Figaschewsky, P. Hönisch, A. Kühhorn, and S. Schrape, “Numerical analysis and validation of the rotor blade vibration response induced by high pressure compressor deep surge,” in *ASME Turbo Expo 2014: Turbine Technical Conference and Exposition*, American Society of Mechanical Engineers, 2014.
- [75] S. A. Long, S. L. Edney, P. A. Reiger, M. W. Elliott, F. Knabe, and D. Bernhard, “Telemetry system integrated in a small gas turbine engine,” *Journal of Engineering for Gas Turbines and Power*, vol. 134, no. 4, p. 044501, 2012.
- [76] B. Beirow, A. Kühhorn, and J. Nipkau, “On the influence of strain gauge instrumentation on blade vibrations of integral blisk compressor rotors applying a discrete model,” in *ASME Turbo Expo 2009: Power for Land, Sea, and Air*, pp. 245–253, American Society of Mechanical Engineers, 2009.
- [77] L. Yam, T. Leung, D. Li, and K. Xue, “Theoretical and experimental study of modal strain analysis,” *Journal of Sound and Vibration*, vol. 191, no. 2, pp. 251 – 260, 1996.
- [78] T. Kranjc, J. Slavi, and M. Boltar, “A comparison of strain and classic experimental modal analysis,” *Journal of Vibration and Control*, 2014.
- [79] F. L. M. Santos, B. Peeters, M. Menchicchi, J. Lau, L. Gielen, W. Desmet, and L. C. S. Góes, “Strain-based dynamic measurements and modal testing,” in *Topics in Modal Analysis II, Volume 8* (R. Allemang, ed.), Conference Proceedings of the Society for Experimental Mechanics Series, pp. 233–242, Springer International Publishing, 2014.
- [80] E. Mucchi, “On the comparison between displacement modal testing and strain modal testing,” *Proceedings of the Institution of Mechanical Engineers, Part C: Journal of Mechanical Engineering Science*, 2015.

- [81] T. Theodorsen, "Propeller vibrations and the effect of the centrifugal force," Tech. Rep. NASA-SP-495, NACA, February 1935.
- [82] J. Simo and L. Vu-Quoc, "The role of non-linear theories in transient dynamic analysis of flexible structures," *Journal of Sound and Vibration*, vol. 119, no. 3, pp. 487–508, 1987.
- [83] T. R. Kane, R. Ryan, and A. Banerjee, "Dynamics of a cantilever beam attached to a moving base," *Journal of Guidance, Control, and Dynamics*, vol. 10, no. 2, pp. 139–151, 1987.
- [84] S. Hanagud and S. Sarkar, "Problem of the dynamics of a cantilevered beam attached to a moving base," *Journal of Guidance, Control, and Dynamics*, vol. 12, no. 3, pp. 438–441, 1989.
- [85] K. W. London, "Comment on 'Dynamics of a cantilever beam attached to a moving base'," *Journal of Guidance, Control, and Dynamics*, vol. 12, no. 2, pp. 284–286, 1989.
- [86] I. Sharf, "Geometric stiffening in multibody dynamics formulations," in *Proceedings of the Fifth NASA(NSF)DOD Workshop on Aerospace Computational Control*, 1993.
- [87] A. Carpinteri, *Structural mechanics: A unified approach*. E&FN Spon, 1997.
- [88] P. Gatti and V. Ferrari, *Applied Structural and Mechanical Vibrations: Theory, Methods and Measuring Instrumentation*. E & FN Spon, 2003.
- [89] M. Géradin and A. Cardona, *Flexible Multibody Dynamics: A finite element approach*. John Wiley and Sons, Ltd., 2001.
- [90] P. Rieutord, *Comportement dynamique des rotors de turbomachines avec couplage fluide-structure. Modélisation tridimensionnelle*. PhD thesis, Institut des Sciences Appliquées de Lyon, 1996.
- [91] M. A. Crisfield, *Non-linear finite element analysis of solids and structures*. John Wiley & Sons, 1991.
- [92] W. Ji, A. M. Waas, and Z. P. Bažant, "Errors caused by non-work-conjugate stress and strain measures and necessary corrections in finite element programs," *Journal of Applied Mechanics*, vol. 77, no. 4, pp. 044504–044504–5, 2010.
- [93] O. Zienkiewicz and R. Taylor, *The Finite Element Method: Solid mechanics*. Butterworth-Heinemann, 2000.
- [94] S. Zhang, *Nonlinear FE Simulation and Active Vibration Control of Piezoelectric Laminated Thin-Walled Smart Structures*. PhD thesis, RWTH Aachen University, 2014.
- [95] *Ansys 15.0 Documentation—Theory reference*, 2013.

- [96] A. Laub, *Matrix Analysis for Scientists and Engineers*. Society for Industrial and Applied Mathematics, 2005.
- [97] A. Kaveh and H. Rahami, "Block circulant matrices and applications in free vibration analysis of cyclically repetitive structures," *Acta Mechanica*, vol. 217, no. 1-2, pp. 51–62, 2011.
- [98] G. S. Óttarsson, *Dynamic modeling and vibration analysis of mistuned bladed disks*. PhD thesis, University of Michigan, 1994.
- [99] G. J. Tee, "Eigenvectors of block circulant and alternating circulant matrices," *New Zealand Journal of Mathematics*, vol. 36, pp. 195–211, 2007.
- [100] F. Tisseur and K. Meerbergen, "The quadratic eigenvalue problem," *SIAM review*, vol. 43, no. 2, pp. 235–286, 2001.
- [101] L. Meirovitch and G. Ryland, II, "Response of slightly damped gyroscopic systems," *Journal of Sound and Vibration*, vol. 67, no. 1, pp. 1–19, 1979.
- [102] N. Maia and J. Silva, *Theoretical and Experimental Modal Analysis*. Engineering Dynamics Series, Research Studies Press, 1997.
- [103] W. Campbell, "Protection of steam-turbine disk wheels from axial vibration," *Proceedings of the ASME Conference 1924*.
- [104] A. Sayma, M. Vahdati, and M. Imregun, "An integrated nonlinear approach for turbomachinery forced response prediction. Part I: Formulation," *Journal of Fluids and Structures*, vol. 14, no. 1, pp. 87–101, 2000.
- [105] H. D. Afolabi, *Vibration of mistuned bladed disc assemblies*. PhD thesis, Imperial College of Science & Technology, 1982.
- [106] E. Seinturier, "Forced response computation for bladed disks-Industrial practices and advanced methods," in *12th IFToMM World Congress*, June 18–21, 2007, Besançon, France.
- [107] T. Yamamoto and Y. Ishida, *Linear and Nonlinear Rotordynamics: A Modern Treatment with Applications*. Wiley Series in Nonlinear Science, Wiley, 2001.
- [108] D. Ewins, "The effects of detuning upon the forced vibrations of bladed disks," *Journal of Sound and Vibration*, vol. 9, no. 1, pp. 65 – 79, 1969.
- [109] S. T. Wei and C. C. Pierre, "Localization phenomena in mistuned assemblies with cyclic symmetry part I: Free vibrations," *Journal of Vibration, Acoustics, Stress, and Reliability in Design*, vol. 110, no. 4, pp. 429–438, 1988.
- [110] G. Óttarsson and C. Pierre, "Vibration localization in mono-and bi-coupled bladed disks-a transfer matrix approach," in *AIAA/ASME/ASCE/AHS/ASC 34th Structures, Structural Dynamics, and Materials Conference*, vol. 1, pp. 3683–3697, 1993.

- [111] L. Meirovitch, *Computational Methods in Structural Dynamics*. Monographs and textbooks on mechanics of solids and fluids. Mechanics: Dynamical systems, Sijthoff & Noordhoff, 1980.
- [112] A. C. Pisoni, C. Santolini, D. E. Hauf, and S. Dubowsky, “Displacements in a vibrating body by strain gauge measurements,” in *Proceedings of the 13th International Conference on Modal Analysis*, pp. 119–125, 1995.
- [113] J. He and Z. Fu, *Modal Analysis*. Butterworth-Heinemann, 2001.
- [114] A. Brandt, *Noise and vibration analysis*. Wiley, 2011.
- [115] R. Pintelon and J. Schoukens, *System Identification: A Frequency Domain Approach*. New York: Wiley, 2004.
- [116] R. Allemang and A. Phillips, “The unified matrix polynomial approach to understanding modal parameter estimation: An update,” in *Proceedings of ISMA2004, International Conference on Noise and Vibration Engineering, Katholieke Universiteit Leuven, Belgium, 2004*.
- [117] H. Van Der Auweraer, P. Guillaume, P. Verboven, and S. Vanlanduit, “Application of a fast-stabilizing frequency domain parameter estimation method,” *Journal of dynamic systems, measurement, and control*, vol. 123, no. 4, pp. 651–658, 2001.
- [118] P. Verboven, *Frequency-domain system identification for modal analysis*. PhD thesis, Vrije Universiteit Brussel, Brussels, 2002.
- [119] B. Peeters, G. Lowet, H. Van der Auweraer, and J. Leuridan, “A new procedure for modal parameter estimation,” *Sound and Vibration*, vol. 38, no. 1, pp. 24–29, 2004.
- [120] P. Guillaume, P. Verboven, S. Vanlanduit, H. Van Der Auweraer, and B. Peeters, “A poly-reference implementation of the least-squares complex frequency-domain estimator,” in *Proceedings of IMAC*, vol. 21, pp. 183–192, 2003.
- [121] P. Lancaster, *Lambda-Matrices and Vibrating Systems*, vol. 94 of *International Series of Monographs on Pure and Applied Mathematics*. Pergamon, 1966.
- [122] T. De Troyer, P. Guillaume, and B. Peeters, “Polyreference frequency-domain least-squares estimation with confidence intervals,” in *Proceedings of the 26th International Modal Analysis Conference, Orlando, Florida, 2008*.
- [123] M. Colomo González, “Influence of bolted items on the results and consistency of modal analysis,” Master’s thesis, Chalmers University of Technology, 2007.
- [124] V. Giurgiutiu, *Structural Health Monitoring with Piezoelectric wafer active sensors*. Burlington: Academic Press, 2008.

- [125] N. W. Hagood, W. H. Chung, and A. Von Flotow, “Modelling of piezoelectric actuator dynamics for active structural control,” *Journal of Intelligent Material Systems and Structures*, vol. 1, no. 3, pp. 327–354, 1990.
- [126] J. B. Min, K. P. Duffy, B. B. Choi, A. Provenza, and N. Kray, “Piezoelectric vibration damping study for rotating composite fan blades,” in *Proceedings of the 14th AIAA Structures, Structural Dynamics, and Materials Conference, Honolulu, HI, April, 2012*.
- [127] V. Ruffini, C. W. Schwingshackl, and J. S. Green, *Proceedings of the 9th IFToMM International Conference on Rotor Dynamics*, ch. Prediction Capabilities of Coriolis and Gyroscopic Effects in Current Finite Element Software, pp. 1853–1862. Springer International Publishing, 2015.
- [128] G. Genta, *Dynamics of Rotating Systems*. Mechanical Engineering Series, Springer, 2005.
- [129] M. Endo, K. Hatamura, M. Sakata, and O. Taniguchi, “Flexural vibration of a thin rotating ring,” *Journal of Sound and Vibration*, vol. 92, no. 2, pp. 261–272, 1984.
- [130] M. Nikolic, *New Insights into the Blade Mistuning Problem*. PhD thesis, Imperial College London, 2006.
- [131] D. Di Maio, *SLDV Technology for Measurement of Mistuned Bladed Disc Vibration*. PhD thesis, Imperial College London, 2007.
- [132] G. Genta, “On the stability of rotating blade arrays,” *Journal of Sound and Vibration*, vol. 273, no. 4–5, pp. 805–836, 2004.
- [133] O. A. Bauchau, *Flexible multibody dynamics*. Springer, 2011.
- [134] A. Muszyńska, *Rotordynamics*. Taylor & Francis, 2005.
- [135] *NX Nastran 8—Rotor Dynamics User’s Guide*, 2011.
- [136] *NX Nastran—NX Nastran 8 Basic Nonlinear Analysis Users Guide*, 2011.
- [137] *NX Nastran—Numerical Methods Users Guide*, 2011.
- [138] V. Ruffini, C. Schwingshackl, and J. Green, “Experimental and analytical study of coriolis effects in bladed disk,” in *ASME 2015 International Design Engineering Technical Conferences and Computers and Information in Engineering Conference*, vol. 8: 27th Conference on Mechanical Vibration and Noise, pp. V008T13A070–V008T13A070, American Society of Mechanical Engineers, 2015.
- [139] B. Beirow, T. Maywald, and A. Kühhorn, “Mistuning and damping analysis of a radial turbine blisk in varying ambient conditions,” in *ASME Turbo Expo 2014: Turbine Technical Conference and Exposition*, American Society of Mechanical Engineers, 2014.

- [140] R. Parker and P. Sathe, “Exact solutions for the free and forced vibration of a rotating disk-spindle system,” *Journal of Sound and Vibration*, vol. 223, no. 3, pp. 445–465, 1999.
- [141] Smart Material Corporation, “Macro-fiber composite catalog,” 2015. Retrieved July 11th 2015 from http://www.smart-material.com/media/Datasheet/MFC_V2.2-web-2015.pdf.
- [142] Physik Instrumente, “E-835 DuraAct™ piezo driver module,” 2015. Retrieved July 11th 2015 from http://www.physikinstrumente.com/download/PI_Datasheet_E-835_20150121.pdf.
- [143] Jordil Technic, “Rotrans™: Rotary signal transmitters. datasheet rotrans 04-08-12, jordil technic 104-002,” 2015. Retrieved January 4th 2015 from http://www.rotrans.ch/fileadmin/documentation/ROTRANS_04_12_E10.pdf.
- [144] Micro-Measurements, “Precision strain gages data book.” Retrieved January 17th 2015 from <http://www.vishaypg.com/docs/50003/precsg.pdf>.
- [145] Micro-Measurements, “Strain gage selection: Criteria, procedures, recommendations.” Retrieved July 12th 2015 from <http://www.vishaypg.com/docs/11055/tn505.pdf>.
- [146] E. O. Doebelin, *Measurements systems*. McGraw-Hill, 1990.
- [147] Micro-Measurements, “Noise control in strain gage measurements.” Retrieved January 17th 2015 from <http://www.vishaypg.com/docs/11051/tn501.pdf>.
- [148] D. Feiner, J. Griffin, K. Jones, J. Kenyon, O. Mehmed, and A. Kurkov, “System identification of mistuned bladed disks from traveling wave response measurements,” in *ASME 2003 International Design Engineering Technical Conferences and Computers and Information in Engineering Conference*, pp. 1231–1240, American Society of Mechanical Engineers, 2003.
- [149] M. Géradin and D. Rixen, *Théorie des vibrations – Application à la dynamique des structures*. Masson, 1993.
- [150] P. Schmiechen, *Travelling wave speed coincidence*. PhD thesis, Imperial College of Science, Technology, and Medicine, 1997.
- [151] R. J. Allemang, “The modal assurance criterion—twenty years of use and abuse,” *Sound and vibration*, vol. 37, no. 8, pp. 14–23, 2003.
- [152] C. Morales, “Comments on the MAC and the NCO, and a linear modal correlation coefficient,” *Journal of Sound and Vibration*, vol. 282, no. 12, pp. 529 – 537, 2005.
- [153] P. Vacher, B. Jacquier, and A. Bucharles, “Extensions of the MAC criterion to complex modes,” in *Proceedings of ISMA International Conference on Noise and Vibration Engineering*, 2010, Leuven, Belgium.

-
- [154] W. Wang and J. Kirkhope, "New eigensolutions and modal analysis for gyroscopic/rotor systems, part 2: Perturbation analysis for damped systems," *Journal of Sound and Vibration*, vol. 175, no. 2, pp. 171 – 183, 1994.
- [155] C. Pierre and D. V. Murthy, "Aeroelastic modal characteristics of mistuned blade assemblies: Mode localization and loss of eigenstructure," *AIAA journal*, vol. 30, no. 10, pp. 2483–2496, 1992.

Appendix A

Data for the benchmark test case models

Stodola-Green rotor

- Shaft length: 250 mm
- Shaft inner diameter: 7 mm
- Shaft outer diameter: 10 mm
- Disc diameter: 80 mm
- Disc thickness: 40 mm
- Density: 7800 kg/m³
- Young's modulus: 207 MPa

Thin ring [129]

- Outer diameter: 176 mm
- Thickness: 0.88 mm
- Width: 20 mm
- Density: 7850 kg/m³
- Young's modulus: 210 MPa

Swept blisk [130, 131]

- Outer diameter: 540 mm
- Diameter at blade root: 188 mm

- Diameter of inner bore: 60 mm
- Blade tip gap: 8 mm
- Thickness: 3.79 mm
- Sweep angle: 15°
- Number of blades: 24
- Density: 7594 kg/m³
- Young's modulus: 207 MPa

Bladed disc-shaft assembly [127]

- Shaft length: 250 mm
- Shaft inner diameter: 7 mm
- Shaft outer diameter: 10 mm
- Disc diameter: 80 mm
- Disc thickness: 40 mm
- Blade length: 300 mm
- Blade width: 40 mm
- Diameter of inner bore: 60 mm
- Blade tip gap: 8 mm
- Blade thickness: 3 mm
- Number of blades: 9
- Density: 7800 kg/m³
- Young's modulus: 207 MPa

Appendix B

Technical drawings

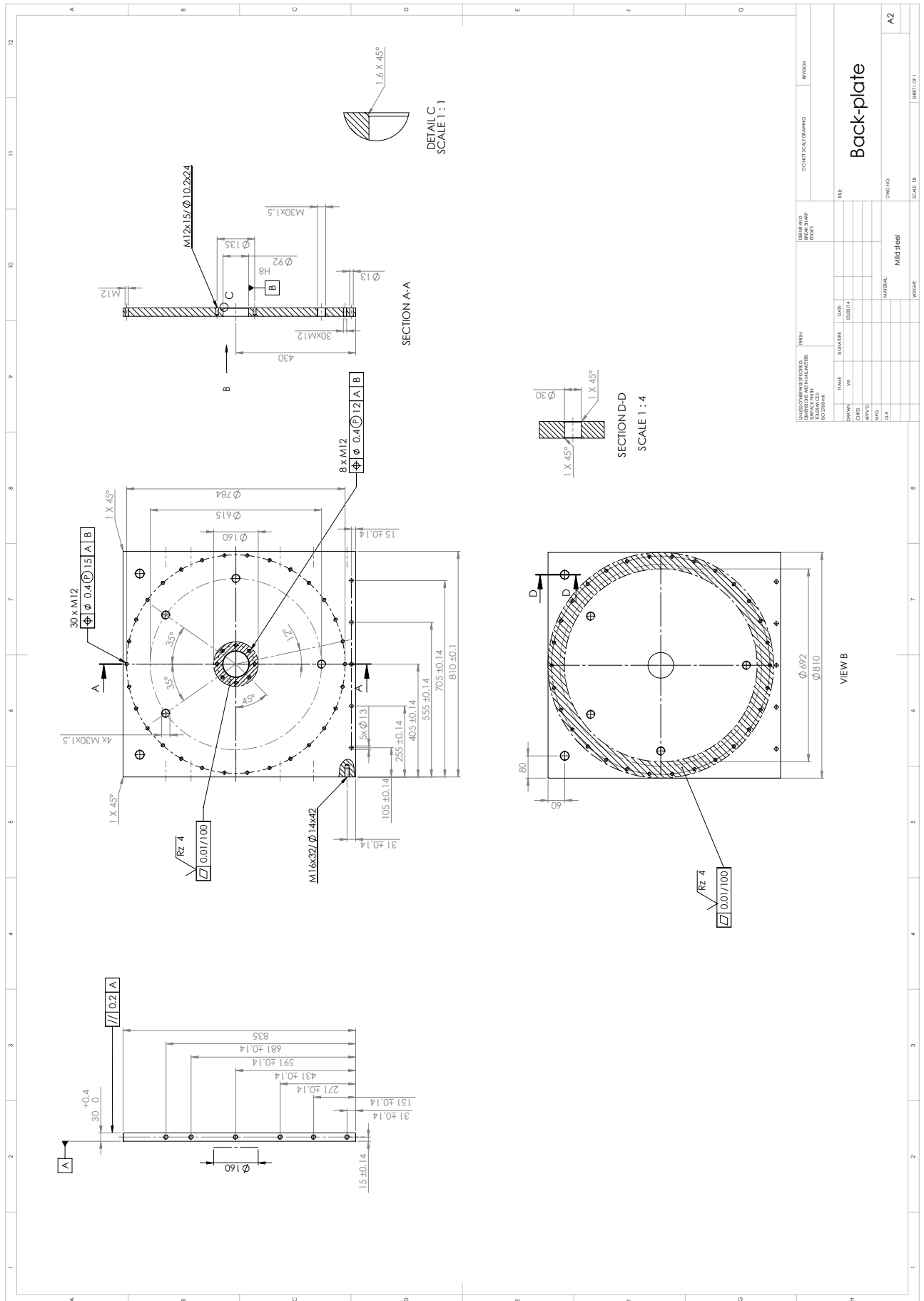


Figure B.1: Vertical back-plate

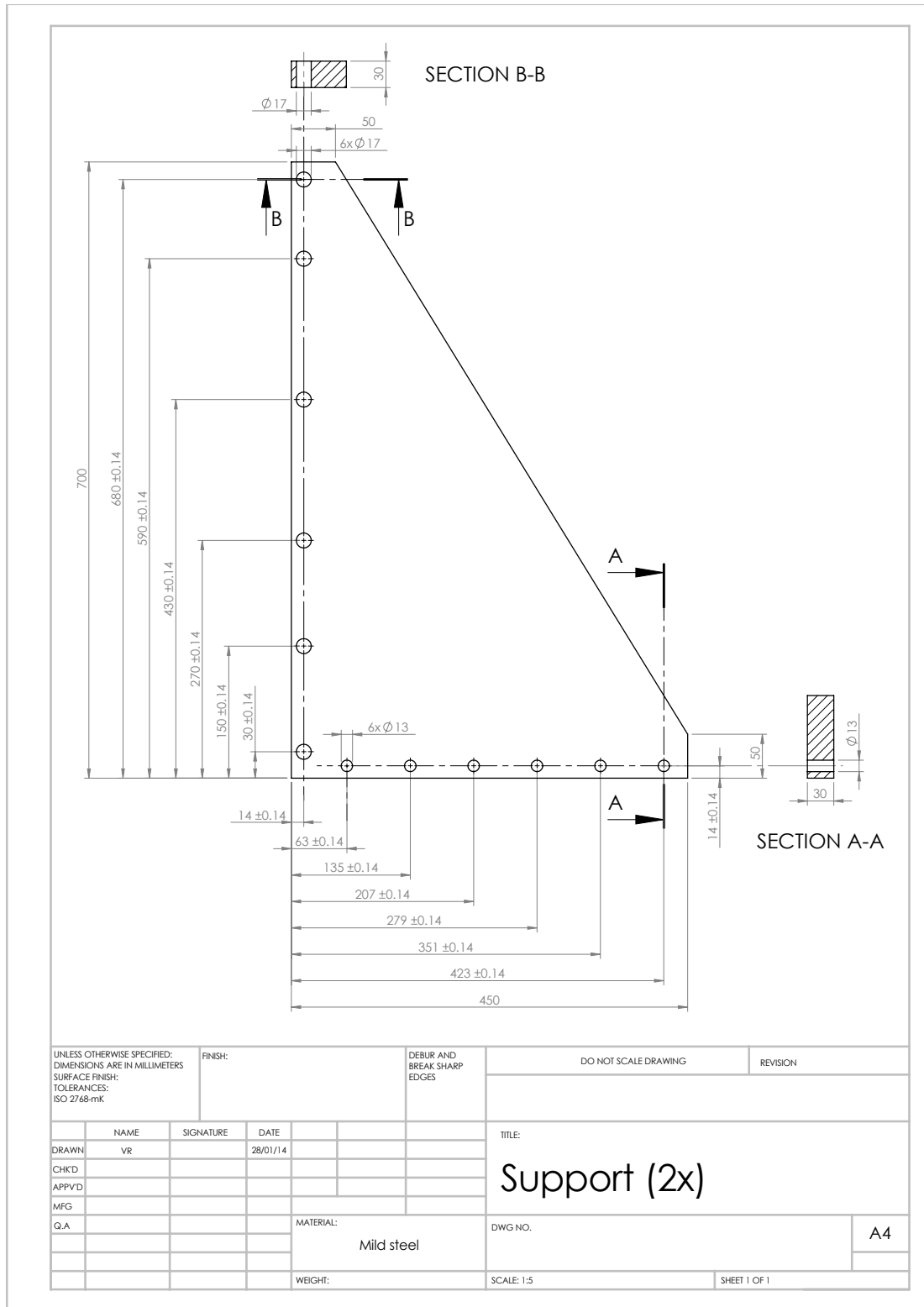


Figure B.3: Lateral supports.

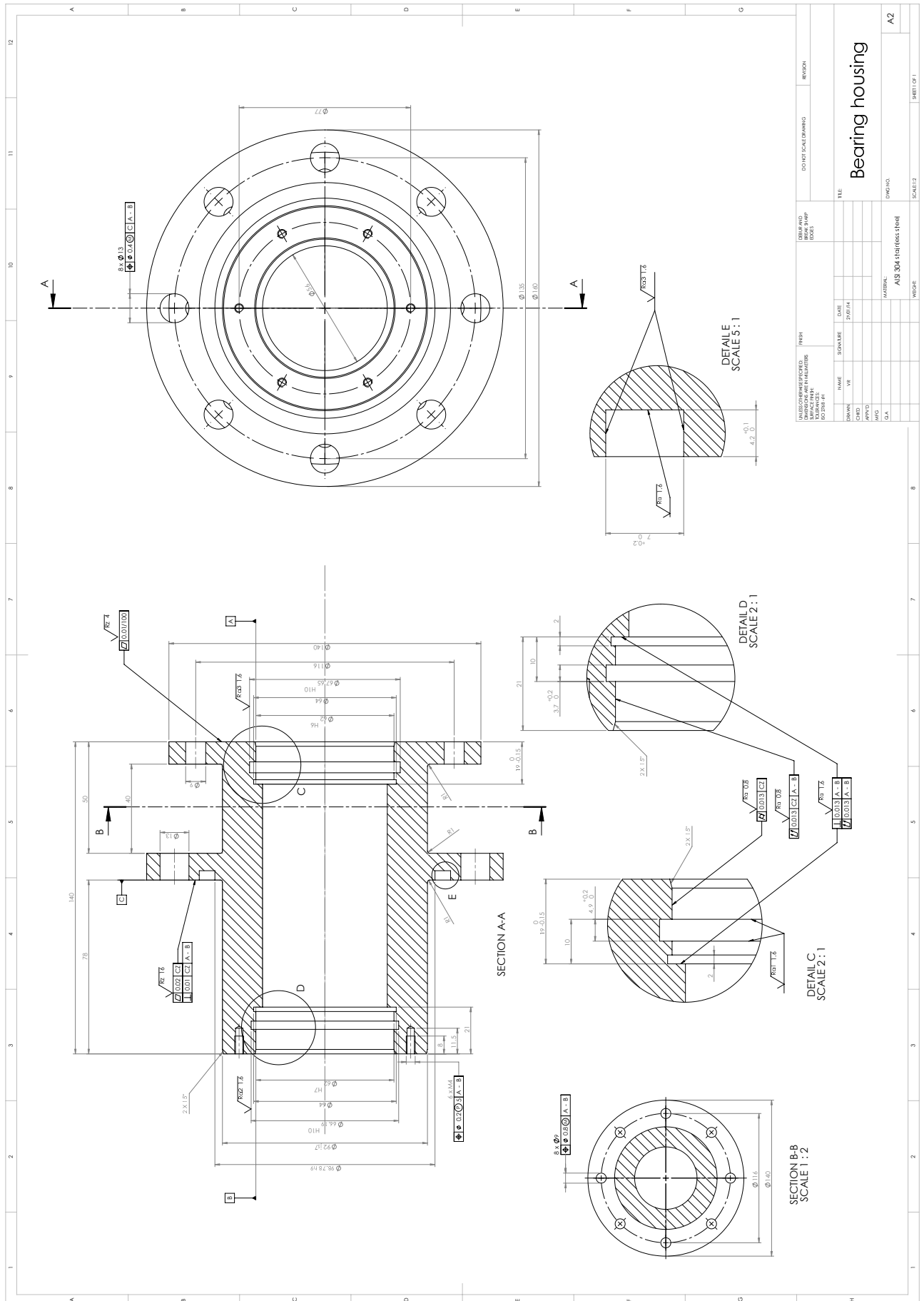


Figure B.6: Bearing housing.

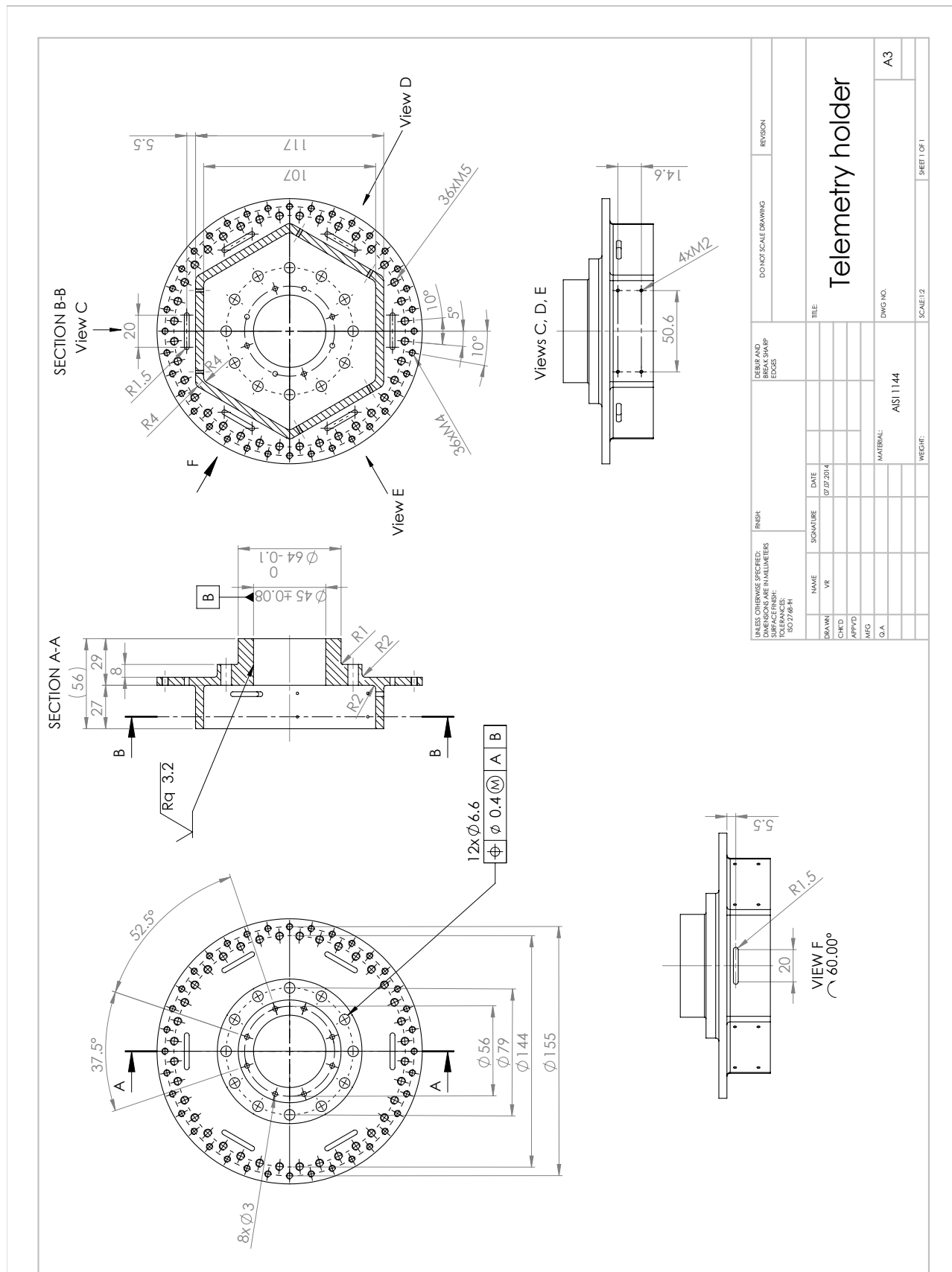


Figure B.7: Multi-function disc: telemetry holder, balancing disc, mounting for test piece.

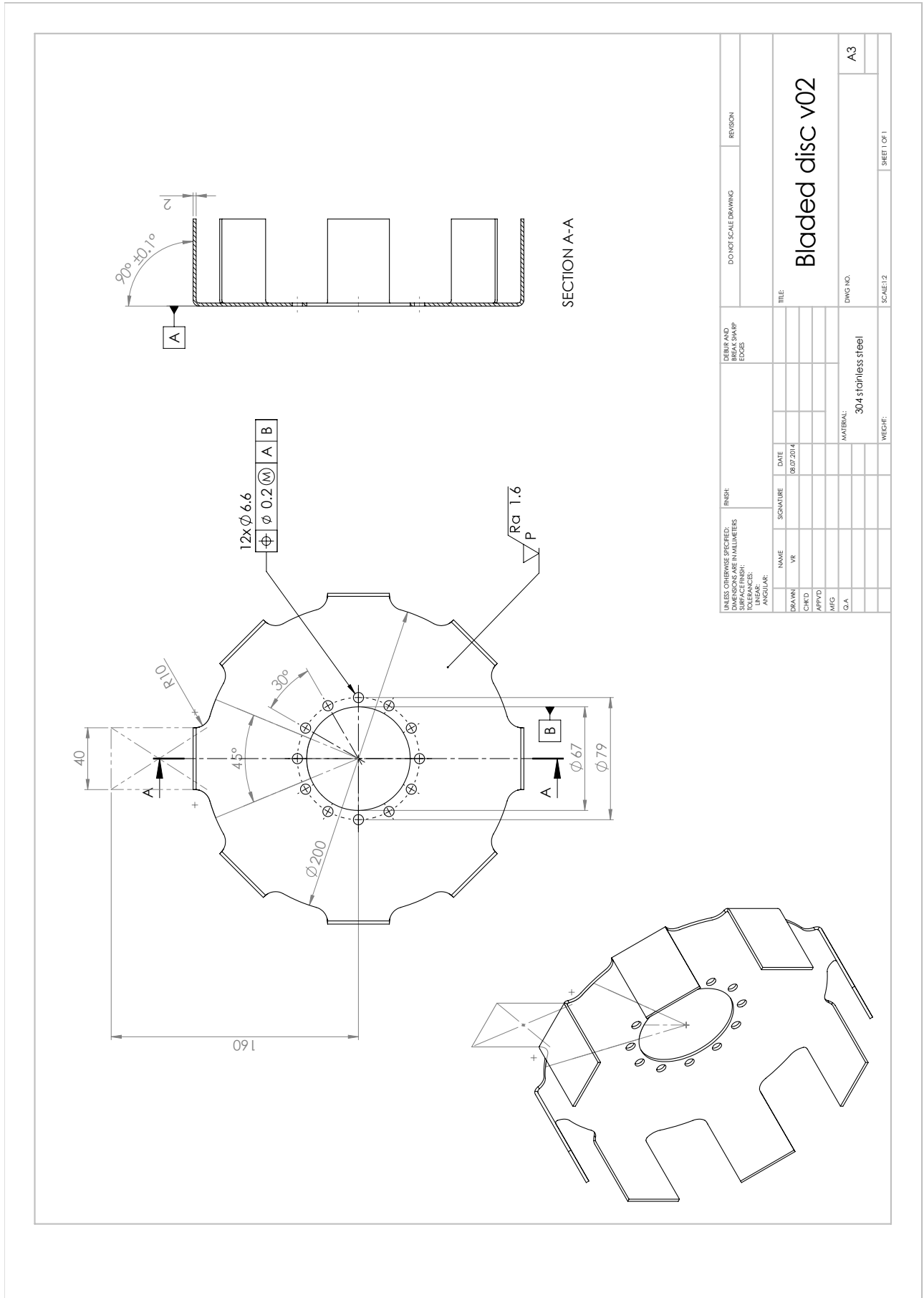


Figure B.8: Test piece.

Appendix C

Permission to reproduce own publication

03.12.2015

Dear Sir,

I am completing my PhD thesis at Imperial College London entitled 'Coriolis effects in bladed discs'.


I seek your permission to reprint, in my thesis, the published version of a paper I published in: Ruffini, V., Schwingshackl, C.W., Green, J.S. "Experimental and analytical study of Coriolis effects in bladed disk." In ASME 2015 International Design Engineering Technical Conferences and Computers and Information in Engineering Conference, 2015.

I would like to include the paper in my thesis which will be added to Spiral, Imperial's institutional repository <http://spiral.imperial.ac.uk/> and made available to the public under a [Creative Commons Attribution-NonCommercial-NoDerivs licence](#).

If you are happy to grant me all the permissions requested, please return a signed copy of this letter. If you wish to grant only some of the permissions requested, please list these and then sign.

Yours sincerely,

Valentina Ruffini



Permission granted for the use requested above:

I confirm that the paper mentioned above under the Rolls-Royce copyright can be included in the PhD thesis which will be made available via the internet, for non-commercial purposes under the terms of the user licence.

Signed:



Name: Akin Keskin

Organisation: Rolls-Royce plc

Job title: Chief of VEDS